Probing diffusion and molecular dynamics to study self-assembly and intermolecular interactions in macromolecular and colloidal systems using NMR diffusometry and spectroscopy

Veera Venkata Shravan Uppala

Dissertation submitted to the faculty of the Virginia Polytechnic Institute and State University in partial fulfilment of the requirements for the degree of

Doctor of Philosophy

In

Chemistry

Louis A. Madsen, Chair

Robert B. Moore

Feng Lin

Rui Qiao

November 15th, 2022

Blacksburg, VA

Keywords: NMR diffusometry, spectroscopy, self-diffusion, polyelectrolytes, molecular weight, block copolymer micelles, unimers, drug partitioning, semiconductor nanoparticles, quantum dot, colloid, ligand exchange

Probing diffusion and molecular dynamics to study self-assembly and intermolecular interactions in macromolecular and colloidal systems using NMR diffusometry and spectroscopy

Veera Venkata Shravan Uppala

ABSTRACT

The growing demand for technological advancements in energy storage and pharmaceuticals, driven by population growth and climate change, has created an urgent need for the development of novel materials with finely tuned and targeted properties. Polymers, with their inherent versatility, have emerged as key players in modulating the functionality of such advanced materials. However, achieving precise control over the performance of the materials requires a deep understanding of the molecular interactions, self-assembly processes, and transport phenomena that govern their behavior at the nanoscale.

This dissertation focuses on the application of advanced nuclear magnetic resonance (NMR) techniques to probe the molecular dynamics and diffusion behavior in complex macromolecular and colloidal systems. Two key NMR techniques – NMR diffusometry and dynamic NMR spectroscopy – are employed to probe the motion and exchange process of molecules within these systems. By providing insights into the dynamics of the constituents, these methods are particularly powerful in unraveling the intermolecular interactions that govern material functionality.

The materials under investigation include block copolymer micelles (BCMs), ligand-capped quantum dots (QDs), and linear polyelectrolyte chains – each with unique structural characteristics and promising applications. Block copolymer micelles are of particular interest for drug delivery applications due to their ability to encapsulate and release therapeutic agents in

controlled manner. Colloidal quantum dots, with their size-tunable electronic properties, have great potential in photovoltaics and biosensing. Linear polyelectrolytes, characterized by their charged backbones, are crucial for energy storage and biomedical applications.

Through a detailed analysis of the translational motion of molecules, this work reveals key molecular insights, including intermolecular interactions, the coexistence of molecules in distinct chemical environments, and their exchange mechanism between these environments. These findings establish critical structure-property relationships in each material system, providing a foundation for rational design and optimization of their functional performance.

The results obtained in this research not only contribute to our fundamental understanding of the molecular behavior of these complex systems but also have practical implications for design of next-generation materials. By leveraging the power of NMR-based techniques, this dissertation offers a pathway for enhancing material properties in the desired applications. The findings emphasize the critical role of molecular characterization techniques in advancing the field of material science and facilitating the development of more efficient, high-performance materials tailored to meet the demands for modern technology.

Probing diffusion and molecular dynamics to study self-assembly and intermolecular interactions in macromolecular and colloidal systems using NMR Diffusometry and Spectroscopy

Veera Venkata Shravan Uppala

GENERAL AUDIENCE ABSTRACT

Rising global challenges, such as energy storage and healthcare, demand innovations for new technologies. At the core of many of these innovations are advanced materials, which must be meticulously designed to meet specific performance requirements. Polymers, in particular, play a key role in these developments due to their versatile properties. To create materials with precise functionality, a deeper understanding of the chemistry and molecular interactions that govern their behavior is essential.

This dissertation focuses on using nuclear magnetic resonance (NMR), a powerful analytical tool, to probe molecular motions and interactions in advanced materials. Specifically, this research has developed NMR methodologies to investigate polymer-based micelles (surfactants) for drug-delivery applications, semiconductor nanoparticles for solar cells and sensor applications, and molecular weight determination of charged polymer chains.

The research aims to reveal new insights into the behavior of these materials and how such knowledge can be harnessed to design more effective systems for applications in medicine and energy. By studying molecular motions and interactions, this work aspires to contribute to the development of next-generation materials capable of addressing some of the world's most pressing challenges.

Acknowledgements

First and foremost, I would like to express my deepest gratitude to my PhD advisor, Dr. Louis A. Madsen, for his unwavering guidance and support, not only in my professional career but also in my personal life over the past seven and a half years. His passion for research, reflected in every aspect of his life, has been a source of inspiration for me to grow and mature as both a scientist and a person. I am deeply thankful for the invaluable skills I have gained under his mentorship while tackling challenging projects. His professionalism and respect have been the guiding light throughout my PhD journey.

I also sincerely appreciate my committee members, Prof. Robert Moore, Prof. Feng Lin, and Prof. Rui Qiao, for their insightful feedback and discussions. Their perspectives have helped me not only to better understand my projects but also to cultivate the ability to see the broader impact of my work. I have learned so much from their expertise in chemistry and physics, and I am deeply grateful for their contributions.

I am equally grateful to my collaborators, Prof. Megan L. Robertson, and Dr. Tyler J. Cooksey from University of Houston, Prof. Ralph H. Colby and Dr. Aijie Han from Pennsylvania State University, and Prof. Jillian L. Dempsey, Jennica Kelm, and Christian Dones Lassalle from University of North Carolina Chapel Hill. Their constant presence, technical support, and stimulating discussions have been crucial in enhancing my understanding of the materials I studied and improving the quality of my work.

I consider myself fortunate to have worked alongside the wonderful members of the Madsen group. Their camaraderie and collective drive for growth have been instrumental in my development as a scientist. I would like to extend special thanks to Dr. Xiuli Li, Dr. Andrew

Korovich, Dr. Rui Zhang, Dr. Deyang Yu, and Dr. Curt Zanelotti, who helped me settle into the group and ensured that I mastered the nuances of NMR instrumentation.

I have also cherished my collaborations with Nicholas Pietra, whose enthusiasm for NMR led to many amazing discussions, and together we developed customized pulse sequences tailored to my project needs. Additionally, I am grateful to have worked with Rebecca Martin, Mehedi Hasan, Jubayer Alam, and Alex Irwin, whose enthusiasm and dedication brought renewed energy during the final stages of my PhD.

I am incredibly thankful for the friends I made at Virgnia Tech, whom I consider my Blacksburg family. I should specially thank Dr. Ayush Asthana, Satyanarayana, Dr. Jopaul Mathew, and many others for their constant guidance and navigating me to take right steps for future. I would also thank my dear friend/sister Rahaf Rousan for patiently supporting me and guiding me in the right direction during my tumultuous period of my PhD. Their constant support has made my life easier when away from my family from India.

Lastly, I owe a deep debt of gratitude to my parents and my brother's family. Their unconditional love, unwavering support, and endless encouragement have been my anchor throughout the highs and lows of my PhD journey. The values they instilled in me have given me the confidence and compassion to navigate this experience. I believe PhD is not the endpoint but the beginning of a new journey, and I look forward to the surprises and challenges that lie ahead.

Table of Contents

Attributions

Multiple peers have helped me, guided me and contributed throughout these research projects. A brief description of their contributions is added here:

Prof. Louis A. Madsen (Research Advisor)

Professor at Department of Chemistry and Macromolecule Innovation Institution, Virginia Tech

Dr. Xiuli Li

Former graduate student in Dr. Madsen's lab at Virginia Tech and collaborator on Chapters 3-5

Prof. Ralph H. Colby

Professor at Department of Materials Science and Engineering, Pennsylvania State University and collaborator on Chapter 3

Dr. Aijie Han

Former graduate student in Dr. Colby's group at Department of Materials Science and Engineering, Pennsylvania State University and collaborator on Chapter 3

Prof. Megan L. Robertson

Professor at Department of Chemical and Biological Engineering, University of Houston and collaborator on Chapter 4

Dr. Tyler J. Cooksey

Former graduate student in Dr. Robertson's lab at Department of Chemical and Biological Engineering, University of Houston and collaborator on Chapter 4

Prof. Jillian L. Dempsey

Professor at Department of Chemistry, University of North Carolina, Chapel Hill and collaborator on Chapter 6

Christian Y. Dones Lassalle

Graduate student in Dr. Dempsey's lab at Department of Chemistry, University of North Carolina, Chapel Hill and collaborator on Chapter 6

Jennica E. Kelm

Graduate student in Dr. Dempsey's lab at Department of Chemistry, University of North Carolina, Chapel Hill and collaborator on Chapter 6

John B. Matson

Professor at Department of Chemistry and Macromolecule Innovation Institution, Virginia Tech and collaborator on Chapter 5

Dr. Ryan J. Carrazzone

Former graduate student at Department of Chemistry and Macromolecule Innovation Institution, Virginia Tech and collaborator on Chapter 5

Chapter 1: Probing molecular diffusion and dynamics to study self-assembly and intermolecular interactions in macromolecular and colloidal systems

1.1. Motivation and goals

The increasing global population and the challenges posed by climate change are driving the demand for new technology advancements, particularly in energy storage and pharmaceuticals. At core of these innovations is the creation of new materials, with polymers playing a crucial role in modulating their functionality. However, to achieve precise control over the performance of these materials, it is essential to deepen our understanding of the fundamental principles of chemistry and materials science that influence their functionality. Characterization tools, such as nuclear magnetic resonance (NMR), are crucial in this endeavor, providing key insights into the molecular interactions that govern the self-assembly and the performance of the materials developed. NMR techniques, like NMR diffusometry and dynamic NMR spectroscopy, are poised to bridge critical knowledge gaps in material development, enabling breakthroughs in material formulations. These techniques hold great potential to unveil deeper insights into the properties and mechanisms underlying advanced materials.

This dissertation introduces NMR-based characterization techniques aimed at probing diffusion and molecular dynamics of macromolecular and colloidal systems. The overarching goal is to leverage these techniques to inform the design and development of materials for advanced applications. The focus is on block copolymer micelles (BCMs), colloidal quantum dots (QDs), and long linear polyelectrolyte chains, materials that have significant potential in drug delivery, photovoltaics, biosensors, and energy storage applications.

This chapter begins with a theoretical exploration of translational motion in small molecules, which extends to the characterization of macromolecular sizes, that govern the self-assembly mechanisms and functionality of the macromolecular and colloidal systems. Section 2 contrasts the unique behavior of polyelectrolyte chains with neutral polymers, introducing the theoretical models for determining the molecular weight of polyelectrolytes. Section 3 examines the core and shell-forming components of the block copolymer micelles (BCMs) for drug-delivery applications, also exploring the effects of drug partitioning and methods to quantify this parameter. Section 4 addresses the design challenges and knowledge gaps in semiconductor colloidal particles, particularly for applications in photovoltaics and biosensors.

Chapter 2 introduces and provides and in-depth overview of NMR diffusometry and dynamic NMR spectroscopy techniques, focusing on their applications in studying molecular transport, thermodynamic partitioning (populations), and kinetic exchange rates. Chapter 3, 4, 5, and 6 will present insights into specific polymer-based (polyelectrolytes and micelles) and nanoparticle (quantum dot) systems gained from these characterization techniques, highlighting key parameters important for the design of next-generation materials. **Figure 1.1** below gives an overview of the materials investigated, the experimental methods utilized, and the key outcomes derived from those studies.

	Polyelectrolytes	Block Copolymer Micelles	Semiconductor Colloids
Materials	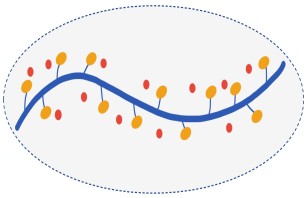	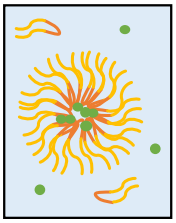	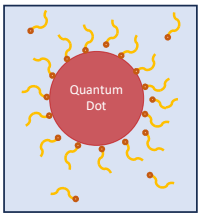
Experimental Methods	• ^{1}H NMR spectroscopy • PFG NMR diffusometry • SAXS • Static light scattering	• ^{1}H NMR spectroscopy • PFG NMR diffusometry • Variable temperature NMR	• ^{1}H NMR spectroscopy • PFG NMR diffusometry • Variable temperature NMR • Dynamic NMR
Key Outcomes	• Simple and accurate molecular weight (M_n) determination • Applicable concentration and molecular weight range	• Micelle size determination • Micelle-unimer coexistence behavior • Drug partitioning (K_p)	• QD size determination • Ligand partitioning • Thermodynamics and kinetics of ligand exchange • $\tau_{exchange}$, ΔH, ΔS, E_a

Figure 1.1: An overview of the materials investigated, experimental methods used, and the key outcomes derived from the studies presented in this thesis.

1.2. Translational motion of molecules

In 1827, Robert Brown observed the random motion of pollen particles suspended in water, concluding that it was not due to living organisms.[1,2] This phenomenon, now known as Brownian motion, was further developed in 1905 when Albert Einstein formulated a theory[3] that linked the diffusion coefficient D to the mean square displacement $\langle x^2 \rangle$ (root-mean-square RMS displacement $r_{RMS} = \sqrt{\langle r^2 \rangle}$) over diffusion time (t) as expressed in the **Equation 1.1.1**.

$$\langle r^2 \rangle = 2Dt \qquad 1.1.1$$

Here, D depends on the average kinetic energy of the molecule as shown in **Equation 1.1.2**

$$D = \mu kT \qquad 1.1.2$$

where, k is the Boltzmann constant, T represents the temperature of the solution, and μ denotes the mobility of the diffusing species, which is inversely related to the drag experienced by the particle. The drag is influenced by both attractive and repulsive interactions with the surrounding

molecules, as well as the forces needed to displace molecules out of the particle's path. As the particle size increases, its mobility decreases due to increased interactions with the surrounding molecules. George Stokes compared these interactions to the bulk viscosity (η) and the particle's hydrodynamic (solvation) radius (r_h), as described in **Equation 1.1.3 [references]**:

$$\mu = \frac{1}{a\pi\eta r_h} \qquad 1.1.3$$

Where a is a friction-related factor. By combining **Equations 1.1.2** and **1.1.3**, the relationship between D, the bulk properties of the solution (viscosity, η), and the particle's size can be expressed using the Stokes-Einstein equation (**Equation 1.1.4**).

$$D = \frac{kT}{a\pi\eta r_h} \qquad 1.1.4$$

Figure 1.2 illustrates the relationship between the size of the particle (both ligand and ligand-capped particle) and its RMS displacement (r_{RMS}). For a simple case of a spherical particle larger than its surrounding environment, Einstein deduced the friction factor $a \approx 6$.[4] By measuring D, we can quantify the size and motions of particles such as BCMs or polymer chains, using **Equation 1.1.4**. This also helps in understanding the dynamics and transient interactions within the system.

Several techniques, such as dynamic light scattering (DLS), fluorescence correlation spectroscopy, neutron scattering, were developed to measure D.[5–8] However, the most powerful method used is pulsed-field-gradient (PFG) NMR diffusometry, due to its non-destructive nature, minimal sample preparation requirements, and high reliability.[9–16] This technique can identify different chemical species and can also quantify the population fractions of species in different states, which is essential for studying the thermodynamics of molecular mechanisms in complex systems. Further details on PFG NMR diffusometry are discussed in Chapter 2.

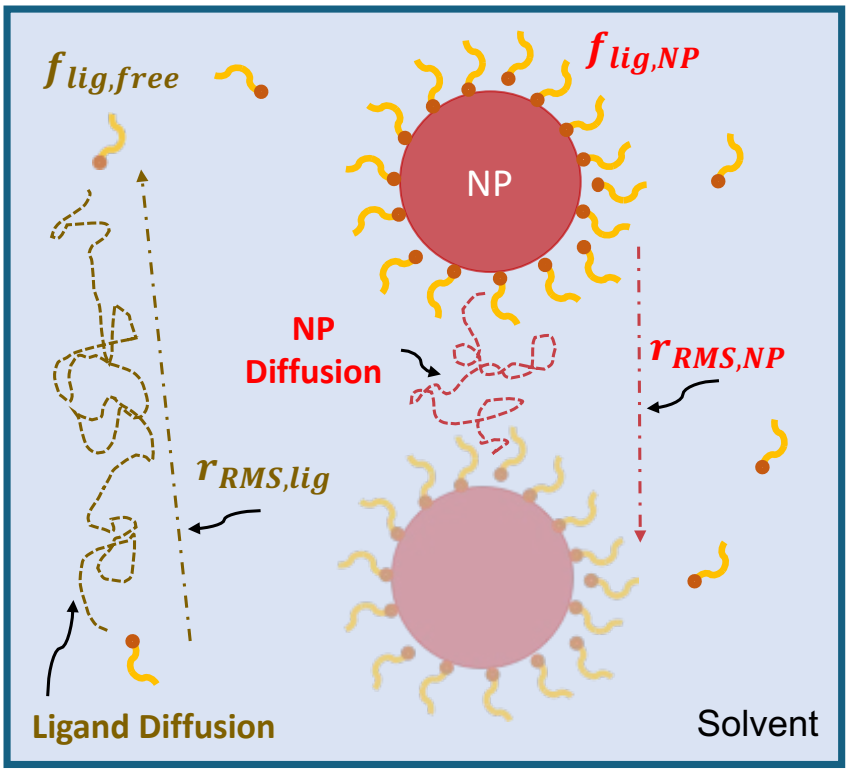

Figure 1.2: A schematic illustrating the Brownian motion of ligand and ligand-capped nanoparticle (NP) in a solvent medium and ligand partitioning ($f_{lig,free}$ and $f_{lig,NP}$) in different phases. Particle diffusion is influenced by particle size, as described by the Stokes-Einstein equation (**Equation 1.1.4**). Due to its large size, the NP diffuses slower compared to the smaller ligands. As a result, the displacement of NP (r_{RMS}, **Equation 1.1.1**) is smaller than that of the free ligand in the medium.

In my thesis, I applied the above translational motion theory to gain a comprehensive understanding on the macromolecular dynamics, specifically polyelectrolytes, block copolymer micelles (BCMs), and semiconductor colloidal particles. For polyelectrolytes, we developed a model combining Stokes-Einstein and the and a scaling theory for polyelectrolytes to determine its molecular weight (more details in section 1.2).[12] This study provides new understanding of polyelectrolytes dynamics and their potential applications in solid-state batteries and separation membranes.

For BCMs, using NMR diffusometry, we quantified the population fractions of polymer chains in different phases (micelles and free unimers) and investigated the effects of polymeric-core mobility (glass transition temperature, T_g)[11] on the polymer chain dynamics. We also examined drug/cargo partitioning in different phases, giving us a critical parameter partition coefficient (K_p),[14] which is crucial for designing and optimizing drug-delivery formulations.

For colloidal particles with a semiconductor quantum dot (QD) core and a ligand shell, we probed ligand dynamics to investigate the thermodynamics of multiple ligand binding modes on the QD surface and kinetics of the ligand exchange mechanism. This study offers insights on the affects of ligand shell on the optoelectronic performance of the QD, allowing us to identify key synthetic parameters essential for tuning the semiconductor properties for various applications.

All these materials were characterized using a combination of different NMR methods, including diffusometry, variable temperature (VT) and dynamic NMR spectroscopy, whose details are discussed in Chapter 2. In the following sections, I introduce the basic concepts on the macromolecular and self-assembled systems that I have studied in my research. I also highlight the existing research gaps which can be effectively addressed by probing molecular dynamics and diffusion.

1.3. Polyelectrolytes

Polyelectrolytes are unique class of polymer chains characterized by ionizable groups along the chain's backbone. Unlike neutral polymers, which lack charged components, polyelectrolytes dissociate in polar solvents like water, resulting in charged polymer chains and the release of counterions into the solution.[17–22] Polyelectrolytes are classified as polycations (positively charged), polyanions (negatively charged), or polyampholytes (containing both positive and negative charges). Due to the electrostatic repulsion between charged groups,

polyelectrolytes typically adopt more extended, rod-like conformations when dissolved in solution, in contrast to the random coil structures typical of neutral polymers, as depicted **Figure 1.3**.[17–21,23]

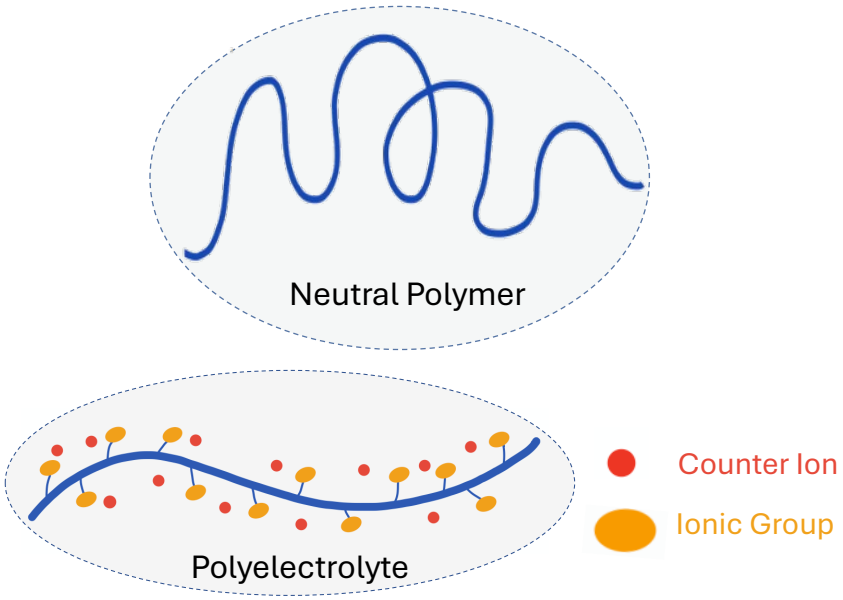

Figure 1.3: A random coil conformation of a neutral polymer under dilute conditions. In contrast, polyelectrolytes adopt an extended conformation due to electrostatic repulsion between ionic groups on the chain.

These long-range electrostatic interactions give polyelectrolytes higher viscosities compared to neutral polymers at similar concentrations, owing to greater transient interactions between polyelectrolyte chains. These interactions also contribute to greater shear thinning, as the disruption of inter-chain electrostatic forces and the alignment of extended chains occur during the flow.[24] Additionally, the counterion cloud surrounding polyelectrolytes makes them more sensitive to environmental factors such as pH, ionic strength, and counterion condensation. The unique dynamics of polyelectrolytes, driven by the electrostatic interactions and counterion effects, result in distinct macroscopic properties compared to neutral polymers. Leveraging their charge-based properties, polyelectrolytes find use in various applications, such as thickeners or emulsifiers in

cosmetics, membranes in waste-water treatment and fuel-cells, and drug-carriers in biomedical applications.[23,25–28]

Despite their potential in numerous applications, polyelectrolytes have been described as the "least understood form of condensed matter," a characterization famously quoted by Nobel laureate P. G. de Gennes.[29] The delicate balance between the electrostatic repulsions along the polymer chain and the entropic penalty for chain stretching leads to unreliable molecular weight measurement when using techniques such as gel permeation chromatography (GPC) developed for neutral polymers.[18,19,21,22,30–32] Chemists synthesizing new ionic polymers face challenges to accurately measure their molecular weight and dispersity, a fundamental requirement that can significantly impact the advancement of materials for various applications. More details on the limitations of different standard techniques are presented in Chapter 4. Thus, we developed a model combining chain conformational dynamics (Rouse model)[17–19,33] and translational dynamics (Stokes-Einstein model) of polyelectrolytes to accurately determine polyelectrolyte's molecular weight and its details are explained in the following section.

1.3.1 Background theory for determining polyelectrolytes' molecular weight

Polyelectrolytes, in dilute conditions without added salt, adopt an extended rod-like conformation due to electrostatic repulsions along the backbone of the chain (**Figure 1.3**). The chain contour length for any polymer is given by $L = \frac{bN}{B}$, where b is the repeat unit length, N is the number of monomer units per chain.[17–20,29,33] Here, B is a dimensionless chain contraction factor and it depends on polyelectrolyte's conformation. Strongly charged polyelectrolytes typically have $B \approx 3$ due to the stretching of the polymer caused by electrostatic repulsions.[34] Let c denote the number density of repeat units in solution (repeat units/Liter) without added salt. c^* denotes the overlap concentration, where the polymers's pervaded volume begin to overlap but do

not entangle. This overlap concentration also marks the boundary for dilute and semidilute unentangled regimes for a polymer as illustrated in **Figure 1.4**. At c^*, monomer number density matches the number density of a single chain within the pervaded volume L^3 given by:

$$c^* \cong \frac{N}{L^3} \cong \frac{B^3}{b^3 N^2} \qquad 1.2.1$$

For neutral polymers in dilute conditions $c^* \propto N^{-1/2}$.[17–19,29,33] Since $c^* \propto N^{-2}$ for polyelectrolytes, it is evident that the overlap concentration c^* for polyelectrolytes is much lower than neutral polymers of the same molecular weight and it further decreases inversely with square of the degree of polymerization N. Therefore, the semidilute regime is an ideal concentration range for probing polyelectrolyte's dynamics, as it contains a sufficient number of chains to study with adequate measurement signal strength. However, if the concentration exceeds the entanglement concentration c_e, chain entanglements further affect the scaling behavior and the dynamics of the polyelectrolyte chains, complicating the model.

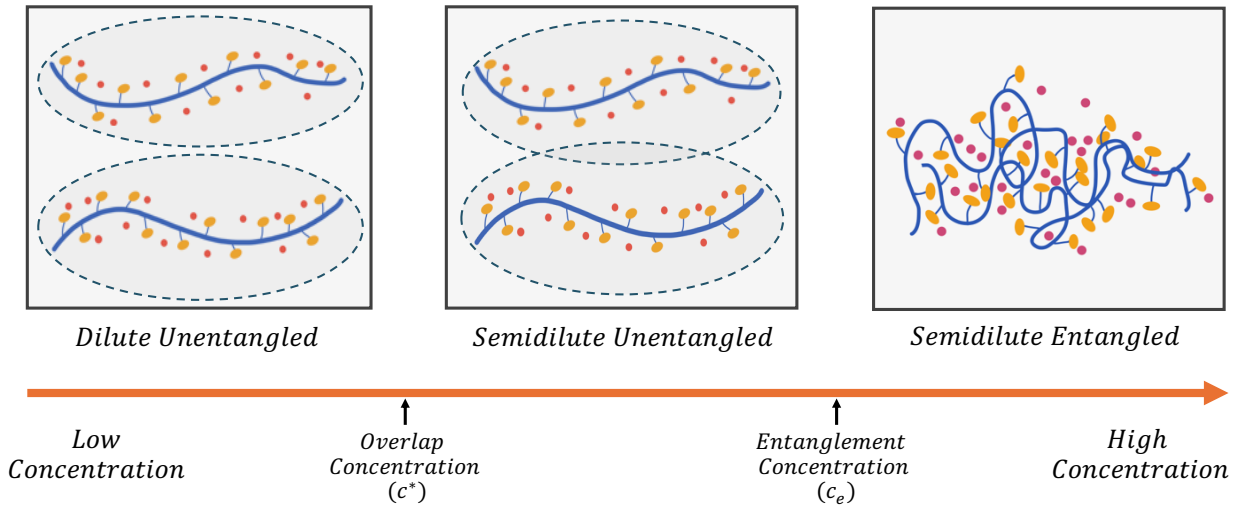

Figure 1.4: Concentration regimes of a polymer. For $c < c^*$(dilute unentangled), polymer chains are unentangled, and their pervaded volumes do not overlap (dotted circles). For $c^* < c < c_e$ (semidilute unentangled), the polymer chains are still unentangled, but their pervaded volumes overlap. For $c > c_e$ (semidilute entangled), the polymer chains begin to entangle affecting the

dynamics of the polymer chains. Due to their extended conformation, polyelectrolytes have very low c^*, resulting in a broad semidilute unentangled concentration range.

Another important parameter to consider in this model is the correlation length scale ξ, which represents the average distance from any monomer on one chain to the nearest monomer on different chain.[35,36] Below ξ length scales, nearly all monomers belong to same polymer chain. Since ξ also represents the effective electrostatic screening length of a polyelectrolyte in semidilute unentangled regime, the expression for ξ is given by:

$$\xi \cong \left(\frac{B}{cb}\right)^{1/2} \left[1 + \frac{2c_s}{fc}\right]^{1/4} \qquad 1.2.2$$

Here, c and c_s are number density of monomers and salt anions/cations in solution respectively, while f denotes the fraction of monomers bearing an effective charge. The term $\frac{2c_s}{fc}$ represents the ratio of number densities of salt ions and free counterions. Under low-salt conditions where $\frac{2c_s}{fc} \ll 1$, then **Equation 1.2.2** simplifies to $\xi \cong \left(\frac{B}{cb}\right)^{1/2}$.

ξ can be easily determined from small-angle X-ray scattering (SAXS) measurements on dilute polyelectrolyte solutions.[35,36] Its scattered spectrum provides a peak at the wavevector $q = 2\pi/\xi$ as illustrated by polystyrene sulfonate polymer (**Figure 1.5)**.

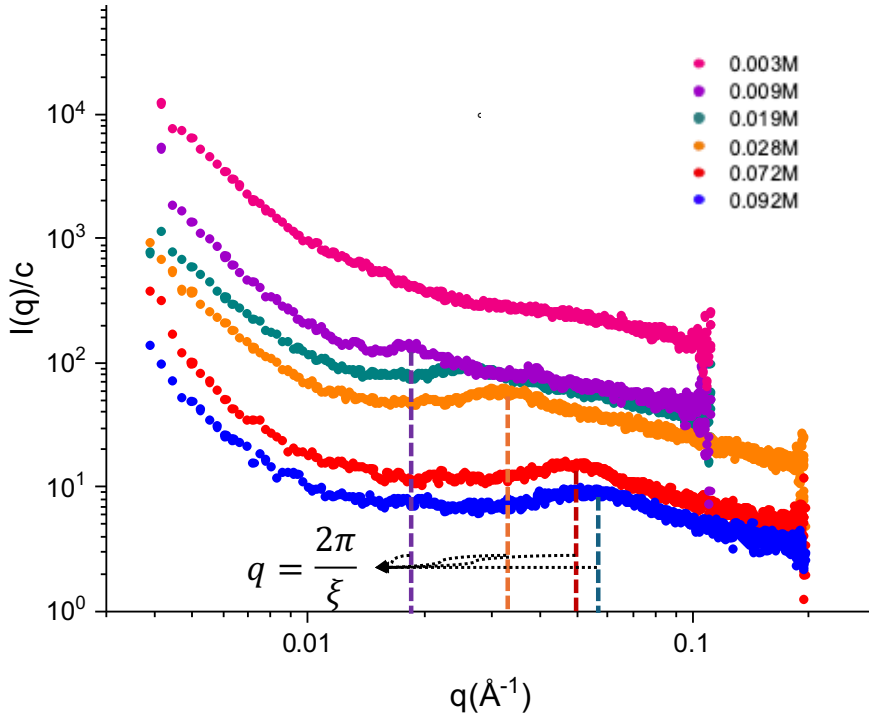

Figure 1.5: SAXS data for poly(styrene sulfonate) (PSS) in water at different concentrations. The peak from the SAXS scattered spectrum enables us to determine the correlation length (ξ) (equation in the figure)

In the semidilute regime, on scales larger than ξ or electrostatic persistence length, the polyelectrolyte chain conformation can be described as a random walk of correlation blobs. Then the end-to-end distance R of the chain is then given by

$$R \cong \left(\frac{b}{cB}\right)^{1/4} \left[1 + \frac{2c_s}{fc}\right]^{-1/8} N^{1/2} \qquad 1.2.3$$

Since, the effects of electrostatic and hydrodynamic interactions are screened at scales beyond ξ, the Rouse model is ideal for describing chain relaxation dynamics. The characteristic relaxation time τ is given by:

$$\tau \cong \frac{\eta_s b^3}{kT} B^{-3/2} N^2 (cb^3)^{-1/2} \left[1 + \frac{2c_s}{fc}\right]^{-3/4} \qquad 1.2.4$$

Here, η_s is the viscosity of the solvent. Relaxation time τ can be measured using a rheometer, which provides the time taken by the polymer chain to diffuse or move a distance of order of its own size. The diffusion coefficient D, which measures molecular diffusion, is related to τ as shown in **Equation 1.2.5**. [20,33] This equation also gives the dependence of the D with degree of polymerization N.

$$D \approx \frac{R^2}{6\tau} \approx \frac{BkT}{6\eta_s bN}\left[1 + \frac{2c_s}{fc}\right]^{1/2} \qquad 1.2.5$$

The ratio of D and ξ^2 (from **Equation 1.2.5** and **1.2.2**) eliminates dependency on the chain contraction factor B, repeat unit length b, and salt concentration c_s yielding:

$$\frac{D}{\xi^2} \cong \frac{ckT}{6\eta_s N} \qquad 1.2.6$$

The term c/N gives the number density of chains, which allows us to determine the molecular weight (MW) of the polymer chain using the **Equation 1.2.7**

$$MW = \frac{c_m N_{Av}}{c/N} = c_m N_{Av}\left(\frac{\xi^2 kT}{6\eta_s D}\right) \qquad 1.2.7$$

where, c_m is the mass concentration of the polyelectrolyte (g/L) and N_{Av} is the Avogadro's number. Thus, by measuring ξ and D from SAXS and NMR diffusometry respectively, we can determine the molecular weight of the polyelectrolytes. **Figure 1.6** gives an overview of the model, and the measurements required to determine the molecular weight of polyelectrolytes. In chapter 3 of the thesis, we purchased poly(styrene sulfonate) (PSS) polymers of known molecular weights to probe chain dynamics and verify the developed model (**Equation 1.2.6** and **1.2.7**). More details on the experimental conditions and conclusions regarding this model are discussed in that chapter.

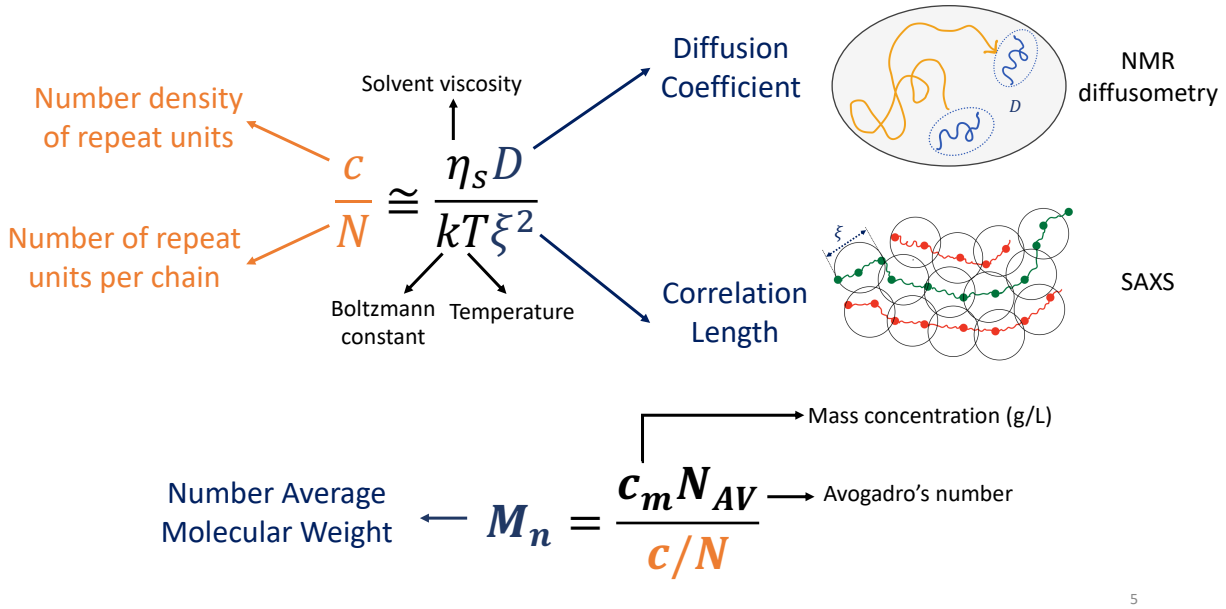

Figure 1.6: Overview of the model developed to determine the molecular weight of polyelectrolytes from NMR diffusometry and SAXS measurements.

1.4. Micelles

Micelles are self-assembled structures formed by amphiphilic molecules, such as surfactants or block copolymers, which contain both hydrophilic and hydrophobic segments. When these amphiphilic molecules are introduced into a selective solvent, they spontaneously aggregate into micellar nanostructures.[37] Micelle formation occurs when the concentration of these amphiphiles exceeds the 'critical micelle concentration'(CMC). Typically, block copolymers exhibit a lower CMC (10^{-6} and 10^{-7} M) compared to surfactants (10^{-4} to 10^{-5} M), due to their relatively higher molecular weights.[38–40] The morphology and physical properties of micelles, including osmotic pressure, conductivity, and interfacial tension, are influenced by environmental factors such as solvent properties, temperature and pH.[11,13,15]

Various techniques, including fluorescence spectroscopy, light scattering, gel permeation chromatography, and NMR have been used to study micelle formation and behavior.[41,42] My

research builds on this knowledge by using ^{1}H NMR and NMR diffusometry to investigate drug partitioning in micellar systems and micelle-unimer coexistence which is detailed more in Chapter 4 and 5 of this thesis.

1.4.1. Block copolymer micelles (BCMs) for drug-delivery applications

The therapeutic efficacy of many drugs is hindered by factors such as, poor solubility, rapid degradation in vivo, and non-specific biodistribution, which can lead to increased toxicity.[43–46] For example, many anticancer drugs are water insoluble, restricting their dosage due to severe side effects. Targeted drug-delivery systems, particularly those utilizing amphiphilic block copolymers, can address these challenges by enhancing drug stability, improving pharmacokinetics and enabling selective release at target sites.

Amphiphilic block copolymers self-assemble into micelles, with their hydrophobic core encapsulating drugs while the hydrophilic shell stabilizes the structure in aqueous environment. The morphology of these micelles can be controlled by tuning parameters such as block length, solvent composition, and chemical modifications. Israelachvili developed a thermodynamic model for self-assembly systems, defined by packing parameter p.[47] The packing parameter p correlates the morphology of self-assembled structures with the relative volumes of the hydrophobic and hydrophilic segments of the block copolymer chain as shown in the equation:

$$p = \frac{v}{a_o l_c} \qquad 1.3.1$$

Where v is hydrophobic volume, a_0 is interfacial area of the hydrophilic block at the core-shell interface, and l_c is hydrophobic chain length normal to the interface (see **Figure 1.7**). By precisely tuning the block copolymer parameters we can exert control over the size and morphology of the

micelles (see **Figure 1.7**).[46] This control is crucial in designing drug-delivery systems, as micelle size directly impacts drug release rate, targeted delivery, and therapeutic efficacy.

Poly(ethylene Glycol) (PEG, also known as PEO) is commonly used as the hydrophilic block due to its biocompatibility, chain flexibility, and ability to shield micelles from non-specific interactions.[48–50] However, alternatives such as, poly(vinyl alcohol) (PVA), poly(vinyl propylene) (PVP) and polysaccharides are also explored to address PEG's limited biodegradability and potential immunogenicity. [38,51]

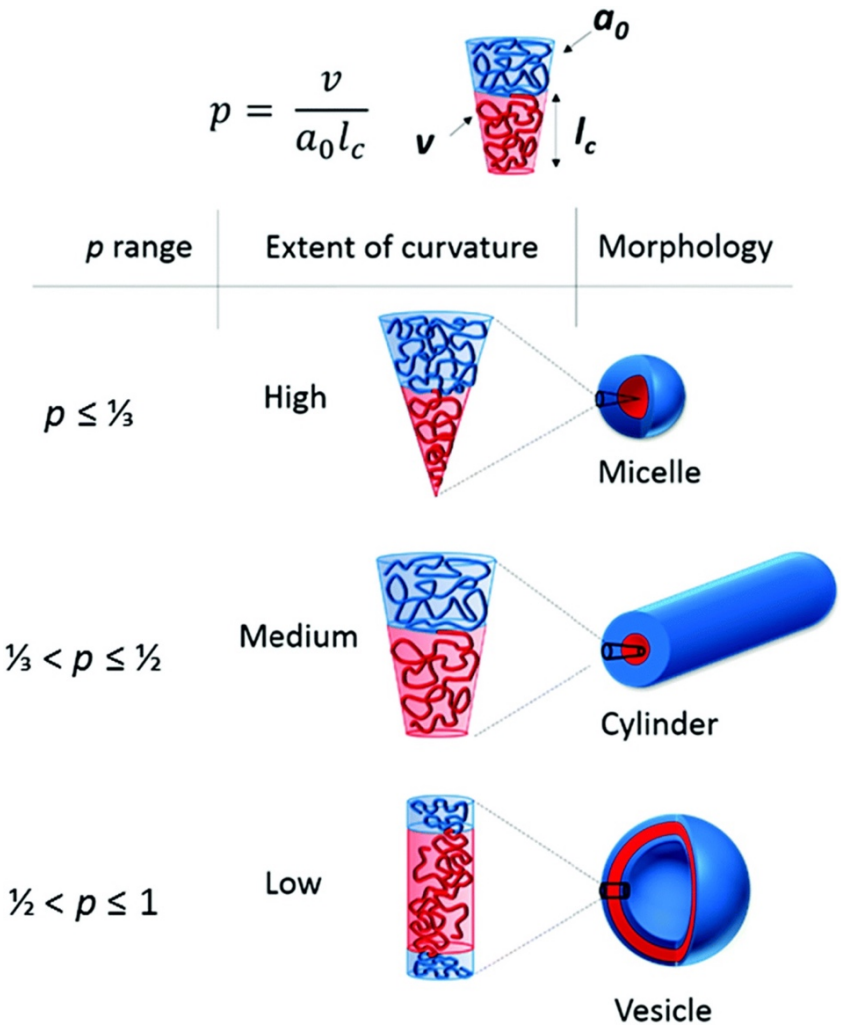

Figure 1.7: The morphology of self-assembled block copolymers depends on the packing parameter p (**Equation 1.3.1**). These polymers can self-assemble into spherical micelles ($p \leq$

$1/3$), cylindrical micelles ($1/3 \leq p \leq 1/2$), and vesicles ($1/2 \leq p \leq 1$). Figure taken from Reference **46**.

1.4.2. Block copolymer (BCP) chain properties and drug/cargo partitioning studies

The hydrophobic core of BCMs drives both micelle formation and drug encapsulation, with drug-polymer interactions typically governed by non-covalent forces such as $\pi - \pi$ stacking, hydrogen bonding, or electrostatic interactions.[44,52–56] Common core-forming polymers include polyethers, polyesters, and polyamino acids. For example, Pluronic® triblock copolymers (PEG-PPO-PEG) have been widely studied for their drug partitioning and micelle stability, although their drug loading capacity is sometimes limited due to poor compatibility with certain drugs.[57,58] As a result, Pluronics are often used in drug-partitioning studies, where variations in polymer concentration and temperature can significantly affect drug distribution and this will aid in understanding and tailoring the properties that affect the functionality of drug delivery systems.[57]

The selection of polymer blocks plays a crucial role in drug solubility and fractionation into micellar carriers ($p_{drug,micelle}$) and into the surrounding aqueous environment ($p_{drug,solv}$) (see **Figure 1.8**). Several factors have been determined to affect the solubilization capacity of micelles, including compatibility between the core-forming polymers and the cargo, micellar size, aggregation number, interfacial tension between aqueous medium and the cargo, and the molecular volume of cargo.[52] However, fewer quantitative studies are available to analyze the impact of the above factors on drug solubilization.

Quantifying drug-distribution in different phases can provide quantitative correlations to the drug-delivery system features such as drug release rates, residence time in the organism, cytotoxicity, and other aspects of biological activity. This distribution can be described using a parameter called partition coefficient (K_p) which can also provide molecular level insights such as

interactions between drug molecules and micelles, including van der Waals forces, hydrophobic interactions and hydrogen bonding.

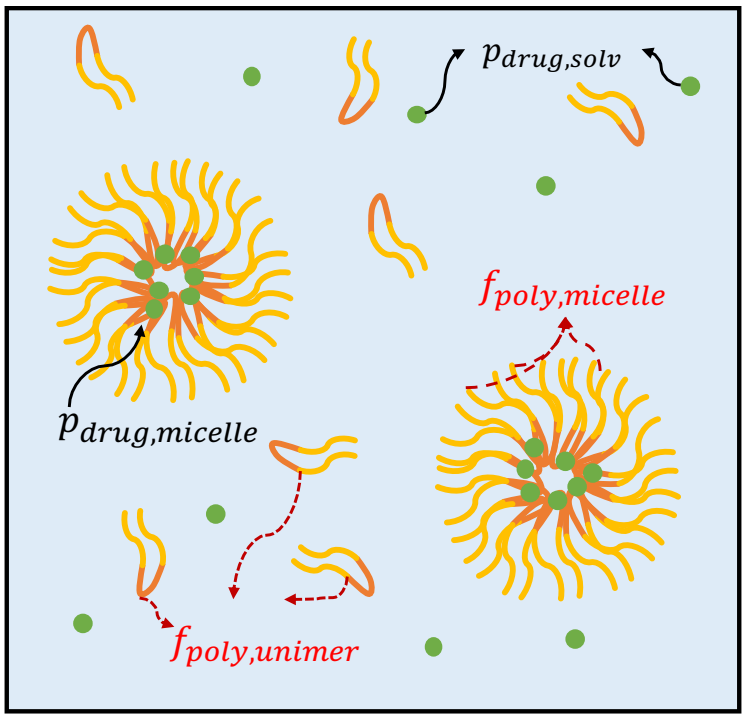

Figure 1.8: Quantification of population fraction (f) of block copolymer chains in micellar phase and free solvent state. Similarly, we can quantify the populations (p) of the drug molecules in the micellar phase and solvent phases. These quantifications are necessary to rationally modulate the pharmacological properties of the drug delivery systems.

K_p can be determined experimentally using techniques such as UV-Vis, high performance liquid chromatography, differential scanning calorimetry, and fluorescence.[59–68] Choucair et al. investigated the solubilization of hydrophobic polar dye 2-nitrodiphenylamine, in polystyrene-b-poly(acrylic acid) micelle solutions.[60] They evaluated the solubilization capacity of micelles and micelle-water partition coefficient K_p using UV-vis spectroscopy, fitting the data to a Langmuir adsorption isotherm, which can be expressed as **Equation 1.3.2**:

$$K_p = \frac{\chi}{\chi_{max}} = \frac{K_{ad}C}{1 + K_{ad}C} \qquad 1.3.2$$

In this equation, χ represent the mole fraction of the drug solubilized in the micellar phase, χ_{max} is the maximum mole fraction, K_{ad} is the adsorption constant, and C is the molar concentration of free unbound dye molecules.

Their findings showed that dye's solubilization in micelles is a binding process, which depends on the micellar surface area and the dye's affinity to the micellar interface. This was the first study to conceptualize solubilization as an adsorption-like phenomenon, offering insights into the interfacial solubilization mechanism in block copolymer aggregates. Sabate et al. also determined the micelle association constant (K_A) by studying the interaction of pinacyanol (PIN) with n-dodecyltrimethylammonium bromide (DTAB) surfactant micelles using UV-visilbe spectrophotometry.[63] Their results indicated that the interaction of the dye (PIN) with DTAB micelles caused a bathochromic shift (a shift to longer wavelength) of the dye's signal on UV-Visible spectrum. This shift enabled them to quantify the partitioning of the dye in different phases.

Lasonder et al. investigated the interactions of dipalmitoyl phosphatidylcholine vesicles with a series of anti-inflammatory agents (like sulindac, sulfide, naproxen, phyenylbutazone, and indomethacin), and structurally similar but physiologically inactive compounds using differential scanning calorimetry.[66] The change in transition temperatures of the vesicles due to cargo loading were measured, and partition coefficients (K_p) were determined using the Hill and Shen method:

$$\frac{C_T}{\Delta \mathrm{T}_m} = \frac{C_m^1}{K_p} + C_m^1 \frac{V_m}{V_w} \qquad 1.3.3$$

Here, $V_m$and V_w are the volume of lipid bilayer and water respectively, C_m^1 is the concentration of drug needed to produce a depression of 1°C, $\Delta \mathrm{T}_m$ is the depression of phase transition temperature compared to the pure surfactant, and C_T is the aqueous concentration of drug. K_p was determined from the plots of $\frac{C_T}{\Delta \mathrm{T}_m}$ and $\frac{V_m}{V_w}$. The partition coefficients, measured using this method, revealed the

cargo partitioning in vesicle and water phases, with indomethacin exhibiting the highest K_p, followed by naproxen and sulindac.

This approach enabled the determination of K_p and provided valuable insight into intermolecular interactions based on thermal transitions. It also offered a pathway to investigate the interactions between physiologically active/inactive compounds and nanocarriers like biological membranes. However, this thermoanalytical method is destructive, and the change in temperature during measurements can disrupt cargo partitioning equilibrium, leading to increased measurement errors.

Teng et al. investigated the uptake and release kinetics of two hydrophobic fluorescent probes, pyrene and phenanthrene, in block copolymer micelles (BCMs) using fluorescence spectroscopy.[67] They quantified the initial fraction of probe released and its concentration in the bulk stock solution samples prior to dilution. Comparative analysis indicated a portion of the probe was solubilized within the micelle corona.

Maity et al. examined the binding interactions of a nonsteroidal anti-inflammatory drug indomethacin (IMC) with various micelle types, including anionic SOS and cationic DTAB. Using steady-state fluorescence, time-resolved fluorescence spectroscopy, and isothermal titration calorimetry (ITC), they measured the spectral differences in IMC-loaded micelles and IMC in aqueous solution.[68] IMC encapsulated in micelles exhibited increased fluorescence intensity and this signal showed a biexponential decay kinetics when KCl salts were added in the solution, indicating the release of IMC in aqueous solutions. The thermodynamic parameters and binding constants determined from IMC-micelle interactions have significant implications for targeted drug design and release kinetics in physiological environments. However, these methods are

limited by the fluorescent properties of the probed molecule probed and the potential alterations in the fluorescent signal caused by molecular associations.

While the traditional techniques successfully quantify drug/carrier partitioning, they often require additional steps such as filtration, dialysis, or fluorescent tagging, which may disrupt system equilibrium and result in inaccurate measurements. In contrast, NMR diffusometry offers a non-destructive approach that preserves equilibrium without additional chemical modifications or extensive sample preparation. This method is particularly effective for quantifying populations of various chemical species (e.g., drug/cargo, unimers, and micelles) in micellar solutions. Furthermore, NMR diffusometry can distinguish the mobile species in both solutions and solid materials with molecular and elemental specificity, making it ideal for probing complex polymeric systems.

In our studies, we employed this non-destructive approach, to investigate the dynamics and partitioning of drug in Pluronic ® micelles, where PEG forms the micelle shell. We analyzed three hydrophobic drugs of varying hydrophobicity and quantified their concentrations in both micellar ($[M]_{drug,mic}$) and aqueous ($[M]_{drug,aq}$) phases. Assuming the activity coefficient of the drug is 1 in both phases, drug partition coefficient (K_p) was determined from the ratio of drug concentrations in each phase using the **Equation 1.3.4**.

$$K_p = \frac{[M]_{drug,mic}}{[M]_{drug,aq}} \qquad 1.3.4$$

K_p values reflect the efficacy of drug encapsulation by BCMs, providing insights into drug-polymer interactions that influence drug release rates, and the cytotoxicity of the drug-delivery systems formulated. Details of drug partitioning in Pluronic® BCMs studies are discussed in Chapter 4.

Additionally, we also explored the effect of BCM polymer core mobility, controlled by varying T_g, on the unimer-micelle coexistence. Poly(butyl acrylate) (PBA) was used as the core-forming block, with chain flexibility modulated by adjusting the n-butyl acrylate (n-BA) to $tert$-butyl acrylate (t-BA) monomer ratio. Details on the insights obtained from this study are presented in Chapter 5.

1.5. Colloidal semiconductor quantum dots

Colloidal semiconductor quantum dots (QDs) are nanoparticles that consist of an inorganic core surrounded by organic surface ligands, as illustrated in **Figure 1.9**. These nanostructures exhibit quantum confinement, where electrons are confined in all three dimensions. This quantum confinement gives rise to unique optical and electronic properties from the nanoparticle's core, including high fluorescence quantum yield, broad absorption spectra, narrow emission peaks, and excellent optical stability.[69] These features make QDs highly desirable for a range of applications, including optoelectronics (e.g., LEDs, lasers), photovoltaics (e.g., solar cells), biomedical imaging and drug-delivery, quantum information processing (e.g., qubits), and display technology (e.g., high-color gamut displays).[70–75]

Colloidal QDs are primarily synthesized using solution-based chemical methods, with colloidal synthesis being the most common. This synthesis involves decomposing precursors at high temperatures to produce metal ions and other atomic building blocks that nucleate and grow into crystalline nanoparticles.[76] This approach offers several advantages, including precise control over the size, shape, and composition of the QDs, as well as scalability for large-batch production, making it suitable for commercial applications. The unique optical properties of colloidal QDs stem from their inorganic core, where energy levels are highly dependent on the core's size. As the core size decreases, the emission wavelength shortens, enabling tunable light emission.[77] This size-

dependent tunability allows the generation of wide range of colors from a single material system, enhancing the versatility of QDs in various applications.

Despite their promising optical properties, direct synthesis of QDs often presents several limitations, such as poor electrical conductivity, limited solubility, and reduced biocompatibility due to the presence of long carbon-chain ligands on QD surface. These limitations can be addressed by exchanging the native ligands used during synthesis with alternative ligands tailored for specific applications.[77,78] For example, QDs treated with alkylamines have demonstrated enhanced fluorescence when optimized ligand-to-QD molar ratio is used.[79] Furthermore, Z-type ligands (more details explained below) have been found to dramatically increase the photoluminescence quantum yield (PLQY) of QDs such as CdTe, CdSe, CdS, and InP, which is critical for solar cell applications.[79] These examples underscore the importance of ligand exchange as a strategy to modify QD surface chemistry and optimize their performance. However, to tailor QD properties and control their interactions with the surrounding environment requires a deeper understanding of the underlying ligand exchange mechanism.

Since organic ligands play a crucial role in determining the properties of the inorganic core, it is essential to classify these ligands based on their state and interaction with the QD surface. In a colloidal solution, ligands can either be bound to the QD surface (via chemical and/or physical interactions) or as remain free in the surrounding solvent. The surface-bound ligands can be categorized into three types – X-type, L-type, and Z-type- depending on how many electrons they donate to interact with the QD surface (see **Figure 1.9**).[77,80–83]

- X-type ligands: These ligands, such as carboxylates ($RCOO^-$) and thiolates (RS^-), bind to the cations on the QD surface by donating a single electron.

- L-type ligands: These ligands, including amines (RNH_2), phosphines (R_3P), thiols, and phosphine oxides (R_3PO), bind to the QD surface by donating a pair of electrons.
- Z-type ligands: These ligands bind by accepting an electron pair from negatively charged surface atoms on the QD. Examples include $ZnCl_3$, $CdCl_2$, and $Pb(RCOO)_2$.

This classification is vital for establishing appropriate ligand exchange models and enhancing control over QD surface chemistry for improved performance in various applications.

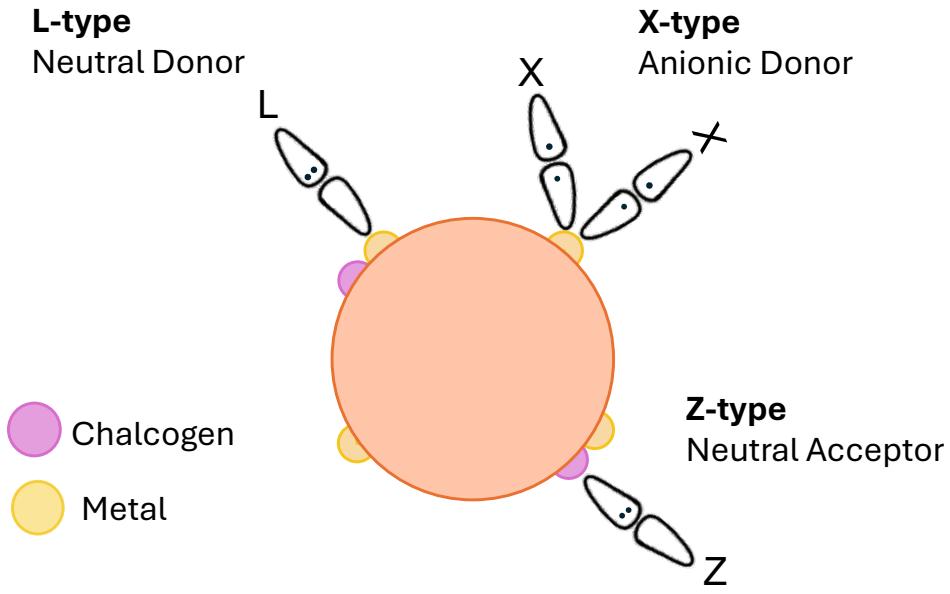

Figure 1.9: A classification of different ligand types interacting with the semiconductor core surface.

Several methods have been developed to study ligand-exchange mechanisms, as these exchanges significantly impact the photophysical properties of colloidal quantum dots (QDs). Techniques such as UV-Vis absorption and photoluminescence (PL) spectroscopy are commonly used to examine changes in optical properties due to ligand exchange.[84,85] Transmission electron microscopy (TEM), ultraviolet photoelectron spectroscopy (UPS), and X-ray photoelectron spectroscopy (XPS) are utilized to monitor changes in core size, energy levels, and surface

composition during ligand exchange.[86,87] Thermogravimetric analysis (TGA), PL spectroscopy, dynamic light scattering (DLS), and mass spectrometry (MS) can characterize the organic ligands on the QD surface.[88–90] Infrared (IR) and Raman spectroscopy are often employed to study the molecular structure of organic compounds, but in surface ligand analysis, these techniques reveal binding modes and surface coordination environments. **Figure 1.10** illustrates the categorization of various characterization tools used to understand ligand exchange mechanisms by probing different components of the colloidal nanoparticle.

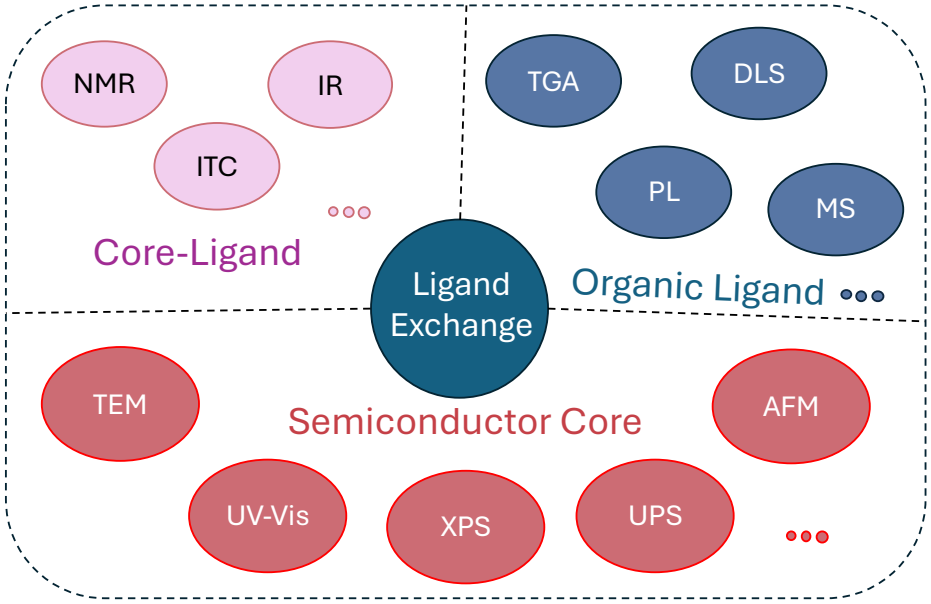

Figure 1.10: Characterization tools used to study ligand exchange. The methods are grouped based on the colloidal particle component studied. Figure adapted from reference number 69.

NMR is a versatile tool for characterizing the QD surface, providing both qualitative and quantitative insights on surface ligands. It confirms successful ligand modification, identifies ligand structures, distinguishes between bound and free ligands, and reveals the dynamics of ligands on the QD surface.[86,91–93] For example, Dempsey et al. used ^{1}H NMR to quantify K_{eq} of an X-type ligand exchange between the CdSe QD surface and in the free solvent.[91,94] They found that carboxylic acids exchanged reversibly with native oleates (OA), while phosphoric acid and

thiol ligands irreversibly replaced the native OA ligands. These thermodynamic insights are crucial for designing QDs with tunable optoelectronic properties.

While those studies provided valuable insights into the equilibrium state of the ligands, a few studies, combining X-ray, neutron scattering, and other spectroscopic techniques have found evidence for more than one binding state on the QD surface (see **Figure 1.11**) proving that system is beyond the classical two-state model.[93,95–99] The primary surface binding of ligands is typically considered as chemisorption, while the secondary binding was speculated to arise from either physisorption or Van der Waals interactions with the QD surface.

To further improve our limited understanding of ligand binding on the surface and the exchange between surface-bound and free ligands in solution, it is necessary to accurately quantify ligand population fractions in each state (denoted as $p_{ads,1}$, $p_{ads,2}$, p_{free}) and determine the ligand exchange rates ($k_{ex,1}$, $k_{ex,1}$, see **Figure 1.11**) as a function of temperature and concentration. These measurements enable us to determine thermodynamic properties like the equilibrium constant (K_{eq}), enthalpy change (ΔH), and entropy change (ΔS), providing valuable insights into the driving forces behind ligand exchange and binding on the QD surface.

^{1}H NMR spectroscopy alone has limitations in quantifying multiple molecular states in a system (more details on the limitations explained in Chapter 6). However, also by probing ligand's diffusion, we can accurately quantify the population fractions of ligands in all states. Madsen et al. previously combined ^{1}H NMR and NMR diffusometry to probe the molecular dynamics in different systems like micellar solutions and battery electrolytes and accurately quantified different molecular states.[10,11,13,14,100,101]

In Chapter 6 of the thesis, I applied similar methodologies by combining techniques such as variable temperature (VT), NMR diffusometry, and dynamic NMR spectroscopy, to quantify

thermodynamics and kinetics of X-type ligand exchange mechanisms (specifically for carboxylates) on PbS QDs. Detailed explanations of these NMR techniques are found in Chapter 2. These implemented methodologies enabled us to probe and quantify multiple QD-ligand interactions, determine thermodynamic energies and kinetic rates, and thus open up new ways to tailor QD properties for a variety of applications.

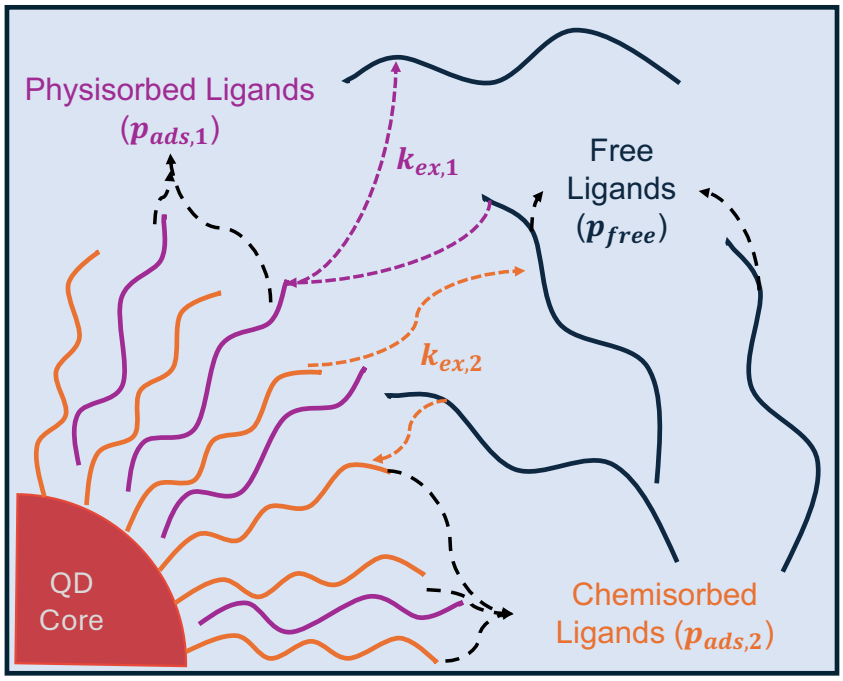

Figure 1.11: Schematic diagram showing the structure of a colloidal quantum dot solution. The core consists of an inorganic semiconductor nanoparticle, while its surface is surrounded with organic ligands. These ligands have multiple binding modes (chemisorbed and/or physisorbed) with the QD surface and can exchange with free ligands in the solvent. Quantifying the population fractions of the ligands in different states ($p_{ads,1}$, $p_{ads,2}$, p_{free}) and the exchange rates ($k_{ex,1}$, $k_{ex,2}$) with respect to concentration and temperature provides us insights into the mechanism of binding and the energetics of ligand exchange.

1.6. Summary

In this chapter, I discussed the significance of molecular diffusion and dynamics in development of innovative materials for applications such as drug delivery systems and green

energy. I examined the functionalities of polyelectrolytes, block copolymer micelles (BCMs), and colloidal semiconductor quantum dots (QDs), and provided the existing knowledge gaps in their respective applications. Chapter 2 introduces the fundamental concepts of NMR theory and details the NMR methods employed to study these materials. Chapter 3 through 6 present new findings on these macromolecular systems, which were investigated using the aforementioned NMR techniques.

References

(1) Brown, R. XXVII. *A Brief Account of Microscopical Observations Made in the Months of June, July and August* 1827, *on the Particles Contained in the Pollen of Plants; and on the General Existence of Active Molecules in Organic and Inorganic Bodies*. *The Philosophical Magazine* 1828, *4* (21), 161–173. https://doi.org/10.1080/14786442808674769.

(2) Stokes, G. G. On the Effect of Internal Friction of Fluids on the Motion of Pendulums. . *Transactions of the Cambridge Philosophical Society* 1851, *9* (8).

(3) Einstein, A. Über Die von Der Molekularkinetischen Theorie Der Wärme Geforderte Bewegung von in Ruhenden Flüssigkeiten Suspendierten Teilchen. *Ann Phys* 1905, *322* (8), 549–560. https://doi.org/10.1002/andp.19053220806.

(4) Costigliola, L.; Heyes, D. M.; Schrøder, T. B.; Dyre, J. C. Revisiting the Stokes-Einstein Relation without a Hydrodynamic Diameter. *J Chem Phys* 2019, *150* (2). https://doi.org/10.1063/1.5080662.

(5) Busch, A.; Kampman, N.; Bertier, P.; Pipich, V.; Feoktystov, A.; Rother, G.; Harrington, J.; Leu, L.; Aertens, M.; Jacops, E. Predicting Effective Diffusion Coefficients in Mudrocks Using a Fractal Model and Small-Angle Neutron Scattering Measurements. *Water Resour Res* 2018, *54* (9), 7076–7091. https://doi.org/10.1029/2018WR023425.

(6) Meyer, A.; Stüber, S.; Holland-Moritz, D.; Heinen, O.; Unruh, T. Determination of Self-Diffusion Coefficients by Quasielastic Neutron Scattering Measurements of Levitated Ni Droplets. *Phys Rev B* 2008, *77* (9), 092201. https://doi.org/10.1103/PhysRevB.77.092201.

(7) Hamada, M.; de Anna, P. A Method to Measure the Diffusion Coefficient in Liquids. *Transp Porous Media* 2023, *146* (1–2), 463–474. https://doi.org/10.1007/s11242-021-01704-0.

(8) Hazel, J. R.; Sidell, B. D. A Method for the Determination of Diffusion Coefficients for Small Molecules in Aqueous Solution. *Anal Biochem* 1987, *166* (2), 335–341. https://doi.org/10.1016/0003-2697(87)90582-3.

(9) Hou, J.; Madsen, L. A. New Insights for Accurate Chemically Specific Measurements of Slow Diffusing Molecules. *Journal of Chemical Physics* 2013, *138* (5). https://doi.org/10.1063/1.4789923.

(10) Madsen, L. A.; Hou, J. NMR Diffusometry for the Study of Energy-Related Soft Materials. 1897, No. 9, 464–496.

(11) Carrazzone, R. J.; Li, X.; Foster, J. C.; Uppala, V. V. S.; Wall, C. E.; Esker, A. R.; Madsen, L. A.; Matson, J. B. Strong Variation of Micelle–Unimer Coexistence as a Function of Core Chain

Mobility. *Macromolecules* 2021, *54* (14), 6975–6981. https://doi.org/10.1021/acs.macromol.1c00635.
(12) Han, A.; Uppala, V. V. S.; Parisi, D.; George, C.; Dixon, B. J.; Ayala, C. D.; Li, X.; Madsen, L. A.; Colby, R. H. Determining the Molecular Weight of Polyelectrolytes Using the Rouse Scaling Theory for Salt-Free Semidilute Unentangled Solutions. *Macromolecules* 2022, *55* (16), 7148–7160. https://doi.org/10.1021/acs.macromol.2c01007.
(13) Kidd, B. E.; Li, X.; Piemonte, R. C.; Cooksey, T. J.; Singh, A.; Robertson, M. L.; Madsen, L. A. Tuning Biocompatible Block Copolymer Micelles by Varying Solvent Composition: Dynamics and Populations of Micelles and Unimers. *Macromolecules* 2017, *50* (11), 4335–4343. https://doi.org/10.1021/acs.macromol.6b02579.
(14) Li, X.; Uppala, V. V. S.; Cooksey, T. J.; Robertson, M. L.; Madsen, L. A. Quantifying Drug Cargo Partitioning in Block Copolymer Micelle Solutions. *ACS Appl Polym Mater* 2020, *2* (9), 3749–3755. https://doi.org/10.1021/acsapm.0c00694.
(15) Li, X.; Cooksey, T. J.; Kidd, B. E.; Robertson, M. L.; Madsen, L. A. Mapping Coexistence Phase Diagrams of Block Copolymer Micelles and Free Unimer Chains. *Macromolecules* 2018, acs.macromol.8b01220. https://doi.org/10.1021/acs.macromol.8b01220.
(16) Kidd, B. E.; Lingwood, M. D.; Lee, M.; Gibson, H. W.; Madsen, L. A. Cation and Anion Transport in a Dicationic Imidazolium-Based Plastic Crystal Ion Conductor. *Journal of Physical Chemistry B* 2014, *118* (8), 2176–2185. https://doi.org/10.1021/jp4084629.
(17) Colby, R. H. Structure and Linear Viscoelasticity of Flexible Polymer Solutions: Comparison of Polyelectrolyte and Neutral Polymer Solutions. *Rheologica Acta*. May 2010, pp 425–442. https://doi.org/10.1007/s00397-009-0413-5.
(18) Dobrynin, A. V; Colby, R. H.; Rubinstein, M. *Scaling Theory of Polyelectrolyte Solutions*; 1995; Vol. 28. https://pubs.acs.org/sharingguidelines.
(19) Rubinstein, M.; Colby, R. H.; Dobrynin, A. V. *PHYSICAL REVIEW LETTERS Dynamics of Semidilute Polyelectrolyte Solutions*; 1994; Vol. 73.
(20) Muthukumar, M. Dynamics of Polyelectrolyte Solutions. *Journal of Chemical Physics* 1997, *107* (7), 2619–2635. https://doi.org/10.1063/1.474573.
(21) Muthukumar, M. 50th Anniversary Perspective: A Perspective on Polyelectrolyte Solutions. *Macromolecules*. American Chemical Society December 26, 2017, pp 9528–9560. https://doi.org/10.1021/acs.macromol.7b01929.
(22) Beer, M.; Schmidt, M.; Muthukumar, M. *The Electrostatic Expansion of Linear Polyelectrolytes: Effects of Gegenions, Co-Ions, and Hydrophobicity*; 1997. https://pubs.acs.org/sharingguidelines.
(23) Lankalapalli, S.; Kolapalli, V. R. M. Polyelectrolyte Complexes: A Review of Their Applicability in Drug Delivery Technology. *Indian J Pharm Sci* 2009, *71* (5), 481. https://doi.org/10.4103/0250-474X.58165.
(24) Kuhn, W.; Künzle, O.; Katchalsky, A. Behavior of Polyvalent Thread Molecular Ions in Solution. *Helv Chim Acta* 1948, *31* (7), 1994–2037. https://doi.org/10.1002/hlca.19480310716.
(25) Durmaz, E. N.; Sahin, S.; Virga, E.; De Beer, S.; De Smet, L. C. P. M.; De Vos, W. M. Polyelectrolytes as Building Blocks for Next-Generation Membranes with Advanced Functionalities. *ACS Applied Polymer Materials*. American Chemical Society September 10, 2021, pp 4347–4374. https://doi.org/10.1021/acsapm.1c00654.
(26) Vijitha, R.; Nagaraja, K.; Hanafiah, M. M.; Rao, K. M.; Venkateswarlu, K.; Lakkaboyana, S. K.; Krishna Rao, K. S. V. Fabrication of Eco-Friendly Polyelectrolyte Membranes Based on Sulfonate Grafted Sodium Alginate for Drug Delivery, Toxic Metal Ion Removal and Fuel Cell Applications. *Polymers (Basel)* 2021, *13* (19). https://doi.org/10.3390/polym13193293.

(27) Khakpour, H.; Abdollahi, M. Synthesis, Characterization, Rheological and Self-Assembly Behavior of Polyelectrolytes Hydrophobically Modified with High Styrene Content: Effect of External Parameters on Thickening Properties and Nano-Associations. *J Dispers Sci Technol* 2020, *41* (5), 751–762. https://doi.org/10.1080/01932691.2019.1611444.
(28) Zhang, S.; She, Y.; Gu, Y. Evaluation of Polymers as Direct Thickeners for CO2 Enhanced Oil Recovery. *J Chem Eng Data* 2011, *56* (4), 1069–1079. https://doi.org/10.1021/je1010449.
(29) de Gennes, P.; Pincus, P.; Velasco, R.; Brochard, F.; De Gennes, P. G.; Velasco, R. M.; Bâtiment, F. Remarks on Polyelectrolyte Conforma-Tion. *Journal de Physique* 1976, *37* (12), 1461–1473. https://doi.org/10.1051/jphys:0197600370120146100ï.
(30) Gruendling, T.; Weidner, S.; Falkenhagen, J.; Barner-Kowollik, C. Mass Spectrometry in Polymer Chemistry: A State-of-the-Art up-Date. *Polymer Chemistry*. July 2010, pp 599–617. https://doi.org/10.1039/b9py00347a.
(31) Drifford, M.; Dalbiez, J. P. Light Scattering by Dilute Solutions of Salt-Free Polyelectrolytes. *J Phys Chem* 1984, *88* (22), 5368–5375. https://doi.org/10.1021/j150666a052.
(32) Krause, R.; Maier, E. E.; Deggelmann, M.; Hagenbuchle, M.; Schulz, S. F.; Weber, R. *STATIC LIGHT SCATTERING BY SOLUTIONS OF SALT-FREE POLYELECTROLYTES*; 1989; Vol. 160.
(33) Rubinstein, M.; Colby, R. H. *Polymer Physics*; Oxford University Press, 2003.
(34) Di Cola, E.; Plucktaveesak, N.; Waigh, T. A.; Colby, R. H.; Tan, J. S.; Pyckhout-Hintzen, W.; Heenan, R. K. Structure and Dynamics in Aqueous Solutions of Amphiphilic Sodium Maleate-Containing Alternating Copolymers. *Macromolecules* 2004, *37* (22), 8457–8465. https://doi.org/10.1021/ma049260h.
(35) Williams, C. E.; Nierlich, M.; Cotton, J. P.; Jannink, G.; Boué, F.; Daoud, M.; Farnoux, B.; Picot, C.; DeGennes, P. G.; Rinaudo, M.; Moan, M.; Wolff, C. Polyelectrolyte Solutions: Intrachain and Interchain Correlations Observed by SANS. *Journal of Polymer Science: Polymer Letters Edition* 1979, *17* (6), 379–384. https://doi.org/10.1002/pol.1979.130170608.
(36) Nierlich, M.; Williams, C. E.; Boué, F.; Cotton, J. P.; Daoud, M.; Boué, F.; Famoux, B.; Jannink, G.; Moan, M.; Wolff, C.; Rinaudo, M.; De Gennes, P. G. Small Angle Neutron Scattering by Semi-Dilute Solutions of Polyelectrolyte. *Journal de Physique* 1979, *40* (7), 701–704. https://doi.org/10.1051/jphys:01979004007070100ï.
(37) Lund, R.; Willner, L.; Richter, D. Kinetics of Block Copolymer Micelles Studied by Small-Angle Scattering Methods; 2013; pp 51–158. https://doi.org/10.1007/12_2012_204.
(38) Jones, M.-C.; Leroux, J.-C. Polymeric Micelles – a New Generation of Colloidal Drug Carriers. *European Journal of Pharmaceutics and Biopharmaceutics* 1999, *48* (2), 101–111. https://doi.org/10.1016/S0939-6411(99)00039-9.
(39) Oerlemans, C.; Bult, W.; Bos, M.; Storm, G.; Nijsen, J. F. W.; Hennink, W. E. Polymeric Micelles in Anticancer Therapy: Targeting, Imaging and Triggered Release. *Pharmaceutical Research*. December 2010, pp 2569–2589. https://doi.org/10.1007/s11095-010-0233-4.
(40) Ma, J.; Guo, C.; Tang, Y.; Xiang, J.; Chen, S.; Wang, J.; Liu, H. Micellization in Aqueous Solution of an Ethylene Oxide-Propylene Oxide Triblock Copolymer, Investigated with 1H NMR Spectroscopy, Pulsed-Field Gradient NMR, and NMR Relaxation. *J Colloid Interface Sci* 2007, *312* (2), 390–396. https://doi.org/10.1016/j.jcis.2007.03.013.
(41) Topel, Ö.; Çakır, B. A.; Budama, L.; Hoda, N. Determination of Critical Micelle Concentration of Polybutadiene-Block-Poly(Ethyleneoxide) Diblock Copolymer by Fluorescence Spectroscopy and Dynamic Light Scattering. *J Mol Liq* 2013, *177*, 40–43. https://doi.org/10.1016/j.molliq.2012.10.013.

(42) Kalyanasundaram, K.; Thomas, J. K. Environmental Effects on Vibronic Band Intensities in Pyrene Monomer Fluorescence and Their Application in Studies of Micellar Systems. *J Am Chem Soc* 1977, *99* (7), 2039–2044. https://doi.org/10.1021/ja00449a004.
(43) Cabral, H.; Miyata, K.; Osada, K.; Kataoka, K. Block Copolymer Micelles in Nanomedicine Applications. *Chemical Reviews*. American Chemical Society July 25, 2018, pp 6844–6892. https://doi.org/10.1021/acs.chemrev.8b00199.
(44) Cabral, H.; Kataoka, K. Progress of Drug-Loaded Polymeric Micelles into Clinical Studies. *Journal of Controlled Release* 2014, *190*, 465–476. https://doi.org/10.1016/j.jconrel.2014.06.042.
(45) Beach, M. A.; Nayanathara, U.; Gao, Y.; Zhang, C.; Xiong, Y.; Wang, Y.; Such, G. K. Polymeric Nanoparticles for Drug Delivery. *Chemical Reviews*. American Chemical Society May 8, 2024, pp 5505–5616. https://doi.org/10.1021/acs.chemrev.3c00705.
(46) Karayianni, M.; Pispas, S. Block Copolymer Solution Self-Assembly: Recent Advances, Emerging Trends, and Applications. *Journal of Polymer Science*. John Wiley and Sons Inc September 1, 2021, pp 1874–1898. https://doi.org/10.1002/pol.20210430.
(47) Israelachvili, J. *Self-Assembly in Two Dimensions: Surface Micelles and Domain Formation in Monolayers*; 1994; Vol. 10. https://pubs.acs.org/sharingguidelines.
(48) Peppas, N. A.; Keys, K. B.; Torres-Lugo, M.; Lowman, A. M. Poly(Ethylene Glycol)-Containing Hydrogels in Drug Delivery. *Journal of Controlled Release* 1999, *62* (1–2), 81–87. https://doi.org/10.1016/S0168-3659(99)00027-9.
(49) Deng, C.; Jiang, Y.; Cheng, R.; Meng, F.; Zhong, Z. Biodegradable Polymeric Micelles for Targeted and Controlled Anticancer Drug Delivery: Promises, Progress and Prospects. *Nano Today* 2012, *7* (5), 467–480. https://doi.org/10.1016/j.nantod.2012.08.005.
(50) Harris, J. M. *Poly(Ethylene Glycol) Chemistry: Biotechnology and Biomedical Applications*.
(51) Jones, M.-C.; Leroux, J.-C. Polymeric Micelles – a New Generation of Colloidal Drug Carriers. *European Journal of Pharmaceutics and Biopharmaceutics* 1999, *48* (2), 101–111. https://doi.org/10.1016/S0939-6411(99)00039-9.
(52) Masayuki, Y.; Mizue, M.; Noriko, Y.; Teruo, O.; Yasuhisa, S.; Kazunori, K.; Shohei, I. Polymer Micelles as Novel Drug Carrier: Adriamycin-Conjugated Poly(Ethylene Glycol)-Poly(Aspartic Acid) Block Copolymer. *Journal of Controlled Release* 1990, *11* (1–3), 269–278. https://doi.org/10.1016/0168-3659(90)90139-K.
(53) Harada, A.; Kataoka, K. Chain Length Recognition: Core-Shell Supramolecular Assembly from Oppositely Charged Block Copolymers. *Science (1979)* 1999, *283* (5398), 65–67. https://doi.org/10.1126/science.283.5398.65.
(54) Harada, A.; Kataoka, K. Formation of Polyion Complex Micelles in an Aqueous Milieu from a Pair of Oppositely-Charged Block Copolymers with Poly(Ethylene Glycol) Segments. *Macromolecules* 1995, *28* (15), 5294–5299. https://doi.org/10.1021/ma00119a019.
(55) Kataoka, K.; Ishihara, A.; Harada, A.; Miyazaki, H. Effect of the Secondary Structure of Poly(<scp>l</Scp> -Lysine) Segments on the Micellization in Aqueous Milieu of Poly(Ethylene Glycol)−Poly(<scp>l</Scp> -Lysine) Block Copolymer Partially Substituted with a Hydrocinnamoyl Group at the N ε -Position. *Macromolecules* 1998, *31* (18), 6071–6076. https://doi.org/10.1021/ma971838i.
(56) Kataoka, K.; Harada, A.; Nagasaki, Y. Block Copolymer Micelles for Drug Delivery: Design, Characterization and Biological Significance. *Adv Drug Deliv Rev* 2001, *47* (1), 113–131. https://doi.org/10.1016/S0169-409X(00)00124-1.

(57) Basak, R.; Bandyopadhyay, R. Encapsulation of Hydrophobic Drugs in Pluronic F127 Micelles: Effects of Drug Hydrophobicity, Solution Temperature, and PH. *Langmuir* 2013, *29* (13), 4350–4356. https://doi.org/10.1021/la304836e.
(58) Douglass, B. S.; Colby, R. H.; Madsen, L. A.; Callaghan, P. T. Rheo-NMR of Wormlike Micelles Formed from Nonionic Pluronic Surfactants. *Macromolecules* 2008, *41* (3), 804–814. https://doi.org/10.1021/ma071807f.
(59) Sharma, P. K.; Bhatia, S. R. Effect of Anti-Inflammatories on Pluronic® F127: Micellar Assembly, Gelation and Partitioning. *Int J Pharm* 2004, *278* (2), 361–377. https://doi.org/10.1016/j.ijpharm.2004.03.029.
(60) Choucair, A.; Eisenberg, A. Interfacial Solubilization of Model Amphiphilic Molecules in Block Copolymer Micelles. *J Am Chem Soc* 2003, *125* (39), 11993–12000. https://doi.org/10.1021/ja036667d.
(61) Letchford, K.; Liggins, R.; Burt, H. Solubilization of Hydrophobic Drugs by Methoxy Poly(Ethylene Glycol)-block-polycaprolactone Diblock Copolymer Micelles: Theoretical and Experimental Data and Correlations. *J Pharm Sci* 2008, *97* (3), 1179–1190. https://doi.org/10.1002/jps.21037.
(62) Zhao, M.; Eghtesadi, S. A.; Dawadi, M. B.; Wang, C.; Huang, S.; Seymore, A. E.; Vogt, B. D.; Modarelli, D. A.; Liu, T.; Zacharia, N. S. Partitioning of Small Molecules in Hydrogen-Bonding Complex Coacervates of Poly(Acrylic Acid) and Poly(Ethylene Glycol) or Pluronic Block Copolymer. *Macromolecules* 2017, *50* (10), 3818–3830. https://doi.org/10.1021/acs.macromol.6b02815.
(63) Sabaté, R.; Gallardo, M.; De la Maza, A.; Estelrich, J. A Spectroscopy Study of the Interaction of Pinacyanol with N-Dodecyltrimethylammonium Bromide Micelles. *Langmuir* 2001, *17* (21), 6433–6437. https://doi.org/10.1021/la010463y.
(64) Barbato, F.; La Rotonda, M. I.; Quaglia, F. Interactions of Nonsteroidal Antiinflammatory Drugs with Phospholipids: Comparison between Octanol/Buffer Partition Coefficients and Chromatographic Indexes on Immobilized Artificial Membranes. *J Pharm Sci* 1997, *86* (2), 225–229. https://doi.org/10.1021/js960233h.
(65) Barbato X, F.; Rotonda, M. I. La; Quaglia, F. *Interactions of Nonsteroidal Antiinflammatory Drugs with Phospholipids: Comparison between Octanol/Buffer Partition Coefficients and Chromatographic Indexes on Immobilized Artificial Membranes*; 1997.
(66) Lasonder, E.; Weringa, W. D. An NMR and DSC Study of the Interaction of Phospholipid Vesicles with Some Anti-Inflammatory Agents. *J Colloid Interface Sci* 1990, *139* (2), 469–478. https://doi.org/10.1016/0021-9797(90)90119-9.
(67) Teng, Y.; Morrison, M. E.; Munk, P.; Webber, S. E.; Procházka, K. Release Kinetics Studies of Aromatic Molecules into Water from Block Polymer Micelles. *Macromolecules* 1998, *31* (11), 3578–3587. https://doi.org/10.1021/ma971721u.
(68) Maity, B.; Chatterjee, A.; Ahmed, S. A.; Seth, D. Interaction of the Nonsteroidal Anti-Inflammatory Drug Indomethacin with Micelles and Its Release. *J Phys Chem B* 2015, *119* (9), 3776–3785. https://doi.org/10.1021/acs.jpcb.5b00467.
(69) Liu, M.; Tang, G.; Liu, Y.; Jiang, F. L. Ligand Exchange of Quantum Dots: A Thermodynamic Perspective. *Journal of Physical Chemistry Letters*. American Chemical Society February 22, 2024, pp 1975–1984. https://doi.org/10.1021/acs.jpclett.3c03413.
(70) Chang, J. C.; Rosenthal, S. J. A Bright Light to Reveal Mobility: Single Quantum Dot Tracking Reveals Membrane Dynamics and Cellular Mechanisms. *J Phys Chem Lett* 2013, *4* (17), 2858–2866. https://doi.org/10.1021/jz401071g.

(71) Michalet, X.; Pinaud, F. F.; Bentolila, L. A.; Tsay, J. M.; Doose, S.; Li, J. J.; Sundaresan, G.; Wu, A. M.; Gambhir, S. S.; Weiss, S. Quantum Dots for Live Cells, in Vivo Imaging, and Diagnostics. *Science (1979)* 2005, *307* (5709), 538–544. https://doi.org/10.1126/science.1104274.
(72) Chuang, C.-H. M.; Brown, P. R.; Bulović, V.; Bawendi, M. G. Improved Performance and Stability in Quantum Dot Solar Cells through Band Alignment Engineering. *Nat Mater* 2014, *13* (8), 796–801. https://doi.org/10.1038/nmat3984.
(73) Carey, G. H.; Abdelhady, A. L.; Ning, Z.; Thon, S. M.; Bakr, O. M.; Sargent, E. H. Colloidal Quantum Dot Solar Cells. *Chem Rev* 2015, *115* (23), 12732–12763. https://doi.org/10.1021/acs.chemrev.5b00063.
(74) Shirasaki, Y.; Supran, G. J.; Bawendi, M. G.; Bulović, V. Emergence of Colloidal Quantum-Dot Light-Emitting Technologies. *Nat Photonics* 2013, *7* (1), 13–23. https://doi.org/10.1038/nphoton.2012.328.
(75) Colvin, V. L.; Schlamp, M. C.; Alivisatos, A. P. Light-Emitting Diodes Made from Cadmium Selenide Nanocrystals and a Semiconducting Polymer. *Nature* 1994, *370* (6488), 354–357. https://doi.org/10.1038/370354a0.
(76) Jing, X.; Zhang, Y.; Li, M.; Zuo, X.; Fan, C.; Zheng, J. Surface Engineering of Colloidal Nanoparticles. *Materials Horizons*. Royal Society of Chemistry January 20, 2023, pp 1185–1209. https://doi.org/10.1039/d2mh01512a.
(77) Kroupa, D. M.; Vörös, M.; Brawand, N. P.; McNichols, B. W.; Miller, E. M.; Gu, J.; Nozik, A. J.; Sellinger, A.; Galli, G.; Beard, M. C. Tuning Colloidal Quantum Dot Band Edge Positions through Solution-Phase Surface Chemistry Modification. *Nat Commun* 2017, *8*. https://doi.org/10.1038/ncomms15257.
(78) Hughes, B. K.; Ruddy, D. A.; Blackburn, J. L.; Smith, D. K.; Bergren, M. R.; Nozik, A. J.; Johnson, J. C.; Beard, M. C. Control of PbSe Quantum Dot Surface Chemistry and Photophysics Using an Alkylselenide Ligand. *ACS Nano* 2012, *6* (6), 5498–5506. https://doi.org/10.1021/nn301405j.
(79) Yin, Y.; Alivisatos, A. P. Colloidal Nanocrystal Synthesis and the Organic–Inorganic Interface. *Nature* 2005, *437* (7059), 664–670. https://doi.org/10.1038/nature04165.
(80) Owen, J. The Coordination Chemistry of Nanocrystal Surfaces. *Science (1979)* 2015, *347* (6222), 615–616. https://doi.org/10.1126/science.1259924.
(81) Chen, P. E.; Anderson, N. C.; Norman, Z. M.; Owen, J. S. Tight Binding of Carboxylate, Phosphonate, and Carbamate Anions to Stoichiometric CdSe Nanocrystals. *J Am Chem Soc* 2017, *139* (8), 3227–3236. https://doi.org/10.1021/jacs.6b13234.
(82) Anderson, N. C.; Hendricks, M. P.; Choi, J. J.; Owen, J. S. Ligand Exchange and the Stoichiometry of Metal Chalcogenide Nanocrystals: Spectroscopic Observation of Facile Metal-Carboxylate Displacement and Binding. *J Am Chem Soc* 2013, *135* (49), 18536–18548. https://doi.org/10.1021/ja4086758.
(83) De Roo, J.; De Keukeleere, K.; Hens, Z.; Van Driessche, I. From Ligands to Binding Motifs and beyond; the Enhanced Versatility of Nanocrystal Surfaces. *Dalton Transactions* 2016, *45* (34), 13277–13283. https://doi.org/10.1039/C6DT02410F.
(84) May, A. M.; Dempsey, J. L. A New Era of LMCT: Leveraging Ligand-to-Metal Charge Transfer Excited States for Photochemical Reactions. *Chemical Science*. Royal Society of Chemistry April 17, 2024, pp 6661–6678. https://doi.org/10.1039/d3sc05268k.

(85) Lee, K. J.; Elgrishi, N.; Kandemir, B.; Dempsey, J. L. Electrochemical and Spectroscopic Methods for Evaluating Molecular Electrocatalysts. *Nature Reviews Chemistry*. Nature Publishing Group January 11, 2017. https://doi.org/10.1038/s41570-017-0039.
(86) Kessler, M. L.; Kelm, J. E.; Starr, H. E.; Cook, E. N.; Miller, J. D.; Rivera, N. A.; Hsu-Kim, H.; Dempsey, J. L. Unraveling Changes to PbS Nanocrystal Surfaces Induced by Thiols. *Chemistry of Materials* 2022, *34* (4), 1710–1721. https://doi.org/10.1021/acs.chemmater.1c03888.
(87) Kelm, J. E.; Dempsey, J. L. Metal-Dictated Reactivity of Z-Type Ligands to Passivate Surface Defects on CdSe Nanocrystals. *J Am Chem Soc* 2024, *146* (8), 5252–5262. https://doi.org/10.1021/jacs.3c11811.
(88) Ji, X.; Copenhaver, D.; Sichmeller, C.; Peng, X. Ligand Bonding and Dynamics on Colloidal Nanocrystals at Room Temperature: The Case of Alkylamines on CdSe Nanocrystals. *J Am Chem Soc* 2008, *130* (17), 5726–5735. https://doi.org/10.1021/ja710909f.
(89) Dewi, M. R.; Laufersky, G.; Nann, T. A Highly Efficient Ligand Exchange Reaction on Gold Nanoparticles: Preserving Their Size, Shape and Colloidal Stability. *RSC Adv.* 2014, *4* (64), 34217–34220. https://doi.org/10.1039/C4RA05035E.
(90) Frazier, J.; Cavey, K.; Coil, S.; Hamo, H.; Zhang, M.; Van Patten, P. G. Rapid and Sensitive Identification and Discrimination of Bound/Unbound Ligands on Colloidal Nanocrystals via Direct Analysis in Real-Time Mass Spectrometry. *Langmuir* 2021, *37* (50), 14703–14712. https://doi.org/10.1021/acs.langmuir.1c02548.
(91) Knauf, R. R.; Lennox, J. C.; Dempsey, J. L. Quantifying Ligand Exchange Reactions at CdSe Nanocrystal Surfaces. *Chemistry of Materials* 2016, *28* (13), 4762–4770. https://doi.org/10.1021/acs.chemmater.6b01827.
(92) Hartley, C. L.; Kessler, M. L.; Dones Lassalle, C. Y.; Camp, A. M.; Dempsey, J. L. Effects of Ligand Shell Composition on Surface Reduction in PbS Quantum Dots. *Chemistry of Materials* 2021, *33* (22), 8612–8622. https://doi.org/10.1021/acs.chemmater.1c01810.
(93) Valdez, C. N.; Schimpf, A. M.; Gamelin, D. R.; Mayer, J. M. Low Capping Group Surface Density on Zinc Oxide Nanocrystals. *ACS Nano* 2014, *8* (9), 9463–9470. https://doi.org/10.1021/nn503603e.
(94) Kessler, M. L.; Starr, H. E.; Knauf, R. R.; Rountree, K. J.; Dempsey, J. L. Exchange Equilibria of Carboxylate-Terminated Ligands at PbS Nanocrystal Surfaces. *Physical Chemistry Chemical Physics* 2018, *20* (36), 23649–23655. https://doi.org/10.1039/c8cp04275f.
(95) Weir, M. P.; Toolan, D. T. W.; Kilbride, R. C.; Penfold, N. J. W.; Washington, A. L.; King, S. M.; Xiao, J.; Zhang, Z.; Gray, V.; Dowland, S.; Winkel, J.; Greenham, N. C.; Friend, R. H.; Rao, A.; Ryan, A. J.; Jones, R. A. L. Ligand Shell Structure in Lead Sulfide-Oleic Acid Colloidal Quantum Dots Revealed by Small-Angle Scattering. *Journal of Physical Chemistry Letters* 2019, *10* (16), 4713–4719. https://doi.org/10.1021/acs.jpclett.9b01008.
(96) Smock, S. R.; Williams, T. J.; Brutchey, R. L. Quantifying the Thermodynamics of Ligand Binding to CsPbBr 3 Quantum Dots . *Angewandte Chemie* 2018, *130* (36), 11885–11889. https://doi.org/10.1002/ange.201806916.
(97) Fritzinger, B.; Capek, R. K.; Lambert, K.; Martins, J. C.; Hens, Z. Utilizing Self-Exchange to Address the Binding of Carboxylic Acid Ligands to CdSe Quantum Dots. *J Am Chem Soc* 2010, *132* (29), 10195–10201. https://doi.org/10.1021/ja104351q.
(98) Kroupa, D. M.; Anderson, N. C.; Castaneda, C. V.; Nozik, A. J.; Beard, M. C. In Situ Spectroscopic Characterization of a Solution-Phase X-Type Ligand Exchange at Colloidal Lead Sulphide Quantum Dot Surfaces. *Chemical Communications* 2016, *52* (96), 13893–13896. https://doi.org/10.1039/C6CC08114B.

(99) Zhou, X.; Pang, Z.; Cao, W.; Cao, Z.; Zhu, J.; Qi, Y.; Peng, X.; Kong, X. Diffusion NMR for Measuring Dynamic Ligand Exchange on Colloidal Nanocrystals. *Anal Chem* 2023, *95* (2), 792–801. https://doi.org/10.1021/acs.analchem.2c02964.
(100) Zhang, Z.; Madsen, L. A. Observation of Separate Cation and Anion Electrophoretic Mobilities in Pure Ionic Liquids. *Journal of Chemical Physics* 2014, *140* (8). https://doi.org/10.1063/1.4865834.
(101) Li, X.; Cooksey, T. J.; Kidd, B. E.; Robertson, M. L.; Madsen, L. A. Mapping Coexistence Phase Diagrams of Block Copolymer Micelles and Free Unimer Chains. *Macromolecules* 2018, *51* (20), 8127–8135. https://doi.org/10.1021/acs.macromol.8b01220.

Chapter 2: NMR techniques to probe dynamics, diffusion, and kinetics in macromolecular systems

Abstract

This chapter overviews the fundamental theories and principles behind various NMR (nuclear magnetic resonance) techniques used to study the diffusion, molecular structure determination, particle size, and kinetics in macromolecular systems like linear polyelectrolyte chains and micelles. Characterizing these properties play a vital role in understanding the functionality of molecular systems in applications like batteries, drug-delivery agents, photovoltaics, and sensors. Among the many characterization tools available for examining macromolecular properties, NMR stands out due to its chemical specificity, isotope selectivity, and non-destructive nature. These features enable researchers to not only determine the molecular structure but also aid in probing molecular interactions, dynamics, kinetics, and transport. By carefully programming the timing of radiofrequency (rf) and magnetic field gradient pulses in NMR instruments, valuable insights on the materials properties can be probed. This chapter explains basic principles of NMR spectroscopy and other powerful pulse sequences like, T_1 Inversion Recovery (T1IR), Carr-Purcell-Meiboom-Gill (CPMG), pulse-field-gradient (PFG) NMR, Dynamic NMR spectroscopy. These methods are used in my thesis to investigate the physical and chemical behavior of macromolecular and semiconductor colloidal systems.

2.1. Basic principles of NMR

Every atomic nucleus has four important physical properties: mass, electric charge, magnetism, and spin.[1,2] Spin is a form of angular momentum, and is an intrinsic property of the nucleus itself. The total nuclear spin angular momentum takes the form $[S(S+1)]^{1/2}\hbar$ where S is the nuclear spin quantum number. Typically, S can be either an integer (i.e. 0, 1, 2…) or a half integer (i.e. 1/2, 3/2, 5/2…).[1,2] Commonly studied nuclei like ^{1}H, ^{13}C, ^{31}P, and ^{15}N are all NMR-active spin-1/2 nuclei. These active nuclei have (2S+1) sublevels, which are degenerate in the absence of the external magnetic field B_0. Thus, for spin-1/2 nuclei, the spin states are two-fold degenerate ($m = \pm 1/2$) in the absence of B_0. When B_0 is applied, these degenerate states split into different energy levels (nuclear Zeeman splitting) with different magnetic moments as shown in **Figure 2.1A** also known as *nuclear Zeeman effect*.[1,2]

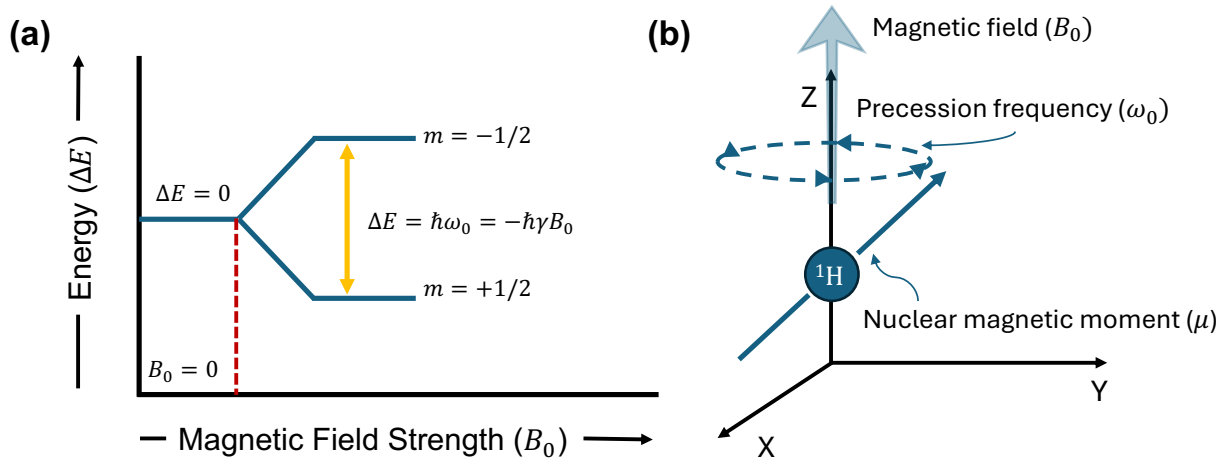

Figure 2.1: **a)** Zeeman splitting of spin ½ (for example ^{1}H) nucleus into two states with $m = \pm$ ½ and the energy difference (ΔE) between the degenerate states depends on the gyromagnetic ratio of the nucleus (γ) and the applied magnetic field B_0. **b**) Classical view of Larmor precession with frequency ω_0 of a ^{1}H nucleus (spin ½) around the direction of the static magnetic field, B_0 (z-axis).

The nuclear magnetic moment μ, which relates to the nuclear spin S by the gyromagnetic ratio γ ($\mu = \gamma S$), begins to precess around the axis of external magnetic field B_0 (z-direction or

longitudinal direction) at the Larmor frequency ω_o as shown in **Figure 2.1B**. This frequency depends on the strength of the external magnetic field B_o as shown in the **Equation 2.1.1**.[1,2] Here γ is a constant specific to each nucleus.

$$\omega_o = -\gamma B_o \tag{2.1.1}$$

2.2. Relaxation measurements

In absence of an applied magnetic field, an ensemble of nuclear spins in a sample orients randomly in all directions (original thermal equilibrium), resulting in the net magnetization $\vec{M}$ (vector sum of all individual nuclear magnetic moments) of the sample equal to zero. When the spins are exposed to an external magnetic field B_0, all nuclear spins begin to precess at the Larmor frequency around B_0 (see **Figure 2.1B**). This ensemble of magnetic moments in random orientations eventually reaches a stable Boltzmann equilibrium (also a thermal equilibrium) resulting in a net magnetizaiton $\vec{M}$ of the sample along B_0. Once B_0 is turned off, the sample's net magnetization begins to relax to its original thermal equilibrium and this relaxation process is termed as the spin-lattice relaxation.[1,2]

The time constant that describes this relaxation rate is known as longitudinal relaxation time (T_1) and depends on molecular motions occurring on the $1/\omega_o$ timescale (nanoseconds).[3] T_1 is influenced by both magnetic field strength and the tumbling rate of the probed molecules.[4–6] Additionally, paramagnetic species in the solution can significantly influence the relaxation rate by shortening T_1 times of the molecules probed, as these species provide efficient relaxation pathways.[7] Thus measuring T_1 provides useful molecular dynamics, which becomes critical while choosing parameters for diffusion measurements. T_1 is often measured using the inversion-recovery pulse sequence (T1IR), as shown in **Figure 2.2** below.[1,2,8]

The sequence (**Figure 2.2a**) starts with a 180° excitation pulse, which is an rf pulse (oscillating magnetic field) at a frequency near ω_o, inverting the net magnetization $\vec{M}$ along the $-z$ axis. This is followed by variable delay time (t_d) during which $\vec{M}$ relaxes along B_0. A 90° rf pulse is then applied to shift the net magnetization along the transverse ($-y$) direction, producing an NMR signal. This acquired signal (I) varies with t_d, as shown in **Figure 2.2b** and this variation in signal can be fitted using **Equation 2.2.1**, to determine the longitudinal relaxation time T_1.[8]

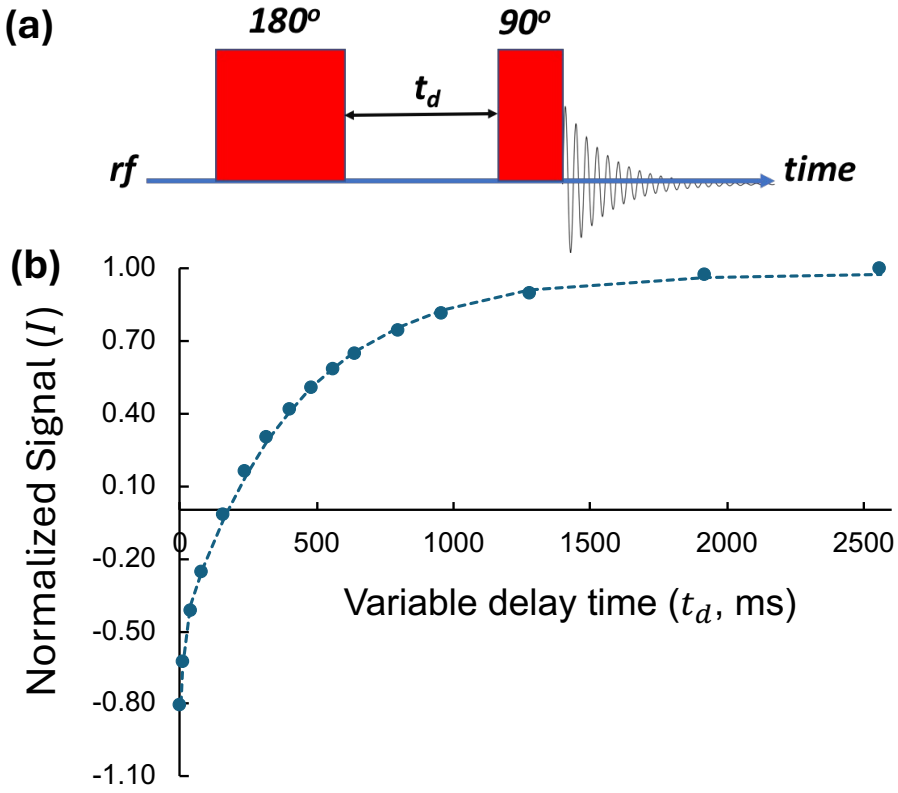

Figure 2.2: **a)** The inversion-recovery pulse sequence is used to determine T_1. **b)** The pulse sequence produces an exponential increase in signal (I) as the variable delay time t_d increases. By fitting the data using **Equation 2.2.1**, we obtain the T_1 time value. In the example plot (b), delay time t_d ranges from 3 μs to 3 s.

$$I = I_0\left(1 - 2e^{-\frac{t_d}{T_1}}\right) \tag{2.2.1}$$

In a typical 1D NMR experiment, a brief 90° rf pulse is applied to rotate the net magnetization vector ($\vec{M}$) of the nuclear spins into the transverse plane. After the pulse is switched off, molecular tumbling induces random fluctuations in the local magnetic fields experienced by individual nuclei. These fluctuation cause variations in the precession frequencies of the nuclear spins, leading to a gradual loss of phase coherence. This loss in phase coherence manifests as a decay in the net transverse magnetization, which is detected as free induction decay (FID) signal. This phenomenon is generally termed spin-spin relaxation or transverse relaxation and is characterized by the time constant T_2, known as spin-spin (transverse) relaxation time.[1,2,9,10]

The T_2 relaxation time significantly impacts the NMR spectrum, with the signal's full width at half maximum (FWHM or linewidth) inversely proportional to the T_2 relaxation time (FWHM $= 1/(\pi T_2)$).[11] Smaller, rapidly tumbling molecules in solutions exhibit longer T_2 values, resulting in narrower linewidths. Conversely, larger molecules with restricted motion have shorter T_2 values, leading to broader linewidths.

T_2 is a crucial property that reflects the molecular dynamics of the system. In complex systems like micelles, polyelectrolytes, and colloidal QDs, accurate T_2 determination is essential for optimizing NMR diffusometry measurements or to accurately determine kinetics of exchange between chemical environments (details in the further section). However, measuring T_2 directly from FWHM can be inaccurate due to inhomogeneous broadening of the NMR signal, a common effect in NMR.[12] This broadening arises from static variations in the local magnetic environment, affecting linewidths and yielding T_2^* times that are shorter than the true T_2 times. To address this issue, more sophisticated methods have been developed, chief among them being the spin-echo technique.

The spin-echo technique, discovered by Erwin Hahn in 1950, minimizes the effects of magnetic field inhomogeneities on NMR measurements.[1,7–10] This technique employs a sequence containing one 90°, to bring the net magnetization along transverse plane, and one 180° rf pulse to refocus the transverse nuclear spins that have lost coherence due to these inhomogeneities. Building on Hahn's work, Carr and Purcell and then Meiboom and Gill developed more advanced pulse sequences, leading to the widely used Carr-Purcell-Meiboom-Gill (CPMG) pulse sequence (**Figure 2.4a**)[12,13] for measuring T_2 relaxation times.

In the CPMG sequence, a series of 180° pulses (the echo train) are applied after 90° pulse, with these 180° pulses separated by a constant delay τ. The spin echo delay time t_s, is varied by changing the number of echoes n, where $t_s = 2n\tau$. By observing the decay of the acquired signal as a function of t_s, researchers can determine the true T_2 relaxation time using the **Equation 2.2.2.**

$$I = I_0 e^{-\left(\frac{2\tau n}{T_2}\right)} \tag{2.2.2}$$

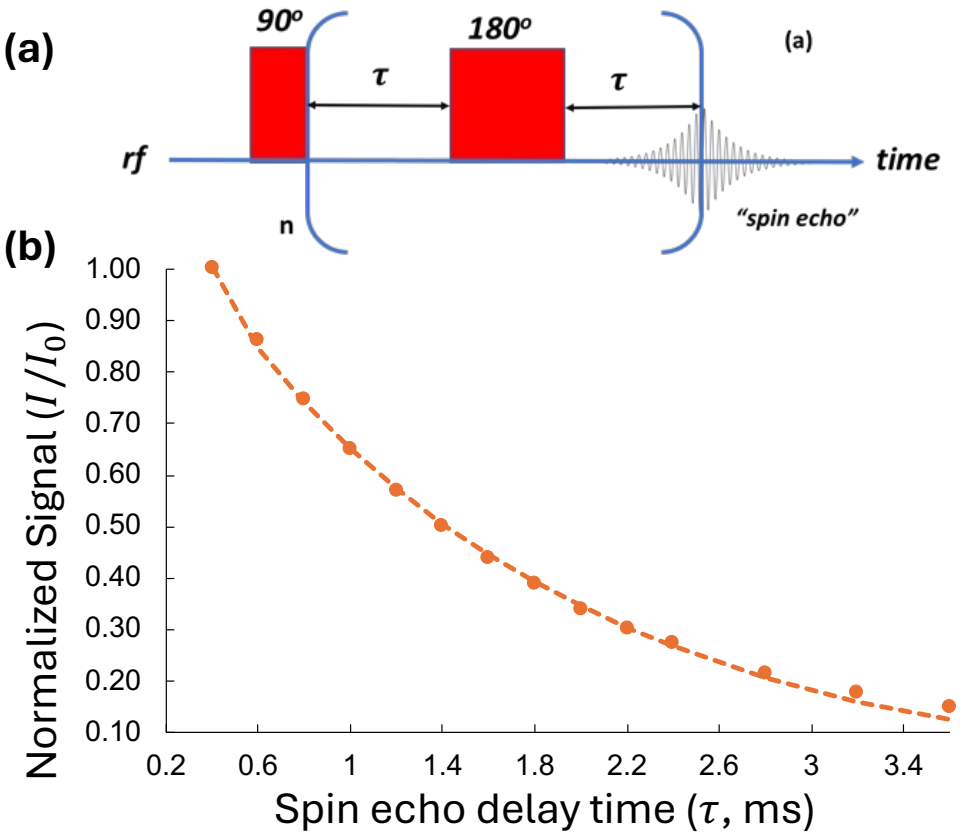

Figure 2.3: **a)** The CPMG pulse sequence generates an exponential decay in the acquired signal as a function of spin echo delay time $t_s = 2n\tau$. **b)** This exponential signal decay is fit with **Equation 2.2.2** to extract the T_2 relaxation time. Here τ is set to 50 μs and n was varied to achieve at least 90% of signal attenuation.

While the CPMG sequence effectively mitigates magnetic field inhomogeneity, it does not fully suppress J-modulations effects on T_2 measurements, which can lead to significant errors. J-modulations arises from J-coupling, a phenomenon observed in NMR spectra caused by interactions between nuclear spins mediated through chemical bonds. Studies have shown that rapid refocusing (with $\tau \ll 1ms$) can quench homonuclear J-modulations.[14] However, to fully compensate for J-modulation effects, a modified CPMG pulse sequence is required as shown in **Figure 2.4**. This sequence, developed by Takegoshi et al. for protein metabolite studies, includes a 90° pulse inserted at the midpoint of a double spin echo. This modification enables coherence

exchange between spins and reverses the sense of J-modulation, which is then refocused by the second half of the double spin echo.[14,15]

The modified sequence has proven valuable in studying protein metabolites and is particularly useful in ligand exchange studies. For instance, in semiconductor colloid research, this sequence allows for accurate determination of T_2 for exchanging ligands, which is crucial for determining ligand exchange rates using dynamic NMR (details explained further below). Moreover, accurate measurements of both T_1 and T_2 relaxation times aid in optimizing NMR diffusometry measurements and obtaining precise diffusion coefficients in complex macromolecular systems. Measuring precise diffusion coefficients is important in studies involving micelles, polyelectrolytes, and colloidal quantum dots, where understanding dynamics is critical for designing new materials.

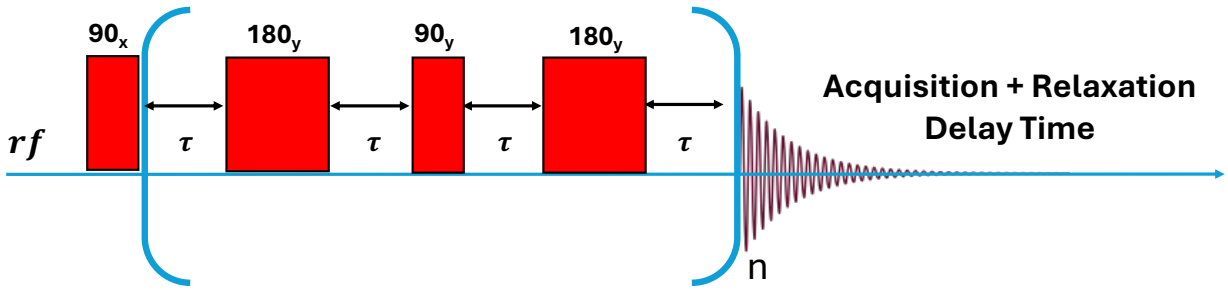

Figure 2.4: Modified CPMG pulse sequence containing 90°$_y$ refocusing pulse to suppress J-modulation effects and to accurately determine spin-spin relaxation time (T_2).

2.3. Pulsed-field-gradient (PFG) NMR diffusometry

Chapter 1.1 introduced the concept of Brownian motion of molecular species, which gives rise to self-diffusion, characterized by the diffusion coefficient D. This coefficient directly correlates to the molecular translational motion, providing insights into the molecular behavior ranging from basic molecular size characterization to complex dynamic analysis in mixtures and aggregates. Various techniques were developed to study molecular diffusion including dynamic

light scattering, neutron scattering, fluorescence, capacity intermittent titration techniques, and centrifuge methods.[16–20] However, these techniques are often limited by their sample preparation requirements, experimental complexity, and the range of concentration they can effectively probe.

In contrast, NMR spectroscopy offers an efficient and versatile tool for investigating molecular dynamics in both chemical and biological systems. NMR is non-invasive, non-perturbative, and does not require labeling of probe molecules.[4,5,21–29] More importantly, NMR allows for direct measurement of D under diverse physical conditions and across a wide concentration range, limited primarily by the signal-to-noise ratio necessary for detection, a constraint that can restrict the applicability of essentially all techniques.

The foundation for NMR diffusometry was laid by Hahn, who first observed that signal attenuation during a spin echo can result from molecular diffusion in the presence of magnetic field inhomogeneity.[8] Building on this observation, Carr and Purcell developed a quantitative model in 1954 to determine the self-diffusion coefficient of the probed species.[30] Later, Stejskal and Tanner expanded this model by incorporating pulsed-field gradients (PFG) during measurements, establishing a correlation between time-dependent diffusion and observed NMR signal attenuation (model explained below).[31]

Figure 2.5 illustrates the evolution of net magnetization $\vec{M}$ in a pulsed-gradient-spin-echo PGSE pulse sequence. As discussed earlier in **Equation 2.1.1**, the intrinsic Larmor frequency ω_o depends on the strength of the applied magnetic field B_0. In a uniform B_0, all nuclei exhibit identical precession frequencies ω_o and remain inphase in the transverse plane following excitation by a 90° pulse. However, the addition of a magnetic field gradient g to the uniform B_0 introduces a spatial dependence to ω_o. For instance, applying a linear gradient pulse with strength

g_z along the z-axis results in a corresponding linear variation in ω_o for nuclear spins along the z-direction, as described by **Equation 2.3.1**:

$$\omega_o = -\gamma(B_o + g_z z) = -\omega_0 - \gamma g_z z \tag{2.3.1}$$

This gradient pulse encodes spatial information into the nuclear spin ensemble by introducing a phase angle $\phi(z) = \gamma B_0 \delta + \gamma z g \delta$. The variation in phase angle $\phi(z)$ along the z-axis creates a "magnetization helix", represented by a blue dotted line in **Figure 2.5** with a wavelength λ given by **Equation 2.3.2**.[32]

$$\lambda = \frac{2\pi}{\gamma g_z \delta} \tag{2.3.2}$$

The characteristics of the induced magnetization helix, including its wavelength λ, can be modulated by varying the strength (g_z) and duration (δ) of the pulse.[33] A subsequent 180° rf pulse inverts the phase of the helix, and a second gradient pulse (with identical g_z and δ as the first) restores all spins to in-phase condition, producing a refocused signal I_0 (see **Figure 2.5A**). However, if molecular translational motion, such as Brownian motion, occurs during the interval Δ (the time between the leading edges of the gradient pulses), the refocusing will be incomplete, resulting in a reduced NMR signal I. This signal attenuation forms the basis for quantifying molecular diffusion using PFG NMR.

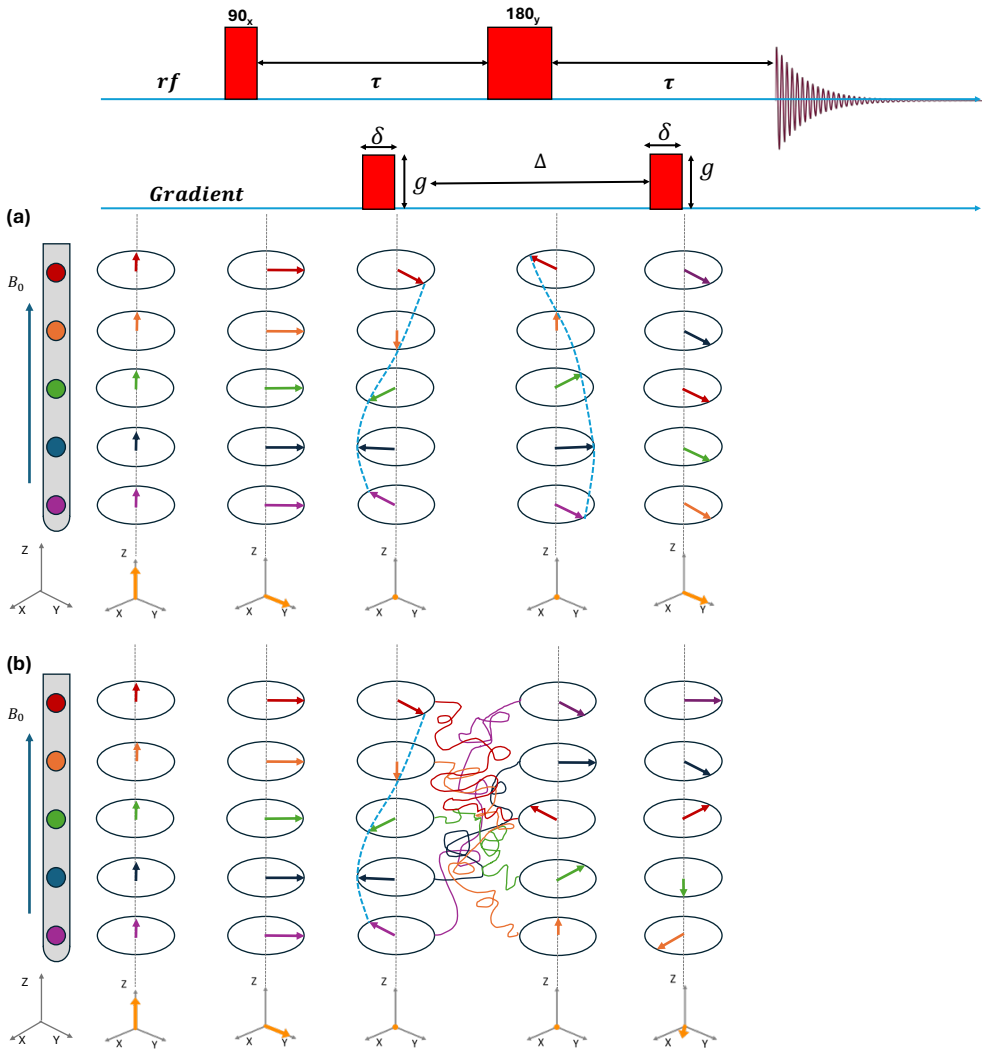

Figure 2.5: The pulse sequence diagram (top) depicts the pulsed-gradient-spin-echo (PGSE) NMR experiment, designed to measure the diffusion coefficient of chemical species in a sample. The diagram illustrates the evolution of net magnetization vector as rf and $gradient$ pulses are applied. The first gradient pulse encodes spatial position information by inducing phase change in Larmor frequency of nuclear spins creating a magnetization helix. **a)** If there is no diffusion occurs during the interval Δ, the second gradient pulse perfectly refocuses the spins, and the total signal is restored. **b)** If diffusion occurs, the translational motion prevents the second gradient pulse from fully refocusing the spins, leading to a reduction in the total signal intensity.

Stejskal and Tanner developed a physical model that accounts for all experimental parameters (g, δ, Δ) influencing the phase angle $\phi(z)$, which is represented as the signal

attenuation I/I_0. This model is now referred to as the Stejskal-Tanner equation (**Equation 2.3.4**).[31,32,34]

$$\frac{I}{I_0} = e^{-Dg^2\delta^2\gamma^2\left(\Delta-\frac{\delta}{3}\right)} \tag{2.3.4}$$

In this equation, Δ (shown in **Figure 2.5**) represents the diffusion time. By varying the gradient strength g while keeping other experimental parameters (Δ, δ) constant, the diffusion coefficient D of the molecular species can be determined by fitting signal attenuation to the Stejskal-Tanner equation (**2.3.4**).

Figure 2.6A presents an example of a PFG NMR diffusometry measurement, illustrating the NMR signal attenuation for a 35 kg/mol polystyrene sulfonate (PSS) polymer in H_2O as a function of the NMR diffusion parameter $b = \mathrm{g}^2\delta^2\gamma^2\left(\Delta - \frac{\delta}{3}\right)$. For improved visualization, the signal attenuation is log-transformed to produce a linear plot (see **Figure 2.6B**), where the slope yields the diffusion coefficient of the molecular species. At room temperature, the measured diffusion coefficient for PSS is $D = 3.3 \times 10^{-11}\mathrm{m}^2 \cdot \mathrm{s}^{-1}$, which is significantly lower than that of water ($D = 2 \times 10^{-9}\mathrm{m}^2 \cdot \mathrm{s}^{-1}$). This difference in diffusion coefficients between the two molecular species reflects their relative sizes, as described by the Stokes-Einstein equation (**1.1.4**). This relationship allows for direct size characterization of particles in a mixture. It's important to note that several other factors must be considered while measuring D in complex systems like soft matter. These considerations will be explained in the following section.

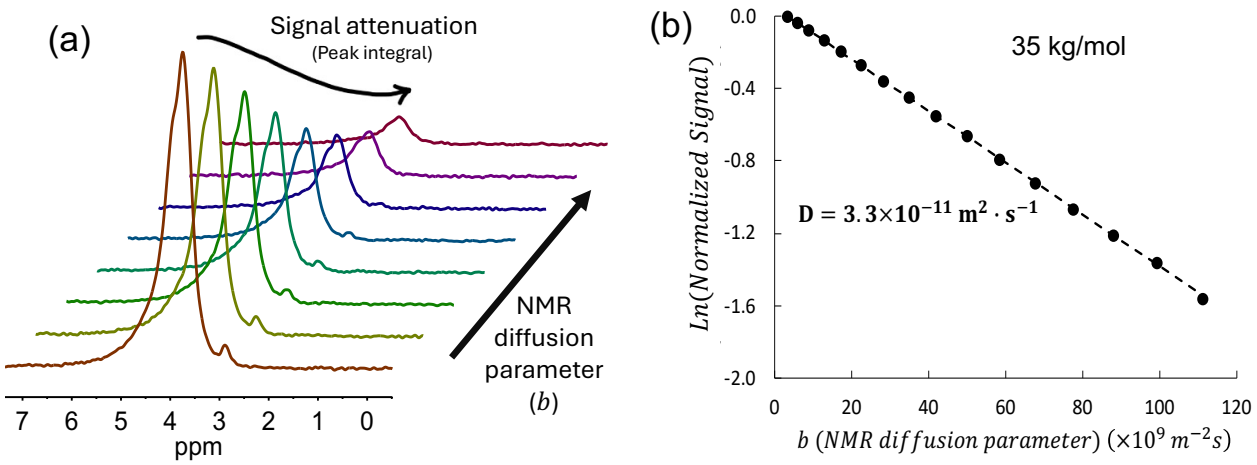

Figure 2.6: **a)** The change in signal as a function of NMR diffusion parameter $b = g^2\delta^2\gamma^2\left(\Delta - \frac{\delta}{3}\right)$, which contains all relevant experimental parameters, for a 35 kg/mol polystyrene sulfonate (PSS) dissolved in H_2O at room temperature. **b)** The slope of the log-transformed signal attenuation with respect to b yields the diffusion coefficient D. For PSS $D = 3.3 \times 10^{-11} m^2 \cdot s^{-1}$ as shown.

2.3.1. Practical Considerations of NMR Diffusometry in Soft Matter and other Complex Systems

As shown earlier, NMR diffusometry allows us to measure the diffusion coefficient D of various diffusing species, enabling us to determine the size, molecular interactions and transport properties in complex systems. However, it is important to consider several challenges when measuring diffusion coefficients in soft matter or other complex systems to ensure accuracy. Some of these considerations are explained in the following sections.

Spin-spin relaxation time (T_2) considerations:

The choice of pulse sequence is crucial when planning a diffusion experiment. In a PGSE experiment, significant signal loss occurs due to spin-spin relaxation in the transverse plane (see **Figure 2.7a**), especially when the diffusion time Δ is equal to or longer than the T_2 of the species

being studied. For instance, small molecules in liquids typically have $T_2 \approx 1\,s$. If a PGSE experiment is run with $\Delta = 30\,ms$ and at a gradient strength $g = 0$ (to avoid signal loss due to diffusion), the observed signal loss is entirely due to spin-spin relaxation, following the relationship $1 - e^{-\frac{\Delta}{T_2}}$ as shown in **Figure 2.7a**. In this case, the signal loss is approximately 3% ($1 - e^{-\frac{0.03}{1}}$). This suggests that when $\Delta \ll T_2$, no significant signal loss occurs.

However, highly viscous solutions or very large polyelectrolyte chains in a solvent typically have $T_2 \approx 30\,ms$. When measured using PGSE with $\Delta = 30\,ms$ at $g = 0$, the signal loss due to spin-spin relaxation is around 63% ($1 - e^{-1}$), significantly reducing the signal-to-noise ratio (SNR). This poses a challenge to measure the diffusion coefficients with greater accuracy.

To address the challenges associated with T_2 relaxation, the pulsed-gradient-stimulated-echo (PGSTE) pulse sequence was developed, employing three 90° rf pulses (see **Figure 2.7b**).[33,34] The sequence begins with an initial 90° rf pulse to excite the nuclear spins. After a brief echo delay time τ_e (where $\tau_e \ll \Delta$), a second 90° rf pulse is applied transferring the spin magnetization to the longitudinal plane and minimizing signal decay due to spin-spin relaxation ($\propto 1 - e^{-\frac{\tau_e}{T_2}}$). Following a longitudinal storage time T ($\approx \Delta$), the third 90° rf pulse is applied. During T, the longitudinal magnetization experiences decay due to spin-lattice relaxation ($\propto 1 - e^{-\frac{T}{T_1}}$). For systems such as polyelectrolytes and viscous solutions, in which $T_1 \gg T_2$, the PGSTE experiment results in considerably less signal loss compared to PGSE, ensuring more precise measurements of diffusion coefficients.

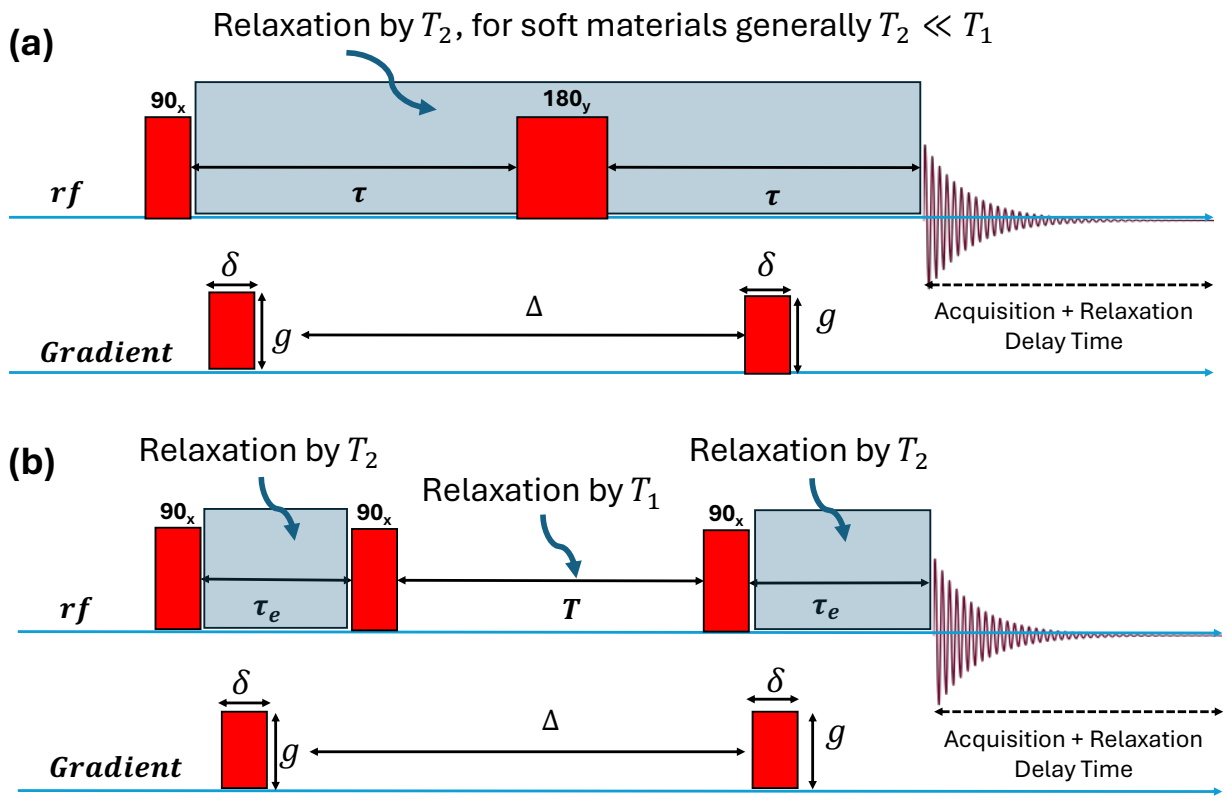

Figure 2.7: Comparison of (a) pulsed-gradient-spin-echo (PGSE) and (b) pulsed-gradient-stimulated-echo (PGSTE) sequence for measuring diffusion coefficients. In a PGSE experiment, substantial signal decay occurs due to T_2 relaxation. In contrast, the PGSTE sequence is less sensitive to the T_2 of the nuclei being probed and is more sensitive to T_1 relaxation because the signal is stored in the longitudinal axis during the storage time T. For typical soft material systems $T_2 \ll T_1$ and thus using the PGSTE can significantly reduce signal loss compared to PGSE.

Thermal convection effects:

Thermal convection across the sample is another factor affecting the accuracy of diffusion measurements using PFG NMR. Convection-driven circulating currents (but in some way quasi random and/or turbulent currents) introduce additional molecular motions that attenuate the signal similarly to true random diffusion, leading to phasing errors and overestimation of diffusion coefficients. This distortion causes the signal decay to deviate significantly from the expected Gaussian relation of signal intensity and gradient strength, resulting in errors when determining *D*

from **Equation 2.3.4**. These convection effects are more pronounced when samples are measured at temperatures significantly different from ambient temperature or when dealing with slow diffusing molecules, such as very large polymer chains.

The onset of convection is determined by a critical balance between hydrostatic and viscous forces, characterized by the Rayleigh-Benard number Ra.[33,35] The critical value of this number, denoted as Ra_c, defines the onset of convection in a fluid. In a typical NMR experiment, the sample is contained within a vertical cylindrical tube, where the radius-to depth ratio (r/l) plays a key role in convection behavior. For such a setup, $Ra_c \propto \frac{l^4}{r^4}$, indicating that reducing the r/l ratio is an effective way to suppress convection. This can be achieved by using narrow outer diameter capillaries, typically ranging from 0.5 mm to 1 mm, placed inside the NMR tube. For low-viscosity solutions, even smaller capillaries ($\leq 0.1\ mm$ outer diameter) may be necessary.

Beyond geometric considerations, higher order pulse sequences can further minimize thermal artifacts.[36] The convection-compensated double stimulated echo (DSTE) sequence is one such example.[37] The DSTE pulse sequence employs bipolar gradient pulses within a scan, effectively cancelling out the phase modulations caused by convection displacments.

In the research projects presented in this dissertation, the aforementioned limitations were carefully addressed through a combination of strategies: appropriate sample preparation, optimization of experimental parameters, and the selection of suitable pulse sequences. This comprehensive approach ensured the accuracy of diffusion coefficient measurements for various species in each sample studied. Detailed descriptions of the specific NMR diffusometry pulse sequence employed, parameter choices made, and experimental conditions utilized are provided in Chapters 3, 4, 5, and 6.

2.4. Principles of chemical exchange in NMR: The two-site exchange model

Section 2.1 and 2.2 described the evolution of the net magnetization for an ensemble of nuclei within a homogeneous magnetic environment. The small local fluctuations in the magnetic field surrounding each nucleus, caused by interactions with the neighboring nuclei, gradually lead to decoherence of the magnetization over time. However, many studies have also reported significant changes in the local molecular magnetic environment of nuclei due to ongoing chemical exchange processes. [38–41]We can quantify the chemical exchange processes by observing the variation of the NMR lineshape as a function of temperature. This technique, which I describe here is often known as 'dynamic NMR'.

These chemical exchanges can arise from bond rotations, isomerization, intermolecular interactions, or polymer chains transitioning between different states of association. When nuclei exchange between sites with different chemical shifts (i.e. magnetic environments), the result is a broadened signal in the NMR spectrum and its chemical shift lies between the chemical shifts of the corresponding environments. Such behavior is observed in semiconductor colloidal systems, where ligands rapidly exchange between free and surface-adsorbed states, producing a broad NMR signal that shifts between the two states. This exchange phenomenon often studied using dynamic NMR spectroscopy is discussed in detail in Chapter 6.

Chemical exchanges, such as bond rotations or isomerization, are classified as mutual exchange processes where the nuclei/molecules swap their chemical environments directly, keeping the total number of molecules in each environment constant. In mutual exchanges, the forward and backward exchange rates are equal, and the equilibrium constant is exactly 1, as the populations of the exchanging species remains equal. However, in non-mutual exchanges,

nuclei/molecules transition between chemical environments without a direct swap, leading to a possible change in population fractions of nuclei/molecules in each environment. In such cases, the forward and backward exchange rates may differ, and the equilibrium constant can deviate from 1. An example of a non-mutual exchange is the ligand exchange between free and surface-adsorbed states, where the exchange rates and their populations are unequal.

To describe the net magnetization and the corresponding NMR spectra, Rogers and Woodbrey developed a generalized model that applies to any non-mutual and mutual exchanges.[42] Gutowsky and Holm applied this model to study the kinetics of amide bond rotation, which is a mutual exchange process.[43]

For a system undergoing a first-order nuclear or molecular exchange between state A and B, the rate of change in the concentration of nuclei/molecule at site/state A is given by equation 2.4.1

$$\frac{d[A]}{dt} = -k_A[A] \tag{2.4.1}$$

As nuclei/molecules are lost from site A, they are assumed to instantaneously appear in site B. Under equilibrium conditions, nuclei/molecules also jump from site B to site A. This exchange alters the net magnetization (**Equation 2.4.2**) at site A. The loss of magnetization at site A, due to nuclei/molecules jumping to site B, is offset by the simultaneous gain in magnetization as they return from site B to site A.

$$\frac{dM_A}{dt} = -k_A M_A + k_B M_B \tag{2.4.2}$$

For a first-order process, the rate constant k_A represents the fraction of the molecules/nuclei jumping from site A to site B (and vice versa for k_B), with the time constant $\tau_A = \frac{1}{k_A}$ representing the average lifetime of the forward reaction. Incorporating these rate constants into the Bloch

equations, which describe the evolution of the magnetization vector in the presence of rf pulses and free precession, leads to the final expression for the NMR signal intensity, $S_{ex}(v)$, for a non-mutual two-site exchange, as shown in **Equation 2.4.3**.[44–46]

$$S_{ex}(\nu) = C_0 \times \left(\frac{P\left[1 + \tau_{ex}\left(\frac{p_B}{T_{2,A}} + \frac{p_A}{T_{2,B}}\right)\right] + QR}{(P)^2 + (R)^2} \right) \tag{2.4.3}$$

In this equation, C_0 is a scaling factor, and p_i represents the population fraction of nuclei/molecules in a chemical environment i. $T_{2,i}$ represents the spin-spin relaxation times of the nuclei in chemical environment i when nuclei are not exchanging. The terms P, Q, and R are defined by the following **Equations 2.4.4** to **2.4.6** below:

$$P = \tau_{ex} \times \left(\frac{1}{T_{2,A} \times T_{2,B}} - 4\pi^2\Delta\nu^2 + \pi^2\delta\nu^2 \right) + \frac{p_A}{T_{2,A}} + \frac{p_B}{T_{2,B}} \tag{2.4.4}$$

$$Q = \tau_{ex} \times (2\pi\Delta\nu - \pi\delta\nu(p_A - p_B) \tag{2.4.5}$$

$$R = 2\pi\Delta\nu\left[1 + \tau_{ex}\left(\frac{1}{T_{2,A}} + \frac{1}{T_{2,B}}\right)\right] + \pi\delta\nu\tau_{ex}\left(\frac{1}{T_{2,A}} - \frac{1}{T_{2,B}}\right) + \pi\delta\nu(p_A - p_B) \tag{2.4.6}$$

Here, $\delta\nu$ represents the difference in chemical shift frequencies of non-exchanging nuclei between the two sites (**Equation 2.4.7**), while $\Delta\nu$ denotes the midpoint of the chemical shift difference of the resonance frequencies between the two sites (**Equation 2.4.8**). $\tau_{ex} = k_{ex}^{-1} = (k_A + k_B)^{-1}$ represents the total exchange lifetime for the nuclei to transition between sites/states and can be determined by fitting the experimental data to the model. The rate constants k_A and k_B can be determined from τ_{ex} based on the population fraction of the nuclei in each state.

$$\delta\nu = |\nu_A - \nu_B| \tag{2.4.7}$$

$$\Delta\nu = \left(\frac{\nu_A + \nu_B}{2}\right) - \nu \tag{2.4.8}$$

$$\tau_{ex} = \frac{p_A}{k_B} = \frac{p_B}{k_A} \tag{2.4.9}$$

Figure 2.8 comprehensively illustrates the lineshapes and the chemical shift behavior of the exchange nuclei/molecules NMR signal of the exchanging nuclei/molecules under different exchange rate regimes and population fractions. In the slow exchanging regime ($k_{ex} \ll \delta\nu$), the spectra show two distinct Lorentzian peaks. As the exchange rate increases into the "intermediate exchange" regime ($k_{ex} \approx \delta\nu$), these peaks broaden and coalesce, with its chemical shift centered at the population-weighted average of the non-exchanging nuclei's chemical shifts. In the "fast exchange" regime ($k_{ex} \gg \delta\nu$), the single coalesced peak narrows further shown in the **Figure 2.8**.

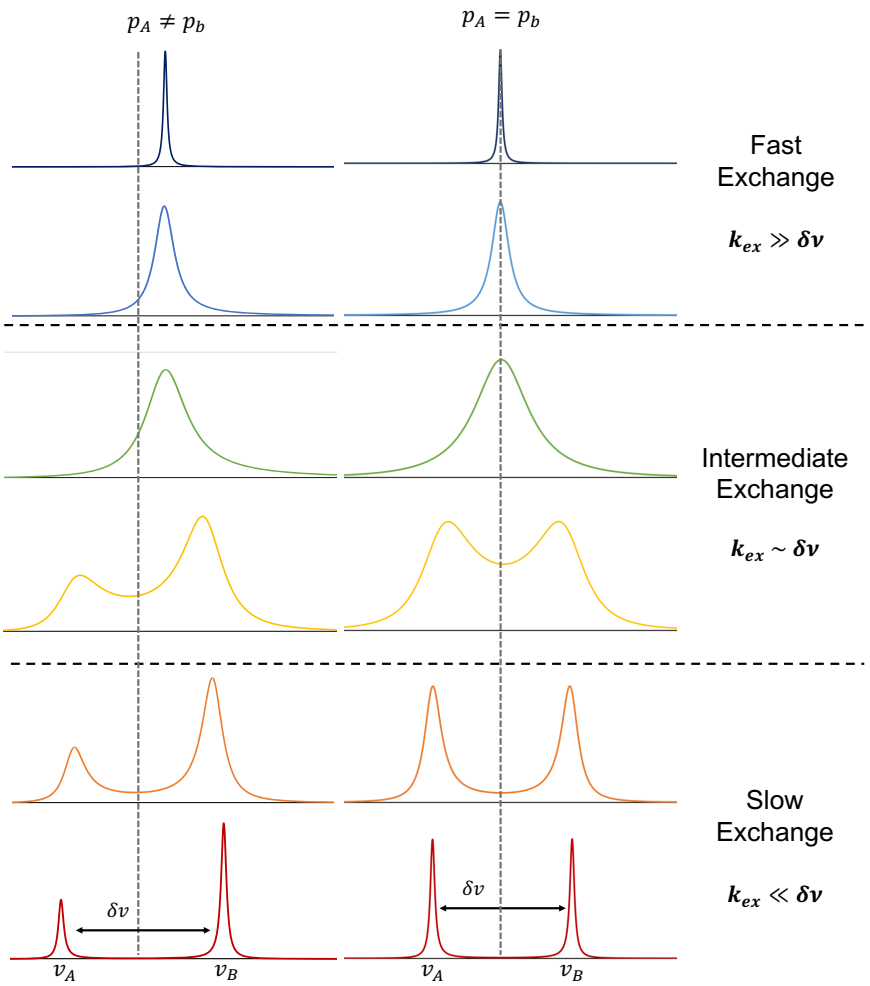

Figure 2.8: The NMR lineshape exhibit distinct variations for nuclear exchange between two sites as the exchange rates (k_{ex}) increases. The dashed line indicates the midpoint between the chemical shifts ($\delta\nu$) of the two environments. In the slow exchange regime ($k_{ex} \ll \delta\nu$), two narrow, and distinct peaks represent nuclei in separate chemical environments. As the exchange rate approaches the intermediate regime ($k_{ex} \approx \delta\nu$), the peaks broaden, shift, and eventually merge into a single coalesced peak. In the fast exchange regime ($k_{ex} \gg \delta\nu$), this coalesced peak becomes narrower as the nuclei rapidly exchange between the two sites/states. For unequal population fractions, the signal of the less populated site is becomes noticeably shifted due to differing exchange dynamics. Thus, the chemical shift of the exchanging nuclei in fast exchange regime is the population weighted-average of the chemical shifts in the very-slow exchange regime.

Determining $\delta\nu$, as required in equations **2.4.3** to **2.4.8**, is not always straightforward. A system exhibiting distinct exchanging states on the spectrum is necessary, which can be achieved

through chemical modifications or temperature variation. In semiconductor colloid studies, chemical shifts of oleic acid ligands in free solvent and adsorbed state were measured using control samples, providing the $\delta\nu$ value. This approach provided sufficient parametric information to determine the rate constants (forward and backward) from dynamic NMR spectroscopic study. By employing this study, we can determine the activation energies of chemical reactions, offering crucial insights into designing next-generation materials for applications such as drug delivery or photovoltaics.

In summary, NMR is a highly versatile technique that leverages the sensitivity of nuclear spins to their local magnetic environment, providing detailed chemical and physical information across various time and length scales. Its non-destructive nature simplifies sample preparation and allows precise measurements of system properties, leading to a deeper understanding of molecular processes that are difficult to assess with other techniques.

References

(1) Levitt, M. h. *Spin Dynamics: Basics of Nuclear Magnetic Resonance*; John Wiley & Sons: Chichester, Uk, 2001.

(2) Roberts, J. D. *ABCs of FT-NMR*; 2000.

(3) Gaeta, M.; Galletta, K.; Cavallaro, M.; Mormina, E.; Cannizzaro, M. T.; Lanzafame, L. R. M.; D'Angelo, T.; Blandino, A.; Vinci, S. L.; Granata, F. T1 Relaxation: Chemo-Physical Fundamentals of Magnetic Resonance Imaging and Clinical Applications. *Insights into Imaging*. Springer Science and Business Media Deutschland GmbH December 1, 2024. https://doi.org/10.1186/s13244-024-01744-2.

(4) Madsen, L. A.; Hou, J. NMR Diffusometry for the Study of Energy-Related Soft Materials. 1897, No. 9, 464–496.

(5) Hou, J.; Madsen, L. A. New Insights for Accurate Chemically Specific Measurements of Slow Diffusing Molecules. *Journal of Chemical Physics* 2013, *138* (5). https://doi.org/10.1063/1.4789923.

(6) Kidd, B. E.; Lingwood, M. D.; Lee, M.; Gibson, H. W.; Madsen, L. A. Cation and Anion Transport in a Dicationic Imidazolium-Based Plastic Crystal Ion Conductor. *Journal of Physical Chemistry B* 2014, *118* (8), 2176–2185. https://doi.org/10.1021/jp4084629.

(7) D'Agostino, C.; Bräuer, P.; Charoen-Rajapark, P.; Crouch, M. D.; Gladden, L. F. Effect of Paramagnetic Species on: T 1, T 2 and T 1/ T 2 NMR Relaxation Times of Liquids in Porous CuSO4/Al2O3. *RSC Adv* 2017, *7* (57), 36163–36167. https://doi.org/10.1039/c7ra07165e.
(8) Hahn, E. L. An Accurate Nuclear Magnetic Resonance Method for Measuring Spin-Lattice Relaxation Times. *Physical Review* 1949, *76* (1), 145–146. https://doi.org/10.1103/PhysRev.76.145.
(9) Hahn, E. L. Spin Echoes. *Physical Review* 1950, *80* (4), 580–594. https://doi.org/10.1103/PhysRev.80.580.
(10) Bloch, ' F; Hahn, ; E L. *Spin Echoes*t*; 1946; Vol. 70.
(11) Adebahr, J. 7Li NMR Measurements of Polymer Gel Electrolytes. *Solid State Ion* 2002, *147* (3–4), 303–307. https://doi.org/10.1016/S0167-2738(02)00014-0.
(12) Meiboom, S.; Gill, D. Modified Spin-Echo Method for Measuring Nuclear Relaxation Times. *Review of Scientific Instruments* 1958, *29* (8), 688–691. https://doi.org/10.1063/1.1716296.
(13) Luz, Z.; Meiboom, S. Nuclear Magnetic Resonance Study of the Protolysis of Trimethylammonium Ion in Aqueous Solution-Order of the Reaction with Respect to Solvent. *J Chem Phys* 1963, *39* (2), 366–370. https://doi.org/10.1063/1.1734254.
(14) Aguilar, J. A.; Nilsson, M.; Bodenhausen, G.; Morris, G. A. Spin Echo NMR Spectra without J Modulation. *Chem. Commun.* 2012, *48* (6), 811–813. https://doi.org/10.1039/C1CC16699A.
(15) Takegoshi, K.; Ogura, K.; Hikichi, K. A Perfect Spin Echo in a Weakly Homonuclear J-Coupled Two Spin- System. *Journal of Magnetic Resonance (1969)* 1989, *84* (3), 611–615. https://doi.org/10.1016/0022-2364(89)90127-3.
(16) Hamada, M.; de Anna, P. A Method to Measure the Diffusion Coefficient in Liquids. *Transp Porous Media* 2023, *146* (1–2), 463–474. https://doi.org/10.1007/s11242-021-01704-0.
(17) Mitra, P. P.; Sen, P. N.; Schwartz, L. M. Short-Time Behavior of the Diffusion Coefficient as a Geometrical Probe of Porous Media. *PhysicalReviewB* 1993, *47* (14), 8565–8574.
(18) Hazel, J. R.; Sidell, B. D. A Method for the Determination of Diffusion Coefficients for Small Molecules in Aqueous Solution. *Anal Biochem* 1987, *166* (2), 335–341. https://doi.org/10.1016/0003-2697(87)90582-3.
(19) Meyer, A.; Stüber, S.; Holland-Moritz, D.; Heinen, O.; Unruh, T. Determination of Self-Diffusion Coefficients by Quasielastic Neutron Scattering Measurements of Levitated Ni Droplets. *Phys Rev B* 2008, *77* (9), 092201. https://doi.org/10.1103/PhysRevB.77.092201.
(20) Busch, A.; Kampman, N.; Bertier, P.; Pipich, V.; Feoktystov, A.; Rother, G.; Harrington, J.; Leu, L.; Aertens, M.; Jacops, E. Predicting Effective Diffusion Coefficients in Mudrocks Using a Fractal Model and Small-Angle Neutron Scattering Measurements. *Water Resour Res* 2018, *54* (9), 7076–7091. https://doi.org/10.1029/2018WR023425.
(21) Hou, J.; Li, J.; Madsen, L. A. Anisotropy and Transport in Poly(Arylene Ether Sulfone) Hydrophilic-Hydrophobic Block Copolymers. *Macromolecules* 2010, *43* (1), 347–353. https://doi.org/10.1021/ma902070h.
(22) Wang, Y.; Gao, J.; Dingemans, T. J.; Madsen, L. A. Molecular Alignment and Ion Transport in Rigid Rod Polyelectrolyte Solutions. *Macromolecules* 2014, *47* (9), 2984–2992. https://doi.org/10.1021/ma500364t.
(23) Li, J.; Wilmsmeyer, K. G.; Hou, J.; Madsen, L. A. The Role of Water in Transport of Ionic Liquids in Polymeric Artificial Muscle Actuators. *Soft Matter* 2009, *5* (13), 2596–2602. https://doi.org/10.1039/b904443d.

(24) Li, J.; Park, J. K.; Moore, R. B.; Madsen, L. A. Linear Coupling of Alignment with Transport in a Polymer Electrolyte Membrane. *Nat Mater* 2011, *10* (7), 507–511. https://doi.org/10.1038/nmat3048.
(25) Yu, Z.; He, Y.; Wang, Y.; Madsen, L. A.; Qiao, R. Molecular Structure and Dynamics of Ionic Liquids in a Rigid-Rod Polyanion-Based Ion Gel. *Langmuir* 2017, *33* (1), 322–331. https://doi.org/10.1021/acs.langmuir.6b03798.
(26) Li, X.; Cooksey, T. J.; Kidd, B. E.; Robertson, M. L.; Madsen, L. A. Mapping Coexistence Phase Diagrams of Block Copolymer Micelles and Free Unimer Chains. *Macromolecules* 2018, *51* (20), 8127–8135. https://doi.org/10.1021/acs.macromol.8b01220.
(27) Li, X.; Uppala, V. V. S.; Cooksey, T. J.; Robertson, M. L.; Madsen, L. A. Quantifying Drug Cargo Partitioning in Block Copolymer Micelle Solutions. *ACS Appl Polym Mater* 2020, *2* (9), 3749–3755. https://doi.org/10.1021/acsapm.0c00694.
(28) Kidd, B. E.; Forbey, S. J.; Steuber, F. W.; Moore, R. B.; Madsen, L. A. Multiscale Lithium and Counterion Transport in an Electrospun Polymer-Gel Electrolyte. *Macromolecules* 2015, *48* (13), 4481–4490. https://doi.org/10.1021/acs.macromol.5b00573.
(29) Kidd, B. E.; Li, X.; Piemonte, R. C.; Cooksey, T. J.; Singh, A.; Robertson, M. L.; Madsen, L. A. Tuning Biocompatible Block Copolymer Micelles by Varying Solvent Composition: Dynamics and Populations of Micelles and Unimers. *Macromolecules* 2017, *50* (11), 4335–4343. https://doi.org/10.1021/acs.macromol.6b02579.
(30) Carr, H. Y.; Purcell, E. M. Effects on Diffusion on Free Precession in Nuclear Magnetic Resonance Experiments. *Physical Review* 1954, *94* (3).
(31) Stejskal, E. O.; Tanner, J. E. Spin Diffusion Measurements: Spin Echoes in the Presence of a Time-Dependent Field Gradient. *J Chem Phys* 1965, *42* (1), 288–292. https://doi.org/10.1063/1.1695690.
(32) Price, W. S. Pulsed-Field Gradient Nuclear Magnetic Resonance as a Tool for Studying Translational Diffusion: Part 1. Basic Theory. *Concepts Magn Reson* 1997, *9* (5), 299–336. https://doi.org/10.1002/(SICI)1099-0534(1997)9:5<299::AID-CMR2>3.0.CO;2-U.
(33) Callaghan, P. T. *Translational Dynamics and Magnetic Resonance: Principles of Pulsed Gradient Spin Echo NMR*; Oxford University Press: New York, 2011.
(34) Price, W. S. *NMR Studies of Translational Motion: Principles and Applications*; Cambridge University Press, 2010. https://doi.org/10.1017/CBO9780511770487.
(35) Madanan, U.; Goldstein, R. J. High-Rayleigh-Number Thermal Convection of Compressed Gases in Inclined Rectangular Enclosures. *Physics of Fluids* 2020, *32* (1). https://doi.org/10.1063/1.5134820.
(36) Cantin, N.; Vincent, A. P.; Yuen, D. A. Large Eddy Simulations of Thermal Convection at High Rayleigh Number. *Geophys J Int* 2000, *140* (1), 163–174. https://doi.org/10.1046/j.1365-246x.2000.00005.x.
(37) Sørland, G. H.; Seland, J. G.; Krane, J.; Anthonsen, H. W. Improved Convection Compensating Pulsed Field Gradient Spin-Echo and Stimulated-Echo Methods. *Journal of Magnetic Resonance* 2000, *142* (2), 323–325. https://doi.org/10.1006/jmre.1999.1941.
(38) Masatami Takeda, B.; Stejskal, E. O.; Gutowsky, H. S.; McCall, W.; Slichter, C. P.; Chem, J. *Chemical Exchange on a High-Resolution N.m.r. Spin-Spin Doublet Analysis of the Effect of Chemical Exchange on a High-Resolution N.m.r. Spin-Spin Doublet: Application to N-Methylacetamide12*; 1953; Vol. 21. https://pubs.acs.org/sharingguidelines.
(39) Tewari, K. C.; Li, N. C. *Nuclear Magnetic Resonance Study of Proton Exchange in the Water-Zpropanol System*; 1970; Vol. 48.

(40) Paterson, W. G. NUCLEAR MAGNETIC RESONANCE MEASUREMENTS OF PROTON EXCHANGE IN ALCOHOL–WATER SYSTEMS: PART II. n-Ch3H7OH-H2O and i-CH3H70H-H2O. *Can J Chem* 1963, *41* (10), 2472–2476. https://doi.org/10.1139/v63-364.
(41) Kreiter, C. G.; Fischer, E. O. Hindered Rotation about the C-O Bond in Methoxy(Methyl)Carbene Ligands. *Angewandte Chemie International Edition in English* 1969, *8* (10), 761–762. https://doi.org/10.1002/anie.196907611.
(42) Rogers, M. T.; Woodbrey, J. C. A PROTON MAGNETIC RESONANCE STUDY OF HINDERED INTERNAL ROTATION IN SOME SUBSTITUTED N,N-DIMETHYLAMIDES. *J Phys Chem* 1962, *66* (3), 540–546. https://doi.org/10.1021/j100809a043.
(43) Gutowsky, H. S.; Holm, C. H. Rate Processes and Nuclear Magnetic Resonance Spectra. II. Hindered Internal Rotation of Amides. *J Chem Phys* 1956, *25* (6), 1228–1234. https://doi.org/10.1063/1.1743184.
(44) Sandstrom, J. *Dynamic NMR Spectroscopy*; Academic Press, 1982.
(45) Kost, D.; Carlson, E. H.; Raban, M. The Validity of Approximate Equations for k c in Dynamic Nuclear Magnetic Resonance. *Journal of the Chemical Society D: Chemical Communications* 1971, No. 13, 656. https://doi.org/10.1039/c29710000656.
(46) Okazawa, N.; Sorensen, T. S. The Line-Shape Analysis of Nuclear Magnetic Resonance Peaks Broadened by the Presence of a “hidden” Exchange Partner. *Can J Chem* 1978, *56* (21), 2737–2742. https://doi.org/10.1139/v78-451

Chapter 3: Determining the molecular weight of polyelectrolytes using the scaling theory for salt-free semidilute unentangled solutions and using NMR diffusometry

Reprinted with permission from Aijie Han, Veera Venkata Shravan Uppala, Daniele Parisi, Christy George, Benjamin J. Dixon, Camila Denise Ayala, Xiuli Li, *Louis A. Madsen, *Ralph H. Colby Macromolecules **2022** 55,16, 7148-7160 © 2022, American Chemical Society.

Abstract

Quantifying the molecular weight and polydispersity of polyelectrolytes using conventional methods like size exclusion chromatography (SEC) is often unreliable due to the low overlap concentration of polyelectrolytes. Investigating the chain dynamics of polyelectrolytes in the semidilute unentangled regime can help in accurately determining their molecular weight. In this chapter, we introduce a model developed that combines the conformational and translational dynamics of polyelectrolytes to determine molecular weight. The model requires parameters – correlation length (ξ) and diffusion coefficients (D) – which were obtained from small angle X-ray scattering (SAXS) and NMR diffusometry respectively. We also developed three additional models for molecular weight determination using polymer rheology, but this chapter focuses on the NMR diffusometry-based model. We studied, five narrow dispersity cesium polystyrene sulfonate (CsPSS) solutions without added salt in the solution, dissolved in both water and anhydrous ethylene glycol (EG). The combination of diffusion coefficient and correlation length in water reliably predicts the number-average molecular weight (M_n) for chains with fewer than 2000 repeat units. We further studied binary blends of these narrowly dispersed CsPSS solutions to predict the dispersity (Đ) of the solution from NMR diffusometry measurements.

3.1. Introduction

Polyelectrolyte solutions have long been recognized as highly complex systems, with Nobel Laureate Pierre-Gilles de Gennes once referring to them as the "least understood form of condensed matter". It has been well established that, in the absence of salt, polyelectrolyte chains in solution adopt very large confirmations due to electrostatic repulsion between ionizable groups along the polymer chain. [1, 2] Consequently, the properties of polyelectrolyte solutions differ significantly from those of neutral polymer solutions. [3] Conventional methods developed for neutral polymers for characterizing the molecular weights, such as osmometry, light scattering and size exclusion chromatography (SEC) are challenging to apply directly to polyelectrolytes.

One key issue is that these techniques typically measure molecular weight in dilute solutions. However, for polyelectrolytes without added salt, the overlap concentration ($c^* \propto N^{-2}$, $N =$ repeat unit) is extremely, making measurements for dilute cconcentrations impractical, especially for long chains. In SEC, the addition of salt is necessary to reduce the chain size and screen electrostatic interactions between the polyelectrolyte and the stationary phase, which also contains ionizable groups. However, aqueous SEC often yields significant errors, as the universal calibration curves are typically based on neutral, water-soluble polymers like poly(ethylene oxide) or dextrans. [4] While sodium polystyrene sulfonate (NaPSS) standards can also be used for calibration at various ionic strength, assuming these curves can be universally applied to different polyanions and polycations can still lead to misleading results. Mori pointed out that early elution of NaPSS is affected by ion exclusion, and the hydrophobic interaction dominates between polyelectrolytes and column substrate materials. [5]

Static light scattering is also problematic due to the multicomponent nature of polyelectrolyte solutions. The refractive index increment (dn/dc) value for polyelectrolyte

solutions at a constant salt concentration is different from that at constant chemical potential. [6-8] Vrij and Overbeek[6] found that using refractive index increment at a constant salt concentration $(dn/dc)_{c_s}$ is different from that at a constant chemical potential $(dn/dc)_{\mu_s}$ for poly(methacrylic acid) and using $(dn/dc)_{c_s}$ causes huge error in M_w extrapolation using a Zimm plot. To obtain $(dn/dc)_{\mu_s}$, the polyelectrolyte solutions must be dialyzed against salt solutions so allow redistribution of salt ions across the membrane. [8] We do precisely that for our NaPSS samples in 0.1 M and 0.5 M NaCl solutions.

Osmometry, commonly used to determine number-average molecular weight (M_n) of neutral polymers in dilute solutions, is also problematic for polyelectrolytes. [9] The osmotic pressure (Π) in polyelectrolyte solutions includes contributions from both polyions and dissociated counterions, [10-12] and the osmotic pressure is proportional to the concentration of all solute species, largely due to the entropy of mixing. As a result, dissociated counterions dominate the osmotic pressure in salt-free polyelectrolyte solutions, leading to a much higher osmotic pressure (Π) than those observed in neutral polymer solutions at the same polymer concentration. [3]

Other methods, such as NMR end-group analysis and matrix-assisted laser desorption/ionization (MALDI) mass spectrometry, are limited to low molecular weight polymers (< 25 kg/mol) and are therefore not ideal for characterizing very large polyelectrolytes. [13-16] This underscores the need for new techniques to determine the molecular weights of polyelectrolytes for fundamental understanding and accelerated development of new polyelectrolyte chemistries and their related technologies. [17-21]

In this study, we aim to develop generalized methods based on the scaling (Rouse) model to determine the molecular weight of polyelectrolytes in the semidilute unentangled regime, given that polyelectrolytes without salt are expected to exhibit a wide concentration range. [3] **Figure 3.1**

illustrates the overarching goal of developing fundamental techniques for molecular weight determination in polyelectrolytes.

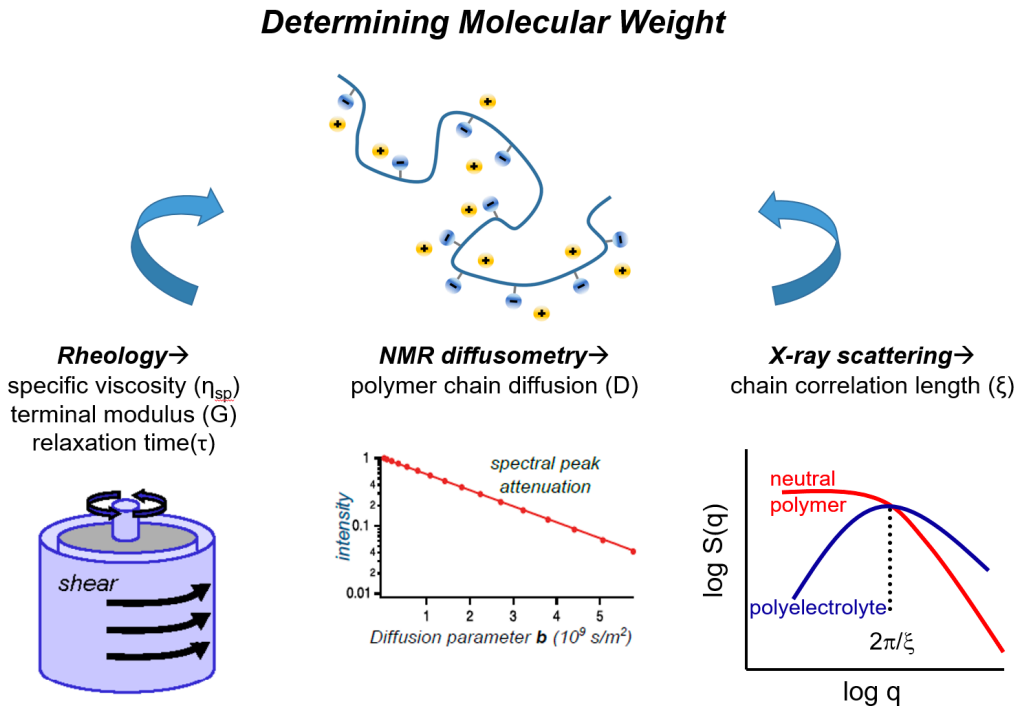

Figure 3.12: Summary of strategies and methods for determining the molecular weight of polyelectrolytes. **Method 1** described in this chapter uses NMR diffusometry to measure the self-diffusion coefficient (D) of the polymer chains and SAXS to determine the chain correlation length (ξ). Other methods use specific viscosity (η_{sp}), terminal modulus (G), and relaxation time (τ) measurements to determine the molecular weight of polyelectrolytes.

To test our methods, we purchased five different molecular weights of sodium polystyrene sulfonate (NaPSS) with narrow molecular weight distribution and ion-exchanged sodium counterions for cesium (Cs) counterions. The Cs ions provide a better electron contrast for measuring correlation lengths using small-angle X-ray scattering. We employed water as solvent[22] to study diffusive properties of cesium polystyrene sulfonate (CsPSS). Water offers low viscosity and minimal spectral interference, making it ideal for diffusion measurement by NMR across a wide range of concentrations and molecular weights of polyelectrolytes.

3.1.1. Background theory for semidilute unentangled polyelectrolyte solutions

Below we outline step by step how we use currently existing models to deduce the proposed molecular weight determination models for polyelectrolytes. The scaling theory of polyelectrolyte solutions pioneered by de Gennes and further developed by Dobrynin *et al.* predicts the dynamic properties of polyelectrolyte solutions across a broad concentration range. [1, 2] The correlation length in the semidilute unentangled regime, in the low salt limit is expected to follow the concentration dependence of $c^{-1/2}$ as shown in **Equation 3.1**,

$$\xi = (\frac{B}{cb})^{1/2}[1 + \frac{2c_s}{fc}]^{1/4} \tag{3.1}$$

where B is the chain contraction factor, defined as the ratio of the fully extended length Nb to the chain contour length L, ($B \equiv Nb/L$). Here c is the number density of monomers of size b, c_s is the number density of each monovalent salt ion, and f is the fraction of monomers with a dissociated counterion. The term $2c_s/fc$ represents the ratio of salt ions to the dissociated counterions, with $2c_s/fc \ll 1$ in the low salt limit and $2c_s/fc \gg 1$ in the high salt limit.

In semidilute regime, polyelectrolyte chains act as random walks of N/g correlation blobs[1, 2] (where N is the number of monomers in the chain and g is the number of monomers in a correlation blob $g = c\xi^3 = (\frac{B}{b})^{3/2}c^{-1/2}$). The chain's end-to-end distance R is given by **Equation 3.2**

$$\mathrm{R} \cong (\frac{\mathrm{b}}{\mathrm{Bc}})^{1/4}\ \mathrm{N}^{1/2}\ [1 + \frac{2\mathrm{c_s}}{f\mathrm{c}}]^{-1/8} \tag{3.2}$$

Since electrostatic and hydrodynamic interactions are screened beyond the length scale ξ, the Rouse model is used to describe the relaxation dynamics of the chain, which consists of correlation blobs. [1] The characteristic relaxation time τ is expressed as:

$$\tau \cong \frac{\eta_s b^3}{kT} B^{-3/2} N^2 (cb^3)^{-1/2} \left[1 + \frac{2c_s}{fc}\right]^{-3/4} \tag{3.3}$$

This makes low-salt polyelectrolytes rheologically unique since t *increases* with dilution. The chain's self-diffusion coefficient can then be derived as follows: [1]

$$D \approx \frac{R^2}{6\tau} \approx \frac{BkT}{6\eta_s bN}\left[1 + \frac{2c_s}{fc}\right]^{1/2} \tag{3.4}$$

At low salt concentrations, D becomes independent of the chain concentration. The properties described above accounts for the presence of additional salt, which can be disregarded if polyelectrolytes are exhaustively dialyzed against deionized water to remove any extra salt. By taking the ratio of D and ξ^2, both B and the salt correction term cancel out, leading to **Equation 3.5**.

$$D \cong \frac{ckT\xi^2}{6\eta_s N} \tag{3.5}$$

Equation 3.5 provides the self-diffusion coefficient of polyelectrolyte chains in a perfectly monodisperse system. According to the scaling model, Rouse dynamics apply to semidilute unentangled solutions, where each chain diffuses independently. For a polydisperse system, the diffusion coefficients of each species are summed up, resulting in **Equation 3.6**:

$$D = \frac{\xi^2 kT}{6\eta_s}\sum_i \frac{c_i}{N_i} = \frac{\xi^2 kT}{6\eta_s}\frac{c}{N_n} = \frac{\xi^2 RT}{6\eta_s}\frac{c_m}{M_n} \tag{3.6}$$

where c_m is the total mass concentration (g/ml) and M_n is the number-average molecular weight. We then solve for M_n which we will be later considered as '**method 1**' for determining molecular weight.

$$M_n = \frac{c_m \xi^2 RT}{6\eta_s D} \tag{3.7}$$

We can multiply τ and ξ^3, which cancels out B and the $\frac{2c_s}{fc}$ terms as shown in **Equation 3.8**.

$$\tau\xi^3 \cong \frac{\eta_s N^2}{c^2 kT} \tag{3.8}$$

The specific viscosity η_{sp}, based on the scaling model, is shown in **Equation 3.9**. Substituting ξ^3 in **Equation 3.9** gives a relationship free of B, f and c_s, making both η_{sp} and ξ experimentally measurable. The only unknown parameter is again c/N.

$$\eta_{sp} \equiv \frac{\eta - \eta_s}{\eta_s} \cong B^{-3/2} N (cb^3)^{1/2} [1 + \frac{2c_s}{fc}]^{-3/4} \cong \frac{N}{c\xi^3} \tag{3.9}$$

The Rouse model for solution predicts $\eta_{sp} \cong \phi N$, where ϕ is the volume fraction of monodisperse chains of N monomers. In a polydisperse solution each chain contributes independently meaning $\eta_{sp} = \sum \phi_i N_i = \phi N_w$. Hence, η_{sp} is governed by the weight-average molecular weight N_w.[23, 24] This provides a method to determine N_w as shown in **Equation 3.10**.

$$N_w = \eta_{sp} \xi^3 c \tag{3.10}$$

The Fuoss Law scaling in Equation 3.9 expects $\eta_{sp} = (\frac{c}{c^*})^{1/2}$ for $c^* < c < c_e$, where c^* is the overlap concentration and c_e is the entanglement concentration. This relation has been observed to hold for many polyelectrolytes, with recent models accounting for minor deviations.[25, 26] The terminal modulus G is the reciprocal of the steady-state compliance, is known to depend on the $N_z N_{z+1}/N_w$ ratio.[24, 27] Therefore, the molecular weight dependence of terminal modulus ($G = ckT/N$ is kT per chain for monodisperse polymers)[1, 3] can be expressed as

$$G = \frac{ckTN_w}{N_z N_{z+1}} \tag{3.11}$$

The relaxation time $\tau = (\eta - \eta_s)/G$ is similarly controlled by $N_z N_{z+1}$ leading to the relation:

$$\tau\xi^3 \cong \frac{\eta_s N_z N_{z+1}}{c^2 kT} \tag{3.12}$$

The correlation length ξ is typically measured using small-angle X-ray scattering (SAXS) or small-angle neutron scattering (SANS).[28-30] Drifford and Dalbiez conducted light scattering

experiments on salt-free NaPSS solutions, obtaining the correlation length at much lower concentrations. [31] All of the scattering results[1, 3, 32-34] suggest that the concentration dependence of ξ for polyelectrolyte solutions without added salt follows the expected power law of $c^{-0.5}$, as shown in **Equation 3.1**.

The self-diffusion coefficient of neutral polymers in dilute solutions can be easily measured using dynamic light scattering (DLS). However, in semidilute solutions, DLS measures the cooperative diffusion coefficients on the length scale of correlation blobs rather than individual chains. [38] For dilute polyelectrolyte solutions, the situation is more complex due to presence of multiple components, including polyions, dissociated counterions and solvent molecules. Analyzing the diffusion results from DLS is difficult because polyelectrolyte solutions without added salt always exhibit two distinct relaxation modes. [39-41]

Oostwal *et al.* successfully performed pulsed-field-gradient nuclear magnetic resonance (PFG-NMR) diffusometry on NaPSS aqueous solutions, providing reliable diffusion coefficients of polyelectrolyte solutions in the semidilute unentangled regime. [42] Following this approach, our study employs NMR diffusometry to determine the self-diffusion coefficients of the samples.

To test our models, we investigate on cesium polystyrene sulfonate (CsPSS) samples with five different molecular weights, all with narrow molecular weight distributions. Cesium is selected as the counterion due to its higher electron contrast with the solvent compared to sodium, which facilitates correlation length measurements through SAXS. These SAXS measurements were made by our collaborator Dr. Aijie Han and Dr. Ralph Colby at Penn State.

3.2. Experimental

3.2.1. Materials

Five NaPSS samples with narrow molecular weight distributions were purchased from from Scientific Polymer Products (Webster, NY; cat no. 622, 624, 626, 627 and 923). The molecular weight data provided by the manufactures are listed in **Table 3.1**. We verfied the molecular weights of NaPSS using static light scattering after dialysis. To exchange Na^+ counterions for Cs^+ counterions, we added a 20-fold excess of cesium chloride salt (CsCl) in solution, resulting in a statistical composition of 5% Na^+ and 95% Cs^+. The samples were extensively dialyzed by flushing at least 20 L of deionized water (Milli-Q) using a 400 mL Amicon® stirred cell (Millipore) under 30 psi argon pressure. Ultrafiltration membranes with molecular weight cut-offs (MWCO) of 100 kDa, 30 kDa, 10 kDa, 3 kDa and 1 kDa (Ultracel) were used for the CsPSS samples with molecular weights 2876K, 1158K, 457K, 101K and 35K, respectively. After dialysis, the solutions were freeze-dried to remove water, and the resulting powder was stored in a vacuum oven at 40°C overnight to eliminate any residual water.

To evaluate the polydispersity, two two mixtures of 20/80 and 50/50 wt% 2876K/35K CsPSS in ethylene glycol solutions were prepared for rheology measurements. The weight-average degree of polymerization (N_w) was measured using static light scattering. The number-average degree of polymerization (N_n) was calculated based on the dispersity reported in **Table 3.1**.

Table 3.1. Molecular weights of five CsPSS samples converted from information provided by the manufacturer using aqueous SEC

M_n (kg/mol)	M_w (kg/mol)	M_w/M_n	%Sulfonation[a]	%Sulfonation (NMR)
42.1	49.2	1.17	97	100
125	130	1.04	95	89

549	588	1.07	99	90
1099	1231	1.12	87	100
2807	3338	1.19	91	100

[a] %Sulfonation is measured from elemental analysis and the values are given by the manufacturer.

3.2.2. Degree of sulfonation

The degree of sulfonation for all polyelectrolyte samples was measured using a 400 MHz Bruker Avance III WB NMR spectrometer. The five polyelectrolyte samples with varying molecular weights were dissolved in D_2O, and ^1H NMR measurements were performed in a 1D setup. An rf pulse length of 4.5 μs was applied, and a relaxation delay time (D1) of at least 5 seconds was set to ensure complete signal relaxation (i.e., ≥ 99%) between scans and for greater accuracy. The degree of sulfonation determined from NMR is presented in **Table 3.1**, with further details and explanation provided in the Results and Discussion section.

3.2.3 Static light scattering

A Brookhaven BI-200SM SLS/DLS instrument was employed to verify the weight-average molecular weights of NaPSS at scattering angles ranging from 40 to 140 °, using a 641 nm diode laser. Prior to preparing aqueous solutions with 0.1 M NaCl and 0.5 M NaCl, NaPSS was dialyzed to remove residual salt. The differential refractive index (dn/dc) for each molecular weight was measured using a Brookhaven differential refractometer equipped with a 620 nm laser for 0.1 M NaCl. For the 0.5 M NaCl solutions, the $(dn/dc)_\mu$ value was extrapolated from literature values at the 641 nm wavelength. [43, 44] Zimm plots were generated for all five molecular weight NaPSS samples to estimate their weight-average molecular weight (M_w).

3.2.4. Small-angle X-ray scattering

Small-angle X-ray scattering (SAXS) was conducted using a Xenocs Xeuss 2.0 SAXS/WAXS system with Cu radiation (λ = 1.54 Å) at Penn State's Materials Characterization Lab. The solution samples were loaded into a stainless-steel liquid cell, which was sealed with two Kapton films and had a path length of 1.2 mm. An exposure time of 1 hour was employed. A Pilatus Hybrid CMOS two-dimensional SAXS detector was used to collect the scattered X-ray signals with a sample-to-detector distance of 2520 mm covering a q range from 0.1 to 1 nm-1.

3.2.5. Pulsed-field-gradient (PFG) NMR diffusometry

^{1}H PFG-NMR diffusometry was performed to determine the self-diffusion coefficients of the polyelectrolytes in salt-free water solutions. A 400 MHz Bruker Avance III WB NMR spectrometer, equipped with a MIC probe coupled to a Diff50 single-axis (z) gradient was mainly used for CsPSS molecular weights below 1100K. For concentrations below 0.01 M of all molecular weights, an 850 MHz Bruker Avance III HD NMR spectrometer, equipped with a MIC probe coupled to a Diff30 single-axis (z) gradient was used for better signal sensitivity and shorter experiment time. The pulsed-gradient stimulated echo (PGSTE) pulse sequence[45] was used with a 90° RF pulse length of 4.5 μs for 400 MHz NMR measurements and 13.5 μs for 850 MHz measurements. To confirm both spectrometers give the same diffusion coefficient D, solution concentrations in the range of 0.01 M to 0.02 M for each molecular weight were measured using both spectrometers.

The spin-lattice relaxation time (T_1) and spin-spin relaxation time (T_2) for polyelectrolyte chains were measured using the inversion-recovery and Carr-Purcell-Meiboom-Gill (CPMG) pulse sequences, respectively. The polyelectrolyte solutions have broad peaks (short T_2 relaxation times). A half sinusoid gradient pulse length δ from 0.785 ms to 3.14 ms (effective rectangular

pulse length varied from 0.5 ms to 2 ms) and the post gradient delay > 1 ms in the pulse sequence were used for ^{1}H diffusion measurements. The diffusion time Δ was varied from 25 ms to 200 ms depending on the molecular weight. The minimum gradient strength applied was in a range of 70-200 $G.cm^{-1}$ to significantly diffusion weight (reduce) the water peak intensity on the first slice of the PGSTE experiment. The maximum gradient strengths were adjusted from 200-2000 $G.cm^{-1}$ to achieve at least 90% of signal attenuation in 16-32 steps. The acquisition times were adjusted to be greater than a factor of three times the signal dephasing in the FID (T^*_2), and the relaxation delay time was optimized to 2 s to get maximum signal-to-noise (SNR) ratio for the polymer peaks with minimum experimentation time. 8-15 Hz line broadening was applied during data processing to reduce excessive acquisition noise. All NMR measurements were performed at 25 ± 1°C.

3.3. Results and Discussion

3.3.1. Degree of sulfonation (DOS)

Degree of sulfonation for CsPSS was determined by dissolving polyelectrolytes in D2O solvent to prevent any overlap of signals from the water peak. Figure 3.2 displays the NMR spectrum of 0.063 M 35K CsPSS in D2O measured at 25 ± 1°C. The Aliphatic (orange-highlighted, around 1 ppm) and aromatic (blue-highlighted, around 7 ppm) proton peaks on the polymer chain are well separated on the spectrum. The ratio of aromatic to aliphatic protons would be 5:3 for polystyrene and 4:3 for fully sulfonated polystyrene (100% DOS). Thus, degree of sulfonation can be determined from signal integral ratio. The determined DOS values all five polymer samples measured from this experiment were close to 100%, as listed in Table 3.1.

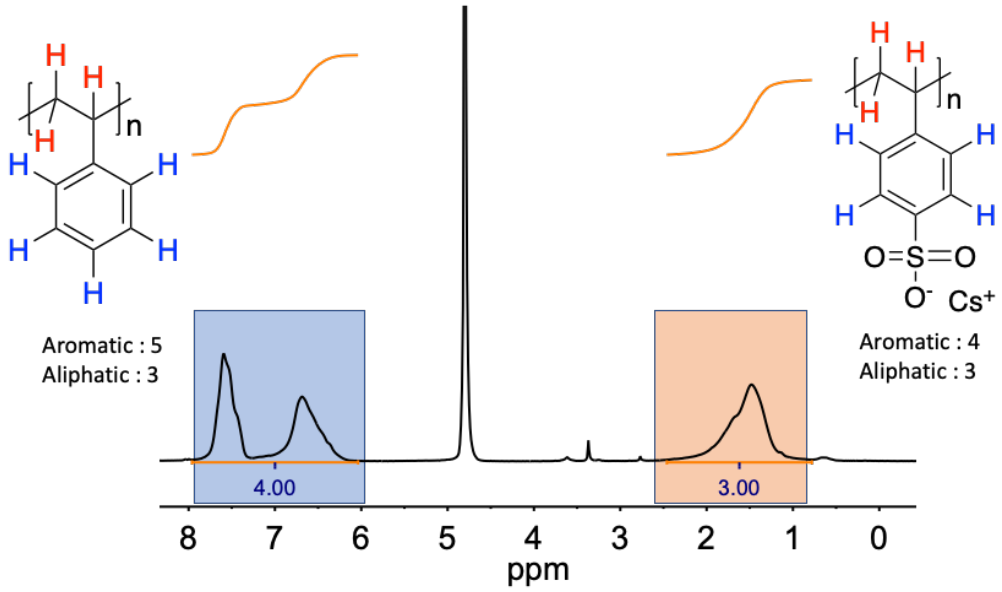

Figure 3.2. ^{1}H NMR spectrum of 0.063M 35K CsPSS in D_2O measured at 25 ± 1°C (HOD peak referenced at 4.8 ppm). Aromatic and aliphatic peaks were assigned with different colors on the chemical structure and on the NMR spectrum. For quantitative accuracy, relaxation delay (RD) times were set to ≥ 5 s to ensure complete T_1 relaxation of the proton peaks. Integrations of aromatic and aliphatic regions for this sample clearly shows that the degree of sulfonation is close to 100% for all samples.

3.3.2 Static light scattering

The molecular weights of as-received NaPSS samples were checked by static light scattering after dialysis in 0.1 M and 0.5 M NaCl/water to confirm the molecular weights reported by the manufacturer. **Figure 3.3** illustrates Zimm plot made for all five different molecular weights of NaPSS (as reported by manufacturer) in 0.1 M NaCl. The dn/dc value is determined as the slope of the difference in refractive index (Δn) plotted as a function of concentration in **Figure 3.3**, which is found to be 0.187 ± 0.0012 ml/g for 1900K NaPSS and 0.2026 ± 0.0008 ml/g for the other four lower molecular weight NaPSS. The M_w values of original NaPSS obtained from both SEC determined by the manufacturer and the Zimm plots are summarized in **Table 3.2**.

Table 3.2. Number-average and weight-average molecular weights of five NaPSS samples

	M_n (kg/mol)[a]	M_w (kg/mol)[a]	M_w (kg/mol)-SLS (0.1 M NaCl)[b]	M_w (kg/mol)-SLS (0.5 M NaCl)[b]	M_w/M_n
29K	28.6	33.4	27	32	1.17
86K	85.6	88.7	72	78	1.04
370K	366.7	393.5	329	326	1.07
740K	740.5	829.5	874	859	1.12
1900K	1885	2242	2297	2256	1.19

[a] The M_n and M_w values are obtained from the manufacturer using aqueous SEC. The eluent for 86K, 370K and 740K is 80/20 H_2O/acetonitrile 0.1 M $NaNO_3$. For 29K and 1900K, the eluent is H_2O/0.05 M sodium styrene sulfonate (NaSS). [b] M_w determined from our static light scattering experiments in 0.1 M NaCl.

Comparing the M_w from the manufacturer and M_w obtained from SLS, the difference between the two M_w values is lower than 10% for the two highest molecular weights. However, the difference is around 15% for the other three lower molecular weights. **Table 3.3** uses the M_w from SLS and calculates M_n using dispersity from **Table 3.2** as our reference M_n molecular weight values, which are also used as sample names. The molecular weights are also confirmed by performing SLS in 0.5 M NaCl and the results are reported in **Table 3.2**.

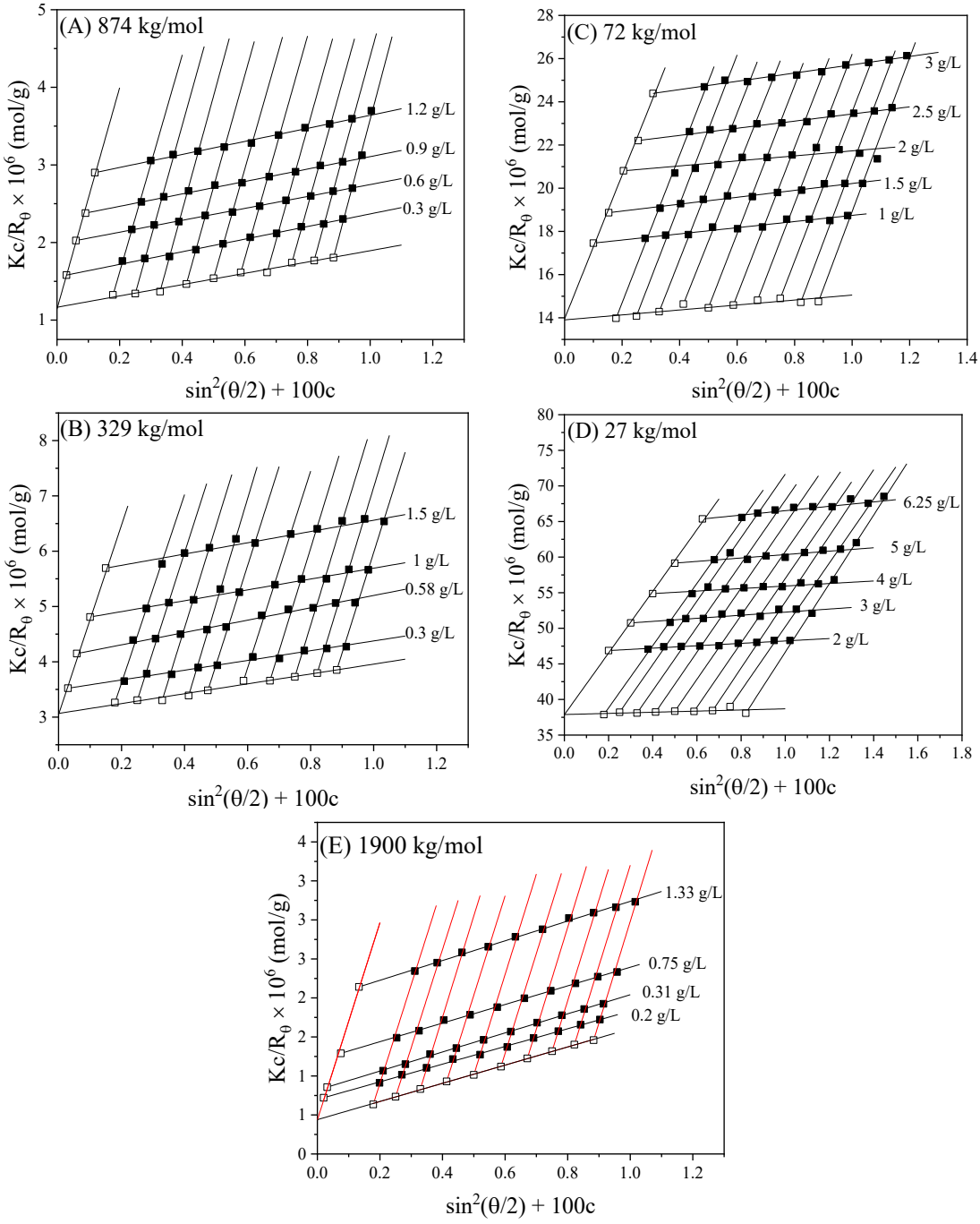

Figure 3.3. Zimm plot for (A) 874 kg/mol, (B) 329 kg/mol, (C) 72 kg/mol, (D) 27 kg/mol, and (E) 1900 kg/mol NaPSS in 0.1 M NaCl. Filled symbols are data at the four indicated dilute concentrations and ten angles θ = 50, 60, 70, 80, 90, 100, 110, 120, 130 and 140°. Open symbols are extrapolations to zero angle (at left) and zero concentration (at bottom).

Table 3.3. SLS results of five NaPSS in 0.1 M NaCl

M_w (kg/mol) NaPSS	M_w (kg/mol)[a] CsPSS	Error[b]	M_n CsPSS[c]
27	39.7	+26%	35K
72	111	+24%	101K
329	490	+20%	457K
874	1310	-5.1%	1158K
2297	3301	-2.4%	2876K

[a] M_w of CsPSS assumes the degree of sulfonation reported by the manufacturer and 95% Cs^+ to Na^+ conversion.
[b]Errors are calculated for M_n obtained from SLS compared with the manufacturer reported M_w from aqueous SEC.
[c] M_n calculated from the CsPSS M_w by dividing by the SEC dispersity, listed in Table 3.2, and used as sample names.

3.3.3 Molecular weight determination using Method 1 $\mathbf{M_n = \frac{c_m RT\xi^2}{6\eta_s D}}$

The number-average degree of polymerization N_n using **Equation 3.7**, combining D and ξ, which each can be easily measured using PFG NMR diffusometry and SAXS. The peak position q_{max} of SAXS profiles determines the correlation length $\xi = 2\pi/q_{max}$ at different concentrations. **Figure 3.3** below illustrates an example SAXS profile of 2876K CsPSS polymer at different concentrations.

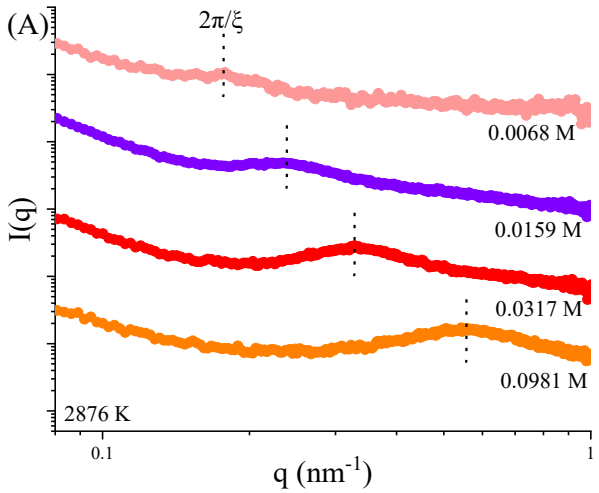

Figure 3.3. The SAXS profiles for 2876K CsPSS aqueous solutions of concentrations (0.0068 M, 0.0159 M, 0.0317 M, and 0.0981 M) in D.I. water with no added salt. All concentrations of CsPSS samples are below the entanglement concentration of the polymer.

The measured ξ from SAXS is plotted in **Fig. 3.4A** as a function of concentration and is clearly independent of molecular weight in the semidilute unentangled regime. [1, 2, 9] For 35K CsPSS aqueous solutions, a dilute-semidilute crossover occurs at $c^* \approx 0.04\ M$ where $\xi \propto c^{-1/3}$ crosses to $\xi \propto c^{-1/2}$. Thus, for 35K CsPSS with $c < c^*$, the peak q_{max} in SAXS represents the average distance between chains in dilute solution. Although c^*can be easily determined for 35K aqueous solutions (0.04 M), it is harder for the other four higher molecular weights to determine c^* directly using the SAXS data because the peak cannot be resolved at lower concentration. The scattering peaks move to lower q as concentration decreases, and the low-q upturn in the SAXS profile eventually covers the entire peak.

We applied the method by Kaji *et al.* to estimate c^* for other molecular weights as shown in **Fig. 3.4B**. [34] In the dilute regime, the distance between chains can be expressed as $(c/N)^{-1/3}$, where c/N is the number density of chains. Therefore, ξ is plotted as a function of c/N_n in **Fig. 3.4B** and all datasets should cross to the same $(c/N_n)^{-1/3}$ dependence as the solution enters the dilute regime, which is set by the dilute results from 35K. The intercept of extrapolated $(c/N_n)^{-1/2}$ and $(c/N_n)^{-1/3}$ gives an estimate of c^* for each molecular weight in water with no salt present. The data in **Fig. 2A** fit the line shown, as $\xi = A/\sqrt{c}$, with $A = 3.37\ nm \times M^{-1/2}$ for CsPSS in water. Similar fittings from the literature yield $A = 3.30\ nm \times M^{-1/2}$ for NaPSS in water, [31, 33] $A = 3.90\ nm \times M^{-1/2}$for CsPSS in EG. [22]

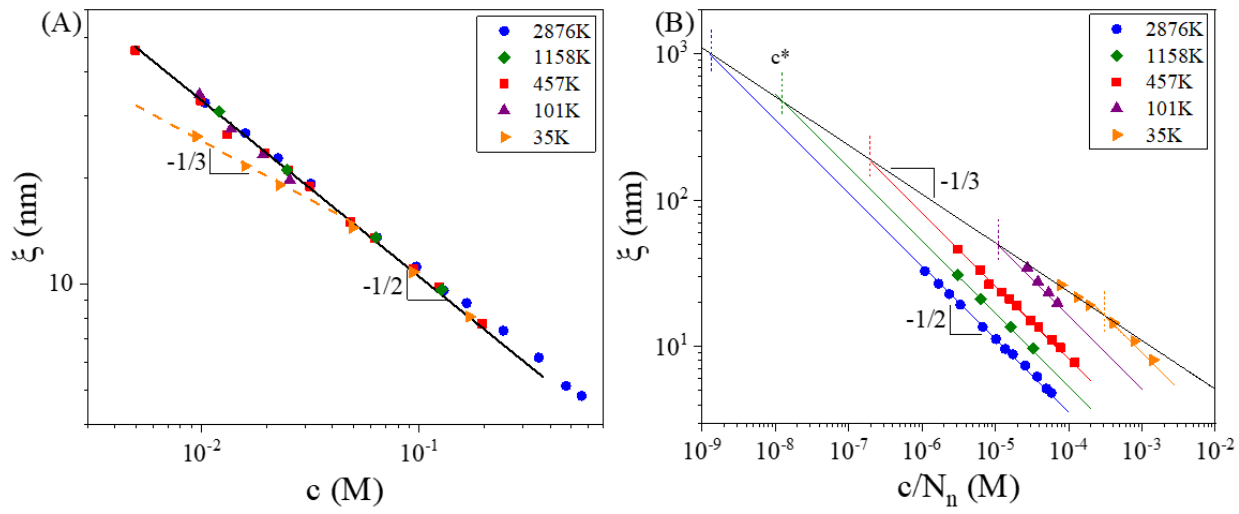

Figure 3.4. (A) Correlation length of CsPSS aqueous solutions as a function of concentration for five different molecular weights. 35K CsPSS reached the dilute regime for $c < 0.04\ M$ where the correlation length ξ becomes the average distance between chains and can be fitted to a power law of $\xi \propto c^{-1/3}$. (B) ξ of CsPSS aqueous solutions as a function of chain number density (number density of monomers c normalized by number-average degree of polymerization N_n). The crossover from $c^{-1/3}$ to $c^{-1/2}$ estimates the overlap concentration for each molecular weight.

3.3.4. PFG NMR experiments

To determine the self-diffusion coefficient of the polyelectrolyte chains, we dissolve the polyelecctrolytes in H_2O. 1D ^1H NMR spectra of CsPSS in water are first measured as shown in **Figure 3.5**. The proton peaks of the polyelectrolyte (color coded) are well resolved from the large H_2O peak. The three major peaks, constituting aromatic and aliphatic protons from the polymer chains, are used for NMR diffusometry measurements to determine the self-diffusion coefficient D of polyelectrolyte chains in solution. These three peaks are actually the overlap of many individual resonances due to the slow timescale of rotational polymer chain dynamics relative to small molecules in solution. Linewidths increase with molecular weight, as shown in **Figure 3.6**.

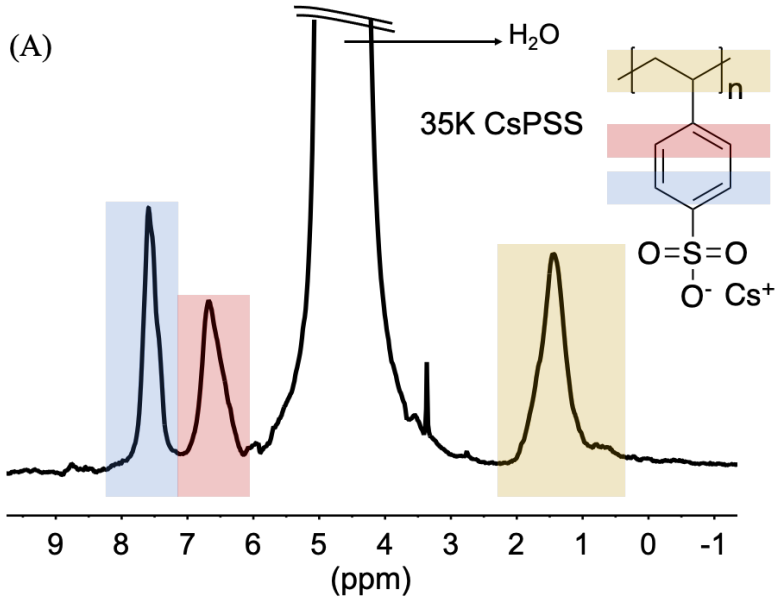

Figure 3.5. ^{1}H NMR spectrum of 0.063 M of 35K CsPSS in H_2O measured at 25 ± 1°C (referenced at 4.8 ppm) is shown in (A). The polymer proton peak assignments are assigned using different colors.

The PGSTE pulse sequence (see **Figure 2.7**) was employed to measure the diffusion coefficient of chains for five different molecular weights, each as a function of concentration. The signal amplitude for each peak was measured as a function of gradient strength (g). The acquired signal intensity I is given by the Stejskal-Tanner equation shown in Eq. 14 [56]

$$\mathrm{I} = \mathrm{I}_0 \mathrm{e}^{-\gamma^2 g^2 \delta^2 \left(\Delta - \frac{\delta}{3}\right) D} \tag{14}$$

where γ is the gyromagnetic ratio of the nucleus, δ is the effective gradient pulse length, Δ is the diffusion time between gradient pulses, I_0 is the signal intensity at $g = 0$, and D is the self-diffusion coefficient of the species measured.

The diffusion time Δ parameter, in a PGSTE sequence, is usually assigned based on the spin-lattice relaxation time (T_1) of the NMR peak that is being observed. T_1 values are determined from the inversion recovery- pulse sequence (see **Figure 2.2a**). The T_1 trend we observe, as shown

in **Table 3.4,** is consistent with Bloembergen-Purcell-Pound (BPP) theory, where the minimum T_1 is achieved when the Larmor frequency (ω_o) of the nucleus matches the inverse rotational correlation time ($1/\tau_c$) of the molecule [**reference**]. For the diffusion experiments, we used Δ values ($\approx$ T defined in **Figure 2.7**) from 25-200 ms, which is well below the T_1 of the CsPSS polyelectrolytes studied, to achieve minimal loss of signal due to spin-lattice relaxation.

Similarly, the gradient pulse time (δ) is assigned based on the spin-spin relaxation time (T_2), or in general the spin dephasing time during the particular experiment used (in this case, PGSTE for diffusometry). T_2 are usually measured using the Carr-Purcell-Meiboom-Gill (CPMG) spin-echo pulse sequence and the values obtained for our samples are shown in **Table 3.4**. We could clearly see the expected trend, where T_2 decreases with increasing molecular weight. [11] However, CPMG experiments to yield a simple T_2 are only accurate for fast tumbling molecules. Hence, the observed (or apparent) T_2 times from CPMG experiments are overestimated. Also, any presence of J-coupling, which arises due to interactions between protons on adjacent carbons, can complicate the decay profiles and may introduce errors in T_2 measurements. Use of specialized pulse sequences (like J-compensated pulse sequence, **Figure 2.4**) can help minimize errors in the determined T_2 and this approach will be explored further in future work.

Table 3.4. T_1 and T_2 values of 5 molecular weights of 0.063 M CsPSS in D_2O

	T_1 (s)	Apparent T_2 (ms)
35K	1.03	88.4
101K	0.93	56.9
457K	0.35	29.4
1158K	0.87	28.6
2876K	0.98	25.7

We can also estimate the signal dephasing times (the T_2^* from the time-domain data or FID) from the full width half maximum (FWHM) of a well resolved peak on the 1D spectrum.

However, for our polymer systems, we do not observe well resolved individual peaks, but observe peak overlaps as seen in **Figure 3.6**. Therefore, FWHM approach also does not give accurate T_2 times although we are working to fit these spectra to extract the dephasing time. Based on previous diffusometry experience with polymers like these, we assigned δ times ≤ 2 ms to achieve adequate signal-to-noise ratio (SNR). Our future goal is to develop a method for accurate estimation of signal dephasing times for such complex polymer systems.

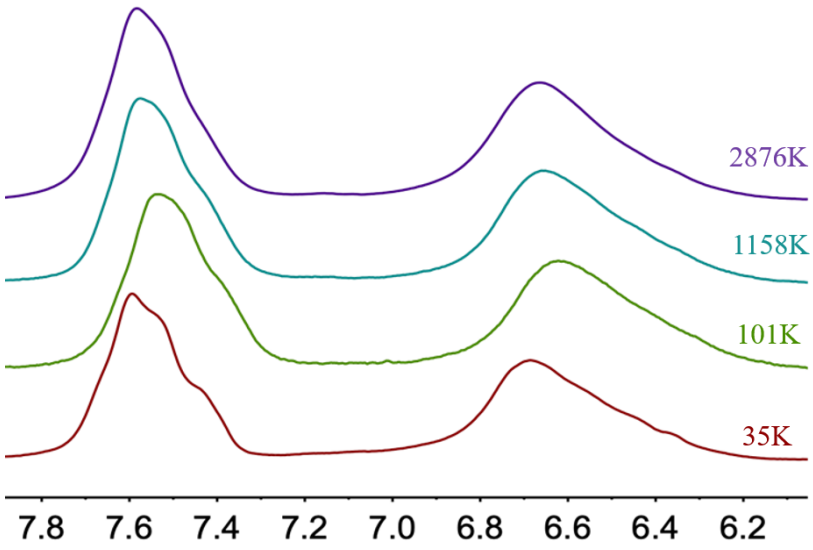

Figure 3.6. ^{1}H NMR spectrum of four molecular weights of 0.063M CsPSS in D_2O measured at 25 ± 1°C (HOD peak referenced at 4.8 ppm). The spectrum is zoomed in on the aromatic region for better visualization of the 2 aromatic peaks. Notice the more distinct multiple peaks within the peak pattern at 7.6 PPM at lower molecular weights. Since these peaks increasingly broaden with increase in molecular weight, the resolution and SNR correspondingly decrease.

From **Figure 3.6**, the linewidths of the signals increase with molecular weight, causing increased signal dephasing during the NMR diffusometry experiment and thus limiting measurement of D to concentrations above ~ 4×10^{-3} M for high M_n. **Figure 3.7** shows an exploration of the significance of molecular weight on the NMR signal in the diffusion measurements via comparison of spectra on 35K and 2876K CsPSS samples at the same concentration (0.063 M). Relative to a simple 1D pulse-acquire spectrum (top, red), the signal

intensity decreases by a factor of three for the first (g = 0) 1D slice of a diffusometry experiment (bottom, teal) for the 35K CsPSS sample, as shown in **Figure 3.7A**. This is due to signal dephasing of the nuclei during the two t periods (2×t = 7 ms) of the PGSTE pulse sequence (see **Figure 2.7**, from Chapter 2).

However, the loss of signal for the 2876K CsPSS sample (**Figure 3.7B**) is greater (7× loss) due to faster NMR signal dephasing for these longer (slower tumbling) chains. This study enables us to better understand the limitations of diffusometry measurements for longer chains. At lower concentrations for higher molecular weight samples, longer experimentation time (by $\propto$ 5× as compared with low M_n samples) is required to determine an accurate diffusion coefficient. Studies are underway to investigate the lower bounds of concentration for PSS and other polymer chemistries, and to improve NMR experimental parameters to extend the range of accessible concentration.

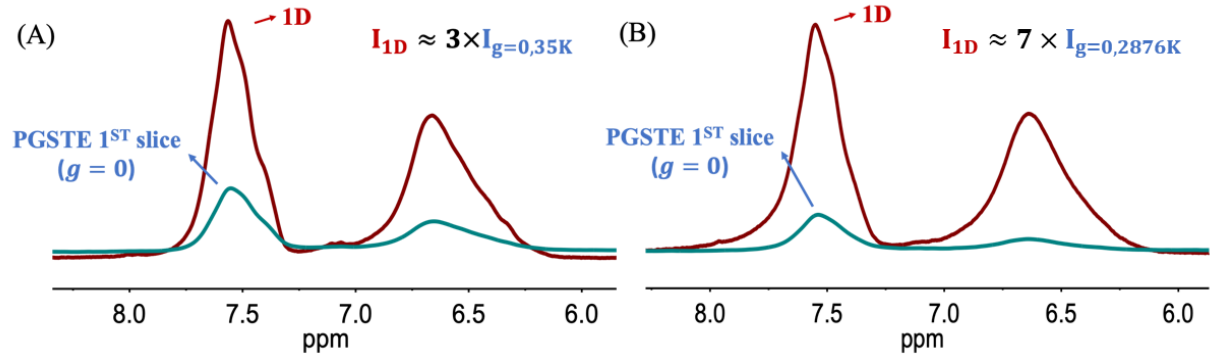

Figure 3.7. ^{1}H NMR spectrum comparison between 1D pulse-acquire experiment and PGSTE (1st slice, $g = 0$) experiment for 0.063 M 35K CsPSS and 2876K CsPSS in D_2O measured at 25 ± 1°C (HOD peak referenced at 4.8 ppm). The loss of signal for the 2876K CsPSS sample is a factor of 2.3 greater than that for the 35K CsPSS sample due to faster signal dephasing for nuclei on the longer chains. This means that one needs $2.3^2 \approx 5\times$ as many scans at the same concentration to get the same SNR, or one can only access concentrations ~ 2.3× higher for 2876K CsPSS as compared to 35K CsPSS samples.

Figure 3.8 shows representative NMR diffusometry signal attenuation (Stejskal-Tanner) plots for five molecular weights as a function of NMR diffusion parameter b ($\gamma^2 g^2 \delta^2 (\Delta - \delta/3)$. The data can be fitted to a single linear regression, suggesting all samples have a single average diffusing species size with narrow distribution, and the slope corresponds to D. The concentrations selected for **Figure 3.9** are in the semidilute unentangled regime where D is independent of concentration as shown in **Figure 3.10A** for 35K, 101K and 457K. The decrease of D as the concentration increases indicates the entanglement effects that restrict the chain motion. The onset of the drop of D is marked by the black dotted line in **Figure 3.10A**.

For molecular weights 457K, 1158K and 2876K, we noticed consistent increase of the diffusion coefficients as concentration decreases which can be fitted to power law exponent of -1/2 at a constant concentration (0.022 M). The power low exponent of -1/2 for concentration dependence of diffusion coefficients is indicative high salt effect. [1] This similar effect was also noticed in the concentration range of 10^{-5} M < c < 5 × 10^{-4} M of CsPSS data and NaPSS data measured by Cohen et al. Cohen *et al.* found $\eta_{sp} \propto c^{1.25}$ for $c < 10^{-5}$ M, which they say is caused by residual salt with $c_s \approx 4 \times 10^{-6}$ M. [46] To understand the intermediate concentration range, we plot the conductivity of solutions as a function of concentration in **Figure 3.8**.

The conductivity is measured inside the concentric cylinder rheometry cup so that all residual salts can be examined by the conductivity measurements. The solution conductivity shows a concentration dependence of $\sigma \propto c$ for $c > 10^{-3}$ M and saturates around 8 μS/cm at low concentrations. The conductivity data are fitted to the form of $\sigma = \sigma_0(1 + c/c_s)$, where σ_0 represents the conductivity of the high salt regime. [55] The possible sources of residual salts are ions from glass vials and carbonic acids, as CO_2 dissolves in water. The transition from $\sigma \propto c$ to the plateau at 8 μS/cm covers a decade of concentration which might be associated with the slightly

stronger concentration dependence $\eta_{sp} \propto c^{0.8}$ in the range of 10^{-5} M < c < 5×10^{-4} M before entering the high salt regime.

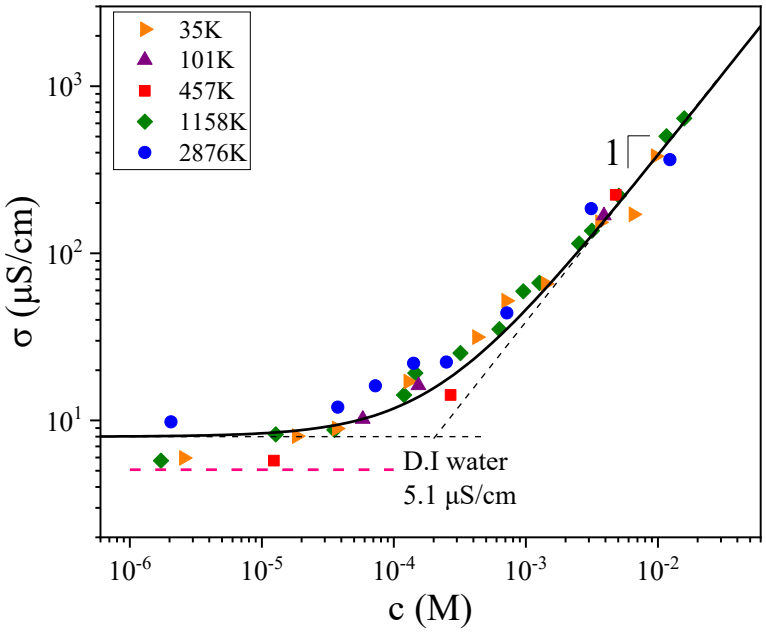

Figure 3.8. Ionic conductivity of CsPSS solutions at room temperature (22 °C). The pink dashed line indicates the conductivity of deionized water stored in a glass vial after 10 days. The crossover from $\sigma \propto c^0$ to $\sigma \propto c$ estimates the residual salt concentration and the solid curve represents the fit to $\sigma = \sigma_0(1 + c/c_s)$ where $\sigma_0 = 8$ µS/cm and $c_s = 2.1 \times 10^{-4}$ M.

Figure 3.8 indicates the c_s for our system is 2.1×10^{-4} M, associated with a Debye length (r_D) of 22 nm. **Figure 3.10B** compares r_D with ξ over the same range of concentration as **Figure 3.10A**. Solutions are in high salt regime at concentrations with $r_D < \xi$. The intersecting concentration between r_D and ξ is also at 0.022 M, confirming the high salt limit observed in **Figure 3.10A**. Although the same high salt limit applies to 101K and 35K, the lower concentrations of these two molecular weight samples are in dilute regime and D is concentration independent in dilute regime with salt. [1] We also plotted the polyelectrolyte size R (**Equation 3.2**)

in semidilute salt-free solutions to compare with ξ, which confirms that 35K is in dilute regime and 101K is approaching dilute regime at $c < 0.022$ M.

For 1158K and 2876K CsPSS solutions, although plateaus are plotted as straight lines, the range where D is independent of concentration is too narrow. As a result, we cannot confidently define this region, since a clear plateau was not observed for either 1158K or 2876K CsPSS solutions. Thus, at this time, method 1 is better suited for CsPSS with $N < 2000$. To test the effects of counterions on the diffusion coefficient, we also measured the diffusion coefficients of the original NaPSS. The result showed that NaPSS and CsPSS with the same chain length exhibit identical diffusion coefficients in the semidilute unentangled regime, indicating that counterions do not influence chain self-diffusion coefficient.

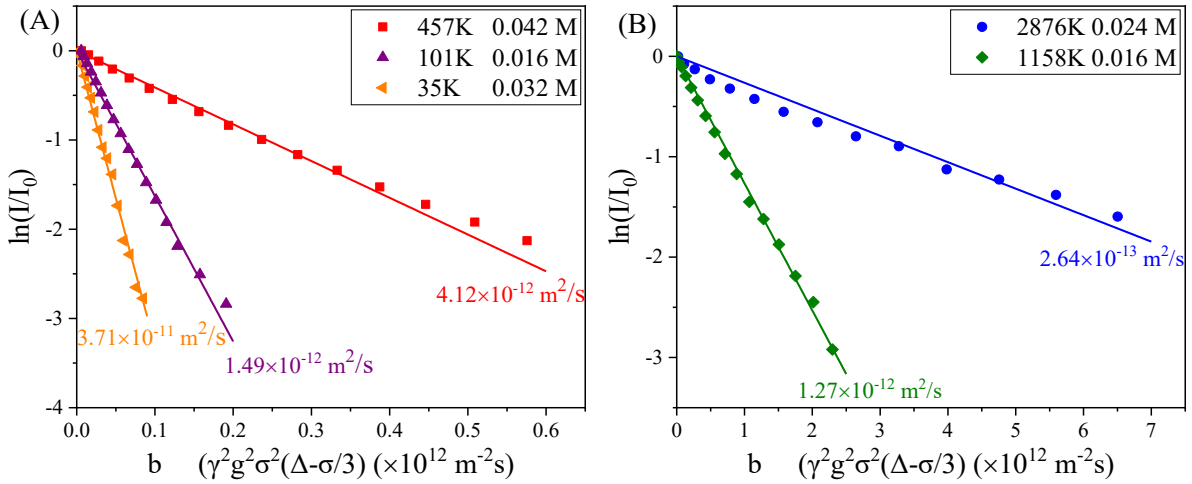

Figure 3.9. Representative NMR signal attenuation (Stejskal-Tanner) plots of CsPSS aqueous solutions of five different molecular weights in the semidilute unentangled concentration regime. Solid lines are single exponential fits for each molecular weight at the indicated concentration. [57] The diffusion coefficient for each solution is shown next to the respective fit lines. Faster attenuation (steeper negative slope) of the lines correlate with faster diffusion (larger D).

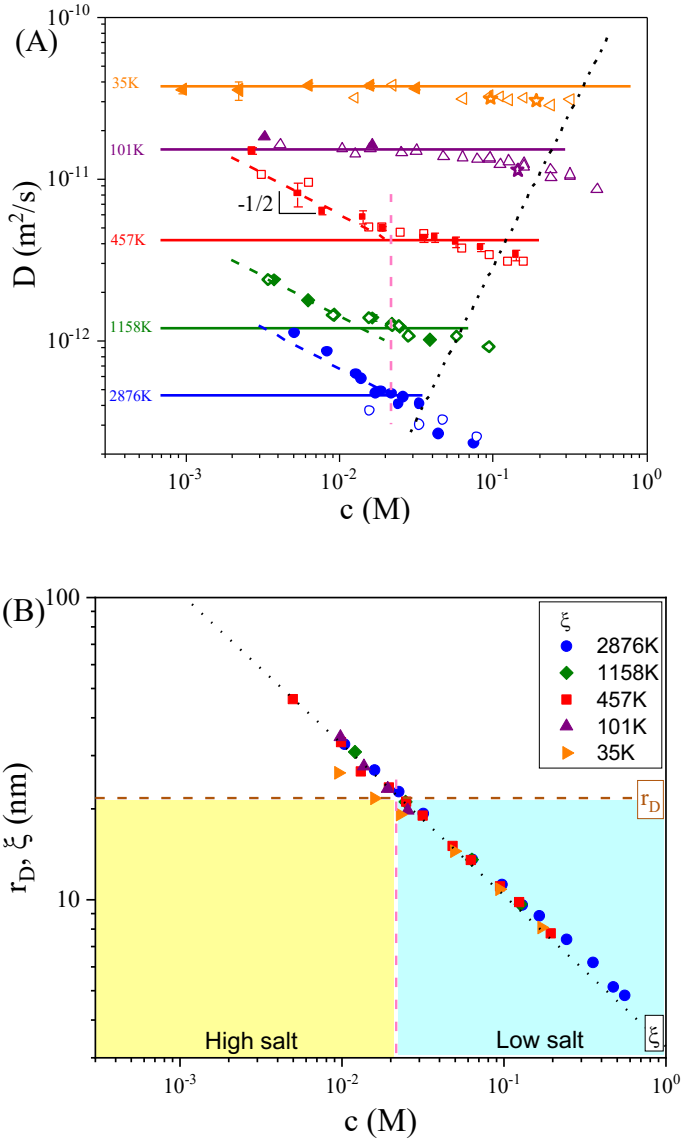

Figure 3.10. (A) Diffusion coefficients as a function of concentration for CsPSS/water solutions. The open symbols are obtained at 400 MHz, and the filled symbols are obtained at 850 MHz. The solid lines indicate the average D in the semidilute unentangled regime without salt effects. The dotted black line indicates entanglement concentration c_e. A few diffusion coefficients for NaPSS are also measured and plotted as stars. The dashed lines are fits to power law exponent of -1/2 which represent the high salt effects on diffusion coefficients. The vertical pink dashed line shows the crossover from $c^{-0.5}$ (high salt regime) to c^0 (low salt regime). (B)The Debye length r_D of 22 nm is determined with residual salt concentration $c_s = 2.1 \times 10^{-4}$ M. The crossover from r_D (brown dashed line) to ξ (black dotted line) estimated the low salt limit of $c > 0.022$ M (pink dashed line

in both parts). This same crossover is observed in (A) as $D \propto c^{-0.5}$ crosses to $D \propto c^{0}$ for 457K, 1158K and 2876K.

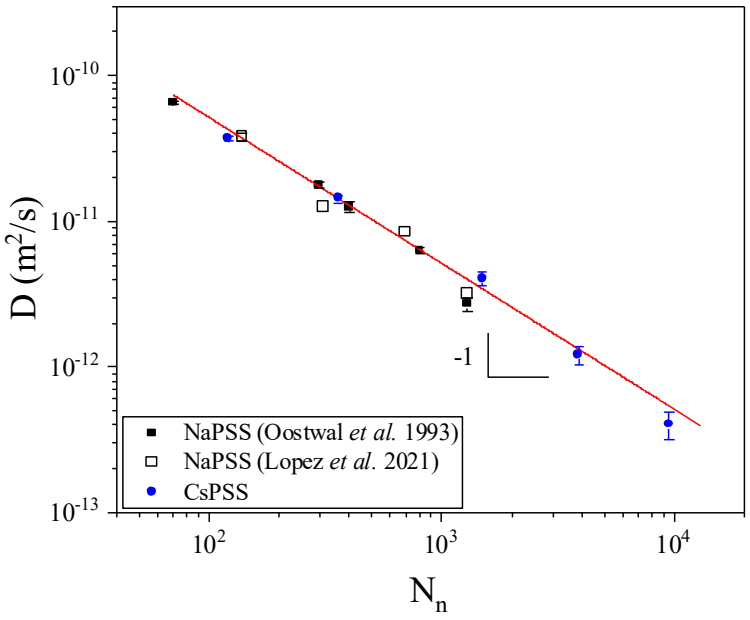

Figure 3.11. Diffusion coefficients in aqueous semidilute unentangled solutions as a function of number-average degree of polymerization of CsPSS in this work (blue circles), NaPSS from ref. 42 (black filled squares) and NaPSS from ref. 52 (black open squares). The error bars are calculated based on the standard deviation of concentrations below entanglement concentration c_e (indicated by black dotted line in **Figure 3.10A**) and above the concentration where D starts to increase with decreasing concentration.

The average diffusion coefficient in the semidilute unentangled regime where D is independent of concentration is plotted as a function of N_n in **Figure 3.11**. The red line in **Fig. 12** is $N_n = kT\xi^2 c/6\eta_s D$. CsPSS data from this work agree well with NaPSS diffusion coefficient data from the literature, [42, 52] and the data obey the Rouse prediction[9] of $D \propto N_n^{-1}$. **Equation 3.5** suggests that DN_n should be concentration independent in the semidilute unentangled regime. In **Figure 3.12**, the diffusion coefficients are multiplied by their respective N_n for CsPSS from this work and for NaPSS from reference 42. We found that the normalized data can be reasonably reduced to a common line, and the concentration-independent regime shows a constant value of

$DN_n = 4.66 \times 10^{-9}\ m^2/s$ for CsPSS and $DN_n = 4.86 \times 10^{-9}\ m^2/s$ for NaPSS shown as green dashed lines.

Oostwal *et al.*'s work has shown that for high molecular weight NaPSS, the PFG-NMR data cannot be fitted to a single exponential due to the dispersity of molecular weights, and only the "initial decay" data were fitted with a single exponential function to obtain the diffusion coefficients in their study. [42] The initial decay is associated with components that diffuse faster, dominated by the lower end of the molecular weight distribution and the slower diffusing components contribute more to the decay curve at higher *b* values. Therefore, the actual diffusion coefficients might be lower than Oostwal's reported values that are plotted in **Figure 3.12B** for the high molecular weight samples.

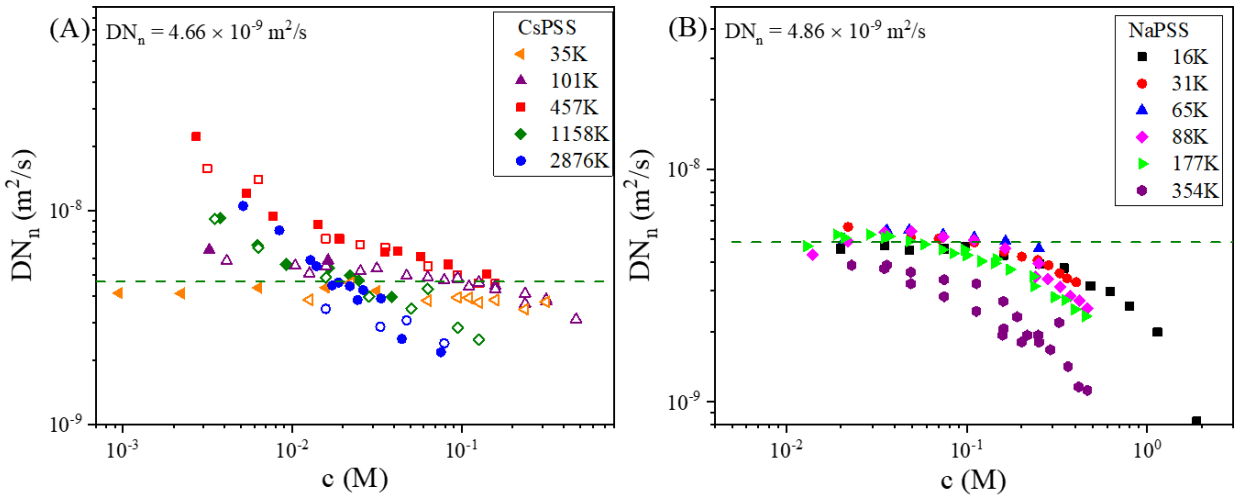

Figure 3.12. Diffusion coefficients in salt-free water normalized by weight-average degree of polymerization N_w for CsPSS (A) from this work and NaPSS (B) from ref. 42. The legends indicate the N_n values for each molecular weight. The dashed lines are average DN_n for the semidilute unentangled regime.

3.4. Conclusions

We described the four models developed to characterize the molecular weight of polyelectrolytes in semidilute unentangled solutions, each with its own limitations regarding the range of molecular weights and concentrations. **Figure 3.13** below illustrates these limitations for each method. In this chapter, we focused on presenting Method 1 ($\mathrm{M_n} = \frac{\mathrm{c_m RT}\xi^2}{6\eta_s D}$), which accurately determines the number-average molecular weight of polyelectrolytes. However, this model is more reliable for relatively shorter polyelectrolytes where the number of repeat units $N < 2000$. For 457K, 1158K, and 2867K CsPSS solutions, a continuous decrease in the D with increasing concentration is observed in the semidilute unentangled regmie, which is likely due to the presence of residual salts. A clear plateau is still observed for 457K in the semidilute unentangled regime for CsPSS solutions as predicted by the scaling model, before reaching the high salt limit. Since DN_n remains constant in the semidilute unentangled regime for a given type for polyelectrolytes, measuring D of polyelectrolyte with an unknown molecular weight allows for a straightforward determination of N_n. Additionally, because the FWHM of a polymer signal increases with molecular weight and decrease with temperature, higher temperatures should be explored for diffusion measurements of polyelectrolytes with $N > 2000$.

For high molecular weight samples, the high salt limit must be avoided to ensure a clear plateau in the semidilute unentangled regime, where D remains independent of concentration. Currently , it is unclear why the diffusion coefficient is so sensitive to residual salt. The crossover between the high and low salt limits appears to occur at $c = 0.022\,M$, where the correlation length coincides with the debye length from the residual salt (indicated by the pink dashed line in Figure 3.10). As we investigate polydisperse polyelectrolyte solutions for our future studies, we will compare our prediction that D can determine $\mathrm{M_n}$ (as shown in **Equation 3.6**) with previous

findings, where NMR diffusometry measurements were used to determine M_w for dilute polymer solutions.[58-60] Finally this approach offers detailed and quantitative insights into molecular weight distribution parameters of the polyelectrolytes, which are not only difficult to study but also hold significant technological importance.

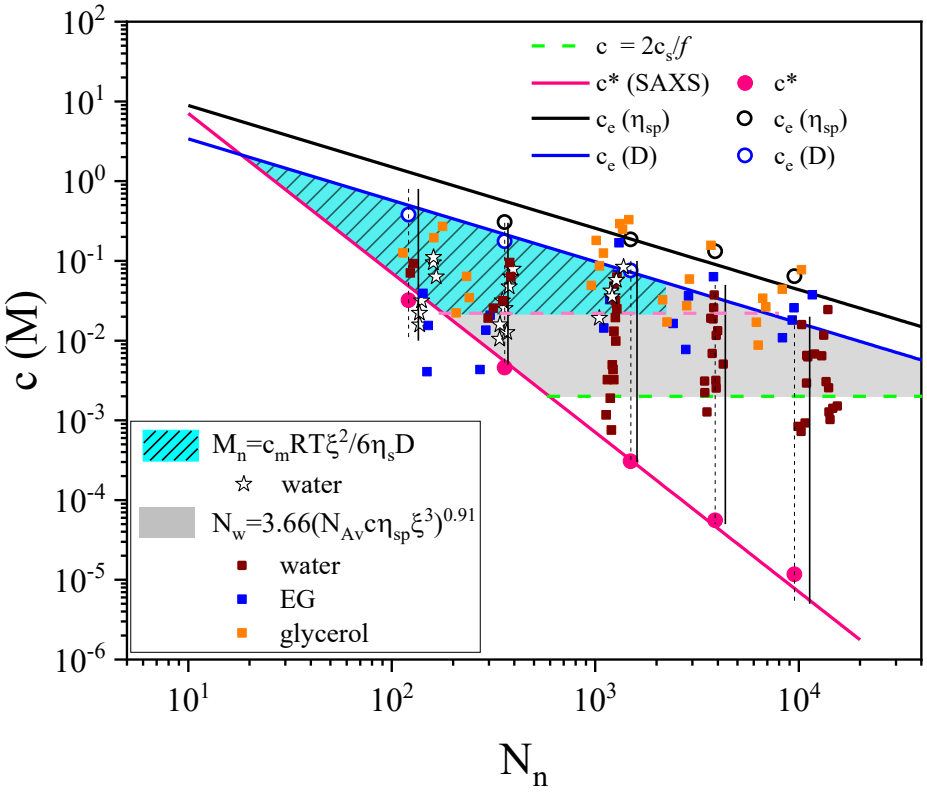

Figure 3.13. The best methods for determining the molecular weight of polyelectrolytes are illustrated by the colored areas represenitng the concentration and molecular weight range in which each approach is applicable. This range is defined by key concentrations: the entangled concentration (c_e, blue and black line), the overlap concentration (c^*, pink line), and the lowest possible concentration where the number density of counterions equals that of salt ions ($c \approx 2c_s/f$, shown as green dashed line). The method $N_w = 3.66(c\eta_{sp}\xi^3)^{0.91}$ is used to determine N_w shown as the filled squares calculated using the reported dispersity of each molecular weight. The blue area indicates the range that $M_n = \frac{c_m RT\xi^2}{6\eta_s D}$ can be used to determine M_n in water (for $N_n <$

2000 and $c > 0.022\,M$, shown as pink dashed line) with open stars representing the data obtained from measuring D. Solid black lines indicate the expected N_w and dashed black lines indicate the expected N_n.

References

(1) Dobrynin, A. V.; Colby, R. H.; Rubinstein, M. Scaling Theory of Polyelectrolyte Solutions. *Macromolecules* **1995**, *28*, 1859-1871.

(2) De Gennes, P. G.; Pincus, P.; Velasco, R. M.; Brochard, F. Remarks on Polyelectrolyte Conformation. *J. phys. (Paris)* **1976**, *37*, 1461-1473.

(3) Colby, R. H. Structure and linear viscoelasticity of flexible polymer solutions: comparison of polyelectrolyte and neutral polymer solutions. *Rheol. Acta* **2010**, *49*, 425-442, journal article.

(4) Rochas, C.; Domard, A.; Rinaudo, M. Aqueous GPC of electrolytes and polyelectrolytes. *Eur. Polym. J.* **1980**, *16*, 135-140.

(5) Mori, S. Secondary effects in aqueous size exclusion chromatography of sodium poly (styrene sulfonate) compounds. *Anal. Chem.* **1989**, *61*, 530-534.

(6) Vrij, A.; Overbeek, J. T. G. Scattering of light by charged colloidal particles in salt solutions. *J. Colloid Sci.* **1962**, *17*, 570-588.

(7) Brüssau, R.; Goetz, N.; Mächtle, W.; Stölting, J. Charakterisierung von Polyacrylatpolumeren / Characterization of Polyacrylate Samples. *Tenside Surfactants Detergents* **1991**, *28*, 396-406.

(8) Brown, W. *Light Scattering: Principles and Development*; Oxford University Press, 1996.

(9) Rubinstein, M.; Colby, R. H. *Polymer Physics*; Oxford University Press, 2003.

(10) Alexandrowicz, Z.; Katchalsky, A. Colligative properties of polyelectrolyte solutions in excess of salt. *Journal of Polymer Science Part A: General Papers* **1963**, *1*, 3231-3260.

(11) Takahashi, A.; Kato, T.; Nagasawa, M. The Second Virial Coefficient of Polyelectrolytes. *J. Phys. Chem.* **1967**, *71*, 2001-2010.

(12) Oosawa, F. *Polyelectrolytes*; M. Dekker, 1971.

(13) Einfeldt, L.; Günther, W.; Klemm, D.; Heublein, B. Peracetylated cellulose: end group modification and structural analysis by means of ^{1}H-NMR spectroscopy. *Cellulose* **2005**, *12*, 15-24.

(14) Shit, S. C.; Maiti, S. Application of NMR spectroscopy in molecular weight determination of polymers. *Eur. Polym. J.* **1986**, *22*, 1001-1008.

(15) Wu, J.; Tan, C.; Zhou, X.; Tan, Y.; Yang, P.; Jiang, Y. Molecular weight analysis of water-soluble poly(phenylene ethynylene)s using MALDI-TOF MS. *J. Polym. Sci., Part A: Polym Chem.* **2017**, *55*, 2537-2543.

(16) Gruendling, T.; Weidner, S.; Falkenhagen, J.; Barner-Kowollik, C. Mass spectrometry in polymer chemistry: a state-of-the-art up-date. *Polymer Chemistry* **2010**, *1*, 599-617, 10.1039/B9PY00347A.

(17) Muthukumar, M. 50th Anniversary Perspective: A Perspective on Polyelectrolyte Solutions. *Macromolecules* **2017**, *50*, 9528-9560.

(18) Rumyantsev, A. M.; Jackson, N. E.; Pablo, J. J. d. Polyelectrolyte Complex Coacervates: Recent Developments and New Frontiers. *Annual Review of Condensed Matter Physics* **2021**, *12*, 155-176.

(19) Ylitalo, A. S.; Balzer, C.; Zhang, P.; Wang, Z.-G. Electrostatic Correlations and Temperature-Dependent Dielectric Constant Can Model LCST in Polyelectrolyte Complex Coacervation. *Macromolecules* **2021**, *54*, 11326-11337.

(20) Sing, C. E.; Perry, S. L. Recent progress in the science of complex coacervation. *Soft Matter* **2020**, *16*, 2885-2914, 10.1039/D0SM00001A.

(21) Larson, R. G.; Liu, Y.; Li, H. Linear viscoelasticity and time-temperature-salt and other superpositions in polyelectrolyte coacervates. *Journal of Rheology* **2021**, *65*, 77-102.

(22) Han, A.; Colby, R. H. Rheology of Entangled Polyelectrolyte Solutions. *Macromolecules* **2021**, *54*, 1375-1387.

(23) Ferry, J. D. *Viscoelastic Properties of Polymers*; Wiley, 1970.

(24) Graessley, W. W. Polymeric Liquids and Networks: Dynamics and Rheology. Garland Science, 2008; pp 721-722.

(25) Chen, G.; Perazzo, A.; Stone, H. A. Electrostatics, conformation, and rheology of unentangled semidilute polyelectrolyte solutions. *Journal of Rheology* **2021**, *65*, 507-526.

(26) Matsumoto, A. Rheology of Polyelectrolyte Solutions: Current Understanding and Perspectives. *Nihon Reoroji Gakkaishi* **2022**, *50*, 43-50.

(27) Ferry, J. D.; Williams, M. L.; Stern, D. M. Slow relaxation mechanisms in concentrated polymer solutions. *The Journal of Physical Chemistry* **1954**, *58*, 987-992.

(28) Essafi, W.; Spiteri, M.-N.; Williams, C.; Boue, F. Hydrophobic Polyelectrolytes in Better Polar Solvent. Structure and Chain Conformation As Seen by SAXS and SANS. *Macromolecules* **2009**, *42*, 9568-9580.

(29) Lopez, C. G.; Rogers, S. E.; Colby, R. H.; Graham, P.; Cabral, J. T. Structure of sodium carboxymethyl cellulose aqueous solutions: A SANS and rheology study. *J. Polym. Sci., Part B: Polym Phys* **2015**, *53*, 492-501.

(30) Essafi, W.; Haboubi, N.; Williams, C.; Boué, F. Weak Temperature Dependence of Structure in Hydrophobic Polyelectrolyte Aqueous Solution (PSSNa): Correlation between Scattering and Viscosity. *J. Phys. Chem. B* **2011**, *115*, 8951-8960.

(31) Drifford, M.; Dalbiez, J. P. Light scattering by dilute solutions of salt-free polyelectrolytes. *J. Phys. Chem.* **1984**, *88*, 5368-5375.

(32) Drifford, M.; Dalbiez, J. P. Light scattering by dilute solutions of salt-free polyelectrolytes. *The Journal of Physical Chemistry* **1984**, *88*, 5368-5375.

(33) Nierlich, M.; Williams, C. E.; Boue, F.; Cotton, J. P.; Daoud, M.; Farnoux, B.; Jannink, G.; Picot, C.; Moan, M.; Wolff, C.; et al. Small-Angle Neutron-Scattering by Semi-Dilute Solutions of Polyelectrolyte. *Journal De Physique* **1979**, *40*, 701-704.

(34) Kaji, K.; Urakawa, H.; Kanaya, T.; Kitamaru, R. Phase diagram of polyelectrolyte solutions. *Journal de Physique* **1988**, *49*.

(35) Boris, D. C.; Colby, R. H. Rheology of Sulfonated Polystyrene Solutions. *Macromolecules* **1998**, *31*, 5746-5755.

(36) Krause, W. E.; Tan, J. S.; Colby, R. H. Semidilute solution rheology of polyelectrolytes with no added salt. *J. Polym. Sci., Part B: Polym Phys* **1999**, *37*, 3429-3437.

(37) Dou, S.; Colby, R. H. Solution Rheology of a Strongly Charged Polyelectrolyte in Good Solvent. *Macromolecules* **2008**, *41*, 6505-6510.

(38) Doi, M.; Doi, P. A. P. M.; Edwards, S. F. *The Theory of Polymer Dynamics*; Clarendon Press, 1986.

(39) Förster, S.; Schmidt, M.; Antonietti, M. Static and dynamic light scattering by aqueous polyelectrolyte solutions: effect of molecular weight, charge density and added salt. *Polymer* **1990**, *31*, 781-792.

(40) Koene, R. S.; Nicolai, T.; Mandel, M. Scaling relations for aqueous polyelectrolyte-salt solutions. 2. Quasi-elastic light scattering as a function of polyelectrolyte concentration and salt concentration. *Macromolecules* **1983**, *16*, 227-231.

(41) Förster, S.; Schmidt, M. Polyelectrolytes in solution. In *Physical Properties of Polymers*, Springer Berlin Heidelberg, 1995; pp 51-133.

(42) Oostwal, M. G.; Blees, M. H.; De Bleijser, J.; Leyte, J. C. Chain self-diffusion in aqueous salt-free solutions of sodium poly(styrenesulfonate). *Macromolecules* **1993**, *26*, 7300-7308.

(43) Hirose, E.; Iwamoto, Y.; Norisuye, T. Chain Stiffness and Excluded-Volume Effects in Sodium Poly(styrenesulfonate) Solutions at High Ionic Strength. *Macromolecules* **1999**, *32*, 8629-8634.

(44) Yashiro, J.; Norisuye, T. Excluded-volume effects on the chain dimensions and transport coefficients of sodium poly(styrene sulfonate) in aqueous sodium chloride. *J. Polym. Sci., Part B: Polym Phys* **2002**, *40*, 2728-2735.

(45) Callaghan, P. T. *Translational Dynamics and Magnetic Resonance: Principles of Pulsed Gradient Spin Echo NMR*; OUP Oxford, 2011.

(46) Cohen, J.; Priel, Z.; Rabin, Y. Viscosity of dilute polyelectrolyte solutions. *Journal of Chemical Physics* **1988**, *88*, 7111-7116.

(47) Chen, S.-P.; Archer, L. A. Relaxation dynamics of salt-free polyelectrolyte solutions using flow birefringence and rheometry. *J. Polym. Sci., Part B: Polym Phys* **1999**, *37*, 825-835.

(48) Prini, R. F.; Lagos, A. E. Tracer diffusion, electrical conductivity, and viscosity of aqueous solutions of polystyrenesulfonates. *Journal of Polymer Science Part A: General Papers* **1964**, *2*, 2917-2928.

(49) Oostwal, M.; Odijk, T. Novel dynamic scaling hypothesis for semidilute and concentrated solutions of polymers and polyelectrolytes. *Macromolecules* **1993**, *26*, 6489-6497.

(50) Üzüm, C.; Christau, S.; von Klitzing, R. Structuring of Polyelectrolyte (NaPSS) Solutions in Bulk and under Confinement as a Function of Concentration and Molecular Weight. *Macromolecules* **2011**, *44*, 7782-7791.

(51) Daoud, M.; Cotton, J. P.; Farnoux, B.; Jannink, G.; Sarma, G.; Benoit, H.; Duplessix, C.; Picot, C.; de Gennes, P. G. Solutions of Flexible Polymers. Neutron Experiments and Interpretation. *Macromolecules* **1975**, *8*, 804-818.

(52) Lopez, C. G.; Linders, J.; Mayer, C.; Richtering, W. Diffusion and viscosity of unentangled polyelectrolytes. *Macromolecules* **2021**, *54*, 8088-8103.

(53) Dobrynin, A. V.; Rubinstein, M. Theory of polyelectrolytes in solutions and at surfaces. *Prog. Polym. Sci.* **2005**, *30*, 1049-1118.

(54) Lopez, C. G. Entanglement properties of polyelectrolytes in salt-frree and excess salt solution. *ACS Macro Letters* **2019**, *8*, 979–983.

(55) Colby, R. H.; Boris, D. C.; Krause, W. E.; Tan, J. S. Polyelectrolyte conductivity. *J. Polym. Sci., Part B: Polym Phys* **1997**, *35*, 2951-2960.

(56) Stejskal, E. O.; Tanner, J. E. Spin Diffusion Measurements: Spin Echoes in the Presence of a Time-Dependent Field Gradient. *Journal of Chemical Physics* **1965**, *42*, 288-292.

(57) Carrazzone, R. J.; Li, X.; Foster, J. C.; Uppala, V. V. S.; Wall, C. E.; Esker, A. R.; Madsen, L. A.; Matson, J. B. Strong Variation of Micelle–Unimer Coexistence as a Function of Core Chain Mobility. *Macromolecules* **2021**, *54*, 6975-6981.

58) Callaghan, P. T.; Pinder, D. N. A pulsed field gradient NMRstudy of self-diffusion in a polydisperse polymer system: dextran inwater. Macromolecules 1983, 16, 968−973.

(59) Chen, A.; Wu, D.; Johnson, C. S. Determination of MolecularWeight Distributions for Polymers by Diffusion-Ordered NMR. J. Am.Chem. Soc. 1995, 117, 7965−7970.

(60) von Meerwall, E.; Ozisik, R.; Mattice, W. L.; Pfister, P. M. Self-diffusion of linear and cyclic alkanes, measured with pulsed-gradientspin-echo nuclear magnetic resonance. J. Chem. Phys. 2003, 118,3867−3873.

Chapter 4: Quantifying drug cargo partitioning in block copolymer micelle solutions

Reprinted with permission from Xiuli Li, Veera Venkata Shravan Uppala, Tyler J. Cooksey, Megan L. Robertson, and Louis A. Madsen. ACS Appl. Polym. Mater. **2020**, 2, 9, 374-375 © American Chemical Society.

Abstract

Understanding molecular partitioning in solution is crucial for design of micelle-based formulations for drug cargo delivery and other molecular encapsulation technologies. Here we present an investigation of the self-assembly of a Pluronic® F127 ($PEG_{99}PPO_{69}PEG_{99}$) triblock copolymer in water and its solubilization of three hydrophobic drugs, hydrochlorothiazide (HCT), indomethacin (IND) and paclitaxel (PTX). Using NMR diffusometry, we have quantified diffusion coefficients of different species in aqueous solution, including the polymers, drug cargo molecules and solvent. We investigate effects of polymer concentration as well as drug chemistry on micelle-drug interactions. We find, for example, that as the F127 concentration increases from 1 to 5% wt/vol, the partition percentages of HCT and IND in micelles (vs. in free solution) both increases. The facile methodology presented enables quantification of drug distribution and dynamics in a micellar system without perturbation of the solution, thus opening opportunities to understand the broader process of drug partitioning in micelles.

4.1. Introduction

Block copolymer micelles (BCMs) are widely used in various applications such as drug delivery, nano-reactors and tissue engineering. [1-2] Specifically, they are served as targeted drug-

delivery vehicles due to their long solution residence time for cargo, low critical micelle concentration (CMC) and *in vivo* degradability.[3-6] Poly(ethylene glycol)-*b*-poly(propylene oxide)-*b*-poly(ethylene glycol) (PEG-PPO-PEG) triblock copolymers offer versatile opportunities for creating microenvironments suitable for incorporating various cargo due to their amphiphilic nature. As a result, PEG-PPO-PEG triblock copolymers find use in a wide range of applications, such as pharmaceutical formulations, foaming agents and advanced coatings.[7]

Commercially available PEG-PPO-PEG copolymers manufactured by BASF under the trade name Pluronic® polymers are utilized as drug delivery media to improve the solubility and reduce the toxicity of poorly water-soluble drugs.[8] The micellization and gelation behavior of Pluronic® polymers have been extensively studied by researchers using neutron scattering,[9] rheology,[10] fluorescence,[11] and NMR spectroscopy.[12] Above the CMC, micelles are formed through an entropy-driven process, with a less polar core-forming PPO block and a water-swollen shell-forming PEG blocks. At even higher concentration of polymer (above the critical gelation concentration, CGC), a thermo-reversible gel forms due to intermolecular associations between the polymer chains.[13]

The particular polymeric materials used in drug delivery can greatly affect the pharmacological properties of drugs, including pharmacokinetics, biodistribution and sustained release.[14] Broad distribution of drugs in the body can result in dose-limiting side effects and affect normal tissues. Using drug delivery carriers, such as PEO-PPO-PEO copolymer micelles, can help to reduce those effects by encapsulating drugs in hydrophobic reservoirs.[15] Therefore, it is important to understand and quantify how drugs are distributed in the delivery carriers and in the surrounding aqueous environment. The partition coefficient (K) defines the distribution of drugs in different phases, which is critical to estimating the release rate and residence time in the

organism, as well as other aspects of biological activity. [16] Knowledge of *K* also provides insight into the nature and strength of molecular interactions between drug molecules and micelles, for example, van der Waals forces, hydrophobic interactions and hydrogen bonding. [17] Several factors have been determined to affect the solubilization capacity of micelles, including compatibility between the core-forming polymers and the cargo, micellar size, aggregation number, interfacial tension between water and the cargo, and the molecular volume of cargo. [18-19] *K* can sometimes be obtained experimentally from UV-Vis, [20] high performance liquid chromatography (HPLC), [21] differential scanning calorimetry (DSC) [22] and fluorescence spectroscopy, [23] etc. Those methods either require additional separation (filtration or dialysis) of micelle-drug solutions or fluorescent probe labeling, which can involve possible drug loss, measurement perturbations, and/or complicated preparation procedures.

Based on our and others' investigations of polymeric micelle structure and dynamics, [13, 24-26] in this article we present a simple and non-destructive NMR diffusometry approach to investigate the drug partitioning behaviors of Pluronic® F127 block copolymer micelle (BCM) solutions. In short, NMR diffusometry can quantify the fractions of drug encapsulated in micelles and drug in free solution.

We can define the drug encapsulated in BCMs as the *micellar phase* (for the drug) and the drug dissolved in the surrounding solvent as the *aqueous phase*. We assume the activity coefficients of drug in both phases are 1 (as in the case of a dilute system), and thus the partition coefficient (*K*) is given by the ratio of model drug concentration in each phase with:

$$K = \frac{[M]_{drug,\,micelle}}{[M]_{drug,\,aqueous}} \tag{4.1}$$

where $[M]_{drug,\,micelle}$ is the concentration of model drug in the micellar phase, and $[M]_{drug,\,aqueous}$ is the concentration of model drug in the aqueous phase.

In this study, we investigate three model drugs with different solubilities — hydrochlorothiazide (HCT), indomethacin (IND) and paclitaxel (PTX) — to understand the hydrophobic drug solubilization and partitioning behaviors in Pluronic® F127 BCMs. Pluronic® F127 formulations have been widely applied to enhance drug solubilization and prolong the release profile for poorly water-soluble drugs. [27-28] HCT is a diuretic and anti-hypertensive drug for the treatment of diabetes, and can be used to treat edema (excess fluid held in body tissues) caused by certain medical problems, such as heart, kidney and liver diseases or estrogen and corticosteroids. [29] IND is an anti-inflammatory drug that reduces fever, pain and inflammation and relieves symptoms of arthritis or gout. [30] PTX is a chemotherapy agent, with activity against lung, breast, prostate and other types of solid tumor cancers. [31] The water solubility of these three model drugs follows the order: PTX < IND < HCT (**Figure 4.1a**).

Common incorporations of water-insoluble drugs into micelles include chemical conjugation and physical entrapment. [32] Drugs can generally be encapsulated into BCMs to enable bloodstream injection with low overall drug dose, and to ensure minimal premature leakage so that a drug can reach its intended target tissue or organ. [33] The quantity of drug loading depends on the drug and polymer structures and resulting intermolecular interactions, which include influences from the block copolymer composition, hydrophobic (block) ratio, and molecular weight. [34] In this study, we have prepared HCT- and IND-loaded Pluronic F127 micelles by a direct dissolution method (**Figure 4.1b**), and prepared PTX-loaded micelles by a solid dispersion method. [35-36]

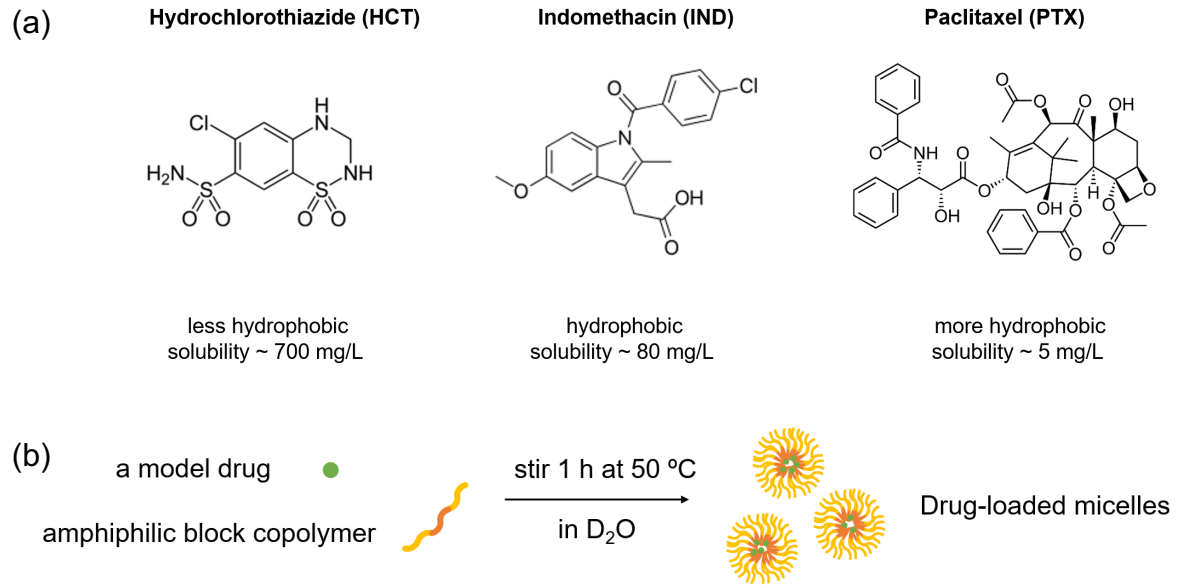

Figure 4.1. (a) Chemical structure and water solubility of model drugs: HCT, IND and PTX. (b) Preparation of drug-loaded Pluronic® BCMs.

Using an NMR methodology that can be applied on many common NMR spectrometers, we are able to gain new insights into the dynamics and distribution of drug cargo in polymeric micelle solutions. These studies and methods also show promise for shedding new light onto understanding of molecular interactions between small molecule cargo and micelle polymers. Employing such new understanding will enable rational design of drug delivery formulations as well as other micelle encapsulation technologies, e.g., micelle-phase "nanoreactor" synthesis.

4.2. Experimental section

4.2.1. Materials and sample preparation

HCT, IND and Pluronic® F127 were purchased from Sigma-Aldrich. Drug-loaded block copolymer micelle solutions were prepared by mixing the drugs, triblock copolymer and deuterated solvent (D_2O) together at 50 °C for 60 min (see **Figure 4.1b**). The transparent solutions

were then transferred to a 5 mm NMR tube after cooling for data acquisition to reduce possible micelle aggregation. Each sample tube was equilibrated at room temperature (25 °C) prior to running NMR diffusometry experiments to ensure the sample is at thermal equilibrium. PTX-loaded BCMs were prepared by a solid dispersion method, where PTX and F127 polymer were dissolved separately in 2 mL DMF solvent to obtain transparent solutions, followed by fully mixing of two solutions and overnight vacuum dry to obtain homogenous solid dispersion. D_2O was then added to the solid dispersion at the same condition mentioned above to prepare PTX-loaded BCMs.

4.2.2. Pluronic® F127 Molecular weight studies using Gel Permeation Chromatography and NMR (GPC)

The molecular weight and the dispersity of the as-received Pluronic® F127 was characterized by a Viscotek GPCmax instrument using THF (OmniSolv, HPLC grade) as the mobile phase. The injected volume was 100 µL of a 1 mg/mL solution, and the flow rate was 1 mL/min at 30 ºC. Universal analysis was employed for the characterization of number-average molecular weight, M_n, and dispersity, $Đ$, utilizing the refractometer and viscometer. 1D ^{1}H NMR measurements were made using 400 MHz Bruker Avance III WB NMR spectrometer. A single 90° RF pulse with length of 4.5 μs is used to obtain spectrum data.

4.2.3. Pulsed-field-gradient (PFG) NMR Diffusometry

Our previous study has shown the utility of NMR in measurement of diffusion coefficients and relative populations of unimers and micelles. [24-25, 43] NMR diffusometry typically applies the pulsed-field-gradient stimulated echo (PGSTE) sequence, which provides information on translational motion of various species in solution. [44-45] The signal amplitude I was measured as a function of gradient strength (g) and was fit with the Stejskal-Tanner equation, [46-48]

$$I = I_0 e^{-g^2\gamma^2\delta^2\left(\Delta-\frac{\delta}{3}\right)D} \quad (4.2)$$

where I_0 is signal amplitude at $g = 0$, γ is gyromagnetic ratio, δ is effective gradient pulse length, Δ is diffusion time between gradient pulses, and D is self-diffusion coefficient. The "b" factor, representing all the known NMR-specific parameters and useful for qualifying diffusion behaviors and artifacts, is given by $b = \gamma^2 g^2 \square^2(\square\square\square\square\square/3)$.

The self-diffusion coefficients of polymer, drug and solvent in solution were determined using a 400 MHz Bruker Avance III WB NMR spectrometer, equipped with a MIC probe coupled to a Diff60 single-axis (z-axis) gradient. The pulsed-gradient stimulated echo (PGSTE) sequence was used with a 90° RF pulse length of 4.5 μs. A half sinusoid gradient pulse length of $\delta = 3.14\ ms$ (effective rectangular pulse length $= 2\ ms$), diffusion time $\Delta = 10 - 100\ ms$, and post-gradient delay $= 4\ ms$ were used for ^{1}H diffusometry measurements. Maximum gradient strengths were adjusted in the range 50 – 600 G·cm^{-1} to achieve 90 – 99% signal attenuation in 8-16 steps. Sufficient signal-to-noise ratio (SNR) for each data point was achieved with 8 – 128 scans. Acquisition times and relaxation delay times were each 1 s, and 8 Hz line broadening was applied during data processing. Relaxation delay times of 1.5 s were used for both polymer and solvent signals. All NMR measurements were performed at 25 ± 1 °C.

4.3. Results and discussion

The molecular weight and the dispersity of the as-received Pluronic® F127, used in this study, was characterized with a combination of gel permeation chromatography (GPC) and nuclear magnetic resonance (1D NMR) spectroscopy as shown **in Figure 4.2** and **Figure 4.3** respectively. The molecular weight distribution from these experiments shows bimodal distribution, indicating the presence of diblock copolymer (PEG-PPO) contaminants. The number average molecular

weight of the purchased sample was $M_n = 14 \frac{kg}{mol}$ and their dispersity $Đ = 1.25$ with ethylene glycol weight fraction equal to 72.2%. These characteristics indicate the polymer composition to be PEG_{115}-PPO_{67}-PEG_{115}.

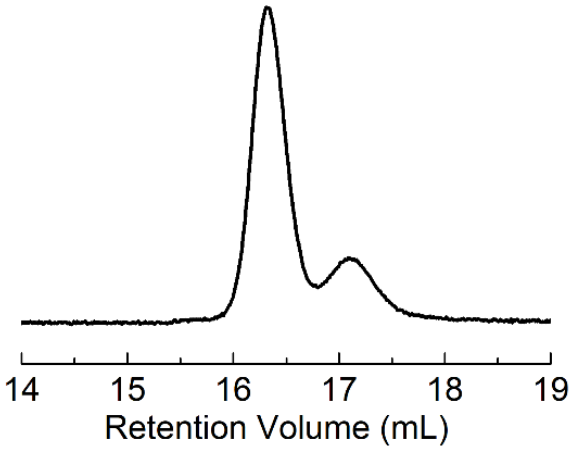

Figure 4.2. GPC data obtained from Pluronic® F127 as received. A bimodal distribution consistent with that seen by Yu et al[4] is seen, representative of diblock contamination (PEG-PPO) in the triblock copolymer (PEG-PPO-PEG).

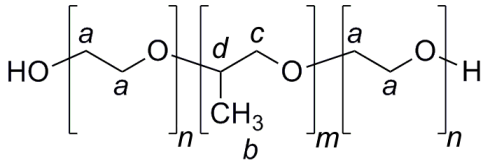

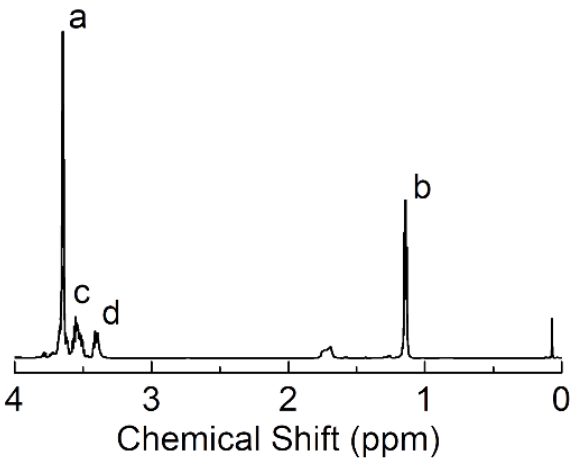

Figure 4.3. 1D NMR data obtained from Pluronic F127 as received. The peak ratio of peak a to peak b was found to be higher than expected, indicating more EG content than normally reported.

We can access diffusion coefficients of polymer chains in micelle solutions (either in the form of free unimers or micelles or both) from Stejskal−Tanner signal attenuation plots. By taking the natural log of normalized NMR signal intensity (I/I_0) and plotting vs. the NMR experimentally defined b ($\gamma 2\delta 2g2(\Delta - \delta/3)$) factor, a single linear regression fit indicates a single component and the slope corresponds to its diffusion coefficient (D). Any deviation from linear fitting (i.e., two straight slopes) represents more than one diffusion coefficient of the species of interests. **Figure 4.4** below shows an example of signal attenuation in 3% w/v BCM solution, where the fast-diffusing species (like unimer chains or small aggregates) significantly contribute to the initial signal decay at lower gradient strengths. The slow-diffusing species (BCMs) contribute to the signal decay at higher gradient strengths, resulting in change in slope of the linear curve as indicated by the red lines drawn in **Figure 4.4**.

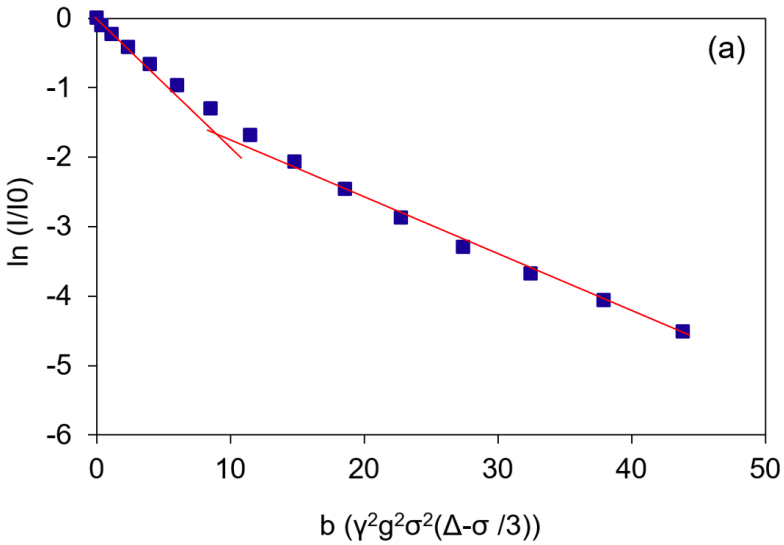

Figure 4.4: Fitting the Stejskal-Tanner signal decay curve in 3% w/v of F127 BCM solution. Figure clearly shows the presence of two polymer diffusion species in BCM solution. The lines are drawn for visual guide and they do not represent the actual fit of the curve.

As a function of F127 concentration, NMR diffusometry demonstrates a gradual decrease in diffusion coefficient (D), indicating that the size (hydrodynamic diameter) of the micelle increases with polymer concentration in the solution. These sizes were determined using Stokes-Einstein equation (**4.3**) and the sizes of the micelles.

$$D_{species} = \frac{2kT}{c\pi\eta d_{H,species}} \tag{4.3}$$

For 5% w/v Pluronic® F127 at 25 °C, the diffusion coefficient of water is 1.9×10^{-9} $m^2\cdot s^{-1}$ and its viscosity is 1.0×10^{-3} Pa·s, [8] we assume the hydrodynamic radius of water remains unchanged because the presence of polymer is insignificant to affect the water molecule structure. However, the viscosity of solution changes with polymer concentration, which can be measured from diffusion coefficients of water in solution with the aid of **Equation 4.3**. Water diffusion coefficients were measured to solve for the viscosities in solution as shown in **Table 4.1**. These viscosities remained the same for solutions with or without drug loading over the full range of polymer concentration explored (1 - 5%). **Figure 4.5** clearly shows that the size of the micelle increased with polymer concentration in the solution. This size variation suggests that more drug can be loaded into the BCMs with greater drug partitioning in micellar phase due to greater less-polar core volume availability.

Table 4.1. Diffusion coefficients of residual water in BCMs with drug loading (HCT and IND at < 1% w/v). The viscosity of the drug-micelle solutions does not change appreciably with polymer concentration.

F127 conc (w/v %)	Water diffusion coefficient ($m^2\cdot s^{-1}$)	Viscosity (Pa·s)
5	1.90×10^{-9}	1.00×10^{-3}
3	2.08×10^{-9}	9.13×10^{-4}
2	2.08×10^{-9}	9.13×10^{-4}
1	2.07×10^{-9}	9.17×10^{-4}
0	2.10×10^{-9}	9.04×10^{-4}

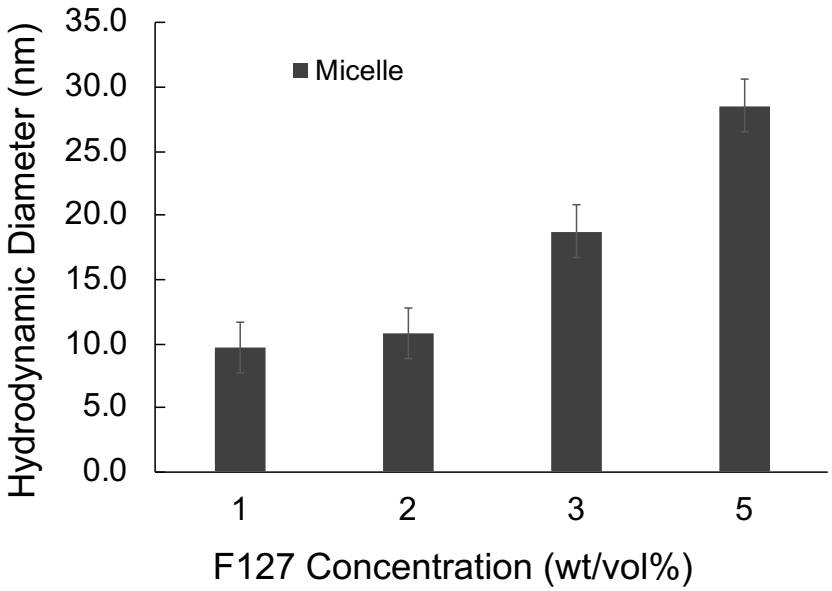

Figure 4.5. Hydrodynamic radius of 1-5 % w/v of Pluronics® F127. The viscosity of the bulk solutions, mentioned in **Table 4.1**, is used to estimate the hydrodynamic diameter of micelle.

To initially understand the molecular structure and solubility of drug-micelle solutions, we present ^{1}H NMR spectra of BCMs with and without drug loading (**Figure 4.6**). Peaks of polymer and solvent are zoomed to better observe drug peaks. Notably, PTX (see spectrum in **Figure 4.6d**) is one of the most efficient and widely applied anticancer drugs, and yet has extremely low water solubility (~ 5 mg/L). [37-38] The solubility of PTX in BCM solutions (0.06% w/v or 600 mg/L, as verified by NMR peak integration) increases more than two orders of magnitude over the intrinsic aqueous solubility of PTX, which reinforces the use of polymeric micelles to increase hydrophobic drug solubility.

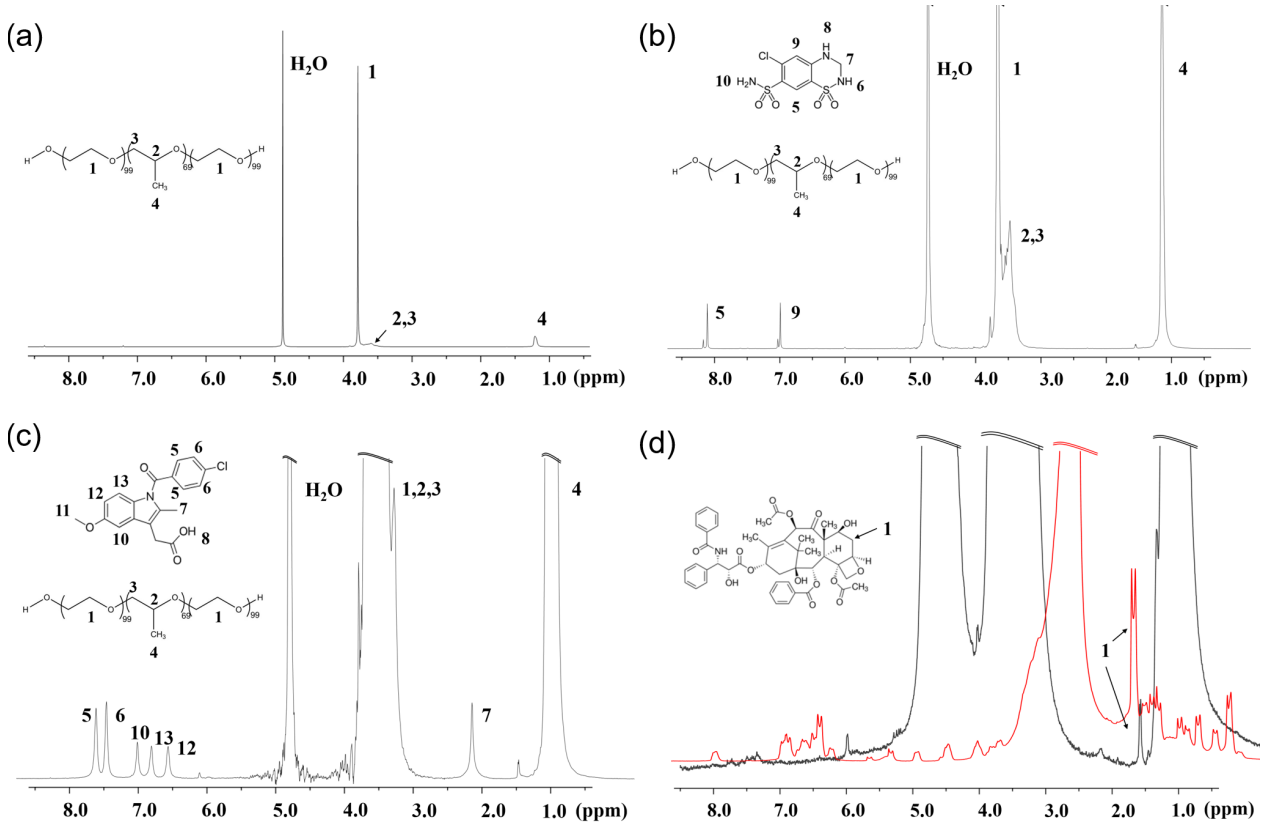

Figure 4.6. ^{1}H NMR spectra of BCMs with and without drug loading. (a) 1% w/v F127 BCM without drug (b) 0.3% w/v HCT solubilized in 2% w/v F127 BCMs. Peak 7 overlaps with the H_2O peak and we barely observe peaks 6, 8, 10 due to deuterium exchange (c) 0.3% w/v IND solubilized in 3% w/v F127 BCMs. Peaks 9, 11 overlap with the PEO peak and we barely observe peak 8 due to deuterium exchange. In (b) and (c), we magnify signal intensity (peak 1, 4 and water off scale) to observe drug peaks. (d) 0.2 % w/v PTX dissolved in DMSO-$_{d6}$ (red) and 0.06% w/v PTX solubilized in 5% w/v F127 BCMs (black). We have magnified signal intensities (polymer and solvents off scale) in both spectra to observe drug peaks.

To further explore micelle and drug dynamics and partitioning of drugs into micelles vs. in free solution, we investigate a range of Pluronic F127 and drug compositions using NMR diffusometry. Due to the separate NMR spectral peaks assigned to drugs and BCP molecules (**Figure 2**), we can separately and simultaneously measure micelle diffusion (via the polymer peaks) and drug diffusion. **Table 1** summarizes these results. In Pluronic® F127 micellar

solutions, NMR diffusometry demonstrates a decrease in self-diffusion coefficient of polymer (D_{poly}) with increasing concentration, due to the increasing diameter of the micelles. In future, we will study Pluronic micelle structural parameters as a function of drug chemistry and temperature using small-angle neutron scattering (SANS) and dynamic light scattering (DLS).

Here, we further quantify the drug diffusion coefficients, both in micellar solutions and in pure water. We then use the combination of diffusion coefficients to extract the percentage of drugs *encapsulated inside micelles* versus *in the surrounding aqueous solution*, and this whole system can be modeled as a two-phase system. [39] The time scale of exchange (τ_{ex}) between micelle core and free solution is an important parameter influenced by drug cargo size, hydrophobicity, and other specific molecular (thermodynamic) interactions with the solvent and with the micelle core.

If solubilized drug molecules are in the "slow exchange" regime relative to the NMR observation time scale, which in this case is the diffusion time (Δ), i.e. $\tau_{ex} \gg \Delta$, we would differentiate and quantify drug concentrations in the two phases from a two-component fit to a Stejskal-Tanner (NMR signal decay) plot. [25, 40] In this case, one component would be for the free-diffusing drug molecules in aqueous solution and the other component for those in the micellar cores. In the present work, however, both HCT and IND exhibit only *one* diffusion coefficient, even when varying the diffusion time Δ down to 10 ms (see **Figure 4.7**). This signifies that these drugs are in fast exchange between the aqueous and micellar phases, i.e. $\tau_{ex} \ll \Delta$, and thus the lifetime of drug residing in the hydrophobic core is shorter than the smallest observation time (10 ms). We discuss the implications of this for drug delivery and quantification of drug partitioning below.

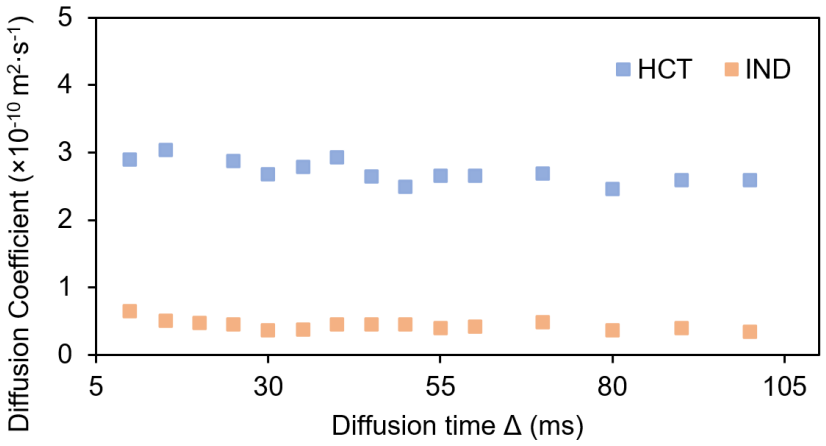

Figure 4.7. Diffusion coefficients of 1% w/v of HCT and 0.3% w/v IND solubilized in 3% w/v and 2% w/v F127 micellar solutions, respectively, with varying diffusion time (Δ). HCT and IND diffuse at an average rate of 2.7×10^{-10} $m^2\cdot s^{-1}$ and 1.1×10^{-10} $m^2\cdot s^{-1}$, respectively, when Δ varies from 10 ms to 100 ms.

We can, however, still quantify the partitioning of drug molecules by using the single-component diffusion coefficient of the drug molecules ($D_{drug,\ avg}$), which is a weighted average of contributions from drug solubilized in the micellar phase and drug dissolved in the aqueous phase in this fast exchange regime, and which obeys the following equation. [26, 41-42]

$$D_{drug,\ avg} = p_{drug,\ micelle} \cdot D_{drug,\ micelle} + p_{drug,\ aqueous} \cdot D_{drug,\ aqueous} \qquad (4.4)$$

$D_{drug,\ micelle}$ represents the diffusion coefficient of drug encapsulated by polymers in the micellar phase and $D_{drug,\ aqueous}$ represents that in the surrounding aqueous phase. $p_{drug,\ micelle}$ is the population (mole fraction) of drug molecules encapsulated in micelles and $p_{drug,\ aqueous}$ is for those diffusing freely in solution. The total mole fraction must equal unity ($p_{drug,\ micelle} + p_{drug,\ aqueous} = 1$).

In order to quantify populations of a model drug in these two phases using **Equation 4.4**, we assume (1) that $D_{drug,\ micelle}$ is the same as the diffusion coefficient of the polymer chains in micelles (D_{poly}), and (2) that $D_{drug,\ aqueous}$ is the same as that of the drug dissolved in solvent in the absence of micelles ($D_{drug,\ soln}$). We can do the following experiments to assess these assumptions.

For assumption (1), it should be reasonable to use the observed polymer diffusion coefficient (D_{poly}) in micellar solution to represent the diffusion coefficient of model drugs in the micellar phase ($D_{drug,\ micelle}$). This is supported by characterizing the diffusion of IND in F127 micelles at 5% w/v. Whereas pure IND in aqueous solution (with no F127 present) has a diffusion coefficient of 4.5×10^{-10} $m^2 \cdot s^{-1}$, IND in the F127 micellar solution shows $D_{drug} = 2.0 \times 10^{-11}$ $m^2 \cdot s^{-1}$. This value is nearly equal to (but is less than) $D_{poly} = 1.8 \times 10^{-11}$ $m^2 \cdot s^{-1}$ (see **Figure 4.8**). Note again that all polymer chains exist in micelles. This result strongly indicates that nearly all of the drug molecules are successfully trapped in micelles, and the drug moves along with the micelles for this "fully encapsulated" IND-F127 sample.

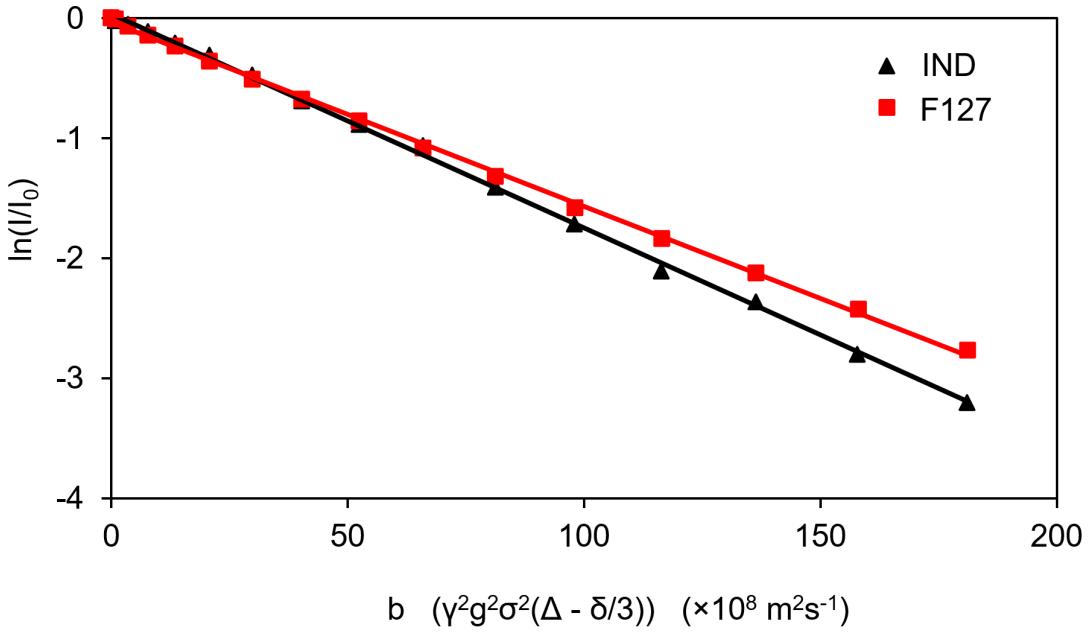

Figure 4.8. Stejskal-Tanner plots of NMR signal intensity for IND 0.3% w/v in 5% w/v F127 BCMs. Both IND and F127 (polymer) signals attenuate simultaneously with increased gradient strength. Fitting yields diffusion coefficients of 2.0×10^{-11} and 1.8×10^{-11} $m^2 \cdot s^{-1}$ for the IND drug molecules and F127 polymer chains (both held in micelles), respectively.

For assumption (2) to be correct, the addition of model drugs should not affect the bulk viscosity. In this case, we used the diffusion of an internal standard (residual H_2O in the solvent)

to track the bulk viscosity, and clearly this species will not influence cargo encapsulation and release. Overall, viscosity of the 1-5% w/v F127 micelle solutions as determined using Stokes-Einstein equation (**4.3**) does not vary in solutions that are saturated with these drugs (up to 1% w/v) as shown in **Table 4.1**.

Using these assumptions and **Equation 4.4**, we can thus extract populations of drugs in micelles for all samples, and therefore probe how drug hydrophobicity and polymer concentration affect partitioning (population) of drugs into micelles. **Table 4.2** contains measured diffusion coefficients and partition percentages of HCT, IND and polymer (F127) in drug-loaded micellar solutions by NMR diffusometry.

Table 4.2. Diffusion coefficients, partition percentages, and equivalent partition coefficients (*K*) of drug (HCT/IND) and polymer (F127) in drug-loaded micelles at different polymer concentrations.

F127	HCT-loaded BCMs				IND-loaded BCMs			
Conc.	D_{poly}	D_{drug}	p_{drug}	*K*	D_{poly}	D_{drug}	p_{drug}	*K*
% w/v	$m^2 \cdot s^{-1}$	$m^2 \cdot s^{-1}$	%		$m^2 \cdot s^{-1}$	$m^2 \cdot s^{-1}$	%	
5	1.7×10^{-11}	2.0×10^{-10}	70	2.37	1.8×10^{-11}	2.0×10^{-11}	99	101
3	2.6×10^{-11}	2.5×10^{-10}	62	1.67	1.5×10^{-11}	4.7×10^{-11}	93	13.1
2	4.4×10^{-11}	3.5×10^{-10}	48	0.93	2.4×10^{-11}	1.1×10^{-10}	79	3.82
1	4.1×10^{-11}	4.4×10^{-10}	33	0.49	3.7×10^{-11}	4.4×10^{-10}	3	0.03
0	N/A	6.3×10^{-10}	0	N/A	N/A	4.5×10^{-10}	0	N/A

Note: At 5, 3, 2, 1% w/v F127 concentrations, HCT additions are 0.25 ±0.05% w/v and IND additions are 0.30 ±0.05% w/v. Added drug concentrations are 0.5% w/v HCT and 0.5% w/v IND in solutions with no polymer, with measurements made after precipitation of excess drug. All diffusion measurements are taken at 25 ± 1 °C with errors in *D* values ≤ ±4%.

Based on the above two assumptions and results, we can compare the measured partition percentages of the HCT and IND model drugs in F127 BCMs (**Figure 4.9a**). For example, for solutions of 2% wt/vol (w/v) of F127, only 48% of HCT is in a micellar phase, while 79% of IND is encapsulated. IND has a lower aqueous solubility, which contributes to a higher compatibility between the drug and core-forming blocks relative to free solution, and thus prefer to reside in the micellar phase. As F127 concentration increases, the IND partition fraction into BCMs rises sharply, and all IND (99%) resides in micelles at F127 of 5% w/v. The less hydrophobic HCT, on the other hand, is not as strongly encapsulated by the BCMs since the drug is substantially soluble in water, and HCTs partition fraction exhibits a steady monotonic rise as F127 concentration increases.

For 1% w/v F127 IND-loaded BCMs, drug partitioning percentage is low, possibly due to the phase behavior of the BCMs in which 1% F127 is on the edge of micelle formation and the core structure may be effectively less hydrophobic at this concentration. We further varied the HCT concentration in the F127 BCMs to study how drug concentration impacts partition fractions and K values. **Table 4.3** summarizes the changes in K values with increasing drug concentration, indicating higher concentrations allow for more drug molecules to be encapsulated in the micellar phase. These results show that NMR diffusometry offers a quick and quantitative method to investigate the micellar dynamics of F127 at varied concentrations and the micellar solubilization of different cargo molecules, such as the model hydrophobic drugs HCT and IND. In **Figure 4.9b**, we conceptually summarize how micellar size and drug solubilization depends on polymer concentration based on NMR diffusometry.

Table S3. Varying drug (HCT) concentrations in the F127 BCMs and the respective partition percentages and *K* values.

F127 Conc (w/v %)	HCT 0.7-1% Loaded Micelles		HCT 0.3-0.5% Loaded Micelles		HCT 0.2-0.3% Loaded Micelles	
	Drug percentage (%)	*K* value	Drug percentage (%)	*K* value	Drug percentage (%)	*K* value
5	84	5.25	78	3.35	70	2.33
3	69	2.22	63	1.70	62	1.63
1	37	0.59	31	0.45	33	0.49

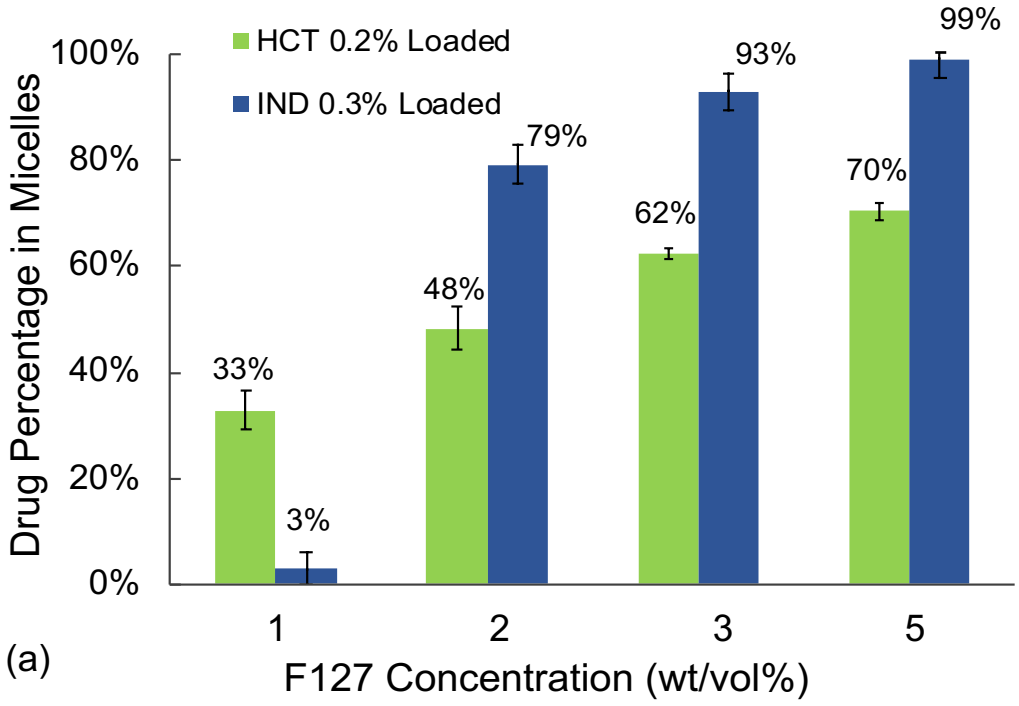

(a)

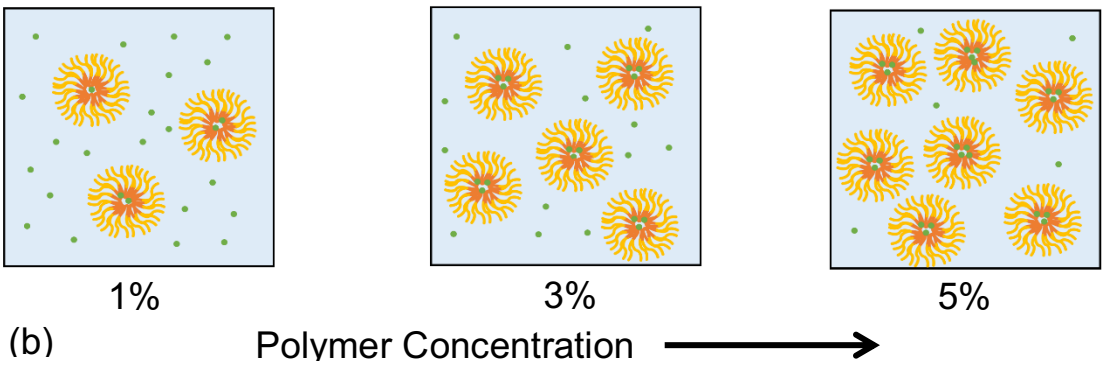

Figure 4.9. (a) Drug (HCT and IND) partition percentages in the F127 BCMs. Drug additions are mentioned in Table 1. The increased amount of drug solubilized is attributed to the increased number of total amphiphilic chains in solution, providing increased reservoirs to trap hydrophobic drugs. (b) Schematic representation of micelle size evolution and distribution of HCT-loaded BCMs by varying the polymer concentration. The overall size of micelles expands as the drug are loaded in the micellar cores.

We also quantified the percentage of HCT drug in the micellar phase at three different temperatures (25, 37, and 50 °C) as shown in **Figure 4.10**. The drug concentration in the micellar phase consistently decreased with increasing temperature across all polymer concentrations (1, 3, and 5 w/v%). This reduction is likely due to the increased solubility of HCT in water at higher temperature, which drives the drug towards entropically favored free aqueous solution, reducing its presence in the micellar phase. Additionally, at elevated temperatures, a higher fraction of polymer chains exists as free unimers [**references**], which decreases the hydrophobic core volume of the micelles to encapsulate the drugs.

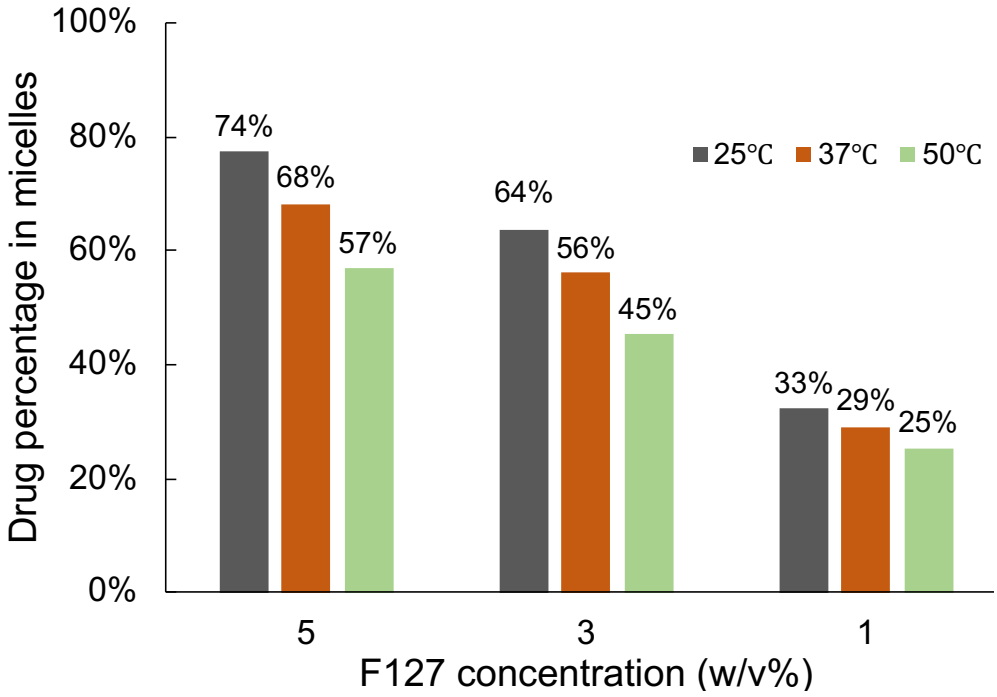

Figure 4.10: Quantified percentage of HCT drug in the micellar phase measured at three different temperatures across varying polymer concentration (1, 3, and 5 w/v%). The drug percentage consistently decreased with increasing temperatures. This is due to greater drug solubility at higher temperature and a reduction in the hydrophobic core volume of the micelles at elevated temperatures.

We have also prepared paclitaxel (PTX)-loaded micelles by a solid dispersion method. [35-36] Our NMR results show that PTX is fully encapsulated within the Pluronic® micellar cores (> 99%), which is sensible based on its strongly hydrophobic nature. This sheds light on the rational design of anti-cancer drug formulations and further studies will be continued to investigate chemotherapy drug-micelle interactions. This technique also informs on the hydrophobic drug's equilibrium existing between micellar and solvent phase due to fast exchange.

Note that previous measurements of drug partition coefficients using UV-Vis, fluorescence or HPLC[20-23] rely on filtration or dialysis of the micelle sample combined with spectroscopy before and after the separation procedure. Since τ_{ex} for the hydrophobic drugs is smaller than the

experimental measurement and separation procedure times, a new equilibrium state is reached before taking spectroscopy measurements, which would give rise to different partition percentages when measured before and after any separation procedures. NMR gives a clear advantage for drug partition measurements as it does not require any separation procedures after micelle-drug formulation, thus enabling determination of more reliable partition percentages.

4.4 Conclusions

In summary, this NMR diffusometry study offers a quick and quantitative approach to investigate the micellar dynamics of Pluronic® F127 triblock copolymer micelles and their interactions with hydrophobic drug molecules and solvents. We explored the effects of key physical parameters – such as polymer concentration, drug composition, drug concentration, and solution temperature – on the behavior of micelles and drug solubilization. Increasing polymer and drug concentrations enhanced the drug loading capacity, while higher temperatures reduced the amount of drug encapsulated, likely due to increased drug solubility in water and changes in micelle structure. Additionally, polymer concentration likely influences important micellar parameters such as core and corona radii and aggregation number, which necessitates for further investigation using small angle neutron scattering (SANS) techniques.

By understanding micellar internal structures, exchange kinetics, and solubilization properties, we can gain valuable insights into optimizing drug formulations and predicting in vitro release profiles for candidate drugs. This study paves the way for improved micellar drug delivery systems and provides a foundation for future research to fine-tune micelle-based formulation for enhanced therapeutic applications.

References

1. Gallou, F.; Isley, N. A.; Ganic, A.; Onken, U.; Parmentier, M., Surfactant technology applied toward an active pharmaceutical ingredient: more than a simple green chemistry advance. *Green Chemistry* **2016,** *18* (1), 14-19.

2. Chiappetta, D. A.; Sosnik, A., Poly(ethylene oxide)–poly(propylene oxide) block copolymer micelles as drug delivery agents: Improved hydrosolubility, stability and bioavailability of drugs. *European Journal of Pharmaceutics and Biopharmaceutics* **2007,** *66* (3), 303-317.

3. Deng, C.; Jiang, Y.; Cheng, R.; Meng, F.; Zhong, Z., Biodegradable polymeric micelles for targeted and controlled anticancer drug delivery: Promises, progress and prospects. *Nano Today* **2012,** *7* (5), 467-480.

4. Ding, H.; Wang, X.; Zhang, S.; Liu, X., Applications of polymeric micelles with tumor targeted in chemotherapy. *Journal of Nanoparticle Research* **2012,** *14* (11), 1-13.

5. Tiwari, G.; Tiwari, R.; Sriwastawa, B.; Bhati, L.; Pandey, S.; Pandey, P.; Bannerjee, S. K., Drug delivery systems: An updated review. *International Journal of Pharmaceutical Investigation* **2012,** *2* (1), 2-11.

6. Raoul, Z., Dynamics in Micellar Solutions of Surfactants. In *Dynamics of Surfactant Self-Assemblies*, CRC Press: 2005; pp 75-160.

7. Escobar-Chávez, J. J.; López-Cervantes, M.; Naik, A.; Kalia, Y.; Quintanar-Guerrero, D.; Ganem-Quintanar, A., Applications of thermo-reversible pluronic F-127 gels in pharmaceutical formulations. *Journal of Pharmacy & Pharmaceutical Sciences* **2006,** *9* (3), 339-58.

8. Pitto-Barry, A.; Barry, N. P., Pluronic® block-copolymers in medicine: from chemical and biological versatility to rationalisation and clinical advances. *Polymer Chemistry* **2014,** *5* (10), 3291-3297.

9. Wu, C.; Liu, T.; Chu, B.; Schneider, D. K.; Graziano, V., Characterization of the PEO−PPO−PEO Triblock Copolymer and Its Application as a Separation Medium in Capillary Electrophoresis. *Macromolecules* **1997,** *30* (16), 4574-4583.

10. Hvidt, S.; Joergensen, E. B.; Brown, W.; Schillen, K., Micellization and gelation of aqueous solutions of a triblock copolymer studied by rheological techniques and scanning calorimetry. *The Journal of Physical Chemistry* **1994,** *98* (47), 12320-12328.

11. Nivaggioli, T.; Alexandridis, P.; Hatton, T. A.; Yekta, A.; Winnik, M. A., Fluorescence Probe Studies of Pluronic Copolymer Solutions as a Function of Temperature. *Langmuir* **1995,** *11* (3), 730-737.

12. Ma, J.; Guo, C.; Tang, Y.; Xiang, J.; Chen, S.; Wang, J.; Liu, H., Micellization in aqueous solution of an ethylene oxide–propylene oxide triblock copolymer, investigated with 1H NMR spectroscopy, pulsed-field gradient NMR, and NMR relaxation. *Journal of Colloid and Interface Science* **2007,** *312* (2), 390-396.

13. Walderhaug, H.; Söderman, O.; Topgaard, D., Self-diffusion in polymer systems studied by magnetic field-gradient spin-echo NMR methods. *Progress in Nuclear Magnetic Resonance Spectroscopy* **2010,** *56* (4), 406-425.

14. Allen, T. M.; Cullis, P. R., Drug Delivery Systems: Entering the Mainstream. *Science* **2004,** *303* (5665), 1818.

15. Allen, T. M., Ligand-targeted therapeutics in anticancer therapy. *Nature Reviews Cancer* **2002,** *2* (10), 750-763.

16. Sharma, P. K.; Bhatia, S. R., Effect of anti-inflammatories on Pluronic® F127: micellar assembly, gelation and partitioning. *International Journal of Pharmaceutics* **2004,** *278* (2), 361-377.

17. Choucair, A.; Eisenberg, A., Interfacial Solubilization of Model Amphiphilic Molecules in Block Copolymer Micelles. *Journal of the American Chemical Society* **2003,** *125* (39), 11993-12000.

18. Letchford, K.; Liggins, R.; Burt, H., Solubilization of hydrophobic drugs by methoxy poly(ethylene glycol)-block-polycaprolactone diblock copolymer micelles: Theoretical and experimental data and correlations. *Journal of Pharmaceutical Sciences* **2008,** *97* (3), 1179-1190.

19. Zhao, M.; Eghtesadi, S. A.; Dawadi, M. B.; Wang, C.; Huang, S.; Seymore, A. E.; Vogt, B. D.; Modarelli, D. A.; Liu, T.; Zacharia, N. S., Partitioning of Small Molecules in Hydrogen-Bonding Complex Coacervates of Poly(acrylic acid) and Poly(ethylene glycol) or Pluronic Block Copolymer. *Macromolecules* **2017,** *50* (10), 3818-3830.

20. Sabaté, R.; Gallardo, M.; de la Maza, A.; Estelrich, J., A Spectroscopy Study of the Interaction of Pinacyanol with n-dodecyltrimethylammonium Bromide Micelles. *Langmuir* **2001,** *17* (21), 6433-6437.

21. Barbato, F.; La Rotonda, M. I.; Quaglia, F., Interactions of Nonsteroidal Antiinflammatory Drugs with Phospholipids: Comparison between Octanol/Buffer Partition Coefficients and Chromatographic Indexes on Immobilized Artificial Membranes. *Journal of Pharmaceutical Sciences* **1997,** *86* (2), 225-229.

22. Lasonder, E.; Weringa, W. D., An NMR and DSC study of the interaction of phospholipid vesicles with some anti-inflammatory agents. *Journal of Colloid and Interface Science* **1990,** *139* (2), 469-478.

23. Teng, Y.; Morrison, M. E.; Munk, P.; Webber, S. E.; Procházka, K., Release Kinetics Studies of Aromatic Molecules into Water from Block Polymer Micelles. *Macromolecules* **1998,** *31* (11), 3578-3587.

24. Li, X.; Cooksey, T. J.; Kidd, B. E.; Robertson, M. L.; Madsen, L. A., Mapping Coexistence Phase Diagrams of Block Copolymer Micelles and Free Unimer Chains. *Macromolecules* **2018,** *51* (20), 8127-8135.

25. Kidd, B. E.; Li, X.; Piemonte, R. C.; Cooksey, T. J.; Singh, A.; Robertson, M. L.; Madsen, L. A., Tuning Biocompatible Block Copolymer Micelles by Varying Solvent Composition: Dynamics and Populations of Micelles and Unimers. *Macromolecules* **2017,** *50* (11), 4335-4343.

26. Momot, K. I.; Kuchel, P. W., Pulsed field gradient nuclear magnetic resonance as a tool for studying drug delivery systems. *Concepts in Magnetic Resonance Part A* **2003,** *19A* (2), 51-64.

27. Kabanov, A. V.; Batrakova, E. V.; Alakhov, V. Y., Pluronic® block copolymers as novel polymer therapeutics for drug and gene delivery. *Journal of Controlled Release* **2002,** *82* (2), 189-212.

28. Kabanov, A. V.; Lemieux, P.; Vinogradov, S.; Alakhov, V., Pluronic® block copolymers: novel functional molecules for gene therapy. *Advanced Drug Delivery Reviews* **2002,** *54* (2), 223-233.

29. Vogt, L.; Waanders, F.; Boomsma, F.; de Zeeuw, D.; Navis, G., Effects of dietary sodium and hydrochlorothiazide on the antiproteinuric efficacy of losartan. *J Am Soc Nephrol* **2008,** *19* (5), 999-1007.

30. Bhargava, K. P.; Gupta, M. B.; Tangri, K. K., Mechanism of ulcerogenic activity of indomethacin and oxyphenbutazone. *European Journal of Pharmacology* **1973,** *22* (2), 191-195.

31. Singla, A. K.; Garg, A.; Aggarwal, D., Paclitaxel and it formulations. *Int. J. Pharm.* **2002,** *235*, 179-192.

32. Jones, M.-C.; Leroux, J.-C., Polymeric micelles – a new generation of colloidal drug carriers. *European Journal of Pharmaceutics and Biopharmaceutics* **1999,** *48* (2), 101-111.

33. Chacko, R. T.; Ventura, J.; Zhuang, J.; Thayumanavan, S., Polymer nanogels: A versatile nanoscopic drug delivery platform. *Advanced Drug Delivery Reviews* **2012,** *64* (9), 836-851.

34. Kadam, Y.; Yerramilli, U.; Bahadur, A.; Bahadur, P., Micelles from PEO–PPO–PEO block copolymers as nanocontainers for solubilization of a poorly water soluble drug. *Colloids and Surfaces B: Biointerfaces* **2011,** *83* (1), 49-57.

35. Shim, W. S.; Kim, S. W.; Choi, E.-K.; Park, H.-J.; Kim, J.-S.; Lee, D. S., Novel pH Sensitive Block Copolymer Micelles for Solvent Free Drug Loading. *Macromolecular Bioscience* **2006,** *6* (2), 179-186.

36. Serajuddin, A. T. M., Solid dispersion of poorly water-soluble drugs: Early promises, subsequent problems, and recent breakthroughs. *Journal of Pharmaceutical Sciences* **1999,** *88* (10), 1058-1066.

37. Louage, B.; Nuhn, L.; Risseeuw, M. D.; Vanparijs, N.; De Coen, R.; Karalic, I.; Van Calenbergh, S.; De Geest, B. G., Well-Defined Polymer-Paclitaxel Prodrugs by a Grafting-from-Drug Approach. *Angewandte Chemie* **2016,** *55* (39), 11791-6.

38. Paciotti, G. F.; Zhao, J.; Cao, S.; Brodie, P. J.; Tamarkin, L.; Huhta, M.; Myer, L. D.; Friedman, J.; Kingston, D. G. I., Synthesis and Evaluation of Paclitaxel-Loaded Gold Nanoparticles for Tumor-Targeted Drug Delivery. *Bioconjugate Chemistry* **2016,** *27* (11), 2646-2657.

39. Karger, J., Influence of 2-phase diffusion on spin-echo attenuation regarding relaxation in measurements using pulsed filed gradients. *Ann Phys* **1971,** *27* (1077), 9.

40. Kidd, B. E.; Forbey, S. J.; Steuber, F. W.; Moore, R. B.; Madsen, L. A., Multiscale Lithium and Counterion Transport in an Electrospun Polymer-Gel Electrolyte. *Macromolecules* **2015,** *48* (13), 4481-4490.

41. Krudopp, H.; Sönnichsen, F. D.; Steffen-Heins, A., Partitioning of nitroxides in dispersed systems investigated by ultrafiltration, EPR and NMR spectroscopy. *Journal of Colloid and Interface Science* **2015,** *452*, 15-23.

42. Nguyen-Kim, V.; Prévost, S.; Seidel, K.; Maier, W.; Marguerre, A.-K.; Oetter, G.; Tadros, T.; Gradzielski, M., Solubilization of active ingredients of different polarity in Pluronic® micellar solutions – Correlations between solubilizate polarity and solubilization site. *Journal of Colloid and Interface Science* **2016,** *477*, 94-102.

43. Wang, X.; Kelkar, S. S.; Hudson, A. G.; Moore, R. B.; Reineke, T. M.; Madsen, L. A., Quantitation of Complexed versus Free Polymers in Interpolyelectrolyte Polyplex Formulations. *ACS Macro Lett* **2013,** *2* (11), 1038-1041.

44. Wilmsmeyer, K. G.; Li, X.; Madsen, L. A., Anisotropic viscoelasticity and molecular diffusion in nematic wormlike micelles. *Liq. Cryst.* **2018,** *45* (6), 844-856.

45. Chen, M.; Dugger, J. W.; Li, X.; Wang, Y.; Kumar, R.; Meek, K. M.; Uhrig, D. W.; Browning, J. F.; Madsen, L. A.; Long, T. E.; Lokitz, B. S., Polymerized ionic liquids: Effects of counter-anions on ion conduction and polymerization kinetics. *Journal of Polymer Science Part A: Polymer Chemistry* **2018,** *56* (13), 1346-1357.

46. Stejskal, E.; Tanner, J., Spin Diffusion Measurements: Spin Echoes in the Presence of a Time-Dependent Field Gradient*. *J. Chem. Phys.* **1965,** *42* (1).

47. Callaghan, P. T., *Translational Dynamics and Magnetic Resonance: Principles of Pulsed Gradient Spin Echo NMR*. Oxford University Press: New York, 2011.

48. Price, W. S., Pulsed-field gradient nuclear magnetic resonance as a tool for studying translational diffusion .1. Basic theory. *Concept Magnetic Res* **1997,** *9* (5), 299-336.

Chapter 5: Strong variation of micelle–unimer coexistence as a function of core chain mobility

Reprinted with permission from Ryan J. Carrazzone, Xiuli Li, Jeffrey C. Foster, Veera Venkata Shravan Uppala, Candace E. Wall, Alan R. Esker, Louis A. Madsen, and John B. Matson. Macromolecules, **2021**, 54, 14, 6975-7981 © American Chemical Society

Abstract

Polymeric micelles coexist in solution with unassembled chains (unimers). We investigated the influence of glass transition temperature (T_g) (i.e., chain mobility) of the micelle core-forming blocks on micelle–unimer coexistence. To achieve this, we synthesized a series of seven PEG-*b*-P(*n*BA-*ran*-*t*BA) amphiphilic block copolymers (PEG = poly(ethylene glycol), *n*BA = *n*-butyl acrylate, *t*BA = *tert*-butyl acrylate) with PEG forms the hydrophilic shell and the random copolymer block as hydrophobic core. The molecular weights for all seven samples were consistent and verified using SEC. The *n*BA / *t*BA molar ratio was varied to systematically tune the mobility (i.e. T_g) of the core block without significant alterations in core's hydrophobicity and micelle size. Using NMR diffusometry, we observed a sharp increase in unimer population from 0% to 54% when the T_g of the core block decreased from 25°C to –46 °C. Moreover, at a fixed polymer composition (and thus constant T_g), the unimer population increased with rising temperature. This study highlights the significant role of core-block mobility in polymer self-assembly and provides insights for designing advanced drug-delivery systems, underscoring the need for refined dynamic models.

5.1 Introduction

Molecular self-assemby, driven by non-covalent interactions, is a fundamental process in nature where molecules spontaneously form higher-order structures, often due to hydrophobicity. [1] This phenomenon is central to many biological structures, including cell membranes [2] actin fibers, [3] and vesicles. [4] Similarly, synthetic amphiphilic block copolymers (BCPs), also self-assemble to generate nanoscopic hydrophobic and hydrophilic domains. These domains are used in a variety of applications such as delivery vehicles for hydrophobic drugs, [5-9] scaffolds for the novel polymer architectures, [10-12] and nanoscale compartments for catalysis. [13-14] Consequently, a deep understanding of the factors that govern self-assembly of both small molecules[15-17] and BCPs[18-19] has been developed.

Amphiphilic BCPs exhibit diverse morphologies both in bulk[20-21] and in solution, [22-23] with their self-assembly being significantly influenced by polymer characteristics such as hydrophobicity of the core-forming block, the ratio of hydrophilic to hydrophobic content and the glass transition temperature (T_g) of the core-forming block. [24-27] Additionally, the solution composition and preparation method also plays a crucial role in self-assembly. [19, 28-30] Despite extensive research research on the morphologies and self-assembly processes of amphiphilic BCPs, there remains a knowledge gap on the equilibrium between nanostructures and free unimers in solution. [31] These concentrations are hard to detect using conventional characterization techniques. [32-34] Since, unimer populations can significantly impact the pharmacokinetics and biodistribution of amphiphilic BCPs, [35-37] there is growing interest to developing methods to precisely quantify unimer populations.

One powerful technique for quantifying the polymer populations in micelles/unimer phase is pulsed-field-gradient (PFG) NMR diffusometry. This non-destructive method can sensitively determine the diffusion coefficients for various mobile species in solution as well as in solid materials. Furthermore, NMR diffusometry can track species with molecular and elemental specificity and thus has been used to observe multiple diffusing species in a wide range of polymeric systems, [38-44] thus making it an ideal tool to study micelle-unimer equilibrium in block copolymer micelle systems. [33-34]

In this study, we aimed to investigate the effects of core block mobility (T_g) on the micelle–unimer equilibrium by synthesizing a series of BCPs containing hydrophobic blocks of similar hydrophobicity but varying chain mobility using NMR diffusometry. This equilibrium was also determined as a function of hydrophobic block composition and temperature to study their influence on the equilibrium. Through this systematic investigation, we aimed to gain deeper understanding of micelle dynamics and offer insights into how micelle properties can be finely tuned for various applications.

5.2. Results and discussion

The properties of micelle core are critical in determining the behavior of self-assembled structures, such as loading capacity, [45,46] and controlled release of active pharmaceutical ingredients. [47] Based on these observations, we hypothesized a correlation between the T_g of the hydrophobic core and micelle–unimer coexistence. To test this hypothesis, we synthesized a series of similar molecular weights BCPs with similar hydrophilicity and hydrophobicity of the polymer blocks but varied their T_gs. We employed copolymerization, a well-established method for modying polymer's T_g. [48-49] Specifically, we used $n$butyl acrylate (nBA) and $tert$-butyl acrylate (tBA), which have similar hydrophobicity but widely different T_g (–50 °C for nBA and 50 °C for

tBA), to achieve fine control on the T_g of the core-forming block. [50,51] This approach allowed us to systematically study the impact of T_g on micelle-unimer equilibrium. **Scheme 5.1** shows the preparation of PEG-*b*-P(*n*BA-*ran*-*t*BA) block copolymers.

Scheme 5.1. Preparation of PEG-*b*-P(*n*BA-*ran*-*t*BA) BCPs.

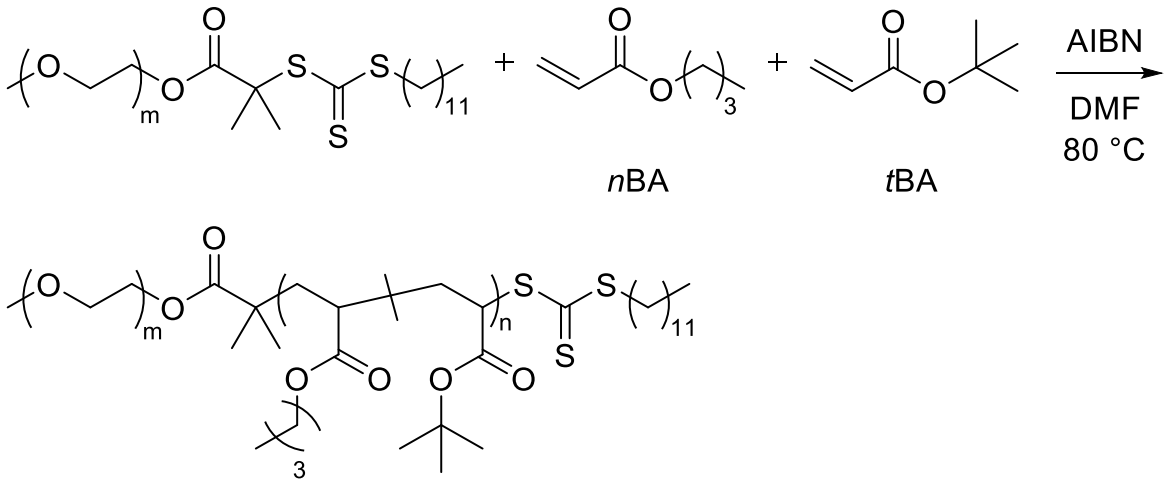

We prepared the series of BCPs with varying core block composition in two steps. First, we synthesized a large batch of trithiocarbonate-terminated PEG ($M_n = 4\ kg/mol$) as the hydrophilic block. The trithiocarbonate group served as a chain transfer agent (CTA) for reversible addition–fragmentation chain-transfer (RAFT) polymerization, ensuring control over molecular weight. In the second step, we used RAFT polymerization to produce seven BCPs (1a-g) with varying nBA/tBA molar ratios. Monomer consumption rates for nBA and tBA were identical, confirming that feed and composition ratios matched. By maintain a consistent hydrophilic/hydrophobic ratio while varying nBA/tBA molar ratio, we achieved a uniform BCP M_n ≈12 kg/mol throughout the series (**Table 5.1**).

Table 5.1. Characterization of PEG-*b*-P(*n*BA-*ran*-*t*BA) block copolymers.

Polymer	Mol % *n*BA[a]	M_n (NMR) (kg/mol)[b]	M_n (GPC) (kg/mol)[c]	$Đ$[c]	T_g (°C)[d]	D_h (nm)[e]	N_{agg}[f]

	Polymer					Micelle	
1a	100	12.0	12.2	1.07	-46	25.1 ± 0.1	83
1b	75	11.3	12.6	1.07	-35	28.9 ± 0.1	103
1c	60	11.9	11.9	1.12	-24	27.9 ± 0.1	101
1d	50	12.1	13.3	1.10	-20	26.2 ± 0.2	80
1e	40	11.6	11.7	1.11	-6	27.1 ± 0.6	77
1f	25	12.6	12.9	1.08	5	27.0 ± 0.2	87
1g	0	11.6	11.8	1.05	25	26.2 ± 0.5	72

[a]*n*BA/*t*BA molar ratio measured by ^{1}H NMR spectroscopy. [b]Measured by end-group analysis *via* ^{1}H NMR spectroscopy (**Figures S4-S20**). [c]M_n measured by GPC in THF at 30 °C with multi-angle light scattering. [d]Of the hydrophobic block measured by DSC with a modulated heating rate (3 °C/min, ± 2.5 °C, 60 s); data reported from second heat cycle (Figures S26-33). [e]Intensity average hydrodynamic diameter measured by dynamic light scattering (DLS) at 5 mg/mL in DI H_2O at rt (**Figure S36**). [f]Aggregation number derived from M_w of polymer and M_w of micelle at 5 mg/mL in DI H_2O at rt; M_w of micelles determined by SLS (**Figure S37**, **Equation S1**).

We evaluated each BCP by differential scanning calorimetry (DSC) to measure the T_g of the hydrophobic blocks in bulk (**Figures 5S26-33**). Instead of measuring the T_g of random polmer (P*n*BA/P*t*BA), we measured for the block copolymers as we expected the PEG-tethered chain ends influence the mobility of the hydrophobic block. **Table 5.1** and **Figure 5.1** show that T_g for the hydrophobic blocks of polymers **1a** (100% *n*BA) and **1g** (100% *t*BA) is –46 °C and 25 °C, respectively. The 100% *t*BA BCP (polymer **1g**) showed a lower T_g than the reported value of 50 °C. [51] We attribute this discrepancy to the relatively low molecular weight of the *t*BA block and the PEG tethered to one chain end, both of which may bring the overall T_g lower. The T_g values of the hydrophobic block for BCPs **1b**–**1f** (75–25% *n*BA) closely fit approximations based on the Fox equation. [48]

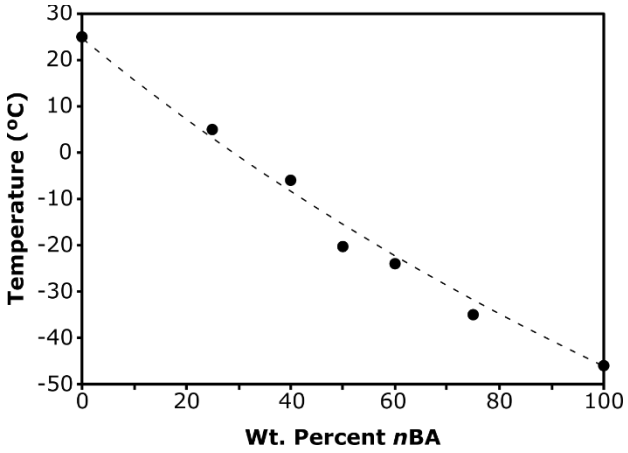

Figure 5.1. T_g for core-forming blocks of polymers **1a–g** (black circles) based on *n*BA/*t*BA molar ratio in the BCPs measured by DSC with a modulated heating rate (3 °C/min, ±2.5 °C, 60 s). The dotted black line represents a fit using the Fox equation (**Equation S5.2**) and the measured homopolymer T_g's. The core-forming block T_g varies predictably with polymer composition, providing access to a wide range of micelle core mobilities.

We evaluated the hydrophobicity of polymers **2a** and **2c** through NMR solubility experiments. Although, P*n*BA was more soluble than P*t*BA in D_2O by a factor of 2.5, both polymers exhibited extremely hydrophobic character (Figures S34 and S35). The solubility of PEG in water at room temperature is around 60 wt%,[53] which is significantly larger than the solubility of either acrylate polymer. As the solubility of the block copolymers in water will be governed primarily be the hydrophilic PEG block, we do not expect this small change in solubility to account for any differences in unimer percentages.

After determining that T_g and hydrophobicity for all seven BCPs of varying nBA/tBA ratio, we proceeded to investigate the change in micelle–unimer coexistence across the series. To prepare BCMs from amphiphilic BCP, we used the solvent switch method. Briefly, we first dissolved each polymer in THF, a good solvent for both blocks. We then diluted these polymer solutions by dropwise addition of H_2O to generate a 12.5% THF in H_2O solution. We subsequently transferred the polymer solutions to dialysis tubing (MWCO 8 kg/mol) and dialyzed against H_2O.

We utilized dynamic light scattering (DLS) to analyze the micelle size distributions from each BCP formulation (**Table 5.1** and **S5.1**, **Figure 5S36**). We observed that the hydrodynamic diameters of the micelles ranged from 25.1 to 28.9 nm, with no apparent trend in micelle size relating to micelle core mobility. This narrow size range is expected due to the similar molecular weights and hydrophobic weight fractions of the BCPs. Additionally, we observed low micelle polydispersity indices for each sample, indicating samples were free of high molecular weight aggregates. We then employed static light scattering (SLS) to obtain the M_w of micelles in solution for each micelle sample (**Figure 5S37**). From the SLS data, we estimated the aggregation number (N_{agg}) of each sample by dividing micelle M_w with BCP M_w (**Table 5.1**, **Equation 5.S1**). We observed N_{agg} ranged from 72 to 103, with no correlation to micelle core mobility, reinforcing that the nBA/tBA molar ratio in the core-forming block did not influence polymer micelle size.

Despite similar micelle sizes, we expected changes in micelle-unimer coexistence due to varying chain mobility of core-forming blocks throughout polymers **1a**–**g**. We initially examined the mobility of the hydrophobic core blocks form 1D ^{1}H NMR spectroscopy. In the NMR spectra, polymer solutions with relatively slow chain dynamics (where spectrometer shims do not determine linewidth) influence the full width at half-maximum (FWHM) of signal, which is inversely proportional to the spin-spin relaxation time (T_2) *via* the relation $FWHM = 1/\pi T_2$.[33, 54] In other words, decreasing T_2 values result in broader signal linewidths, indicating restrictions for molecular mobility. **Figure 5.2A** clearly shows that nBA and tBA alkyl proton signal appear in the range 0.5–2 ppm in spectra for BCPs (**1a**, **1d**, and **1g**). For 100% nBA polymer micelles (polymer **1a**, shown in purple), the alkyl proton sginal(s) $FWHM\ is\ \approx 40\ Hz$ compared to $\approx 80\ Hz$ for 50% nBA polymer micelles (polymer **1d**, shown in green) and $\approx 200\ Hz$ for 0% nBA polymer micelles (polymer **1g**, shown in red). The broadening of alkyl signals, with

increasing *t*BA, signifies the reduced chain mobility in the micelle cores. This result agrees with the trend of increasing measured T_g for the core blocks with increasing *t*BA content.

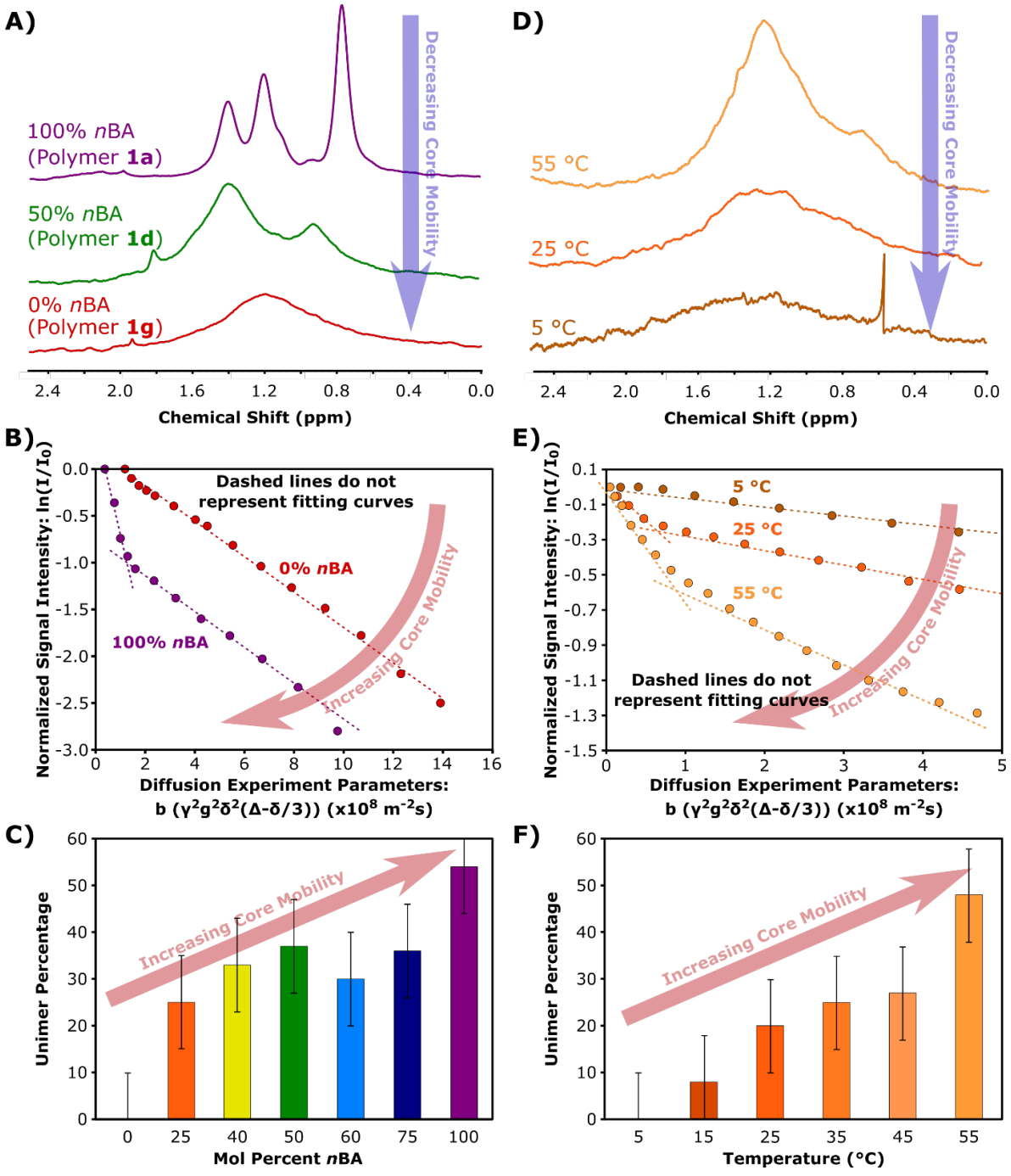

Figure 5.2. A) 1D ^{1}H NMR spectra overlay of micelle solutions made from 100, 50, and 0 mol% *n*BA BCPs (polymers **1a**, **1d**, and **1g**, respectively) at 5 mg/mL in H_2O solvent. B) Stejskal−Tanner plots of micelle solutions as a function of core-forming block composition at 25 °C (*b* is the

Stejskal–Tanner factor, g is the magnetic gradient strength, γ is the gyromagnetic ratio of the nucleus probed, δ is the gradient pulse duration, and Δ is the gradient pulse spacing). C) Unimer percentages derived from signal decay curves for micelle solutions as a function of core-forming block composition. D) ^{1}H NMR spectra overlay of 25% nBA polymer micelle solutions (from polymer **1f**) at 5, 25, and 55°C at 5 mg/mL. (See also Figure S50 for similar plots for 0% and 50% nBA polymers.) E) Stejskal−Tanner plots of polymer **1f** micelle solutions as a function of temperature with dashed lines as a guide to the eye for single- or two-component diffusion coefficients (they do not represent fit lines). F) Unimer percentages derived from signal decay curves for polymer **1f** micelle solutions as a function of temperature. Strikingly, core mobility strongly correlates with micelle–unimer coexistence. Error bars are ±10% for unimer percentages.

To further explore the effects of core-forming block T_g on micelle dynamics and on populations of unimers and micelles in solution, we utilized NMR diffusometry to probe translational motion of different mobile species. NMR diffusometry operates on the principle that chemical species with distinct mobilities – provided that they do not exchange quickly relative to the diffusion time ($\Delta = 25\,ms$ in this study, see **SI** for details) – will exhibit distinct diffusion coefficients. In amphiphilic BCP systems, diffusion unimeric polymer chains and assembled nanostructures (micelles) are sufficiently different, thus allowing us to quantify the relative populations of each species. [33-34]

We measured these populations using Stejskal−Tanner signal attenuation plots. By plotting the log-transformed of normalized NMR signals (I/I_o) versus the experimental parameter b (contains all known NMR parameters, ($\gamma^2\delta^2g^2 2(\Delta\text{-}\delta/3)$) in a signal attenuation curve, we extract diffusion coefficients D from linear regressions. A single linear fit suggests the presence of a single diffusing species, while multi-component fitting indicates multiple diffusing species in the solution.

In micellar systems, fast-diffusing unimers cause a rapid signal decay at lower magnetic gradient strengths (g) while slower diffusing micelles lead to a more gradual decay at higher higher

gradient strengths. A sample containing both micelles and unimers shows a rapid signal decay followed by a more gradual one as shown in **Figure 5.2B, 5.2E**. The relative contributions of these decay regimes give us the population fractions of micelle and unimer in the solution.

Throughout this BCP series, we observed notable changes in the signal decay curves, indicating shift in micelle-unimer equilibrium. In **Figure 5.2B**, 100% and 0% *n*BA polymer micelles (polymer **1a** purple and polymer **1g** red) showed different signal decay curves. The 0% *n*BA polymer micelles' signal decay fit with single component indicating only micelles are present in the solution. In contrast, the 100% *n*BA polymer micelles exhibited signal decay curve with a two-component fit, indicating the presence of two diffusing species in solution which corresponds to micelles and unimers. Since the experimental timescale ($25\ ms$) is much faster than unimer exchange, the observed differences in micelle-unimer coexistence cannot be attributred to unimer exchange kinetics. Furthermore, we measured free unimer content on heating and cooling on other block copolymer micelles and obtained same free vs. micelle-associated unimer fractions. [34]

To assess the influence of core block T_g on micelle–unimer coexistence, we determined the micelle and unimer populations for solutions of polymers **1a**–**g** from the fits to their signal decay curves, shown in **Figure 5.2C** (also **Figures S38-42**). The stark difference in unimer populations between the 100% and 0% *n*BA micelles suggests that the 0% *n*BA micelles exist in a 'frozen core' state at 25 °C. [55] Interestingly, diffusometry experiments before and after thermal annealing of the samples showed no changes in unimer percentage (**Figures 5S43–45**). This suggests that the variation in unimer fraction is due to difference in chain mobility and not due to due to a result of kinetically trapped micelles. Additionally, diffusometry experiments on 25% *n*BA micelles (polymer **1f**) at concentrations ranging from 3–10 mg/mL revealed no changes in unimer percentages (**Figure 5S46**). We observed a general trend: unimer population increased with

decreasing core-forming block T_g, with three distinct regimes of unimer percentage (0–10, 20–30, and 40–50%). These findings suggest a correlation between core mobility and unimer population. Classical micellization theories, [15-16, 18-19] typically do not predict core molecular dynamics influence on micelle-unimer equilibrium partitioning, but our results indicate a need for updated theoretical models.

We also conducted temperature-dependent diffusometry measurements on a 25% nBA micelle sample (polymer **1f**, $T_g = 5\ ^\circ C$). As expected, the micelle core mobility increased with temperature, reflected by narrower signal linewidths at higher temperature (**Figure 5.2D**). The NMR signal decay curves of 25% nBA at different temperatures (**Figure 5.2E**) revealed a significant rise in unimer population as temperature increased, consistent with trend observed in compositional experiments (**Figure 5.2C**). Unimer populations derived from these curves (**Figure 5.2F** and **Figures 5S47-49**) aligned with the three observed regimes, reinforcing our hypothesis that micelle core mobility directly influences micelle-unimer coexistence.

Additionally, variable temperature NMR diffusometry experiments of two other micelle compositions (polymers **1d** and **1g**, 50% and 0% nBA, respectively) confirmed this trend. Polymer **1d** showed a consistent unimer population of 40-50% for high core mobility micelles, while polymer **1g** transitioned from 0% to 25% unimers as temperatures rose beyond its T_g (**Figure 5S50**). However, we acknowledge that temperature affects other factors, such as solvent quality and interfacial tension, [56] meaning the observed results may not solely reflect core mobility changes with temperature.

We also explored the time required to reach quasi-equilibrium for these micelles. For various compositions and temperatures (**Figures 5S43 – 50**), diffusion coefficients were measured immediately after temperature changes at 5–10-minute intervals. We found that diffusion

coefficients and unimer fractions reached stable values after 30 minutes and remained constant at least for a month. This indicates that once formulated, these micellar systems rapidly attain quasi-equilibrium and remain stable over time, which is crucial for drug delivery applications.

The assembly of polymer amphiphiles into micelles is a thermodynamic process, driven by the increased entropy of water molecules excluded from the core and the increased hydrophobic interactions of the core-forming block. [18] Because mobility of the core-forming block should not theoretically impact micelle–unimer coexistence and would instead be more important for kinetic processes (i.e., unimer exchange), we are working to further investigate how micelle core mobility impacts unimer populations.

5.3. Conclusion

In conclusion, we thoroughly investigated the relationship between micelle core mobility and micelle-unimer coexistence in a series of amphiphili BCPs with varying nBA/tBA molar ratios in the hydrophobic blocks. Our findings reveal a clear ttrend of increasing unimer populations with decreasing T_g of the core-forming block. We confirmed that the observed effects of core chain mobility, modulated by T_g and experimental temperature, were independent of micelle core hydrophobicity, as demonstrated NMR solubility experiments on nBA/tBA homopolymers, which showed no significant variation in hydrophobicity with molar ratio.

Through variable temperature NMR spectroscopy and diffusometry experiments, we observed that both unimer populations and core chain mobility increased with rising temperature. These results challenge traditional micellization theories, which posit that core chain mobility should not influence micelle-unimer equilibrium. This suggests potential new directions for theoretical studies of micellar systems. We anticipate that these insights will lead to deeper understanding of micellar behavior and provide valuable guidance for the design of amphiphilic

block copolymer systems, particularly in applications where controlling unimer concentrations could impact performance, whether as a advantage/disadvantage.

References

1. Richard, G. J.; Christopher, K. O.; Philip, H.; Pavel, K.; Graeme, M.; Michel, V., Terminology for aggregation and self-assembly in polymer science (IUPAC Recommendations 2013). *Pure Appl. Chem.* **2012**, *85* (2), 463-492.

2. Bangham, A. D., Liposomes: the Babraham connection. *Chem. Phys. Lipids* **1993**, *64* (1), 275-285.

3. Dobson, C. M., Protein folding and misfolding. *Nature* **2003**, *426* (6968), 884-890.

4. Discher, D. E.; Eisenberg, A., Polymer Vesicles. *Science* **2002**, *297* (5583), 967.

5. Allen, T. M.; Cullis, P. R., Liposomal drug delivery systems: From concept to clinical applications. *Adv Drug Deliv Rev* **2013**, *65* (1), 36-48.

6. Allen, T. M.; Cullis, P. R., Drug Delivery Systems: Entering the Mainstream. *Science* **2004**, *303* (5665), 1818.

7. Adams, M. L.; Lavasanifar, A.; Kwon, G. S., Amphiphilic block copolymers for drug delivery. *J. Pharm. Sci.* **2003**, *92* (7), 1343-1355.

8. Biswas, S.; Kumari, P.; Lakhani, P. M.; Ghosh, B., Recent advances in polymeric micelles for anti-cancer drug delivery. *Eur. J. Pharm. Sci.* **2016**, *83* (Supplement C), 184-202.

9. Kataoka, K.; Harada, A.; Nagasaki, Y., Block copolymer micelles for drug delivery: Design, characterization and biological significance. *Adv. Drug Deliv. Rev.* **2012**, *64*, 37-48.

10. Cheng, C.; Qi, K.; Khoshdel, E.; Wooley, K. L., Tandem Synthesis of Core−Shell Brush Copolymers and Their Transformation to Peripherally Cross-Linked and Hollowed Nanostructures. *J. Am. Chem. Soc.* **2006**, *128* (21), 6808-6809.

11. Ievins, A. D.; Moughton, A. O.; O'Reilly, R. K., Synthesis of Hollow Responsive Functional Nanocages Using a Metal–Ligand Complexation Strategy. *Macromolecules* **2008**, *41* (10), 3571-3578.

12. Moughton, A. O.; O'Reilly, R. K., Noncovalently Connected Micelles, Nanoparticles, and Metal-Functionalized Nanocages Using Supramolecular Self-Assembly. *J. Am. Chem. Soc.* **2008**, *130* (27), 8714-8725.

13. Gallou, F.; Isley, N. A.; Ganic, A.; Onken, U.; Parmentier, M., Surfactant technology applied toward an active pharmaceutical ingredient: more than a simple green chemistry advance. *Green Chem.* **2016**, *18* (1), 14-19.

14. Klingelhöfer, S.; Heitz, W.; Greiner, A.; Oestreich, S.; Förster, S.; Antonietti, M., Preparation of Palladium Colloids in Block Copolymer Micelles and Their Use for the Catalysis of the Heck Reaction. *J. Am. Chem. Soc.* **1997**, *119* (42), 10116-10120.

15. Israelachvili, J. N.; Mitchell, D. J.; Ninham, B. W., Theory of self-assembly of hydrocarbon amphiphiles into micelles and bilayers. *J. Chem. Soc., Faraday Trans.* **1976**, *72* (0), 1525-1568.

16. Israelachvili, J. N.; Marčelja, S.; Horn, R. G., Physical principles of membrane organization. *Q. Rev. Biophys.* **1980**, *13* (2), 121-200.

17. Fong, C.; Le, T.; Drummond, C. J., Lyotropic liquid crystal engineering–ordered nanostructured small molecule amphiphile self-assembly materials by design. *Chem. Soc. Rev.* **2012**, *41* (3), 1297-1322.

18. Mai, Y.; Eisenberg, A., Self-assembly of block copolymers. *Chem. Soc. Rev.* **2012**, *41* (18), 5969-5985.

19. Riess, G., Micellization of block copolymers. *Prog. Polym. Sci.* **2003**, *28* (7), 1107-1170.

20. Darling, S. B., Directing the self-assembly of block copolymers. *Prog. Polym. Sci.* **2007**, *32* (10), 1152-1204.

21. Bates, F. S.; Fredrickson, G., Block copolymers-designer soft materials. *Physics today* **2000**, *52*.

22. Williams, R. J.; Pitto-barry, A.; Kirby, N.; Dove, A. P.; Reilly, R. K. O., Cyclic Graft Copolymer Unimolecular Micelles: E ff ects of Cyclization on Particle Morphology and Thermoresponsive Behavior. *Macromolecules* **2016**.

23. Zhang, L.; Eisenberg, A., Multiple Morphologies and Characteristics of "Crew-Cut" Micelle-like Aggregates of Polystyrene-b-poly(acrylic acid) Diblock Copolymers in Aqueous Solutions. *J. Am. Chem. Soc.* **1996**, *118* (13), 3168-3181.

24. Shen, H.; Eisenberg, A., Block Length Dependence of Morphological Phase Diagrams of the Ternary System of PS-b-PAA/Dioxane/H2O. *Macromolecules* **2000**, *33* (7), 2561-2572.

25. Figg, C. A.; Carmean, R. N.; Bentz, K. C.; Mukherjee, S.; Savin, D. A.; Sumerlin, B. S., Tuning Hydrophobicity To Program Block Copolymer Assemblies from the Inside Out. *Macromolecules* **2017**, *50* (3), 935-943.

26. Yamamoto, Y.; Yasugi, K.; Harada, A.; Nagasaki, Y.; Kataoka, K., Temperature-related change in the properties relevant to drug delivery of poly (ethylene glycol)–poly (d, l-lactide) block copolymer micelles in aqueous milieu. *J Control Release* **2002**, *82* (2-3), 359-371.

27. Foster, J. C.; Varlas, S.; Couturaud, B.; Jones, J. R.; Keogh, R.; Mathers, R. T.; O'Reilly, R. K., Predicting Monomers for Use in Polymerization-Induced Self-Assembly. *Angew. Chem. Int. Ed.* **2018**, *57* (48), 15733-15737.

28. Choucair, A.; Eisenberg, A., Control of amphiphilic block copolymer morphologies using solution conditions. *Eur. Phys. J. E* **2003**, *10* (1), 37-44.

29. Zhang, L.; Eisenberg, A., Thermodynamic vs Kinetic Aspects in the Formation and Morphological Transitions of Crew-Cut Aggregates Produced by Self-Assembly of Polystyrene-b-poly(acrylic acid) Block Copolymers in Dilute Solution. *Macromolecules* **1999**, *32* (7), 2239-2249.

30. Cui, H.; Chen, Z.; Zhong, S.; Wooley, K. L.; Pochan, D. J., Block Copolymer Assembly via Kinetic Control. *Science* **2007**, *317* (5838), 647.

31. Oerlemans, C.; Bult, W.; Bos, M.; Storm, G.; Nijsen, J. F. W.; Hennink, W. E., Polymeric Micelles in Anticancer Therapy: Targeting, Imaging and Triggered Release. *Pharm. Res.* **2010**, *27* (12), 2569-2589.

32. Nakamura, K.; Endo, R.; Takeda, M., Surface properties of styrene–ethylene oxide block copolymers. *J. Polym. Sci., Polym. Phys. Ed.* **1976**, *14* (7), 1287-1295.

33. Kidd, B. E.; Li, X.; Piemonte, R. C.; Cooksey, T. J.; Singh, A.; Robertson, M. L.; Madsen, L. A., Tuning Biocompatible Block Copolymer Micelles by Varying Solvent Composition: Dynamics and Populations of Micelles and Unimers. *Macromolecules* **2017**, *50* (11), 4335-4343.

34. Li, X.; Cooksey, T. J.; Kidd, B. E.; Robertson, M. L.; Madsen, L. A., Mapping Coexistence Phase Diagrams of Block Copolymer Micelles and Free Unimer Chains. *Macromolecules* **2018**, *51* (20), 8127-8135.

35. Batrakova, E.; Lee, S.; Li, S.; Venne, A.; Alakhov, V.; Kabanov, A., Fundamental Relationships Between the Composition of Pluronic Block Copolymers and Their Hypersensitization Effect in MDR Cancer Cells. *Pharm. Res.* **1999**, *16* (9), 1373-1379.

36. Batrakova, E. V.; Li, S.; Li, Y.; Alakhov, V. Y.; Elmquist, W. F.; Kabanov, A. V., Distribution kinetics of a micelle-forming block copolymer Pluronic P85. *J Control Release* **2004**, *100* (3), 389-397.

37. Panova, I. G.; Spiridonov, V. V.; Kaplan, I. B.; Trubinov, S. S.; Elizova, N. V.; Melnichenko, A. A.; Orekhov, A. N.; Yaroslavov, A. A., Inhibitory effect of polyethylene oxide and polypropylene oxide triblock copolymers on aggregation and fusion of atherogenic low density lipoproteins. *Biochem.-Moscow* **2015**, *80* (8), 1057-1064.

38. Pettersson, E.; Topgaard, D.; Stilbs, P.; Söderman, O., Surfactant/Nonionic Polymer Interaction. A NMR Diffusometry and NMR Electrophoretic Investigation. *Langmuir* **2004**, *20* (4), 1138-1143.

39. Frise, A. E.; Pagès, G.; Shtein, M.; Pri Bar, I.; Regev, O.; Furó, I., Polymer Binding to Carbon Nanotubes in Aqueous Dispersions: Residence Time on the Nanotube Surface As Obtained by NMR Diffusometry. *J. Phys. Chem. B* **2012**, *116* (9), 2635-2642.

40. Ulrich, K.; Galvosas, P.; Kärger, J.; Grinberg, F., Effects of Self-Assembly on Diffusion Mechanisms of Triblock Copolymers in Aqueous Solution. *Phys. Rev. Lett.* **2009**, *102* (3), 037801.

41. Thieu, L. M.; Zhu, L.; Korovich, A. G.; Hickner, M. A.; Madsen, L. A., Multiscale Tortuous Diffusion in Anion and Cation Exchange Membranes. *Macromolecules* **2019**, *52* (1), 24-35.

42. Wilmsmeyer, K. G.; Li, X.; Madsen, L. A., Anisotropic viscoelasticity and molecular diffusion in nematic wormlike micelles. *Liq. Cryst.* **2018**, *45* (6), 844-856.

43. Kidd, B. E.; Forbey, S. J.; Steuber, F. W.; Moore, R. B.; Madsen, L. A., Multiscale Lithium and Counterion Transport in an Electrospun Polymer-Gel Electrolyte. *Macromolecules* **2015**, *48* (13), 4481-4490.

44. Bostwick, J. E.; Zanelotti, C. J.; Iacob, C.; Korovich, A. G.; Madsen, L. A.; Colby, R. H., Ion Transport and Mechanical Properties of Non-Crystallizable Molecular Ionic Composite Electrolytes. *Macromolecules* **2020**, *53* (4), 1405-1414.

45. Yamamoto, T.; Yokoyama, M.; Opanasopit, P.; Hayama, A.; Kawano, K.; Maitani, Y., What are determining factors for micelle carriers? Consideration stable drug incorporation into polymeric on physical and chemical characters of the micelle inner core. *J Control Release* **2007**, *123* (1), 11-18.

46. Yan, Q.; Yuan, J. Y.; Yuan, W. Z.; Zhou, M.; Yin, Y. W.; Pan, C. Y., Copolymer logical switches adjusted through core-shell micelles: from temperature response to fluorescence response. *Chem. Comm.* **2008**, (46), 6188-6190.

47. Foster, J. C.; Carrazzone, R. J.; Spear, N. J.; Radzinski, S. C.; Arrington, K. J.; Matson, J. B., Tuning H_2S Release by Controlling Mobility in a Micelle Core. *Macromolecules* **2019**, *52* (3), 1104-1111.

48. FOX, T., Influence of Diluent and Copolymer Composition on the Glass Temperature of a Polymer System. *Bull. Am. Phys. Soc.* **1956**, *1*, 123.

49. Saby-Dubreuil, A. C.; Guerrier, B.; Allain, C.; Johannsmann, D., Glass transition induced by solvent desorption for statistical MMA/nBMA copolymers — Influence of copolymer composition. *Polymer* **2001**, *42* (4), 1383-1391.

50. Yamauchi, K.; Lizotte, J. R.; Long, T. E., Thermoreversible Poly(alkyl acrylates) Consisting of Self-Complementary Multiple Hydrogen Bonding. *Macromolecules* **2003**, *36* (4), 1083-1088.

51. Tsui, O. K. C.; Wang, X. P.; Ho, J. Y. L.; Ng, T. K.; Xiao, X., Studying Surface Glass-to-Rubber Transition Using Atomic Force Microscopic Adhesion Measurements. *Macromolecules* **2000**, *33* (11), 4198-4204.

52. Min, K.; Kwon Oh, J.; Matyjaszewski, K., Preparation of gradient copolymers via ATRP in miniemulsion. II. Forced gradient. *J. Polym. Sci., Part A: Polym. Chem.* **2007**, *45* (8), 1413-1423.

53. Chen, J.; Spear, S. K.; Huddleston, J. G.; Rogers, R. D., Polyethylene glycol and solutions of polyethylene glycol as green reaction media. *Green Chem.* **2005**, *7* (2), 64-82.

54. Levitt, M. H., *Spin Dynamics*. John Wiley and Sons Ltd.: England, 2008; Vol. 2.

55. Dai, J.; Alaei, Z.; Plazzotta, B.; Pedersen, J. S.; Furó, I., Release of Solubilizate from Micelle upon Core Freezing. *J. Phys. Chem. B* **2017**, *121* (45), 10353-10363.

56. Doncom, K. E. B.; Pitto-Barry, A.; Willcock, H.; Lu, A.; McKenzie, B. E.; Kirby, N.; O'Reilly, R. K., Complementary light scattering and synchrotron small-angle X-ray scattering studies of the micelle-to-unimer transition of polysulfobetaines. *Soft Matter* **2015**, *11* (18), 3666-3676.

Chapter 6: Quantification of oleic acid dynamics and kinetics to understand ligand interactions on PbS quantum dot surfaces

This chapter is in preparation and will be submitted for publication with the following co-authors: *Veera Venkata Shravan Uppala[1], Jennica E. Kelm[2], Christian Y. Dones Lassalle[2], Jillian L. Dempsey[2], and Louis A. Madsen[1]*

Abstract

Semiconductor quantum dots (QDs) exhibit unique quantum confinement effects, making them promising materials for various applications. These QDs are typically stabilized by surface-bounds ligands such as oleic acid (OAH). This study presents precise quantification of the thermodynamics (equilibrium constants and energetics) and kinetics (exchange rates) of OAH ligand binding to the QD surfaces. By utilizing the alkenyl proton on OAH as a unique marker in ^{1}H NMR spectroscopy and diffusion measurements, we accurately quantified ligand population fractions in different states. Our quantification analysis revealed the existence of a third ligand state in addition to bound and free ligands, when excess of free OAH was titrated to oleate (OA)-capped PbS QD solution. This suggests a more complex ligand binding mechanism than the previously accepted two-state model. Through temperature and concentration variations, we quantified the energetics of different ligand binding motifs to the PbS QD surface. Additionally, using dynamic NMR and a complete lineshape equation, we determined rapid exchange rates ($<$ 1 ms) between surface-bound and solution-state ligands. By combining these NMR techniques, we identify two distinct ligand binding motifs and elucidated their binding energetics. These findings have the potential to enable precise tuning of QD properties, significantly influencing the innovation of next-generation materials for their optoelectronic applications.

6.1. Introduction

Semiconductor quantum dots (QDs) have garnered significant attention since their discovery due to their remarkable size-tunable photoelectronic properties. These nanoscale crystals have been extensively investigated for their potential in diverse applications, including photovoltaic cells, light emitting diodes (LEDs), and biological imaging.[1,2] The unique characteristics of QDs, particularly their optical and electronic properties, stem from quantum confinement effects and can be precisely tailored by adjusting the size of the particle. However, the successful integration of QDs into optoelectronic devices relies strongly on the nature of their surface, a consequence of their high surface-to-volume ratio. The surface composition and passivation significantly influence optical and electronic properties of QDs, driving extensive research into QD surface chemistry.[3–8] Understanding and optimizing surface properties are crucial for improving QD performance in technological applications.

Understanding the QD surface requires knowledge of the inorganic crystal lattice, the organic ligand shell, and the interface of these two components. The inorganic component of the QD can vary in crystal structure, faceting, and morphology.[3,6,9–11] Additionally, the surface ions may vary in oxidation state and coordination number. The organic ligands that interface with surface ions vary in binding motif as defined by Green's covalent bond classification and by coordination geometry, which influences the binding energy between the ligand and surface. Green's covalent bond classification classifies ligands as either X-type, L-type or Z-type.[12,13] X-type ligands are anionic and compensate for excess cationic charge by donating one electron to the surface metal cation. L-type ligands are neutral two electron donors and generally do not impact the QD charge. Z-type ligands are two-electron accepting species and coordinate to surface

chalcogen anions. Each ligand classification can participate in unique reactivity with the QD surface, and X-type exchange is the reaction of interest in this work.

Ligand exchange reactions, commonly employed to alter QD solubility or functionality of the QD surface, can vary depending on the surface anchoring group and chain length. The simplest example of ligand exchange is that between ligands with the same binding group (e.g. a carboxylate). When the exchange ligand and the native ligand differ in binding group, complex and potentially multi-mechanism exchange reactions can result.[14] Controlled tunability of the QD surface requires both a mechanistic understanding of ligand exchange, and a quantitative technique to monitor the process. Several studies have utilized techniques like photoluminescence spectroscopy, ^{1}H NMR spectroscopy, Nuclear Overhauser effect spectroscopy (NOESY)[15–18] to monitor reactivity and decipher reaction mechanisms. ^{1}H NMR spectroscopy is arguably the most popular technique to extrapolate quantitative surface reactivity due to the unique line shape of ligands bound to the QD surface.[13,19–23]

In most ligand exchange mechanisms, the exchange between the native and the exchanging ligands is assumed to rely on a two-component system where ligands are exclusively bound to the surface or freely diffusing in solution.[14,21,24,25] In this scenario, the exchange proceeds with a one step process. However, a few studies have found evidence for a third state beyond the classically defined bound and free states.[26–30] In 2010, work by Fritzinger et al. proposed a two-step exchange mechanism where free/exchanging ligands are "physisorbed" to the QD surface before "chemisorption" to replace the native ligand.[28] Others have found evidence for a third state beyond the classically defined bound and free states including work by Weir and coworkers.[6,26–31] In 2019, Weir and coworkers found greater than monolayer coverage of oleic acid on PbS QDs with small-

angle X-ray and neutron scattering suggesting the presence of physisorbed ligands.[27] The following year, Liu et al. utilized a suite of spectroscopic techniques to propose a "two-step ligand exchange", and related the physisorption of ligands to Van der Waals interactions.[29]

It has become evident that ligand exchange at the QD surface is more nuanced than a two-state model describing only bound and free ligands. In order to explore the limited understanding of ligand association and exchange, we elected to study oleate (OA) capped PbS QDs. (**Figure 6.1)**. Quantifying ligand exchange rates and their population fractions in various states (both free in solution and bound to the QD surface) facilitates understanding of the energetics (thermodynamics) of the ligand-binding mechanism. Quantifying energetic parameters establishes a basis to innovate next-generation materials for diverse applications. By employing multimodal NMR methods, thermodynamic parameters can be precisely quantified.

In this study, we employ ^{1}H NMR diffusometry and spectroscopy to examine the dynamics of OA-capped PbS QDs. Through this, we identify three different subpopulations of ligands (free, bound, and adsorbed), and quantify the fractions of each subpopulation within our QD samples.

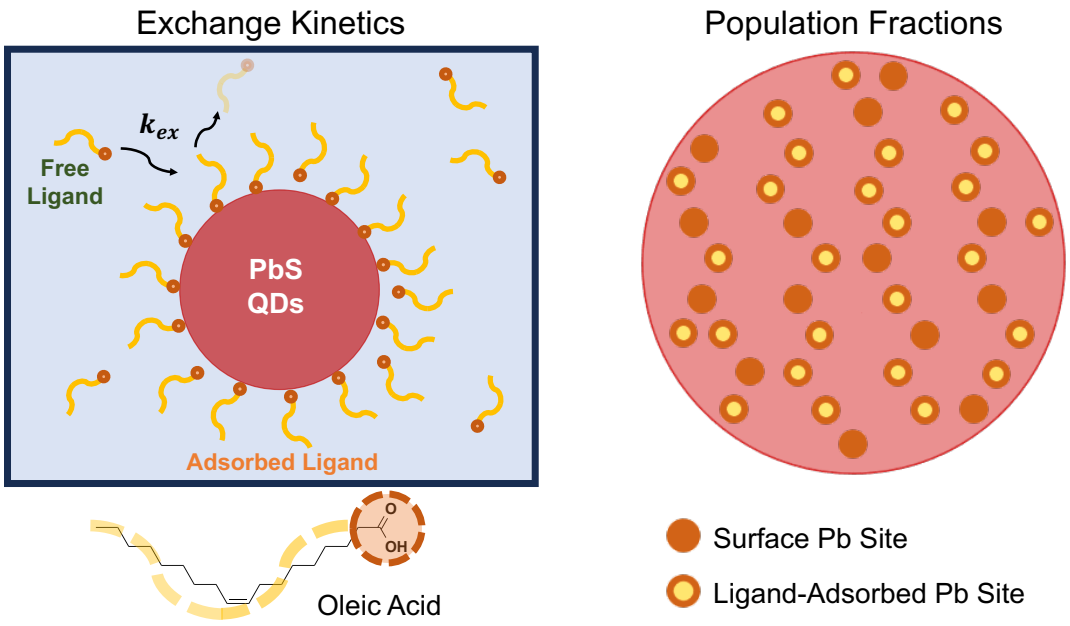

Figure 6.13: Solution and surface studies of oleic acid (OA) capped PbS QDs by NMR. Quantifying ligand exchange rates and population fractions of OA ligands in different states by NMR reveals the energetics and dynamics of ligand binding mechanism and provides valuable insights toward developing next-generation QD -based materials.

We further quantify the equilibrium constants for ligand-QD association and determine their standard enthalpy and entropy changes to further understand ligand binding mechanisms. We also study the exchange kinetics of ligands between each state to further understand the QD surface-ligand transient interactions and dynamics by employing a Dynamic NMR technique, broadening our understanding on the exchange mechanism. Our results expand the knowledge of thermodynamics and kinetics of ligand binding and exchange processes, allowing more informed modification of QD surfaces to desired optoelectronic or catalytic properties for targeted applications. The employed NMR methodologies can be implemented on many common NMR spectrometers and on many chemical functionalities, enabling wide accessibility to understand diverse QD-ligand interactions.

6.2. Experimental

6.2.1. General solvent and starting material considerations

Solvents, including toluene, acetone, and pentane which are used for purification of QDs and for UV-visible and NIR absorbance measurements, were purchased from VWR. Toluene-d_8 was purchased from Cambridge Isotope Laboratories. Lead (II) oxide (99.999%), oleic acid (OA) (90%), 1-octadecene (ODE) (90%) and ferrocene (98%) were purchased from Sigma-Aldrich and used as received. Bis(trimethylsilyl) sulfide ($(TMS)_2S$) (≥98%) was purchased from Sigma-Aldrich and stored under N_2.

6.2.2. Synthesis and purification of PbS QDs

Standard Schlenk line techniques were used for maintaining inert conditions during the PbS QDs synthesis. A modified version of the procedure established by Hines and Scholes was followed.[32] Lead (II) oxide (0.91 g, 4 mmol), oleic acid (OA) (2.54 mL, 8 mmol), and ODE (35.5 mL) were combined in a 100 mL three-neck round-bottom flask and stirred under vacuum at 100 ºC for 2.5 h. The mixture was then heated to 120 ºC under a N_2 atmosphere to yield a clear, colorless solution.

Next, $(TMS)_2S$ (0.42 mL, 2 mmol) and ODE (5 mL) were combined in a 25 mL pear-shaped flask under inert atmosphere. The $(TMS)_2S$ solution was injected swiftly into the $Pb(oleate)_2$ solution at 125 ºC. The reaction proceeded at 123 ºC for 2.5 min, turning dark brown as it continued. The reaction flask was removed from the heating mantle, and the QD solution was quenched by submerging first in a room-temperature oil batch for 3 min followed by an ice batch for 4 min. Three milliliter aliquots of the reaction mixture were transferred to centrifuge tubes,

diluted with 1 mL of toluene, precipitated with 9 mL of acetone, and centrifuged at 9000 rpm for 10 min.

After decanting the supernatant, the QDs were resuspended in 4 mL of pentane, precipitated by adding 4 mL methanol and 4 mL acetone, and centrifuged at 10,600 rpm for 10 min. Four more total precipitation-centrifugation cycles were carried out with alternating 2 mL pentane or toluene, 8 mL acetone for the first two steps and 6 mL acetone for the last two. The PbS QDs were isolated from pentane by evaporation, yielding 0.9967 g of QDs.

6.2.3. ^{1}H NMR spectroscopy for titrations

Samples for ^{1}H NMR spectroscopy were prepared by determining the concentration of a PbS QD stock solution in toluene-d_8 after measuring the absorbance of 10 mL of PbS QD stock solution in 3.0 mL of toluene. A predetermined volume of stock solution was diluted with toluene-d_8 to obtain a concentration of 150 mM QDs in 590 mL. An internal standard solution of ferrocene was prepared by dissolving a precise amount (ca. 10 mg in 1.0 mL of toluene-d_8) and 10 μL of this solution added to each NMR tube. A precise solution of OA in toluene-d_8 was then prepared and additions of 50 (7.3 mM), 100 (14.3 mM) and 200 (27.2 mM) equivalents per QD particle were added to the NMR tubes. All samples were prepared in inert N_2 conditions. Four 1 mm capillaries were added to each NMR tube to prevent artifacts in diffusion measurements due to thermal convection. All samples were flame sealed to preserve the inertness and ensure the longevity of the sample.

All ^{1}H NMR measurements were made on a 600 MHz Bruker Avance III spectrometer equipped with a 5 mm TCI Prodigy cryoprobe (^{1}H inner coil). All measurements were acquired

over a temperature range of - 10 to + 23 °C. For quantitative (q-NMR) measurements, 8 scans with 15° pulse angle and a very long relaxation delay of 100 s between each were used. This is because ferrocene in inert conditions have a very long spin-lattice relaxation time (T_1). More details on the choice of parameters are explained in the **SI section 6**. This will ensure that >99.9% signal is recovered for each scan enabling accurate quantification. All spectra were processed using MNova and the multipeak fitting function was used to integrate the alkenyl peaks in the ^{1}H NMR to determine the concentration of bound and unbound ligands.

6.2.4. 1H Pulsed-field-gradient (PFG) NMR diffusometry

All NMR diffusometry experiments were performed using a 400 MHz Bruker Avance III WB NMR spectrometer equipped with a ^{1}H 5 mm coil coupled to a diff50 single-axis (z-axis) gradient system. We employed pulsed-field-gradient stimulated echo (PGSTE) sequence to measure the diffusion coefficients of ligand species present in different states of the solution. In this experiment, the signal intensity I for each distinct peak observed in ^{1}H NMR spectroscopy, is measured as a function of gradient strength (g). This acquired intensity I is given by the Stejskal-Tanner equation[34–36]

$$I = I_0 \mathrm{e}^{-\gamma^2 g^2 \delta^2 \left(\Delta - \frac{\delta}{3}\right) D} = I_0 e^{-bD} \qquad (6.1)$$

where I_0 is signal amplitude at $g = 0$, γ is gyromagnetic ratio, δ is effective gradient pulse length, Δ is diffusion time between gradient pulses, and D is self-diffusion coefficient. The "b" factor, representing all the known NMR-specific parameters and useful for quantifying diffusion behaviors, is given by $b = \gamma^2 g^2 \delta^2 (\Delta - \delta/3)$. The sequence was used with a 90° RF pulse length of 4.5 µs, and with effective gradient pulse length of 1 ms. The diffusion time Δ was set to 25 ms.

The maximum gradient strength (g_{max}) was varied from 60-400 G. cm^{-1} to achieve more than 95% of signal attenuation in 8-16 steps. Faster diffusing species require smaller g_{max} and slower diffusing species require larger g_{max}. A sufficient signal-to-noise ratio (SNR) was achieved with 64-256 scans and acquisition times of 0.2-2 s depending on the chemical species probed (longer acquisition time for solvent molecules).

Spin-lattice relaxation time (T_1) measurements using the inversion-recovery sequence and the same RF pulse lengths as above yield T_1 values for bound and free ligand of 0.85 s and for ferrocene it is 30 s. A modified CPMG pulse sequence was used (see **Appendix II 6S9** for more details) to compensate J-modulation effects and get accurate spin-spin relaxation times T_2 for ligands and toluene molecules.[37] T_2 values for bound and free ligands are listed in the **Table 6S6** in **Appendix II**. The parameters used for PGSTE experiments, as mentioned above, did not produce any significant differential signal intensity component weighting (including in two-component fits, see below in **Figure 6.2**) due to T_1 and T_2 spin relaxation variations.

Relaxation delay times of 2 s was used between each scan while probing ligand signals and a relaxation delay of 6 s was used for solvent toluene-d_8 signal to get sufficient SNR to measure their respective diffusion coefficients. 2 Hz line broadening was applied during data processing to reduce excessive acquisition noise. All NMR experiments were also performed at variable temperatures ranging from -10 ± 1°C to room temperature 23 ± 1°C to observe the changes in thermodynamics and kinetics of ligand associations with QD particles.

6.3. Results and discussion

6.3.1 Evidence for associated ligands by ^{1}H NMR and NMR diffusometry techniques

To initially understand the molecular structure of the oleate (R-COO$^-$, OA) ligand and its role in binding to PbS QDs, we first examine the ^{1}H NMR spectra of free oleic acid (R-COOH, OAH) ligand in toluene-d_8 (**Figure 6.2A**). The OAH shows a distinct alkenyl proton handle, ν_{free} (chemical shift of OAH), near 5.6 ppm that is well resolved from the toluene-d_8 solvent peak at around 7 ppm and from the other alkyl proton signals of OAH below 2.4 ppm. This well-resolved ν_{free} signal provides a clear "handle" for studying the dynamics of the ligand. For absolute quantification, we added ferrocene as an inert internal standard at a known concentration (as described in the Experimental section), which gives a well-separated peak at 4.1 ppm (**Figure 6.2A**). The alkenyl proton signal from the OAH has a full width at half maximum ($FWHM$) of 7 Hz (**Figure 6.2B**, black trace), which is characteristic of a small molecule undergoing rapid tumbling in the solvent.

We also examined a control sample containing 150 μM PbS QDs capped with oleate (OA) ligands in toluene-d_8. In this case, the alkenyl proton signal of the QD-bound OA ligand (ν_{bound}) shifts downfield to $5.8\ ppm$ due to an aromatic solvent-induced shift (ASIS)[38], as shown by the red trace in **Figure 6.2B**. This shift occurs because the aromatic solvent is excluded from the ligand shell, meaning the alkene protons of the QD-bound OA do not experience the same aromatic environment as those of full solvated free OAH ligand. Additionally, the ν_{bound} signal broadened with $FWHM = 60$ Hz. This broadening is attributed to homogeneous line broadening in the NMR spectrum, which results from the restricted motion of the QD-bound OA ligands in the solution.

When free oleic acid (OAH, 7.5 mM) was titrated into the OA-capped PbS QD solution, we observed two broad alkenyl proton signals in the range of 5.5 – 6 ppm (**Figure 6.2B**, blue trace). The first broad signal at 5.78 ppm, with $FWHM = 60$ Hz (**Figure 6.2C**), can be characterized as QD-bound OA ligand, as its chemical shift and width matches the QD-bound OA signal (ν_{bound}) from the control sample (**Figure 6.2B**, red trace). The second broad signal appears at $5.68\ ppm$, which is positioned between the chemical shifts QD-bound OA ($5.78\ ppm$) and free OAH ($5.58\ ppm$). Therefore, we refer to this as an "intermediate" signal for now. Peak deconvolution (**Figure 6.2C**) shows that this intermediate signal has a $FWHM = 43$ Hz, which is broader than the free OAH signal (7 Hz) but narrower than the bound OA ligand signal (60 Hz).

As we increased the titration concentration of free OAH ligands (7.5 mM, 15 mM, and 30 mM), this intermediate signal shifted up-field from $5.68\ ppm$ to $5.62\ ppm$, approaching the chemical shift of free ligand signal ($\nu_{free} = 5.58\ ppm$). Additionally, the signal width narrowed from 43 Hz to 33 Hz (see **Figure 6S3** in **Appendix II section 3**). This concentration-dependent shift indicates that the intermediate signal is influenced by the amount of free OAH ligands. This behavior can be explained by Rogers and Woodbrey model [39] for a system undergoing exchange between two distinct states (further discussion on the model in **Section 6.4** of **Results and Discussion**).

The intermediate signal's chemical shift and width, lying between those of QD-bound OA and free OAH ligands, suggests that it arises due to a fast exchange between two states. If the exchange between bound and free ligands were rapid on the NMR timescale exchanging compared to NMR time scale (concepts of NMR time scale explained in detail in **Appendix II Section 1**), the two peaks would coalesce into one peak (**Figure 6S7**). Instead, we observe a gradual up-field shift of the intermediate signal as more OAH is titrated, while the chemical shift and width of the

QD-bound OA signal remain unchanged. This indicates that the exchange between QD-bound OA and free OAH is much slower than the NMR time scale of measurement, ($\tau_{ex,bind} \gg 3.9\ ms$, see Section 1 for NMR timescale discussion).

Rather than a single-step exchange between QD-bound OA and free OAH, we find evidence for a multi-exchange mechanism consistent with prior studies suggesting such processes [references]. Since the QD-bound OA ligands do not participate in the observed rapid exchange, this exchange must occur between free OAH and QD-associated (i.e. physisorbed 3rd state) ligands. Therefore, we attribute this intermediate signal to the rapid exchange between QD-associated and free OAH ligands, whose chemical shift (ν_{ex}) depends on the concentration of free OAH ligands.

The concepts for the spectral change dependency with the exchange rate and the timescale of NMR measurements is explained more detail in **Appendix II section 8**. 1D ^{1}H NMR spectroscopy allows us to qualitatively estimate the exchange rates of the system. However, the fast exchange rate between the free and QD-associated OAH ligands was accurately quantified, and the quantification details are explained in **section 4** of **Results and discussion**.

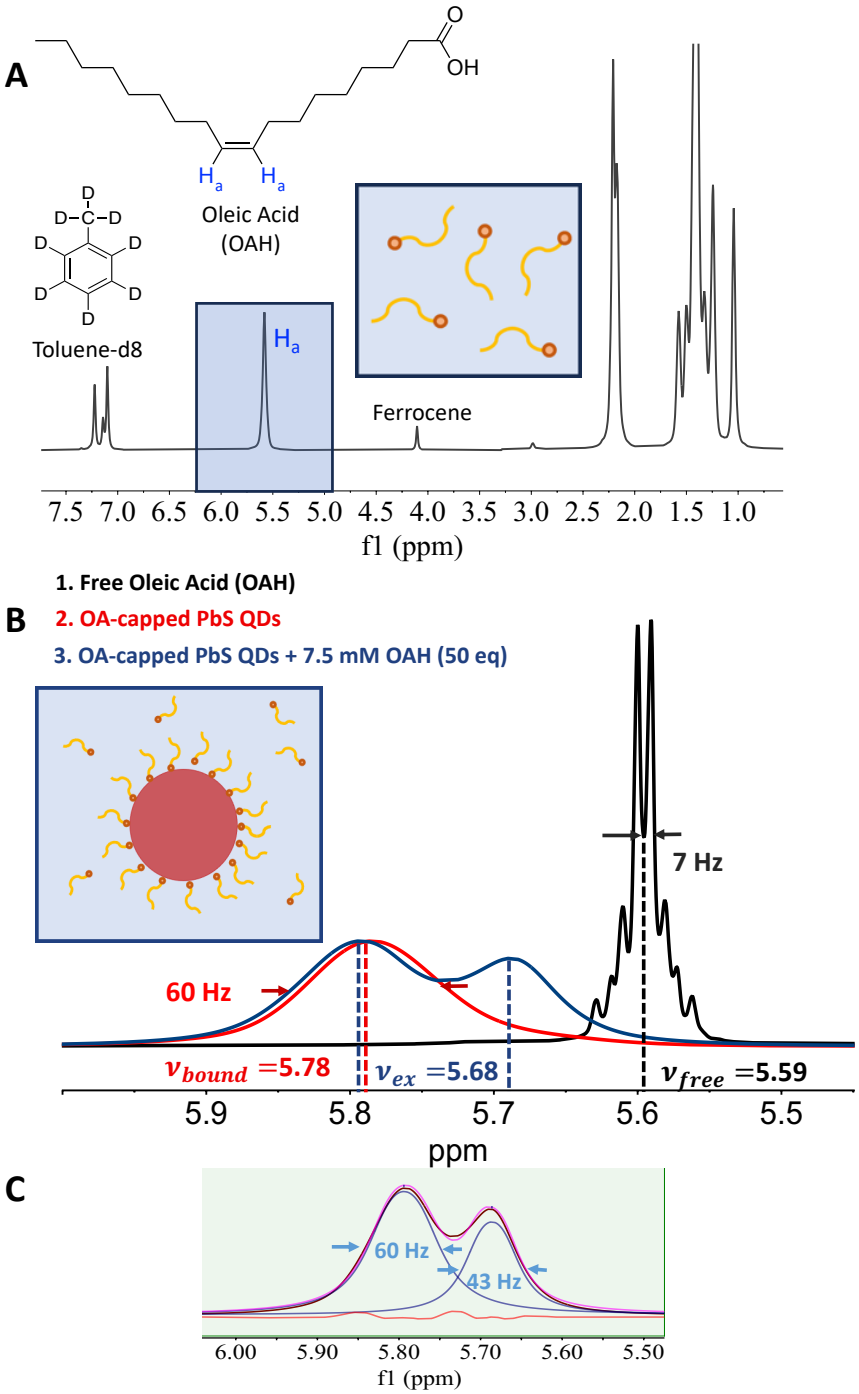

Figure 6.14: **A**. ^{1}H NMR spectrum of free oleic acid (OAH) in toluene-d_8 solvent with ferrocene as inert internal standard. The signals for the alkenyl protons of OAH (H_a) and ferrocene are well resolved from other signals enabling clear study of these species. **B**. The ^{1}H NMR spectrum of free OAH (black trace, 1), QD-bound OA (red trace, 2) and 7.5 mM OAH titrated into the OA-capped PbS QD solution (blue trace, 3) with their chemical shifts and FWHM of each signal. **C**. Deconvoluted ^{1}H NMR spectrum of 3rd sample (blue trace) using MNova to get FWHM of the signals

To further confirm the fast exchange between free and QD-*associated* OAH ligands, we employed NMR diffusometry with the PGSTE pulse sequence to probe the Brownian motion of the ligands in different states. As expected, free OAH at 5.6 ppm (black trace) exhibited a faster diffusion coefficient, D_{free}= $7.1 \times 10^{-10} m^2 \cdot s^{-1}$, compared to QD-bound OA at 5.8 ppm, which had a much slower diffusion coefficient, $D_{bound} = 1.3 \times 10^{-10}\ m^2 \cdot s^{-1}$, at 23□C. The slower diffusion of the QD-bound OA is due to the larger hydrodynamic diameter of the PbS QD particle to which OA is bound. Since the species being probed (free OAH and QD-bound OA) are in one diffusion environment, both sets of experimental data fit well with a single diffusion component as shown in **Figure 6.3**.

When excess of free OAH (7.5 mM to 30 mM) is titrated into a solution containing ligand-bound PbS QDs, the alkenyl proton signal proton shows two diffusion species as evidenced by the two dashed lines for all three titrated solutions (**Figure 6.3**). For each of these two-component Stejskal-Tanner (NMR signal intensity attenuation) plots, the slower diffusing species has diffusion coefficient equal to D_{bound} (dashed lines are parallel to ligand-bound QD sample's line) indicating these species are QD-bound OA ligands (see **Table 6.1**, values listed within errors). This experiment further suggests that the binding/unbinding of QD-bound OA ligands from the surface is very slow compared to the NMR diffusometry timescale of measurement, which is simply equal to the diffusion time Δ. There are no significant changes observed in the OA's alkenyl proton signal and dynamics when $\Delta = 200\ ms$, indicating the exchanging time for binding/unbinding of OA is $\tau_{ex,bind} > 200\ ms$. As the titration concentration increased from 7.5 mM to 30 mM, the diffusion coefficient of the faster species increased but were slower than D_{free} as shown in **Figure 6.3** and the values are reported in **Table 6.1**. Because this diffusion coefficient (D_{ex}) is in between entirely bound or entirely free ligands, this suggest that the signal arises from rapid exchange ($\tau_{ex} \ll \Delta$)

between QD-associated and free OAH ligands. With the direct evidence of three ligand states – bound, associated, and free – we sought to quantify the partition fraction of the ligand in each state.

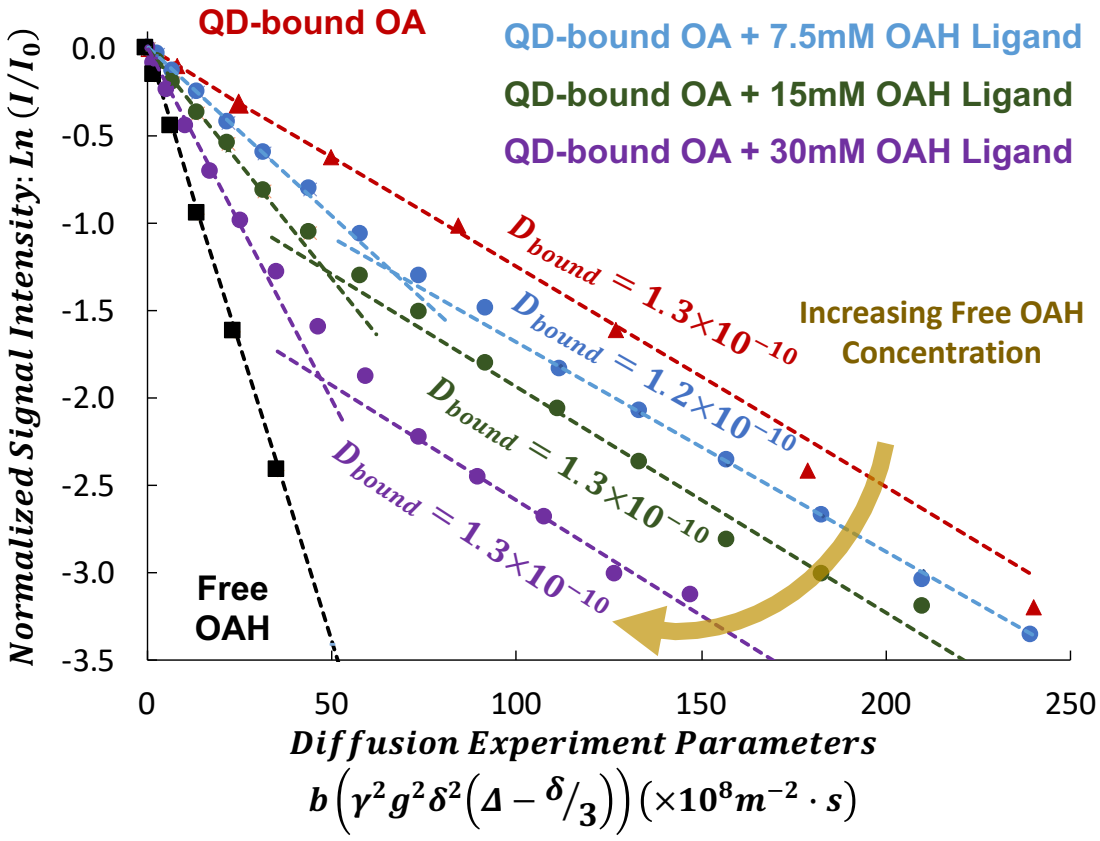

Figure 6.15: Variation in NMR signal attenuation of alkenyl proton signal of the ligand (integrated from 5.5 – 6 ppm) as a function of free OAH concentration titrated into solution containing oleate-capped PbS QDs measured at 23°C. b is the diffusometry experiment parameter, that contains all known NMR experimental parameters. The dashed lines provide a guide to the eye and represent single- or two-component diffusion coefficients (lines do not actual fit to experimental data). Increasing the titrated ligand concentration increased the D of faster diffusing species while D for slower diffusing species unchanged highlighting the very slow exchange for the ligand binding/unbinding process ($> 200\ ms$).

6.3.2. Quantifying partition fractions of ligands in different states using NMR diffusometry

The peak deconvolution (MNova) enabled us to determine the partition fraction of the bound (f_{bound}) and the exchanging (f_{ex}) signals in the spectrum with the constraint $f_{bound} +$

$f_{ex} = 1$. However, to further quantify the population fraction of free and QD-*associated* ligands in the solution, we used the measured diffusion coefficients of different ligand species (**Table 6.1**).

Since the observed D_{ex} is the weighted average of D_{free} and D_{assoc}, we can determine the population fractions of free (f_{free}) and of QD-associated (f_{assoc}) ligands using the equation

$$D_{ex} = \frac{f_{free}}{f_{ex}} \cdot D_{free} + \frac{f_{assoc}}{f_{ex}} \cdot D_{assoc} \tag{6.2}$$

The total population fraction is equal to exchange signal's population fraction ($f_{free} + f_{assoc} = f_{ex}$) since only free and QD-*associated* ligands contribute to the exchanging signal. Although QD-associated ligands have different chemical interactions with the QD surface compared to bound ligands (evident from the exchange rates with free ligands), it is reasonable to assume the unknown D_{assoc} is equal to the measured D_{bound} (**Table 6.1**) as they both represent the Brownian motion of the colloidal QD.

Since ν_{ex} depends on the population fraction and chemical shifts of QD-*associated* and free OA ligands in the solution, we can use **Equation 6.3** to determine the chemical shift of the QD-*associated* ligand ν_{assoc}

$$\nu_{ex} = \nu_{free} \cdot \frac{f_{free}}{f_{ex}} + \nu_{assoc} \cdot \frac{f_{assoc}}{f_{ex}} \tag{6.3}$$

The determined ν_{assoc}, determined for all three titration solutions (7.5 mM, 15mM, and 30 mM), equals ν_{bound} (see **Table 6S5** from **Appendix II**). This suggests that the probed alkenyl proton signal for bound, and QD-associated ligands have similar environment although the ligand interactions with the QD surface differ. This chemical similarity further supports $D_{assoc} = D_{bound}$ assumption. **Table 6.1** lists the population fraction and diffusion coefficients of ligands in the three distinct states for different titration concentrations of OA ligand. The above experimental

observations can be conceptually summarized in **Figure 6.4** illustrating the existence of ligands in three separate states that are constantly exchanging.

Table 6.1: Population fractions and diffusion coefficients of ligands in different states

Temperature (23°C)	Population Fractions of Ligands (%)				Diffusion Coefficients of Ligands ($\times 10^{-10}\ m^2/s$)			
Sample	f_{bound}	f_{ex}	f_{free}	f_{assoc}	D_{bound}	D_{ex}	D_{free}	D_{assoc}
QD	100	0.0	0.0	0.0	1.3 ± 0.1	0.0	0.0	1.3 ± 0.1
QD + 7.5mM OA	64	36	10	26	1.2 ± 0.1	2.9 ± 0.1	7.1 ± 0.1	1.2 ± 0.1
QD + 15mM OA	46	54	32	22	1.3 ± 0.1	4.7 ± 0.2	7.1 ± 0.1	1.3 ± 0.1
QD + 30 mM OA	31	69	51	18	1.3 ± 0.1	5.4 ± 0.3	7.1 ± 0.1	1.3 ± 0.1

f_{bound}, f_{ex} are from the bound and exchanging signals and the fractions are derived by deconvoluting the ^{1}H NMR spectrum. f_{free} and f_{assoc} are determined from **Equation 6.2** and the constraint $f_{free} + f_{assoc} = f_{ex}$. D_{free} is the diffusion coefficient of free ligands in solution and is the same in all samples because the concentrations in all samples are too low to change the viscosity of the solution. D_{bound} is the diffusion coefficient of bound ligands determined by probing the bound signal ν_{bound} at 5.78 ppm. D_{assoc} is the diffusion coefficient of QD-*associated* ligand and $D_{assoc} = D_{bound}$.

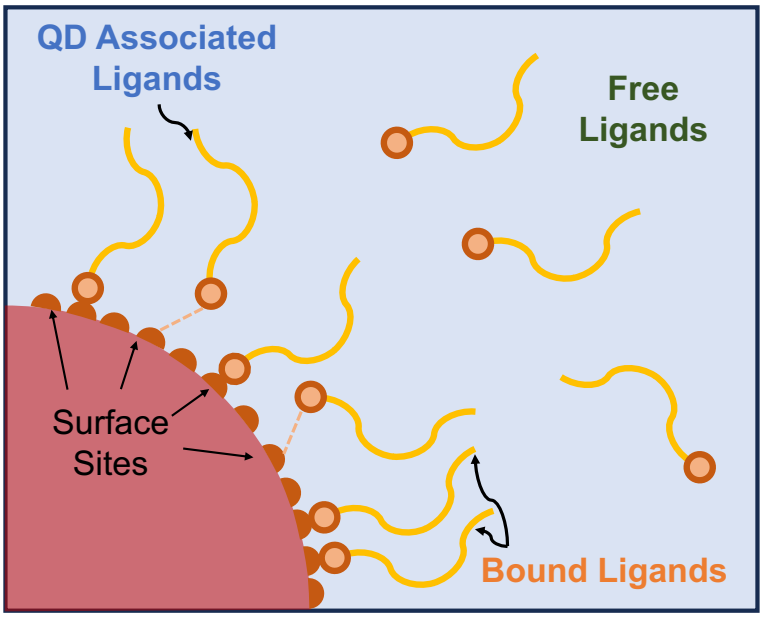

Figure 6.4: Illustration of Ligand-PbS QD association/binding. The free ligands exist in solvent along with bound and QD-*associated* state ligands on the surface of QD. QD-*associated* and bound ligands are assumed to have equal diffusion coefficients and chemical shifts (within errors) and the assumption is supported by **Equations 6.2** and **6.3**.

6.3.3. Ligand-QD exchange mechanism and model to predict equilibrium constants

As oleate (OA) capped PbS QDs are titrated with oleic acid (OAH), we assume that two processes occurring simultaneously. First, the free ligand weakly associates with an 'associated-site' (Pb metal) on QD surface forming a 'QD-*associated'* ligand. To confirm this weak association between the ligand and the surface Pb metal, we performed a control NMR diffusometry experiment using 1-octadecene (ODE), a molecule similar to OAH but lacks a carboxylic acid headgroup. Upon titrating an excess of ODE into the solution containing OA-capped PbS QDs, we observed no change diffusion coefficient of ODE in this solution compared to free ODE (see SI Section 2 for more details). This suggests that ligands association at the QD surface requires a head group, in this case, a carboxylic acid. Due to the weak nature of this association, a fast exchange ($\tau_{ex} < 3.9\ ms$) occurs between the free and QD-*associated* ligand, resulting in a fast-exchanging signal that appears ($5.68\ ppm$) between free OAH ($5.58\ ppm$) and QD-bound OA ($5.78\ ppm$) chemical shifts on ^{1}H NMR spectrum (see **Figure 6.2B**, blue trace).

Second, the free ligand also chemically binds with a 'bound site' (Pb metal) on QD surface forming a 'QD-bound' ligand. The exchange time between the bound and free ligands, however, is longer compared to NMR measurement timescale ($\tau_{ex,bind} \gg 3.9\ ms$). Hence, we observe an unchanged bound signal (both chemical shift and *FWHM*) in the NMR spectrum when excess of free OAH is titrated into the ligand-bound PbS QD solution.

We also tested our monolayer assumption measuring the particle size using NMR diffusometry. Using the Stokes-Einstein equation (**Equation 6S7**), we determined the size of OA-

capped PbS QD particle to be 5.6 nm. Notably, the particle size remain unchanged after titrating free OAH into the solution. From the NMR diffusometry, we measured the ligand shell to 1 nm thick, allowing us to estimate the PbS QD core size as 3.6 nm (within error, see **Table 6S2**). TEM measurements provided a QD particle diameter of 3 nm, which is in good agreement with the NMR data when accounting for experimental error. More details on the particle size determination from NMR are discussed in **Appendix II section 4**. These consistent measurements from NMR and TEM supports our theory of a single layer of ligands on the QD surface. Therefore, we applied Langmuir adsorption model[40] to determine the equilibrium constants for both free ⇌ associated and free ⇌ bound ligand exchange processes. The Langmuir model for ligand binding and association are defined as:

$$K_{assoc} = \frac{[Ligand - Associated\ Site]}{[Free\ Ligand][Total\ Associated\ Site]} \tag{6.4}$$

$$K_{bind} = \frac{[Ligand - Bound\ Site]}{[Free\ Ligand][Total\ Bound\ Sites]} \tag{6.5}$$

We define K_{assoc} and K_{bind} using concentrations rewritten as number of ligands (or sites) per QD. This simplifies molecular level interpretation of the quantities and only requires us to define the QD concentration equal to 1. With that consideration, $[Free\ Ligand]$ is defined as the average number of free ligands per QD in solution. $[Ligand - Bound\ Site]$ is defined as the average number of bound ligands per QD, and $[Ligand - Associated\ Site]$ is defined as the average number of QD-*associated* ligands per QD. $[Total\ Bound\ Sites]$ is the average total number of surface sites per QD particle available for ligand binding. Similarly, $[Total\ Associated\ Site]$ is the average total number of surface sites per QD particle available for ligand association.

Historically, it is well studied that an anionic ligand (X-type, e.g. carboxylate group) interacts with metal atoms on the QD surface[8,9,21,22,41,42], in this case Pb atoms. This is also supported by a control NMR diffusometry study on the ligand 1-octadecene (see **Appendix II section 2**). Since it is difficult to distinguish and quantify bound and associated Pb sites on the QD surface, we assume both $[Total\ Bound\ Sites]$ and $[Total\ Associated\ Sites]$ are equal to the average total number of surface Pb sites estimated per QD. For a QD of diameter 3.6 nm, we estimate there are 260 Pb surface atoms on the QD that are potentially the surface sites for a ligand to either weakly associate or chemically bind to the QD. This estimated number depends on the size and crystal structure of the PbS QD, and the assumptions to quantify the number are further explained in **Appendix II section 5**.

By combining ^{1}H NMR spectroscopy and NMR diffusometry, we quantified the population fractions of ligands in three distinct states (**Table 6.1**). The total number of ligands per QD were quantified by comparing signal integrals of the alkenyl protons from OA ligand and the proton signal from ferrocene. More details on the ligand quantification are provided in **Appendix II section 6**. This quantified number enabled us to determine $[Free\ Ligand]$, $[Ligand - Bound\ Site]$, $[Ligand - Associated\ Site]$, and $[Total\ Associated\ Site]$ (**Table 6S4**) from determined population fractions (**Table 6.1**). **Figure 6.5A**, shows the number of ligands per QD at room temperature (23°C), partitioned in the different states.

As the concentration of free OAH increased (from 7.5 mM to 30 mM), we observed a gradual decrease in the number of bound ligands per QD, as shown in **Figure 6.5A**. One possible explanation for this decrease is that the acidic proton from free OAH may weaken the chemical bond of oleate (OA) on the QD surface, leading to a reduction in the NMR signal. However, confirming this hypothesis requires additional experiments which is subject of future work.

Notably, despite the decrease in bound ligands, the total number of ligands on the QD surface (including both QD-*associated* and bound) remained constant with increasing OAH concentration. This phenomenon could be attributed to the higher enthalpy of free OAH ligands in a non-polar solvent like toluene. The free ligands exhibit a thermodynamic preference for binding or associating with the QD surface to achieve lower enthalpy states, thereby maintaining a constant total number of surface ligands. This observation provides valuable insights into the dynamic equilibrium of ligand binding on QD surfaces and the interplay between solvent effects and surface interactions.

We also measured the variation in ligand population fractions with respect to temperature for a solution containing OA-capped PbS QDs titrated with 15 mM of free OAH into the solution. As the temperature of the solution was lowered from 23°C to –10°C (**Figure 6.5B**), a notable shift occurs in the ligand population: the fraction of free OAH ligands in solution decreases while the fraction bound/associated to the QD surface increases. This behavior can be explained through thermodynamic principles. At higher temperatures, the system favors states with higher entropy, allowing free ligands to maintain more degrees of freedom. However, as the temperature decreases, the entropic contributions to the Gibbs free energy becomes less significant, making the exothermic binding/association of ligands to the QD surface more favorable. Consequently, the reduced entropic cost associated with ligands adopting a less entropic state near the QD surface promotes greater ligand binding, resulting in fewer OAH ligands in solution. This temperature-dependent behavior is crucial for understanding and controlling the surface chemistry of QDs, which significantly influence their optical and electronic properties.

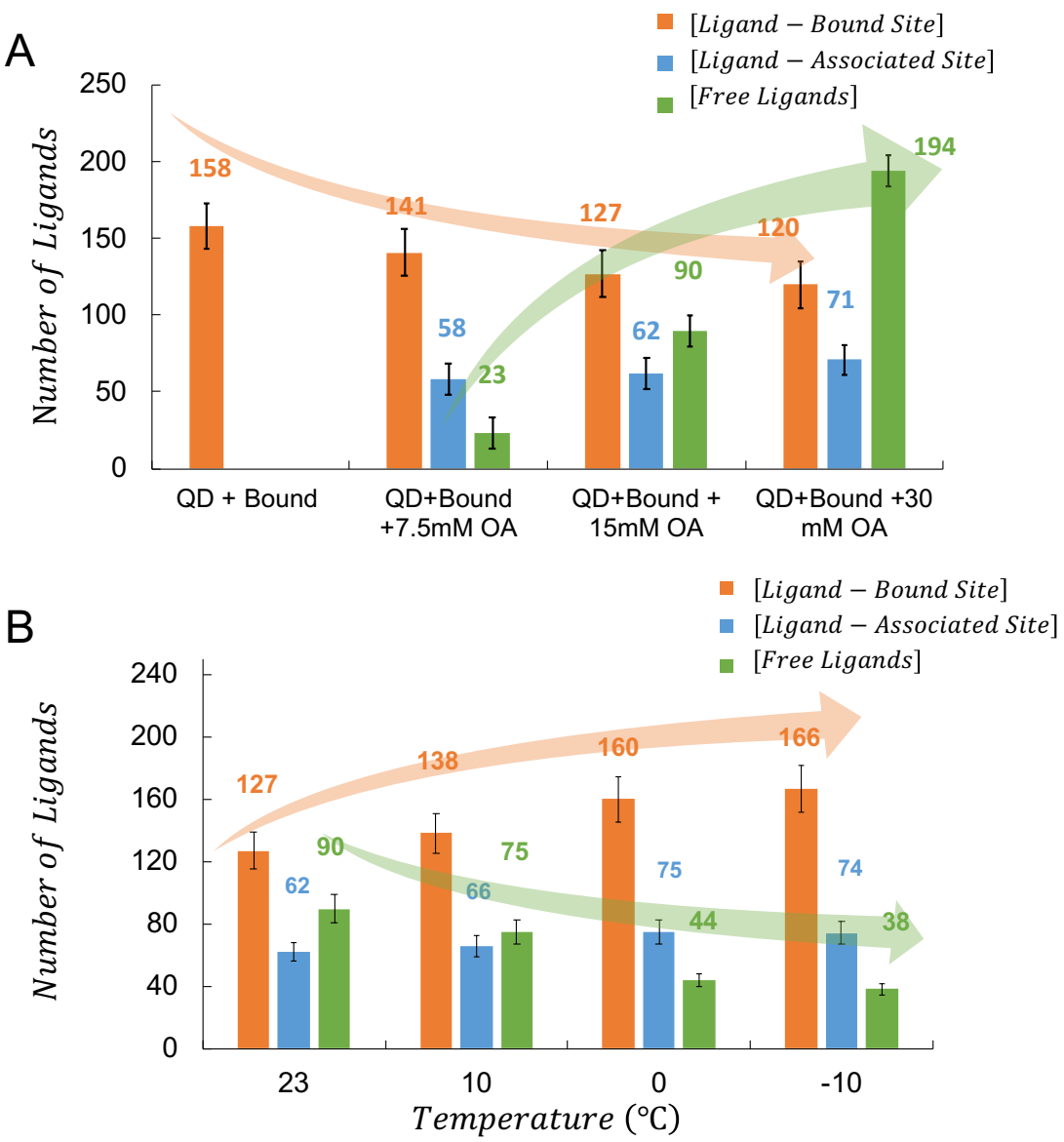

Figure 6.5: **A**. Average number (populations) of OA ligands in different states per QD (on the surface and in the free solution) measured at 23°C. The populations change as the titrated concentration of OA into the solution changes. **B**. Ligand population changes for as sample with ligand-bound PbS QDs with 15 mM of OA titrated into the solution upon cooling from 23°C to -10°C. Increasing the acidity of the solution reduced OA binding on the QD surface and lowering the temperature improved ligand binding on the QD surface.

To further understand the energies of ligand binding and association on the QD surface, we measured the equilibrium constants, K, for both processes using **Equation 6.4** and **6.5** at four different temperatures (23°C to –10°C). The number of ligands per QD are used as concentrations to determine the equilibrium constants, K_{bind} and K_{assoc}. **Table 6S4** in **Appendix II section 6** lists

number of OA ligands per QD in different states for all concentrations of free OAH ligands (0 to 30 mM) titrated into the OA-capped PbS QD solution. The table also contains the variation in the number of ligands per QD in different states as the temperature of the sample was lowered from 23°C to –10°C. The van't Hoff graphs plotted from equilibrium constants and temperature provide us with the enthalpic (ΔH) and the entropic ($T\Delta S$) energy changes for the ligand to either associate or chemically bind to the QD surface (**Figure 6.6A** and **6.6B**). The Gibbs free energy changes for binding and association with respect to sample concentration and encapsulation process at 25°C are shown in **Figur**e **6.6C** and **6.6D** respectively.

Both ligand binding and association processes are exothermic as observed from the negative ΔH. The enthalpy change is more negative in binding (ΔH_{bind}) than association (ΔH_{assoc}), indicating that the ligand binding is stronger compared to association, as hypothesized earlier from NMR measurements where the bound signal did not change after titrating free OAH ligands. We also observe an entropic penalty ($\Delta S < 0$) when ligands are on QD surface because the ligands are restricted when they bind/associate to the surface of the QD particle. Clearly these processes are enthalpy driven and thus the ligand coverage on QD surface is more favorable at lower temperatures.

Also, as the concentration of free OAH titrated into the solution increased, we observed an increase in enthalpy of binding (ΔH_{bind}), while the entropy of binding (ΔS_{bind}) remained constant. Consequently, the Gibbs free energy of binding ΔG_{bind} ($\Delta H_{bind} - T\Delta S_{bind}$) increased, indicating a decrease in the spontaneity of ligand binding. This phenomenon can be attributed to two primary factors. First, the increase in free OAH concentration introduces more acidic protons, which may weaken the binding of OA ligands already on the QD surface, contributing to the increase in ΔH_{bind}. Second, as free OAH concentration increases, fewer surface sites are available for binding,

potentially leading to an increase in the enthalpy of binding for the remaining free ligands. These factors collectively result in an increase in ΔG_{bind} as free OAH concentration increases, explaining the observed decrease in ligand binding spontaneity.

The thermodynamic analysis of ligand binding and association processes on QD surfaces reveal distinct behaviors as the concentration of free OAH in solution changes. The enthalpy of association (ΔH_{assoc}) is less negative compared to enthalpy of binding ($\Delta H_{assoc} > \Delta H_{bind}$), indicating that ligand binding is indeed stronger than association, as expected. For the ligand association process, both ΔH_{assoc} and ΔS_{assoc} became more negative as the OAH titration concentration increased from from 7.5 mM to 15 mM. However, a further increase in titration concentration from 15 mM to 30 mM resulted in more positive values for both ΔH_{assoc} and ΔS_{assoc}. The Ligand association is slightly less spontaneous compared to ligand-binding as hypothesized and its spontaneity decreases with increase in the free OA titration concentration in the solution. Similar to ligand binding, this decrease in spontaneity is attributed to saturation of Pb associated sites on QD surface.

These thermodynamic studies aid in optimizing ligand substitution process. For X-type binding, the acidity of the solution affects native ligand binding energies, providing better control over the degree of substitution and functionality of the QD surface. Additionally, the steric effects of the ligand on substitution can be predicted from these studies. However, these effects may be minimal, particularly at lower titration concentration and with larger surface area available on the QD. By providing a quantitative understanding of the ligand-QD interactions, thermodynamic energies help researchers make informed decisions in designing and optimizing QD systems for various applications. Quantifying these energies enables researchers to optimize QD dispersibility,

electronic properties, and optoelectronic performance for various applications in fields like solar cells, light-emitting devices and other optoelectronic systems [**references**].

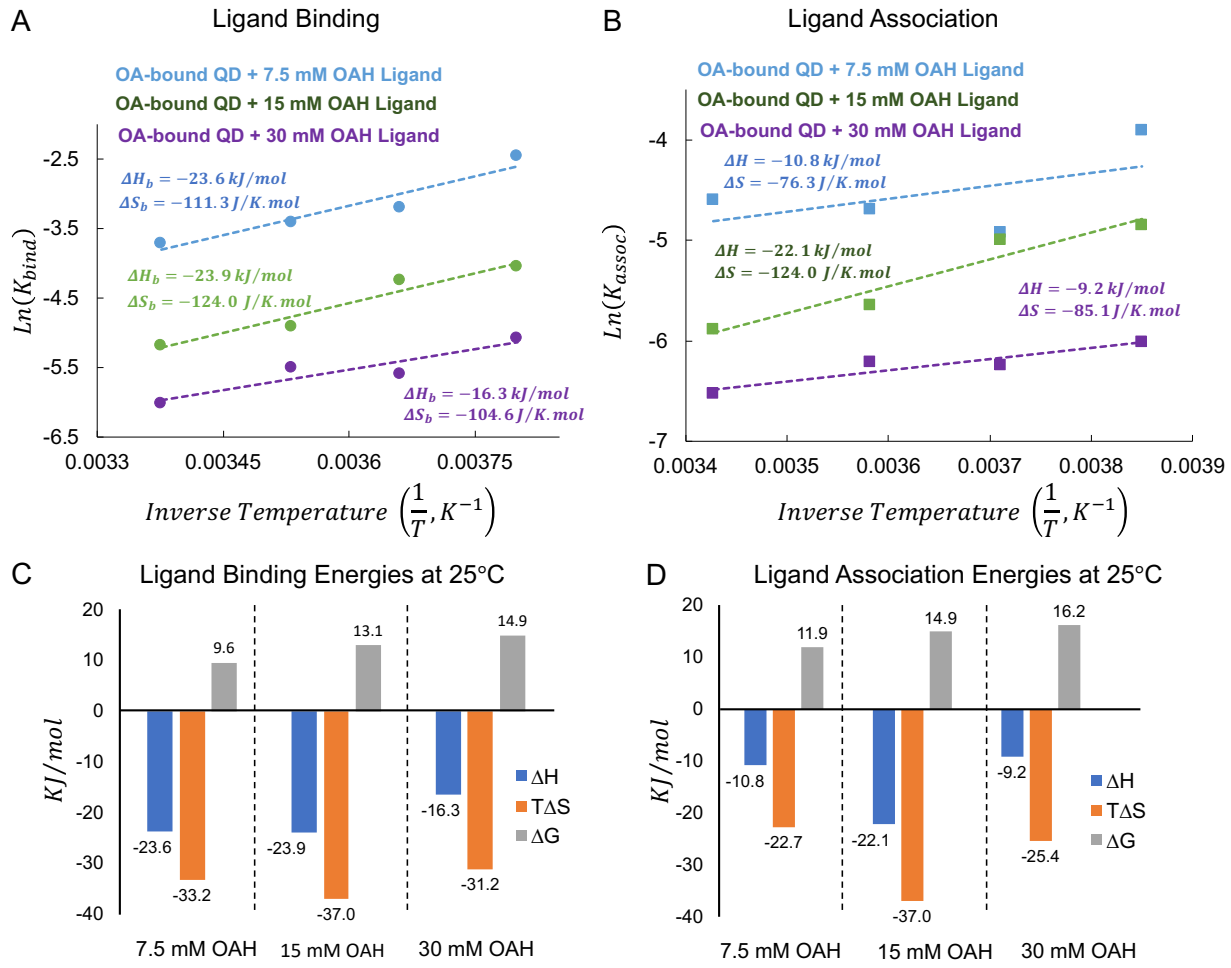

Figure 6.6: **A, B**. Van't Hoff (natural log of K_{eq} vs. inverse temperature) plots for binding and association of OA on PbS QDs for three different concentrations of free ligands titrated into QD solution. **C, D.** The enthalpy (ΔH), entropy (ΔS), and Gibbs (ΔG) free energy for ligand binding and association processes for all three samples at 25°C. The positive ΔG indicates that the ligand binding and association processes are weighted towards reactants at room temperature, and that they are enthalpy-favored reactions.

6.3.4. Kinetics of fast exchange between free Ligands and QD-associated ligands

Chemical exchange commonly appears in an NMR spectrum, primarily evident from the broad signals arising in the ^{1}H spectra of hydroxyls and amines.[43–49] Such exchange appears in our samples (**Figure 6.2B**, blue trace), where we observe a broad exchanging signal (which is same as

the 'intermediate' signal) near 5.7 ppm. The signal arises from fast exchange (compared to the NMR timescale of measurement, **Appendix II section 1**) between free and associated ligands. In this timescale (3.9 ms), we observe the simultaneous occurrence of both forward association and backward dissociation of OA ligand to an associated PbS QD surface site with rate constants k_{assoc} and k_{dissoc}, respectively, and as given by

$$\text{Free Ligand} + \text{Associated Site on QD} \underset{k_{dissoc}}{\overset{k_{assoc}}{\rightleftharpoons}} \text{QD-Associated Ligand} \quad (6.6)$$

The lineshape and chemical shift of this exchanging peak (intermediate peak) depends on the exchange rate of the probed nuclei and the population fraction of the ligands between two states, as shown **Figure 6S7** in **Appendix II section 8**. From ^{1}H NMR (**Figure 6S3)** and NMR diffusometry measurements (**Table 6.1**) we can confirm that OAH ligand exchanges rapidly between free and QD-associated states for all three of our OA-titrated samples (7.5 mM, 15 mM, and 30 mM). To accurately quantify such exchange rates, Rogers and Woodbrey[43] developed a generalized lineshape function $S_{ex}(v)$ for a two-site exchange model as described below (**Equations 6.7-6.12**). Gutowsky and Holm later applied this model for first time to study amide bond rotation kinetics.[47]

$$S_{ex}(\nu) = C_0 \times \left(\frac{P\left[1 + \tau_{ex}\left(\frac{p_{solv}}{T_{2,assoc}} + \frac{p_{assoc}}{T_{2,\,free}}\right)\right] + QR}{(P)^2 + (R)^2} \right) \quad (6.7)$$

$$P = \tau_{ex} \times \left(\frac{1}{T_{2,assoc} \times T_{2,free}} - 4\pi^2\Delta\nu^2 + \pi^2\delta\nu^2 \right) + \frac{p_{assoc}}{T_{2,assoc}} + \frac{p_{free}}{T_{2,free}} \quad (6.8)$$

$$Q = \tau_{ex} \times \left(2\pi\Delta\nu - \pi\delta\nu(p_{assoc} - p_{free}\right) \quad (6.9)$$

$$R = 2\pi\Delta\nu\left[1 + \tau_{ex}\left(\frac{1}{T_{2,assoc}} + \frac{1}{T_{2,free}}\right)\right] + \pi\delta\nu\tau_{ex}\left(\frac{1}{T_{2,assoc}} - \frac{1}{T_{2,free}}\right) + \pi\delta\nu(p_{assoc} - p_{free}) \quad (6.10)$$

$$\delta\nu = \left|\nu_{assoc} - \nu_{free}\right| \tag{6.11}$$

$$\Delta\nu = \left(\frac{\nu_{free} + \nu_{assoc}}{2}\right) - \nu \tag{6.12}$$

$$\tau_{ex} = \frac{p_{assoc}}{k_{assoc}} = \frac{p_{free}}{k_{dissoc}} \tag{6.13}$$

The above lineshape function $S_e(\nu)$ depends on the exchange lifetime τ_{ex}, which represents the overall exchange time for ligand association and dissociation. This exchange time is the reciprocal of the overall exchange rate constant $k_{ex} = k_{assoc} + k_{dissoc} = {\tau_{ex}}^{-1}$. Despite its complexity, the lineshape function requires only six known parameters to fit the experimental data and determine τ_{ex}. These parameters are the spin-spin relaxation times ($T_{2,\,free}$, $T_{2,assoc}$) and the chemical shifts (ν_{free}, ν_{assoc}) for non-exchanging free and QD-*associated* ligands, and population fractions ($p_{free} = \frac{f_{free}}{f_{ex}}, p_{assoc} = \frac{f_{assoc}}{f_{ex}}$) for exchanging free and QD-associated ligands. In this function, $\delta\nu$ represents the chemical shift difference between the two exchanging sites and $\Delta\nu$ denotes the midpoint frequency between the free and associated ligand signals as shown in the **Equations 6.11, 6.12**. C_0 is a scaling factor determined by fitting the experimental data with lineshape function.

We determined the spin-spin relaxation times for the non-exchanging free ligand ($T_{2,\,free}$) and QD-associated ligand ($T_{2,\,assoc}$) proton nuclei using a modified CPMG pulse sequence, which minimizes J-modulation effects and enables more accurate determination of T_2 values (see **Appendix II section 9**). Since alkenyl protons of QD-bound and QD-*associated* ligands have similar chemical environments, we can assume that $T_{2,assoc} = T_{2,bound}$. We measured $T_{2,bound}$ using the modified CPMG pulse sequence on a control dialyzed sample containing only bound ligands without excess of OA. We determined population fractions p_{free} and p_{assoc} from NMR

diffusometry measurements using **Equation 6.2**, as explained above. We determined ν_{free} from a sample with only free OA in toluene-d_8 and determined ν_{assoc} using **Equation 6.3**.

Due to the overlap of the exchanging and bound peaks (**Figure 6.2B,** also **Figure 6S8 in Appendix II section 8**), we deconvoluted the signals using MNova. We fit the separated exchanging signal data using complete lineshape function (**Equations 6.6-6.11**) and the bound signal integrals and line positions (chemical shifts) using the following Lorentzian lineshape function

$$S_{bound}(\nu) = \frac{C_1}{2\pi} \times \left(\frac{\frac{w}{2}}{(\nu - \nu_0)^2 + \left(\frac{w}{2}\right)^2} \right) \tag{6.14}$$

where, ν_0 is the resonance frequency (in Hz) of the bound signal, w is the defined above FWHM (Hz) of the bound signal, and C_1 is a scaling factor. We determined ν_0 and w from the deconvoluted bound signal.

We then determined the exchange lifetime τ_{ex}, by least-squares fitting the deconvoluted exchange NMR signal with **Equation 6.7**. We performed this fitting process using Python (code details are presented in the **Appendix III)**. Similarly, we fit the bound signal with **Equation 6.14**. **Figure 6.7** (dashed line) displays the fits of the acquired 1D spectra (solid line) of a sample containing ligand-bound PbS QDs titrated with 15 mM of OA into the solution, measured at 23°C. The spectral fitting confirms that the obtained τ_{ex} accurately represents the expected exchange between QD-associated and free ligands. **Table 6.2** lists the parametric values used to determine τ_{ex} and in turn determine k_{assoc} for ligand association. At low titration concentrations, we observe faster exchange due to more available sites for ligand association. This determined exchange rate

decreases with increasing ligand titration concentration, which we attribute to the saturation of associated sites on QD surface, reducing the availability of sites for ligand association.

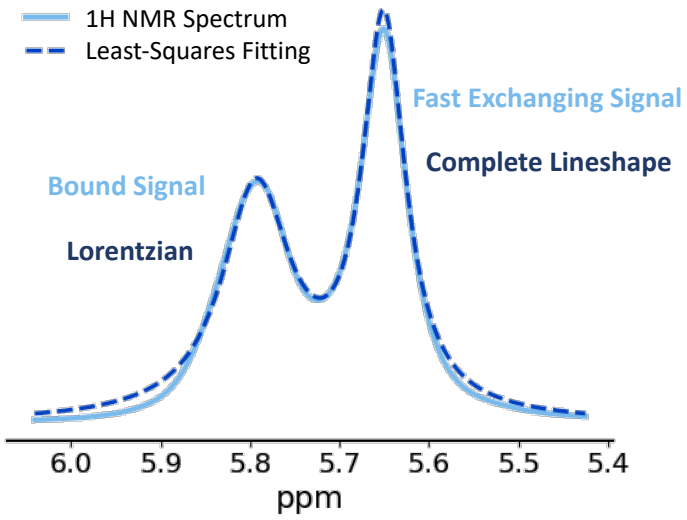

Figure 6.7: Least-squares fitting (dashed line) of an acquired alkenyl proton spectrum (solid line) for a sample containing ligand-bound PbS QDs titrated with 15 mM OAH, measured at 23°C. The fitted curve, a linear combination of optimized lineshape and Lorentzian functions, closely matches the acquired data, indicating the accuracy of the determined exchange lifetime, τ_{ex}.

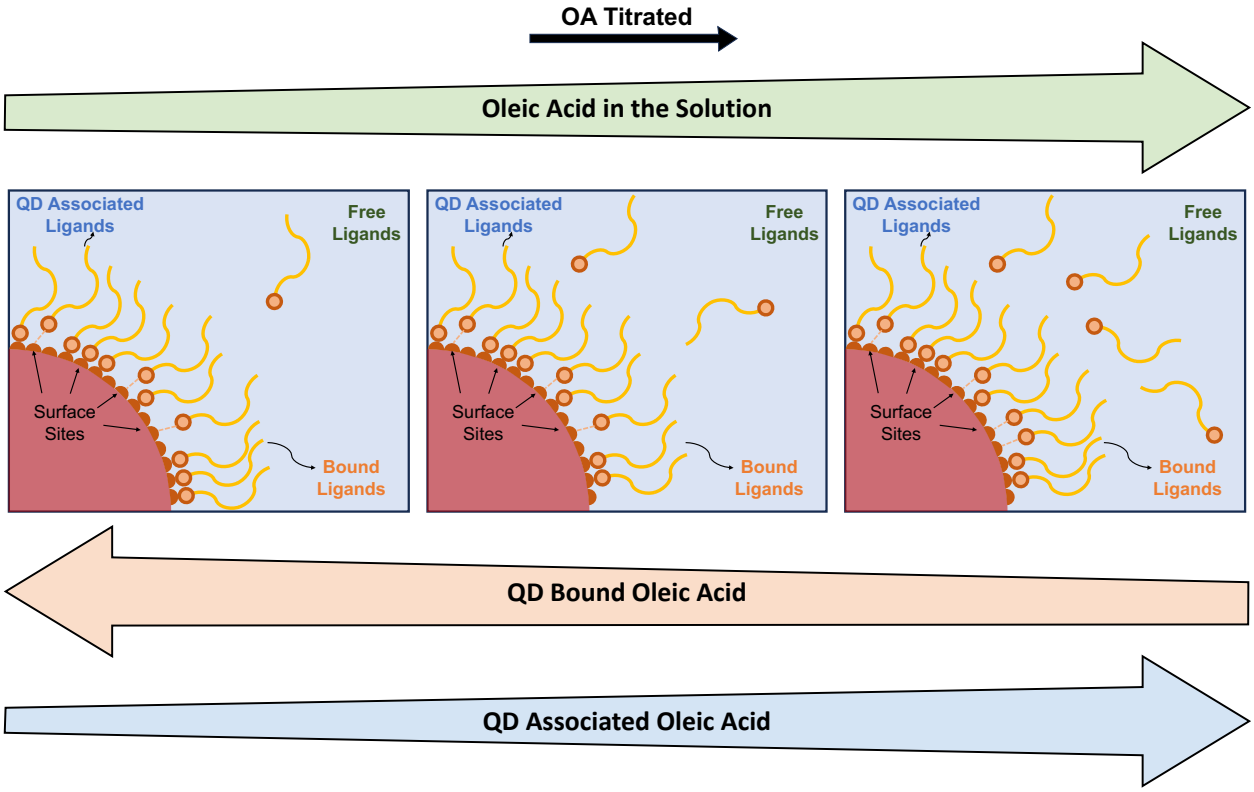

Figure 6.8: Change in population fraction of the ligand in different states (bound, QD-associated, and free) with increase in OAH titratation concentration.

Table 6.2: Ligand association rate (k_{assoc}) dependence on concentration of titrated OA

Sample	p_{assoc} (%)	p_{free} (%)	ν_{free} (ppm)	ν_{assoc} (ppm)	$T_{2,free}$ (s)	$T_{2,assoc}$ (s)	τ_{ex} (s)	k_{assoc} (s^{-1})
QD +7.5mM OA	29	71	5.58	5.74	0.78	0.053	8.9×10^{-4}	490±50
QD + 15mM OA	59	41	5.58	5.76	0.78	0.053	9.1×10^{-4}	450±50
QD +30 mM OA	73	27	5.58	5.76	0.78	0.053	1.5×10^{-3}	300±50

Ligand association rate, k_{assoc}, is determined from exchange lifetime τ_{ex}, and **Equation 6.13**. k_{assoc} did not change (490±50 s^{-1}, values within error) when the titration concentration increased from 7.5 mM to 15 mM, because the associated-Pb sites on QD surface are not completely saturated. When the ligand concentration was further increased to 30 mM, k_{assoc} decreased which is attributed to saturation of associated-Pb sites.

We further measured the energetics of this ligand association process from the kinetics by determining the activation energies of the exchange process. To achieve this, we measured the

temperature dependency of k_{assoc} to determine the activation energy ($E_{a,assoc}$) of the ligand association process. Since this fast exchange process is a physical phenomenon, we can represent its temperature dependency using the Arrhenius equation.

$$k_{assoc} = k_{\infty,assoc} e^{-E_{a,assoc}/RT} \quad (6.15)$$

In this equation, k_{assoc} is the ligand association rate, R is the gas constant, and T is the temperature of solution. $k_{\infty,assoc}$ denotes the association rate at infinite temperature, also known as the "barrierless reaction rate." This empirical relationship enables us to determine $E_{a,assoc}$, the activation energy for ligand association.

Table 6.3 presents the activation energies, $E_{a,assoc}$, for samples containing varying titration concentrations of free OAH ligands. At low titration concentrations (7.5 mM), the activation energy required for ligand association with Pb sites on the QD surface is minimal. However, as the concentration increases, a corresponding increase in the activation energy for association is observed. We attribute this phenomenon to the progressive saturation of associated Pb sites on the QD surface with increasing free OAH concentration.

The surface saturation induces a 'chain-crowding effect' elevating the energy barrier for ligand association (physisorption) on the surfaces.[50,51] Furthermore, the increase in free OAH concentration in solvent alters the apparent pKa of the solution, influencing the entropy and enthalpy of association. These factors synergistically enhance the ligands' tendency to remain free in the solution, thereby increasing the OAH association on the QD surface.

Utilizing $k_{\infty,assoc}$ derived from **Equation 6.15** we estimated the activation energies for the slow OA ligand-binding process (see **Appendix II section 10**). The quantified energetics of the ligand exchange mechanism, as illustrated in **Figure 6S10**, provides a comprehensive picture of the ligand binding and association processes. Notably, the activation energy for ligand binding is

approximately 5-6 times greater than that for ligand association on the QD surface. Consequently, the ligand exchange rate between bound and free states is significantly lower than the exchange rate for ligand association.

This enhanced understanding of ligand exchange kinetics and thermodynamics is crucial for several reasons

1. It provides insights into the nature of ligand-QD surface interactions, fundamental to controlling QD surface chemistry.
2. By elucidating the ligand exchange process, we can better assess how ligands influence the collision frequency of desired reactants on the QD surface, critical for optimizing QD performance in optoelectronic applications
3. The energetics data offers a quantitative basis for predicting and manipulating ligand behavior on QD surfaces.
4. This knowledge can guide the design of more efficient QD-based devices by allowing for precise control over surface properties.

These findings contribute significantly to our understanding of the complex interplay between ligands and QD surfaces, providing a solid foundation for further advancements in QD-based technologies.

Table 6.3: Temperature dependent ligand association rates of OA ligands and their activation energies derived from Arrhenius equation.

	QD +Bound+ 7.5mM OA (50 equivalent)		**QD + Bound + 15mM OA (100 equivalent)**		**QD + Bound + 30mM OA (200 equivalent)**	
Temperature	$\boldsymbol{K_{assoc}}$ (s^{-1})	$\boldsymbol{E_a}$ (Kj/mol)	$\boldsymbol{K_{assoc}}$ (s^{-1})	$\boldsymbol{E_a}$ (Kj/mol)	$\boldsymbol{K_{assoc}}$ (s^{-1})	$\boldsymbol{E_a}$ (Kj/mol)

23	490 ± 50	5.2 ± 5	450 ± 50	20.5 ± 5	300 ± 50	15.5 ± 5
10	290 ± 50		390 ± 50		280 ± 50	
0	315 ± 50		170 ± 50		240 ± 50	
-10	360 ± 50		190 ± 50		130 ± 50	

6.4. Conclusions

In this project, we significantly advanced our understanding of oleic acid ligand association and binding to PbS quantum dots (QDs) by updating the simple two-state ligand model (bound and free) to a more comprehensive three-state model (bound, QD-*associated*, and free). This updated model was determined and validated through non-destructive ^{1}H NMR spectroscopy and NMR diffusometry measurements. These measurements allowed us to quantify the population fractions of OA ligands in three different state and observed population changes by varying the solution temperature and free OA titration concentration. This study enabled us to determine the thermodynamic properties of the ligand binding/association process by applying the Langmuir adsorption model.

Leveraging NMR's capability to probe exchange kinetics, we studied kinetics of our QD system. Specifically, we observed fast OAH exchange between free and QD-*associated* ligand states and determined their rates using dynamic NMR. This method aided us in determining the activation energy of the system, providing crucial insights into the energetics of ligand-QD interactions. Our research demonstrated the power of NMR spectroscopy in studying complex molecular systems using both 1D and 2D techniques. This enabled in model validation and probing dynamic and kinetic properties of the system. We combined experimental data with theoretical models to achieve a comprehensive analysis of OA ligand behavior on QD surfaces. Future studies

will be aimed at exploring the energetics of ligand association/binding when the incoming ligand differs from the native OA ligand.

This study lays the groundwork for several promising research avenues, including computational modeling, investigation of structure-property relationships, development of in-situ studies, and novel-ligand design. Our work not only advances the fundamental understanding of QD surface chemistry but also provides a powerful tool for rational design and optimization of QD-based materials and devices.

References

(1) Martynenko, I. V.; Litvin, A. P.; Purcell-Milton, F.; Baranov, A. V.; Fedorov, A. V.; Gun'Ko, Y. K. Application of Semiconductor Quantum Dots in Bioimaging and Biosensing. *Journal of Materials Chemistry B*. Royal Society of Chemistry 2017, pp 6701–6727. https://doi.org/10.1039/c7tb01425b.

(2) García de Arquer, F. P.; Talapin, D. V.; Klimov, V. I.; Arakawa, Y.; Bayer, M.; Sargent, E. H. Semiconductor Quantum Dots: Technological Progress and Future Challenges. *Science (New York, N.Y.)*. NLM (Medline) August 6, 2021. https://doi.org/10.1126/science.aaz8541.

(3) Kessler, M. L.; Kelm, J. E.; Starr, H. E.; Cook, E. N.; Miller, J. D.; Rivera, N. A.; Hsu-Kim, H.; Dempsey, J. L. Unraveling Changes to PbS Nanocrystal Surfaces Induced by Thiols. *Chemistry of Materials* **2022**, *34* (4), 1710–1721. https://doi.org/10.1021/acs.chemmater.1c03888.

(4) Loiudice, A.; Segura Lecina, O.; Bornet, A.; Luther, J. M.; Buonsanti, R. Ligand Locking on Quantum Dot Surfaces via a Mild Reactive Surface Treatment. *J Am Chem Soc* **2021**, *143* (33), 13418–13427. https://doi.org/10.1021/jacs.1c06777.

(5) Elimelech, O.; Aviv, O.; Oded, M.; Banin, U. A Tale of Tails: Thermodynamics of CdSe Nanocrystal Surface Ligand Exchange. *Nano Lett* **2020**, *20* (9), 6396–6403. https://doi.org/10.1021/acs.nanolett.0c01913.

(6) Valdez, C. N.; Schimpf, A. M.; Gamelin, D. R.; Mayer, J. M. Low Capping Group Surface Density on Zinc Oxide Nanocrystals. *ACS Nano* **2014**, *8* (9), 9463–9470. https://doi.org/10.1021/nn503603e.

(7) Bullen, C.; Mulvaney, P. The Effects of Chemisorption on the Luminescence of CdSe Quantum Dots. *Langmuir* **2006**, *22* (7), 3007–3013. https://doi.org/10.1021/la051898e.

(8) Hartley, C. L.; Kessler, M. L.; Dones Lassalle, C. Y.; Camp, A. M.; Dempsey, J. L. Effects of Ligand Shell Composition on Surface Reduction in PbS Quantum Dots. *Chemistry of Materials* **2021**, *33* (22), 8612–8622. https://doi.org/10.1021/acs.chemmater.1c01810.

(9) Kessler, M. L.; Dempsey, J. L. Mapping the Topology of PbS Nanocrystals through Displacement Isotherms of Surface-Bound Metal Oleate Complexes. *Chemistry of Materials* **2020**, *32* (6), 2561–2571. https://doi.org/10.1021/acs.chemmater.0c00014.

(10) Bowen Katari, J. E.; Colvin, V. L.; Alivisatos, A. P. *X-Ray Photoelectron Spectroscopy of CdSe Nanocrystals with Applications to Studies of the Nanocrystal Surface*; 1994; Vol. 98. https://pubs.acs.org/sharingguidelines.

(11) Moreels, I.; Lambert, K.; Smeets, D.; De Muynck, D.; Nollet, T.; Martins, J. C.; Vanhaecke, F.; Vantomme, A.; Delerue, C.; Allan, G.; Hens, Z. Size-Dependent Optical Properties of Colloidal PbS Quantum Dots. *ACS Nano* **2009**, *3* (10), 3023–3030. https://doi.org/10.1021/nn900863a.
(12) Green, M. L. H.; Parkin, G. Application of the Covalent Bond Classification Method for the Teaching of Inorganic Chemistry. *J Chem Educ* **2014**, *91* (6), 807–816. https://doi.org/10.1021/ed400504f.
(13) Anderson, N. C.; Hendricks, M. P.; Choi, J. J.; Owen, J. S. Ligand Exchange and the Stoichiometry of Metal Chalcogenide Nanocrystals: Spectroscopic Observation of Facile Metal-Carboxylate Displacement and Binding. *J Am Chem Soc* **2013**, *135* (49), 18536–18548. https://doi.org/10.1021/ja4086758.
(14) Kessler, M. L.; Starr, H. E.; Knauf, R. R.; Rountree, K. J.; Dempsey, J. L. Exchange Equilibria of Carboxylate-Terminated Ligands at PbS Nanocrystal Surfaces. *Physical Chemistry Chemical Physics* **2018**, *20* (36), 23649–23655. https://doi.org/10.1039/c8cp04275f.
(15) Morris-Cohen, A. J.; Malicki, M.; Peterson, M. D.; Slavin, J. W. J.; Weiss, E. A. Chemical, Structural, and Quantitative Analysis of the Ligand Shells of Colloidal Quantum Dots. *Chemistry of Materials*. April 23, 2013, pp 1155–1165. https://doi.org/10.1021/cm302108j.
(16) Gomes, R.; Hassinen, A.; Szczygiel, A.; Zhao, Q.; Vantomme, A.; Martins, J. C.; Hens, Z. Binding of Phosphonic Acids to CdSe Quantum Dots: A Solution NMR Study. *Journal of Physical Chemistry Letters* **2011**, *2* (3), 145–152. https://doi.org/10.1021/jz1016729.
(17) Hens, Z.; Martins, J. C. A Solution NMR Toolbox for Characterizing the Surface Chemistry of Colloidal Nanocrystals. *Chemistry of Materials*. April 23, 2013, pp 1211–1221. https://doi.org/10.1021/cm303361s.
(18) Donakowski, M. D.; Godbe, J. M.; Sknepnek, R.; Knowles, K. E.; Olvera de la Cruz, M.; Weiss, E. A. A Quantitative Description of the Binding Equilibria of Para-Substituted Aniline Ligands and CdSe Quantum Dots. *The Journal of Physical Chemistry C* **2010**, *114* (51), 22526–22534. https://doi.org/10.1021/jp109381r.
(19) Aldana, J.; Wang, Y. A.; Peng, X. Photochemical Instability of CdSe Nanocrystals Coated by Hydrophilic Thiols. *J Am Chem Soc* **2001**, *123* (36), 8844–8850. https://doi.org/10.1021/ja016424q.
(20) Majetich, S. A.; Carter, A. C.; Belot, J.; Mccullough, R. D. **H NMR Characterization of the CdSe Nanocrystallite Surface*; 1994; Vol. 98. https://pubs.acs.org/sharingguidelines.
(21) Knauf, R. R.; Lennox, J. C.; Dempsey, J. L. Quantifying Ligand Exchange Reactions at CdSe Nanocrystal Surfaces. *Chemistry of Materials* **2016**, *28* (13), 4762–4770. https://doi.org/10.1021/acs.chemmater.6b01827.
(22) Kessler, M. L.; Starr, H. E.; Knauf, R. R.; Rountree, K. J.; Dempsey, J. L. Exchange Equilibria of Carboxylate-Terminated Ligands at PbS Nanocrystal Surfaces. *Physical Chemistry Chemical Physics* **2018**, *20* (36), 23649–23655. https://doi.org/10.1039/c8cp04275f.
(23) Kelm, J. E.; Dempsey, J. L. Metal-Dictated Reactivity of Z-Type Ligands to Passivate Surface Defects on CdSe Nanocrystals. *J Am Chem Soc* **2024**, *146* (8), 5252–5262. https://doi.org/10.1021/jacs.3c11811.
(24) Kroupa, D. M.; Anderson, N. C.; Castaneda, C. V.; Nozik, A. J.; Beard, M. C. In Situ Spectroscopic Characterization of a Solution-Phase X-Type Ligand Exchange at Colloidal Lead Sulphide Quantum Dot Surfaces. *Chemical Communications* **2016**, *52* (96), 13893–13896. https://doi.org/10.1039/C6CC08114B.

(25) Ritchhart, A.; Cossairt, B. M. Quantifying Ligand Exchange on InP Using an Atomically Precise Cluster Platform. *Inorg Chem* **2019**, *58* (4), 2840–2847. https://doi.org/10.1021/acs.inorgchem.8b03524.
(26) Smock, S. R.; Williams, T. J.; Brutchey, R. L. Quantifying the Thermodynamics of Ligand Binding to CsPbBr 3 Quantum Dots . *Angewandte Chemie* **2018**, *130* (36), 11885–11889. https://doi.org/10.1002/ange.201806916.
(27) Weir, M. P.; Toolan, D. T. W.; Kilbride, R. C.; Penfold, N. J. W.; Washington, A. L.; King, S. M.; Xiao, J.; Zhang, Z.; Gray, V.; Dowland, S.; Winkel, J.; Greenham, N. C.; Friend, R. H.; Rao, A.; Ryan, A. J.; Jones, R. A. L. Ligand Shell Structure in Lead Sulfide-Oleic Acid Colloidal Quantum Dots Revealed by Small-Angle Scattering. *Journal of Physical Chemistry Letters* **2019**, *10* (16), 4713–4719. https://doi.org/10.1021/acs.jpclett.9b01008.
(28) Fritzinger, B.; Capek, R. K.; Lambert, K.; Martins, J. C.; Hens, Z. Utilizing Self-Exchange to Address the Binding of Carboxylic Acid Ligands to CdSe Quantum Dots. *J Am Chem Soc* **2010**, *132* (29), 10195–10201. https://doi.org/10.1021/ja104351q.
(29) Liu, M.; Wang, Y. Y.; Liu, Y.; Jiang, F. L. Thermodynamic Implications of the Ligand Exchange with Alkylamines on the Surface of CdSe Quantum Dots: The Importance of Ligand-Ligand Interactions. *Journal of Physical Chemistry C* **2020**, *124* (8), 4613–4625. https://doi.org/10.1021/acs.jpcc.9b11572.
(30) Zhou, X.; Pang, Z.; Cao, W.; Cao, Z.; Zhu, J.; Qi, Y.; Peng, X.; Kong, X. Diffusion NMR for Measuring Dynamic Ligand Exchange on Colloidal Nanocrystals. *Anal Chem* **2023**, *95* (2), 792–801. https://doi.org/10.1021/acs.analchem.2c02964.
(31) Kroupa, D. M.; Vörös, M.; Brawand, N. P.; McNichols, B. W.; Miller, E. M.; Gu, J.; Nozik, A. J.; Sellinger, A.; Galli, G.; Beard, M. C. Tuning Colloidal Quantum Dot Band Edge Positions through Solution-Phase Surface Chemistry Modification. *Nat Commun* **2017**, *8*. https://doi.org/10.1038/ncomms15257.
(32) Hines, M. A.; Scholes, G. D. Colloidal PbS Nanocrystals with Size-Tunable Near-Infrared Emission: Observation of Post-Synthesis Self-Narrowing of the Particle Size Distribution. *Advanced Materials* **2003**, *15* (21), 1844–1849. https://doi.org/10.1002/adma.200305395.
(33) Moreels, I.; Lambert, K.; Smeets, D.; De Muynck, D.; Nollet, T.; Martins, J. C.; Vanhaecke, F.; Vantomme, A.; Delerue, C.; Allan, G.; Hens, Z. Size-Dependent Optical Properties of Colloidal PbS Quantum Dots. *ACS Nano* **2009**, *3* (10), 3023–3030. https://doi.org/10.1021/nn900863a.
(34) Price, W. S. Pulsed-Field Gradient Nuclear Magnetic Resonance as a Tool for Studying Translational Diffusion: Part 1. Basic Theory. *Concepts Magn Reson* **1997**, *9* (5), 299–336. https://doi.org/10.1002/(SICI)1099-0534(1997)9:5<299::AID-CMR2>3.0.CO;2-U.
(35) Stejskal, E. O.; Tanner, J. E. Spin Diffusion Measurements: Spin Echoes in the Presence of a Time-Dependent Field Gradient. *J Chem Phys* **1965**, *42* (1), 288–292. https://doi.org/10.1063/1.1695690.
(36) Callaghan, P. T. *Translational Dynamics and Magnetic Resonance: Principles of Pulsed Gradient Spin Echo NMR*; Oxford University Press, 2011. https://doi.org/10.1093/acprof:oso/9780199556984.001.0001.
(37) Aguilar, J. A.; Nilsson, M.; Bodenhausen, G.; Morris, G. A. Spin Echo NMR Spectra without J Modulation. *Chemical Communications* **2012**, *48* (6), 811–813. https://doi.org/10.1039/c1cc16699a.
(38) De Roo, J.; Yazdani, N.; Drijvers, E.; Lauria, A.; Maes, J.; Owen, J. S.; Van Driessche, I.; Niederberger, M.; Wood, V.; Martins, J. C.; Infante, I.; Hens, Z. Probing Solvent-Ligand

Interactions in Colloidal Nanocrystals by the NMR Line Broadening. *Chemistry of Materials* **2018**, *30* (15), 5485–5492. https://doi.org/10.1021/acs.chemmater.8b02523.
(39) Gutowsky, H. S.; Holm, C. H. Rate Processes and Nuclear Magnetic Resonance Spectra. II. Hindered Internal Rotation of Amides. *J Chem Phys* **1956**, *25* (6), 1228–1234. https://doi.org/10.1063/1.1743184.
(40) Irvinq Langmuir, B. *ADSORPTION OF GASBS ON GLASS, MICA AND PLATINUM. THE ADSORPTION OF GASES ON PLANE SURFACES OF GLASS, MICA AND PLATINUM*; 1918. https://doi.org/https://doi.org/10.1021/ja02242a004.
(41) Hartley, C. L.; Dempsey, J. L. Revealing the Molecular Identity of Defect Sites on PbS Quantum Dot Surfaces with Redox-Active Chemical Probes. *Chemistry of Materials* **2021**, *33* (7), 2655–2665. https://doi.org/10.1021/acs.chemmater.1c00520.
(42) Hartley, C. L.; Kessler, M. L.; Dempsey, J. L. Molecular-Level Insight into Semiconductor Nanocrystal Surfaces. *J Am Chem Soc* **2021**, *143* (3), 1251–1266. https://doi.org/10.1021/jacs.0c10658.
(43) Rogers, M. T.; Woodbrey, J. C. A PROTON MAGNETIC RESONANCE STUDY OF HINDERED INTERNAL ROTATION IN SOME SUBSTITUTED N,N-DIMETHYLAMIDES. *J Phys Chem* **1962**, *66* (3), 540–546. https://doi.org/10.1021/j100809a043.
(44) Tewari, K. C.; Li, N. C. *Nuclear Magnetic Resonance Study of Proton Exchange in the Water-Zpropanol System*; 1970; Vol. 48.
(45) Masatami Takeda, B.; Stejskal, E. O.; Gutowsky, H. S.; McCall, W.; Slichter, C. P.; Chem, J. *Chemical Exchange on a High-Resolution N.m.r. Spin-Spin Doublet Analysis of the Effect of Chemical Exchange on a High-Resolution N.m.r. Spin-Spin Doublet: Application to N-Methylacetamide12*; 1953; Vol. 21. https://pubs.acs.org/sharingguidelines.
(46) Paterson, W. G. NUCLEAR MAGNETIC RESONANCE MEASUREMENTS OF PROTON EXCHANGE IN ALCOHOL–WATER SYSTEMS: PART II. n-Ch3H7OH-H2O and i-CH3H70H-H2O. *Can J Chem* **1963**, *41* (10), 2472–2476. https://doi.org/10.1139/v63-364.
(47) Gutowsky, H. S.; Holm, C. H. Rate Processes and Nuclear Magnetic Resonance Spectra. II. Hindered Internal Rotation of Amides. *J Chem Phys* **1956**, *25* (6), 1228–1234. https://doi.org/10.1063/1.1743184.
(48) Luz, Z.; Meiboom, S. Nuclear Magnetic Resonance Study of the Protolysis of Trimethylammonium Ion in Aqueous Solution-Order of the Reaction with Respect to Solvent. *J Chem Phys* **1963**, *39* (2), 366–370. https://doi.org/10.1063/1.1734254.
(49) Kreiter, C. G.; Fischer, E. O. Hindered Rotation about the C-O Bond in Methoxy(Methyl)Carbene Ligands. *Angewandte Chemie International Edition in English* **1969**, *8* (10), 761–762. https://doi.org/10.1002/anie.196907611.
(50) Shillcock, J. C.; Thomas, D. B.; Ipsen, J. H.; Brown, A. D. Macromolecular Crowding Is Surprisingly Unable to Deform the Structure of a Model Biomolecular Condensate. *Biology (Basel)* **2023**, *12* (2). https://doi.org/10.3390/biology12020181.
(51) Alfano, C.; Fichou, Y.; Huber, K.; Weiss, M.; Spruijt, E.; Ebbinghaus, S.; De Luca, G.; Morando, M. A.; Vetri, V.; Temussi, P. A.; Pastore, A. Molecular Crowding: The History and Development of a Scientific Paradigm. *Chemical Reviews*. American Chemical Society March 27, 2024, pp 3186–3219. https://doi.org/10.1021/acs.chemrev.3c00615.

Chapter 7: Summary and future work

7.1. Summary

This dissertation explores the application of a suite of NMR techniques to investigate the dynamics and diffusion of block copolymer micelle, long polyelectrolyte chains, and semiconductor nanoparticle colloids. These studies provide crucial insights into the molecular interactions and self-assembly mechanisms, which can guide the rational design of materials with properties tailored to specific applications. Chapter 2 introduces the foundational concepts of NMR techniques, including spectroscopy, relaxation, and diffusometry, which are used to measure the dynamics and diffusion of mobile species and assess their influence on material functionality.

Chapter 3 focuses on determining the number-average molecular weight (M_n) of polyelectrolytes from chain's conformational (Rouse) and translational (Stokes-Einstein) dynamics. By employing NMR diffusometry and SAXS, we determined the M_n of CsPSS of five different known molecular weights and assessed the limitations of this model. The model proved most effective for polyelectrolyte chains with fewer than 2000 monomer ($N < 2000$). For larger chains ($N > 2000$), diffusion coefficients increased continuously with decreasing concentration, likely due to residual salts in the solution.

In Chapter 4, we investigated the hydrophobic drug encapsulation capability of self-assembled of block copolymer Pluronic ® F127 (PEG_{99}-PPO_{69}-PEG_{99}) micelles in water. We successfully encapsulated three hydrophobic drugs – indomethacin (IND), hydrochlorothiazide (HCT), and paclitaxel (PTX) – in F127 micelles. By measuring the diffusion coefficients of the drug and polymer species, we quantified the drug partitioning in the micelles. The partitioning was dependent on the drug's hydrophobicity, with nearly all paclitaxel encapsulated in the micelle.

Additionally, HCT and IND partition percentages increased with polymer concentration, while HCT partitioning percentage in micelle decreased with increasing temperature. This study provides a direct approach to understanding the molecular interactions of drug with micelles and aid in designing drug-delivery systems specific to the application requirements.

Chapter 5 examines how molecular modulation influences the macroscopic behavior of block copolymer micelles. We synthesized a block copolymer comprising hydrophilic PEG and the hydrophobic block poly-($tert$-butyl acrylate-ran-n-butyl acrylate). By adjusting the ratio of $tert$-butyl acrylate and n-butyl acrylate monomer concentrations, we varied the glass transition temperature T_g of the hydrophobic core from -46°C to 25°C. This modification the equilibrium between micelles and unimers in solution, demonstrating that chemical modifications can be used to control micelle design for specific applications.

Finally, Chapter 6 focuses on the ligand exchange mechanisms in oleate (OA)-capped PbS quantum dots titrated with excess free oleic acid (OAH). Combining ^{1}H NMR spectroscopy and diffusometry, I accurately quantified the ligand population fractions in three states and tracked the changes in these fractions with temperature and OAH titration concentration. I determined the thermodynamic parameters for two ligand binding modes (strong and weak) using a Langmuir adsorption model and determined kinetic exchange rates and activation energies through dynamic NMR. This comprehensive study, combining experimental data and theoretical models, offers significant insights into ligand-QD interactions and lays the foundation for future work on ligand design and the development of quantum dot interactions and lays the foundation for future work on ligand design and the development of QD materials for various applications.

7.2. Future Work

7.2.1. Dispersity studies in polyelectrolytes

As detailed in Chapter 3, we determined the molecular weight of the polyelectrolytes in semidilute unentangled regime using NMR diffusometry. However, many synthetic polyelectrolytes exhibit a disperse of molecular weights. Characterizing their molecular weight dispersity, is a fundamental requirement for advancing these materials in various applications. NMR diffusometry offers a robust technique to characterize the distribution of sizes (hydrodynamic radii) of diffusing species and thus their molecular weights.

Using NMR diffusometry, the polydispersity of polyelectrolytes can be determined by a blend of polyelectrolytes with known molecular weights and low dispersity are very low (Đ ≈ 1), in the semidilute unentangled regime. Specifically fitting the NMR diffusometry signal decay of the polyelectrolyte blends using a discrete multi-component Rouse model as shown in **Equation 7.1**.

$$\frac{I}{I_0} = \sum_i \phi_i e^{-bD_i} \tag{7.1}$$

In this equation, ϕ_i represent the mass fraction of polymer chain "i" in a polymer blend, where the diffusion coefficient is D_i and $\sum_i \phi_i = 1$. Since $D \propto N^{-1}$ for a polyelectrolyte in a semidilute unentangled regime (where N is number of repeat units), we can determine the number-average N_n and weight-average N_w using **Equations 7.2** and **7.3** respectively.

$$N_n = \frac{ckT\xi^2}{6\eta_s} \frac{\sum_i {\phi_i}^2/D_i}{\sum_i \phi_i} \tag{7.2}$$

$$N_w = \frac{ckT\xi^2}{6\eta_s} \frac{\sum_i {\phi_i}^3/{D_i}^2}{\sum_i {\phi_i}^2/D_i} \tag{7.3}$$

We analyzed the dispersity from NMR diffusometry by preparing a binary blend of equal mass fraction (50:50) of 35K and 457K cesium polystyrene sulfonate (CsPSS) polymers. These blends were dissolved in H_2O and their overall concentrations were varied from 0.046 M to 0.091 M. The NMR signal attenuation, from NMR diffusometry experiment, was fit using **Equation 7.1** to get the parameters ϕ_i and D_i for 35K and 457K CsPSS polyelectrolyte chains. **Figure 7.1** shows the log-transformed NMR signal decay plots of binary blends and **Table 7.1** lists the parametric values for these blends. The dotted lines in the figure represent the diffusion coefficients of neat 35K and 457K CsPSS polymer chain solutions at 0.063 M (semidilute unentangled regime).

Table 7.2: Mass fractions and diffusion coefficients of 35K and 457K polymer chains determined using a multicomponent rouse model in a 50:50 polymer blend.

	Concentration (M)	ϕ_{35K}	ϕ_{457K}	D_{35K} (10^{-12} m^2/s)	D_{457K} (10^{-12} m^2/s)
50-50 35K-457K Binary Blend	0.0426	64%	36%	27	5.7
	0.063	48%	52%	24	5.3
	0.091	55%	45%	28	5.6
Neat 35K	0.063	100%	0%	33	NA
Neat 45K	0.063	0%	100%	NA	4.3

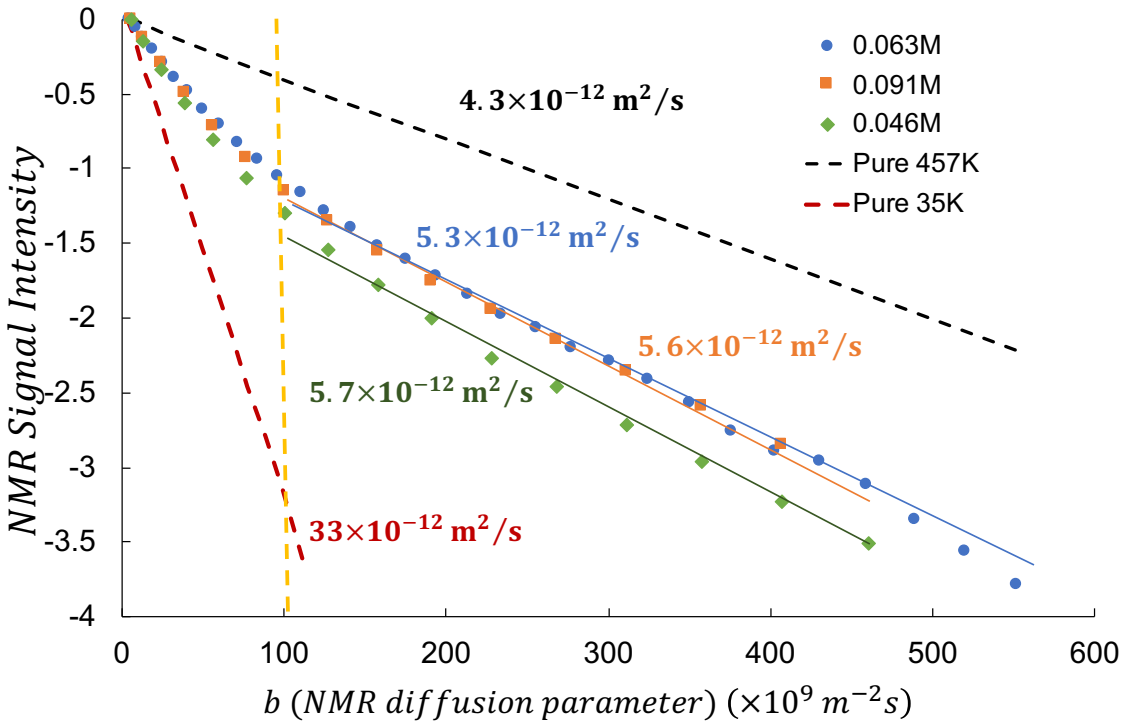

Figure 7.16: Stejskal-Tanner plots (NMR signal attenuation curve) for a 50:50 (wt%) binary mixture of 35K and 457K CsPSS polyelectrolytes with overall polymer concentration varied from 0.046 M to 0.091 M. The dashed lines show the linear NMR signal decays for neat 35K and 457K solutions (D values indicated). The solid lines for the blends are drawn for visual guide but do not represent the actual fits from the rouse model.

The diffusion coefficients obtained from the fits reveal notable differences between the 35K and 457K CsPSS polymer chains in blends compared to their diffusion coefficients in neat solutions. Resolving these discrepancies, either by fixing the developed Rouse model or by adjusting the experimental setup, could enable more accurate determination of dispersity in polyelectrolyte blends. It is well established that the nuclear spin dynamics in highly viscous samples or for polymers with very-high molecular weight are more complex, necessitating further investigation, particularly through studies of relaxation dynamics.

An alternate to fitting the NMR signal attenuation using the discrete Rouse model is to apply a diffusion distribution function, such as the gamma function or normal distribution function.

This approach would allow us to utilize fewer parameters while still determining the molecular weight dispersity. This approach, along with the corresponding studies will be focus of future work.

7.2.2. Ligand exchange studies using different native and incoming ligands

In chapter 5, we studied the ligand exchange mechanism, by titrating free oleic acids (OAH) into a solution containing oleate (OA)-capped PbS quantum dots (QDs). Although both the native ligand (OA) and the incoming ligand (OAH) share same chemical structure, introducing a ligand with different binding moiety and chemical structure can alter the chain kinetics and dynamics and thereby influencing the energetics of the exchange mechanism. Consequently, in future studies, I aim to titrate OA-capped PbS QD solution with undec-10-eonic acid (UDA). UDA presents a distinct terminal alkenyl proton, detectable in the NMR spectrum as shown in **Figure** 7.2 below. This allows for the measurement of diffusion coefficients of UDA and OA in the solution and quantify their population fractions in different states. This study will provide critical insights into the design parameters necessary for optimizing and tuning QD properties for various applications.

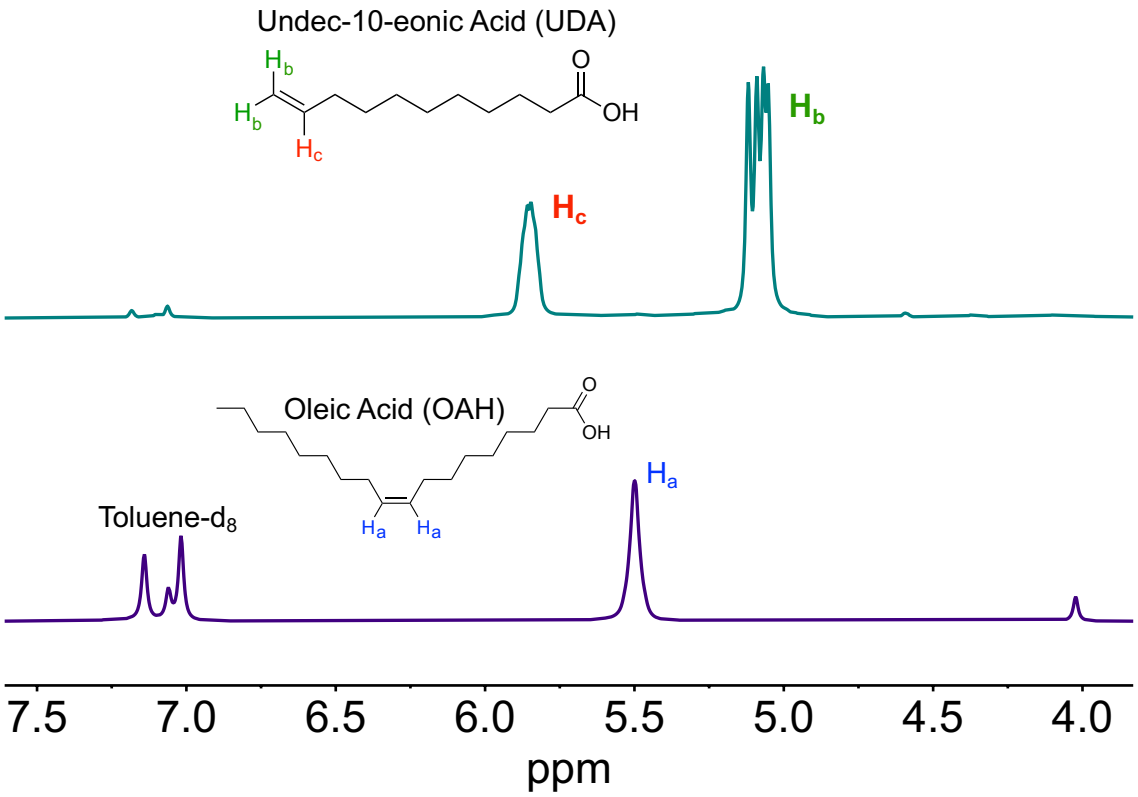

Figure 7.17: ^{1}H NMR spectrum of Oleic Acid (OAH) and undec-10-eonic acid (UDA) in toluene-d_8 solvent. Alkenyl proton signal for OAH (H_a) and UDA (H_b, H_c) are well resolved and hence allowing us to quantify their population fractions in different states using NMR diffusometry and study the ligand exchange mechanism.

In summary, this dissertation aimed to provide more insights into the fundamental properties of materials by probing molecular transport, quantifying molecules in different chemical environments, and determining molecular exchange rates in complex systems, with each of these insights covering a range of time and length scales. These measurements were critical in correlating the design and performance metrics of the materials and their advancements for newer technologies.

Appendix I. Supporting Information for: Strong Variation of Micelle-Unimer Coexistence as a Function of Core Chain Mobility

Ryan J. Carrazzone,[†,⊥] Xiuli Li,[†,⊥] Jeffrey C. Foster,[‡] Candace Wall,[†] Alan R. Esker,[†] Louis A. Madsen,[*,†] and John B. Matson[*,†]

†*Department of Chemistry and Macromolecules Innovation Institute, Virginia Tech, Blacksburg, VA, 24061, United States*
‡ *School of Chemistry, University of Birmingham, Edgbaston, B15 2TT Birmingham, United Kingdom*
⊥*R. J. Carrazzone and X. Li contributed equally to this work*

Materials

All reagents were obtained from commercial vendors and used as received unless otherwise stated. 2,2′-Azobis(2-methylpropionitrile) (AIBN) was recrystallized from methanol prior to use. Monomers *n*-butyl acrylate (*n*BA) and *tert*-butyl acrylate (*t*BA) were purchased from Alfa Aesar and passed through a plug of basic alumina prior to use. Dry solvents were purified by passage through a solvent purification system (MBraun).

Methods

NMR spectra for characterization of molecular structures were measured on an Agilent 400 MHz spectrometer. ^{1}H and ^{13}C NMR chemical shifts are reported in ppm relative to internal solvent resonances. Yields refer to chromatographically and spectroscopically pure compounds unless otherwise stated. Size exclusion chromatography (SEC) was carried out in THF at 1 mL/min at 30 °C on two Agilent PLgel 10 μm MIXED-B columns connected in series with a Wyatt Dawn Heleos 2 multi-angle light scattering detector and a Wyatt Optilab Rex refractive index detector. No calibration standards were used, and d*n*/d*c* values were obtained by offline differential refractive index measurements. Dynamic light scattering (DLS) was conducted using a Malvern Zetasizer Nano operating at 25 °C. A solution of micelles was prepared at 5 mg/mL and filtered with a 0.2 μm filter prior to scanning. Calculations of the particle size distributions and distribution averages were conducted using CONTIN particle size distribution analysis routines with number, volume, and intensity averages. Measurements were made in triplicate and errors reflect standard deviations. Static light scattering measurements were performed with a Wyatt Dawn Heleos 2 multi-angle light scattering detector operating in batch mode. Micelle solutions were prepared at known concentrations and filtered with a 0.2 μm filter prior to scanning. Absolute weight-average molecular weights of aggregates were calculated using Wyatt ASTRA software. Differential

scanning calorimetry (DSC) studies were carried out on a Q-2000 DSC in aluminum pans operated with a dry nitrogen purge from -10 °C to 100 °C with a heating and cooling rate of 5 °C/min modulated ±3 °C/min. Results are reported from the second heat cycle and figures are shown as exo down.

Synthesis of 2-methyl-2-(dodecylsulfanylthiocarbonyl)sulfanyl propanoic acid (CTA)

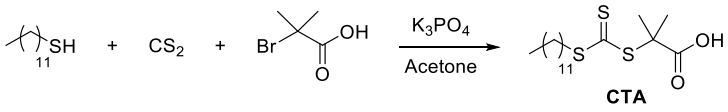

Dodecanethiol (5 mL, 20.9 mmol) was dissolved in acetone (30 mL) in a round bottom flask. To the flask was added tribasic potassium phosphate (8.86 g, 41.7 mmol). The reaction mixture was stirred at rt for 10 min. CS_2 (3.78 mL, 62.6 mmol) was added dropwise, and the reaction mixture was stirred for an additional 1 h. To the flask a solution of 2-bromo-2-methyl propanoic acid (3.91 g, 23.4 mmol) in 5 mL of acetone was added dropwise. The reaction mixture was stirred overnight at rt. Reaction conversion was monitored by TLC using CH_2Cl_2 as eluent and visualized via UV lamp. The reaction mixture was diluted with ~100 mL of CH_2Cl_2, transferred to a separatory funnel, and washed consecutively with 1N HCl and brine. The organic layer was dried over Na_2SO_4 and concentrated via rotary evaporation. Silica gel was added to the concentrated solution before removing the rest of the solvent via rotary evaporation. The silica was dry-loaded onto a silica gel column, and the product was eluted with CH_2Cl_2. The product containing fractions, as determined by TLC (CH_2Cl_2 eluent and UV lamp visualization), were combined and concentrated via rotary evaporation to yield a yellow solid. The crude product was recrystallized from hexanes to yield yellow crystals (4.88 g, 64% yield).The ^{1}H and ^{13}C NMR spectra matched those from published reports. [1]

^{1}H NMR (400 MHz, $CDCl_3$) δ (ppm): 3.25 (2H, t, J = 7.4 Hz, H_d); 1.70 (6H, s, H_e); 1.64 (2H, m, H_c); 1.37 (2H, m, H_b); 1.25 (18H, m, H_b); 0.88 (3H, t, J = 6.9 Hz, H_a)

^{13}C NMR (400 MHz, $CDCl_3$) δ (ppm): 220.78 (C_d); 178.84 (C_g); 55.59 (C_e); 37.12 (C_c); 31.89-26.21 (C_b); 23.69 (C_f); 14.13 (C_a)

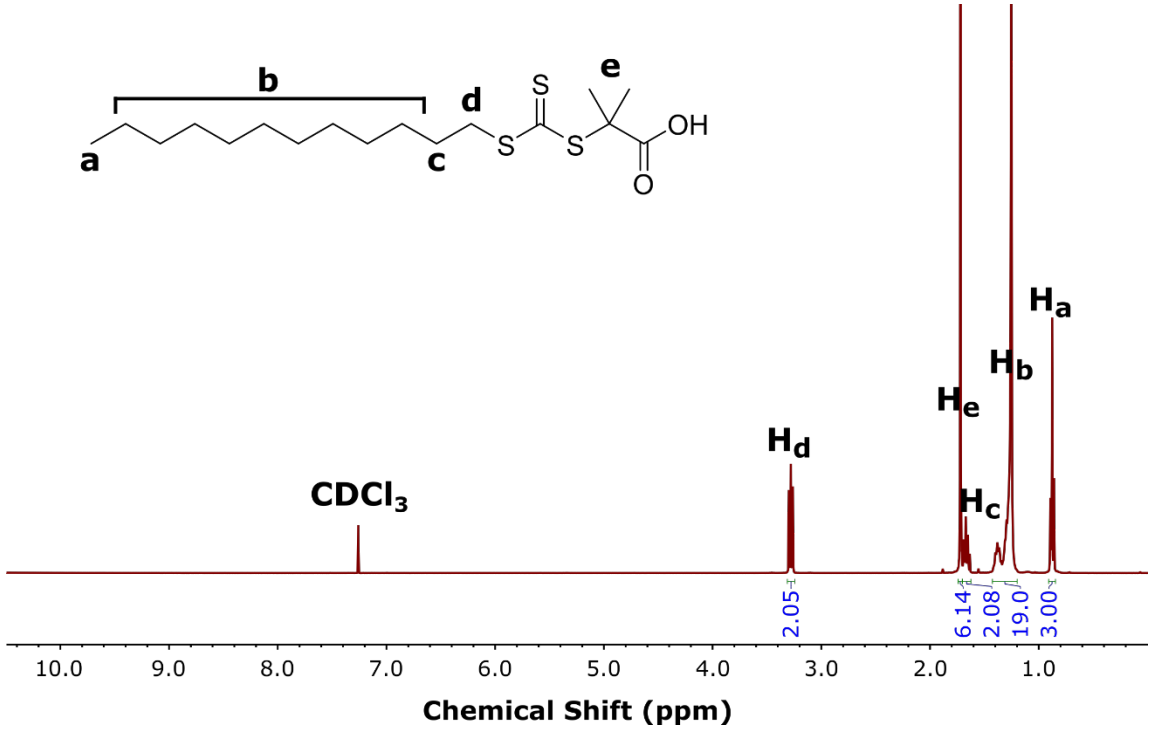

Figure 5S1. ^{1}H NMR spectrum of 2-methyl-2-(dodecylsulfanylthiocarbonyl)sulfanyl propanoic acid **(CTA)**.

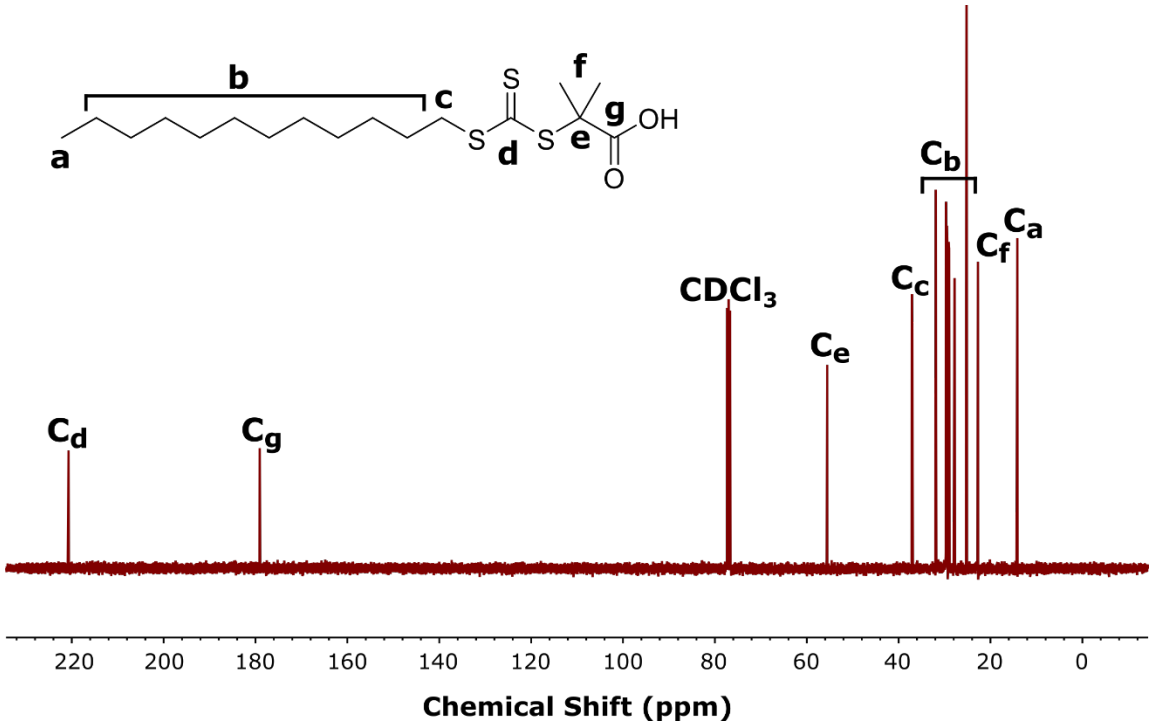

Figure 5S2. ^{13}C NMR spectrum of 2-methyl-2-(dodecylsulfanylthiocarbonyl)sulfanyl propanoic acid **(CTA)**.

Synthesis of macroCTA

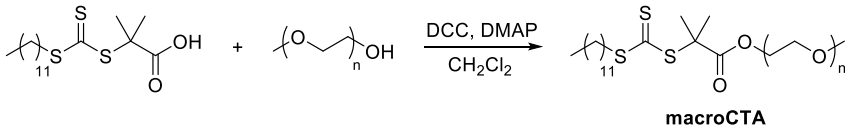

A round bottom flask was charged with **CTA** (0.91 g, 2.50 mmol), polyethylene glycol monomethyl ether (M_n = 4,000 g/mol, 5.0 g, 1.25 mmol), 4-dimethylamino pyridine (0.15 g, 1.25 mmol), and anhydrous CH_2Cl_2 (5.0 mL). *N*,*N*'-Dicyclohexylcarbodiimide (DCC) (0.52 g, 2.50 mmol) was dissolved in 5.0 mL of anhydrous CH_2Cl_2 in a vial. The DCC solution was added dropwise to the flask containing the other reagents, and the reaction mixture was stirred at rt overnight. Reaction conversion was followed by TLC using CH_2Cl_2 as eluent and visualized via UV lamp. The precipitated solids were removed by filtration. The desired product was isolated via precipitation from diethyl ether and was purified by repeated precipitations (2-4) from CH_2Cl_2 into

diethyl ether until complete removal low molecular weight side products was confirmed by ^{1}H NMR spectroscopy to afford the product as a yellow solid (1.50 g, 69% yield). The ^{1}H NMR spectrum matched those from published reports. [2]

^{1}H NMR (400 MHz, $CDCl_3$) δ (ppm): 4.24 (2H, t, J = 5.0 Hz, H_f); 3.81 (2H, t, J = 4.8 Hz, H_g); 3.63 (~360H, m, H_h); 1.37 (2H, m, H_b); 3.37 (3H, s, H_i); 3.25 (2H, t, J = 7.4 Hz, H_d); 1.69 (6H, s, H_e); 1.64 (2H, m, H_c); 1.25 (18H, m, H_b); 0.87 (3H, t, J = 6.6 Hz, H_a)

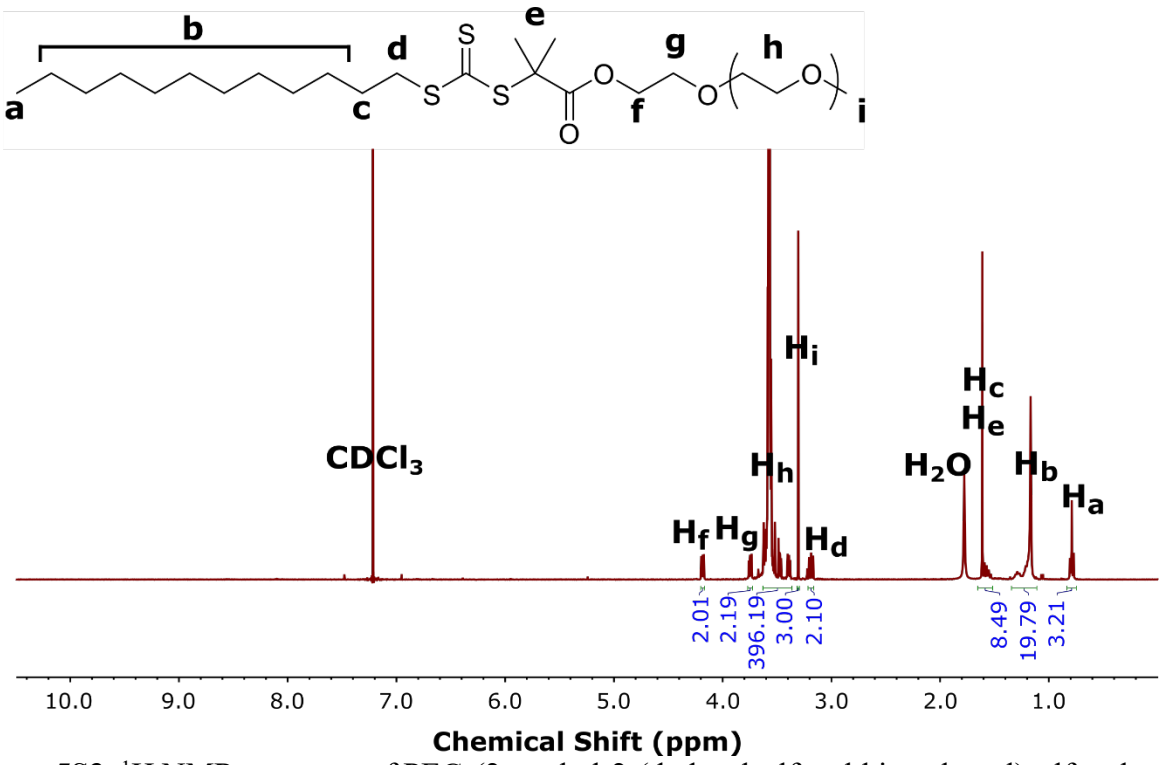

Figure 5S3. ^{1}H NMR spectrum of PEG-(2-methyl-2-(dodecylsulfanylthiocarbonyl)sulfanyl propanoic acid) **(macroCTA)**.

Synthesis of PEG-b-poly(nBA-ran-tBA) copolymers

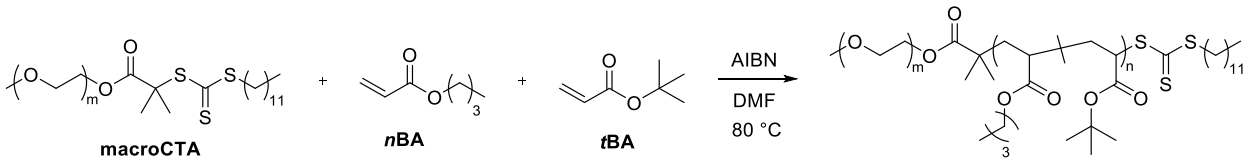

A typical polymerization procedure is as follows: An oven-dried Schlenk tube was equipped with a magnetic stir bar and was evacuated on a Schlenk line and refilled with N_2 gas. Next, **macroCTA** (200 mg, 0.046 mmol), ***n*BA** (0.185 mL, 1.29 mmol), ***t*BA** (0.187 mL, 1.29 mmol), and 1.5 mL of anhydrous DMF were added via gas-tight syringe through a septum under N_2 flow. A separate solution of AIBN was prepared by dissolving 3.8 mg (0.023 mmol) in 1 mL of anhydrous DMF in a vial. 100 µL of this solution was added to the Schlenk tube. The tube was then deoxygenated by subjecting the contents to three freeze−pump−thaw cycles. The Schlenk tube was then backfilled with N_2 and submerged in an oil bath maintained at 80 °C. Samples were removed periodically by N_2-purged syringe to monitor molar mass evolution by SEC and monomer conversion by ^{1}H NMR spectroscopy. The polymerization was quenched by submerging the tube into liquid N_2 and exposing the reaction mixture to air. The resulting PEG-*b*-poly(*n*BA-*ran*-*t*BA) was isolated via precipitation into a large excess of cold 1:1 hexanes:ether. If necessary, further precipitations from CH_2Cl_2 into cold 1:1 hexanes:ether were performed to remove residual monomer.

Synthesis of poly(nBA-ran-tBA) copolymers

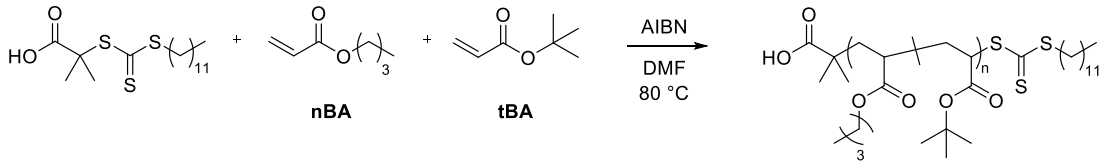

A typical polymerization procedure is as follows: An oven-dried Schlenk tube was equipped with a magnetic stir bar and was evacuated on a Schlenk line and refilled with N_2 gas. Next **CTA** (25 mg, 0.069 mmol), ***n*BA** (980 µL, 6.9 mmol), ***t*BA** (990 µL, 6.9 mmol), and 1.5 mL of anhydrous DMF were added via gas-tight syringe through a septum under N_2 flow. A separate solution of AIBN was prepared by dissolving 11 mg (0.069 mmol) in 1 mL of anhydrous DMF in a vial. 100 µL of this solution was added to the Schlenk tube. The tube was then deoxygenated by subjecting the contents to three freeze−pump−thaw cycles. The Schlenk tube was then backfilled with N_2 and submerged in an oil bath maintained at 80 °C. Samples were removed periodically by N_2-purged syringe to monitor molar mass evolution by SEC and monomer conversion by ^{1}H NMR spectroscopy. The polymerization was quenched by submerging the tube into liquid N_2 and exposing the reaction mixture to air. The resulting Poly(*n*BA-*ran*-*t*BA) was isolated via precipitation into a large excess of cold 3:1 hexanes:ether. If necessary, further precipitations from CH_2Cl_2 into cold 3:1 hexanes:ether were performed to remove residual monomer.

PEG-b-P(nBA-ran-tBA) micelle assembly

A typical micelle assembly procedure is as follows: A scintillation vial equipped with a stir bar was charged with polymer (50 mg) and THF (1 mL). Distilled H_2O (7 mL) was added dropwise to the vial via syringe pump over 70 minutes, and the solution was allowed to stir afterwards for 15 min. The solution was transferred to dialysis tubing (6-8 kD MWCO) and dialyzed against distilled water for 18 h, changing the water once after 2 h and again after 4 h. The resulting aqueous solution

was removed from the dialysis tubing and diluted with distilled water to a final volume of 10.0 mL (5 mg/mL polymer concentration).

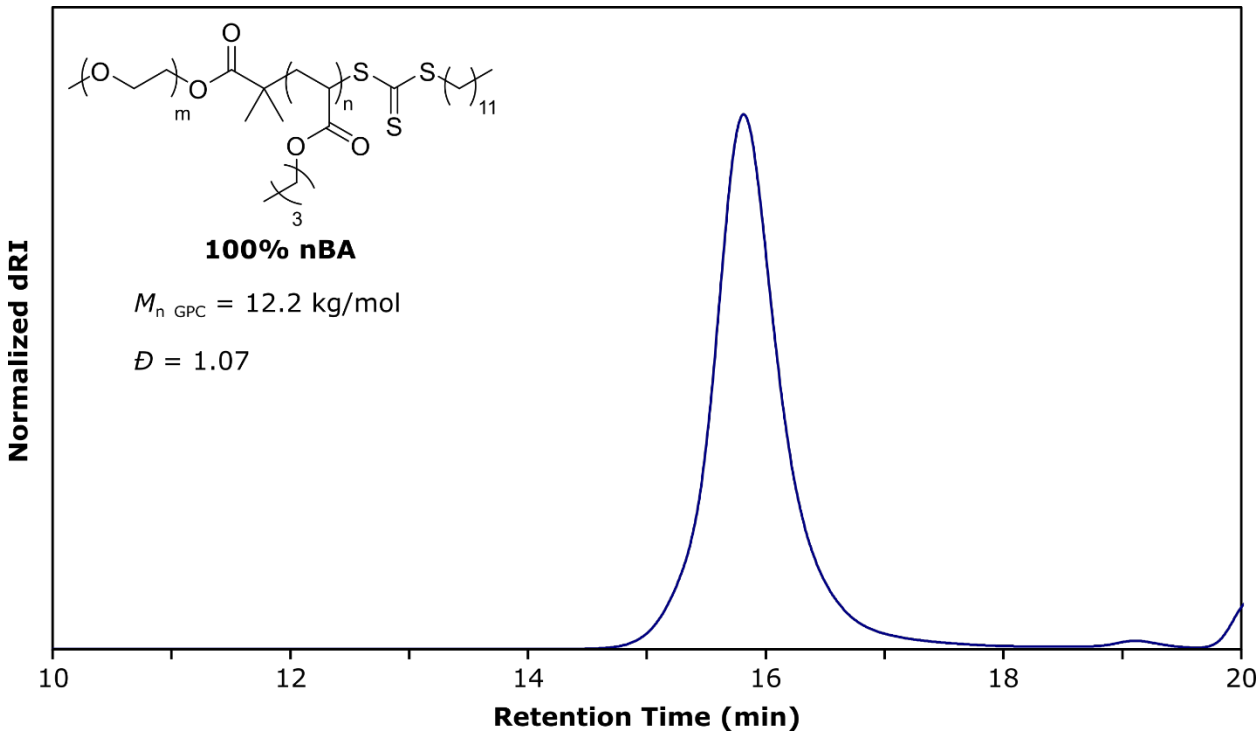

Figure 5S4. SEC trace of polymer **1a** (PEG-*b*-P(*n*BA)).

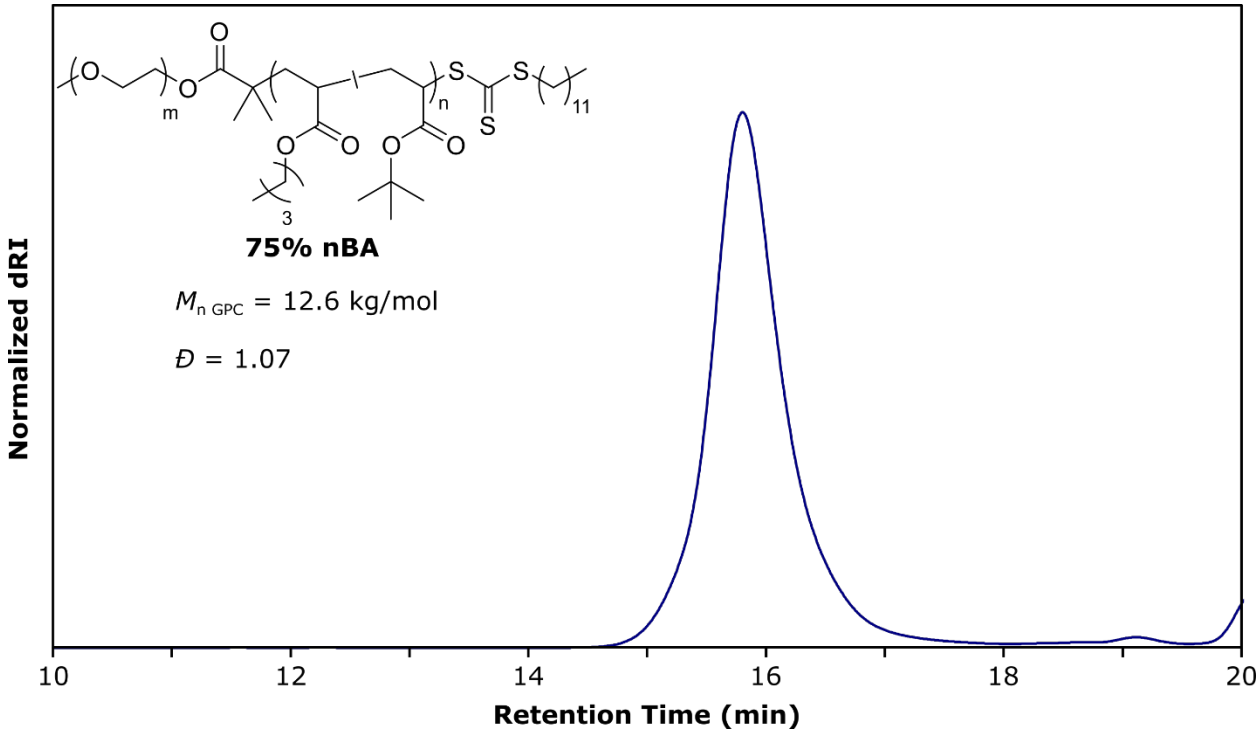

Figure 5S5. SEC trace of polymer **1b** (PEG-*b*-P(*n*BA-*ran*-*t*BA)).

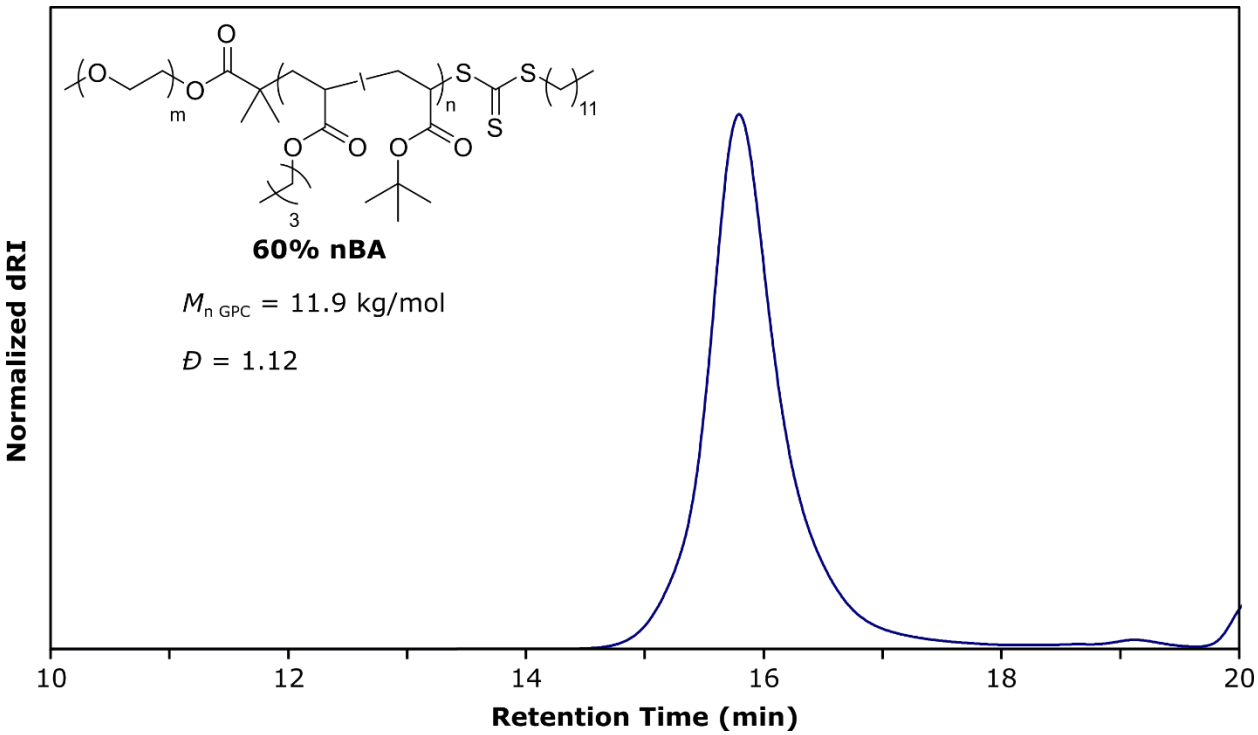

Figure 5S6. SEC trace of polymer **1c** (PEG-*b*-P(*n*BA-*ran*-*t*BA)).

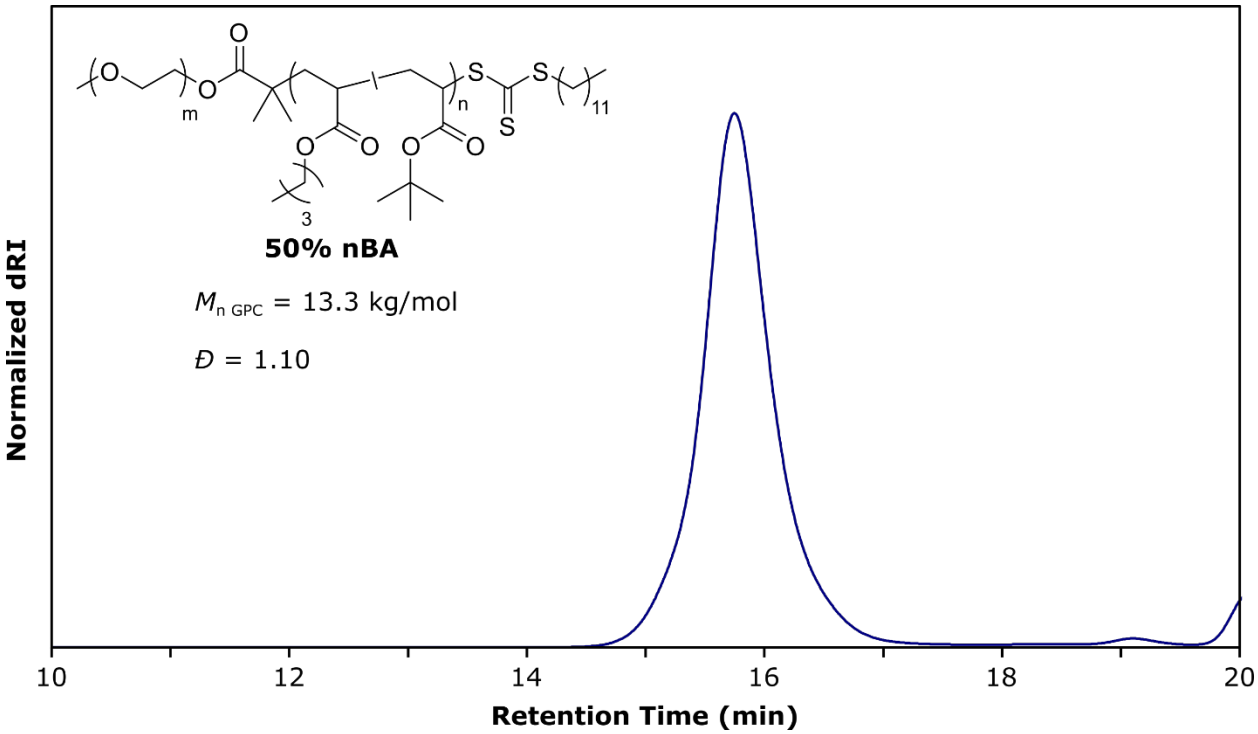

Figure 5S7. SEC trace of polymer **1d** (PEG-*b*-P(*n*BA-*ran*-*t*BA)).

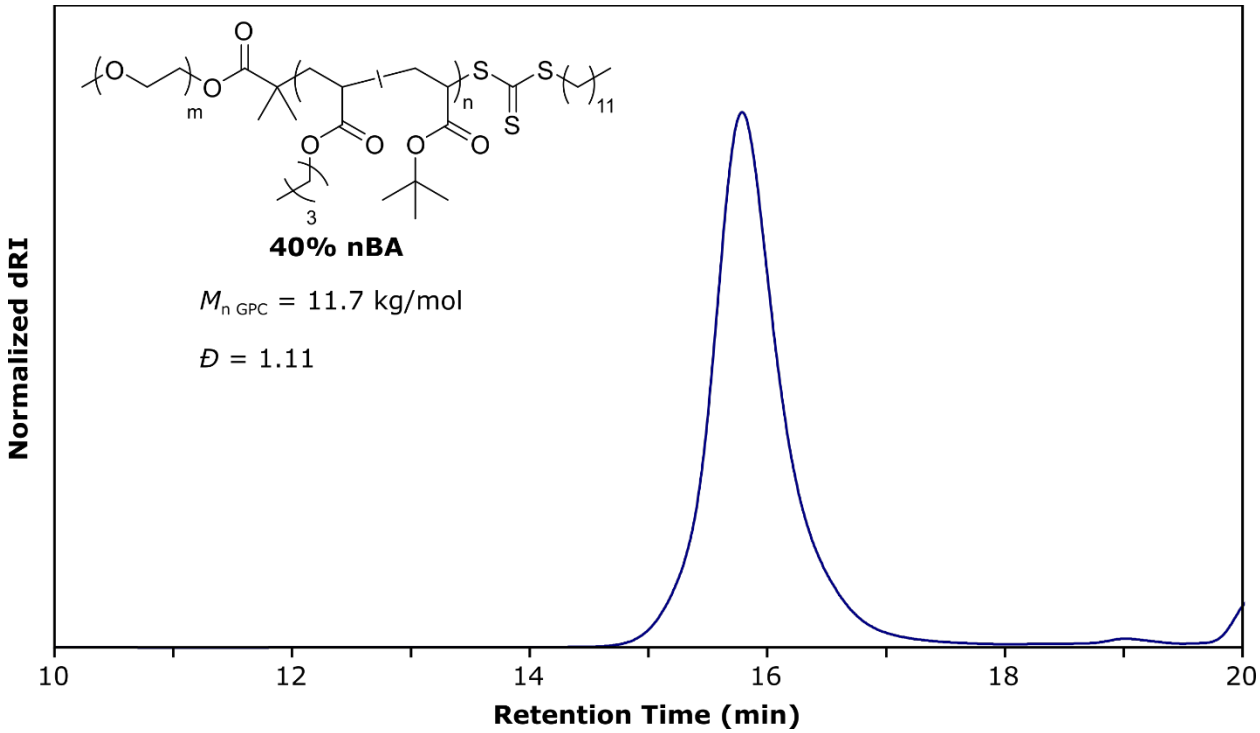

Figure 5S8. SEC trace of polymer **1e** (PEG-*b*-P(*n*BA-*ran*-*t*BA)).

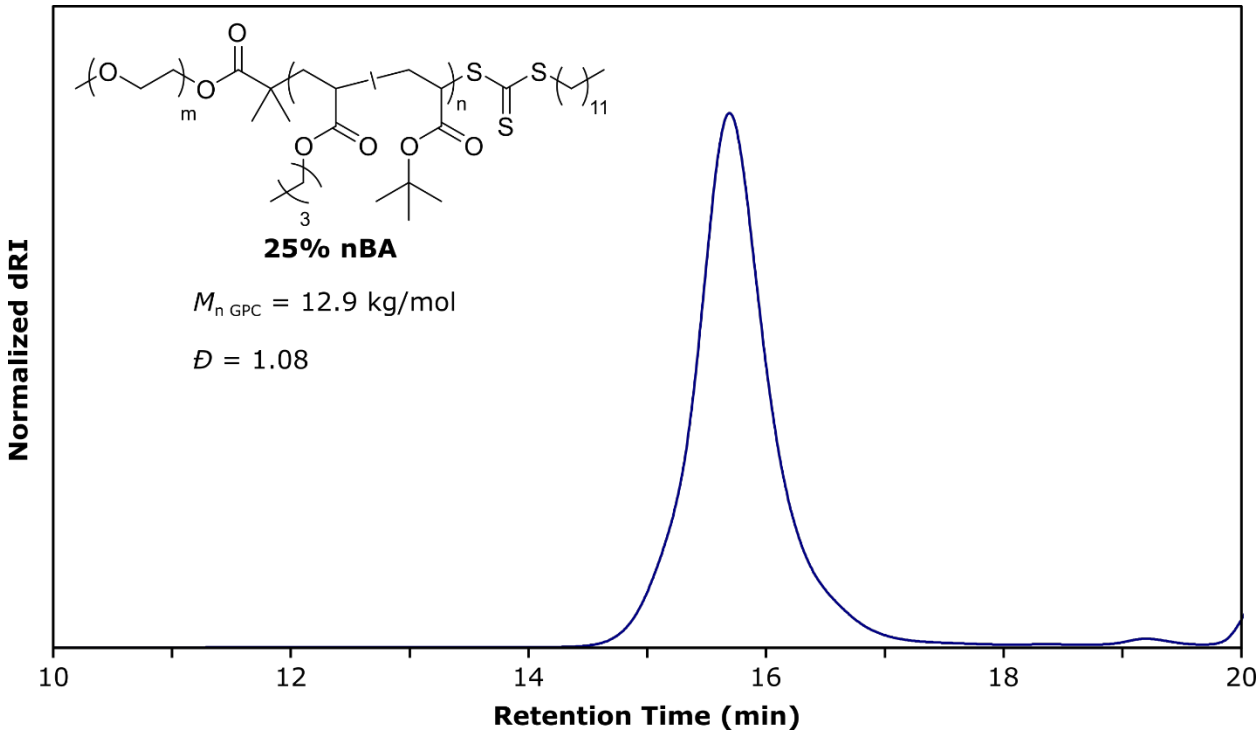

Figure 5S9. SEC trace of polymer **1f** (PEG-*b*-P(*n*BA-*ran*-*t*BA)).

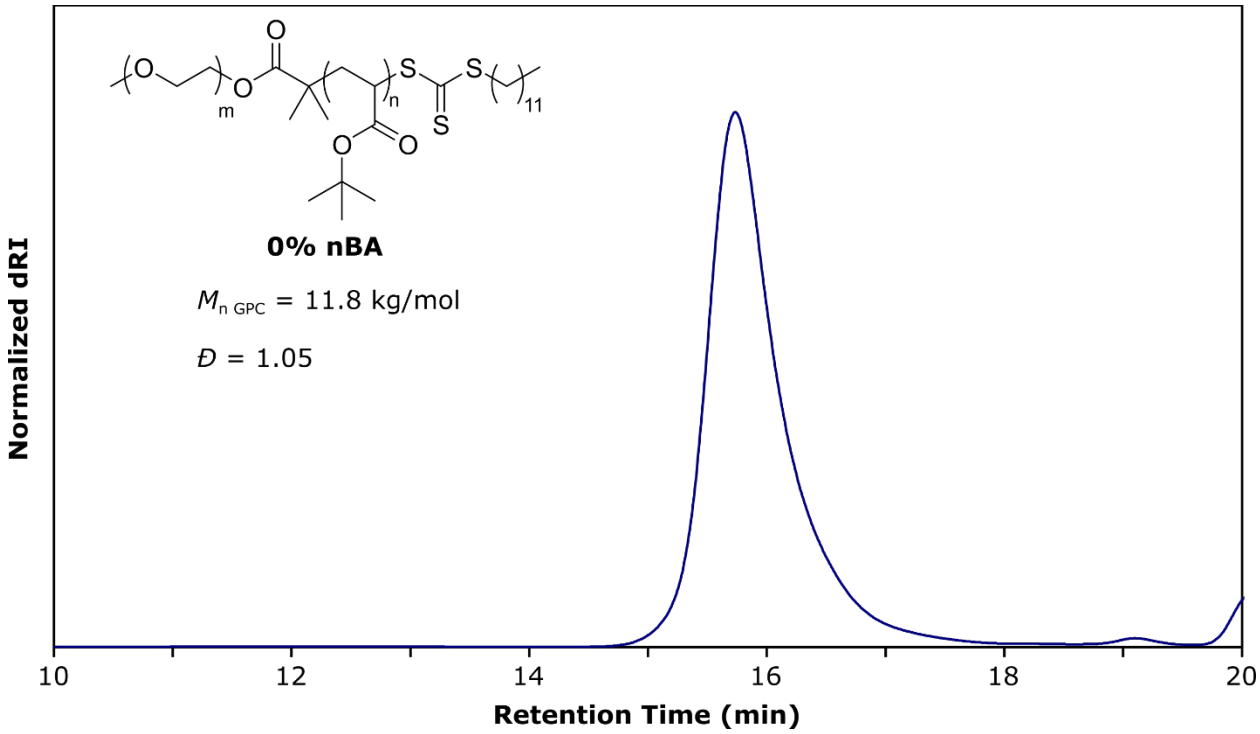

Figure 5S10. SEC trace of polymer **1g** (PEG-*b*-P(*t*BA)).

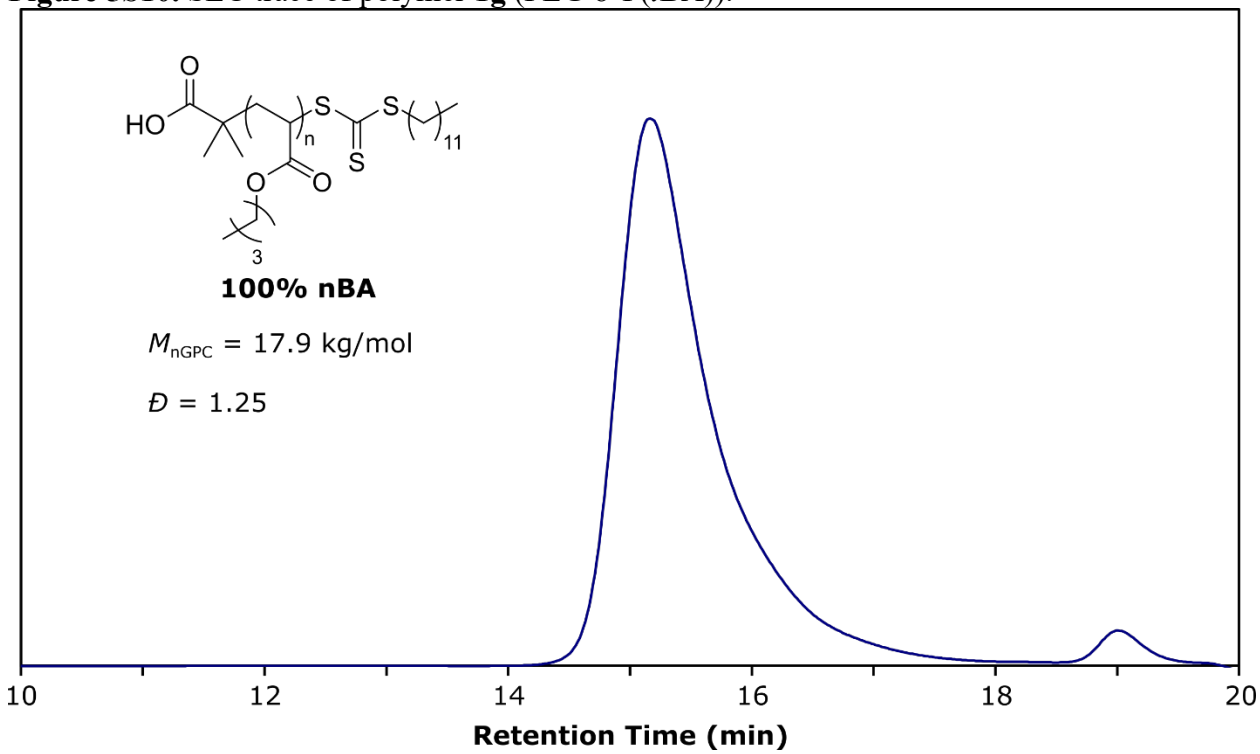

Figure 5S11. SEC trace of polymer **2a** (P(*n*BA)).

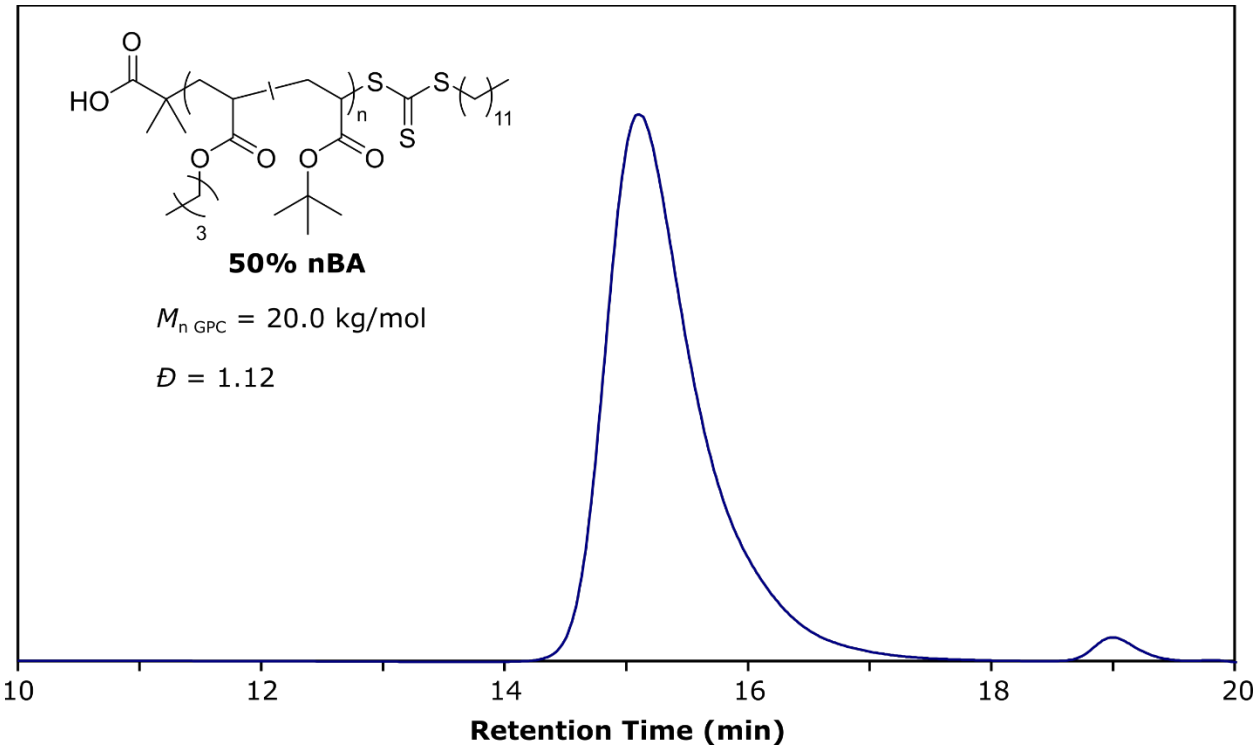

Figure 5S12. SEC trace of polymer **2b** (P(*n*BA-*ran*-*t*BA)).

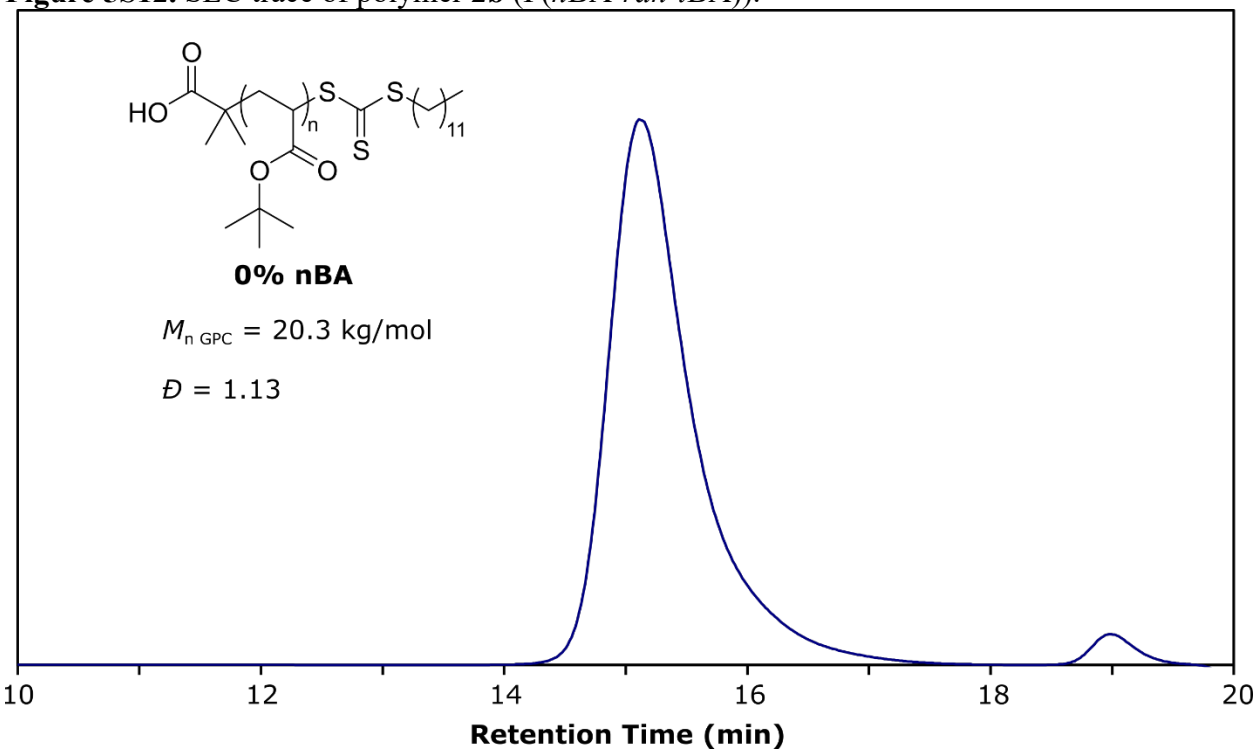

Figure 5S13. SEC trace of polymer **2c** (P(*t*BA)).

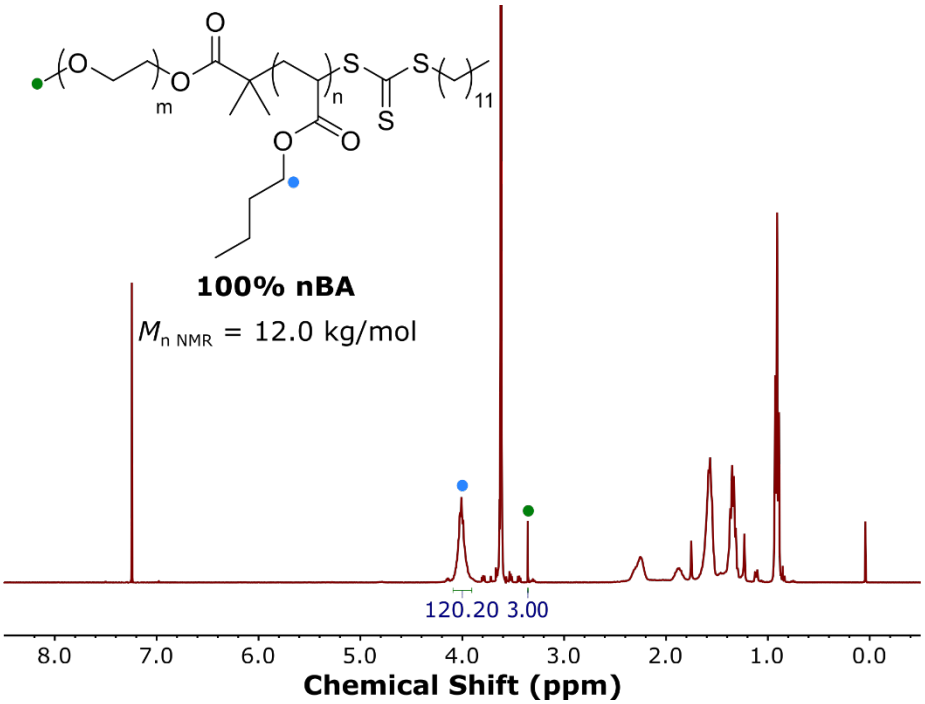

Figure 5S14. ^{1}H NMR spectrum of polymer **1a** (PEG-*b*-P(*n*BA)).

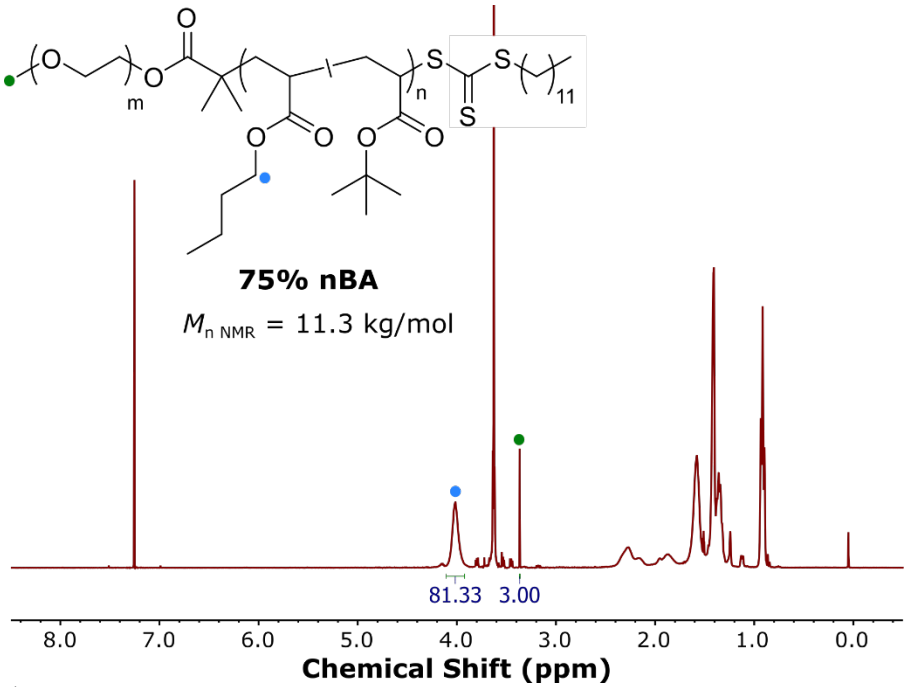

Figure 5S15. ^{1}H NMR spectrum of polymer **1b** (PEG-*b*-P(*n*BA-*ran*-*t*BA)).

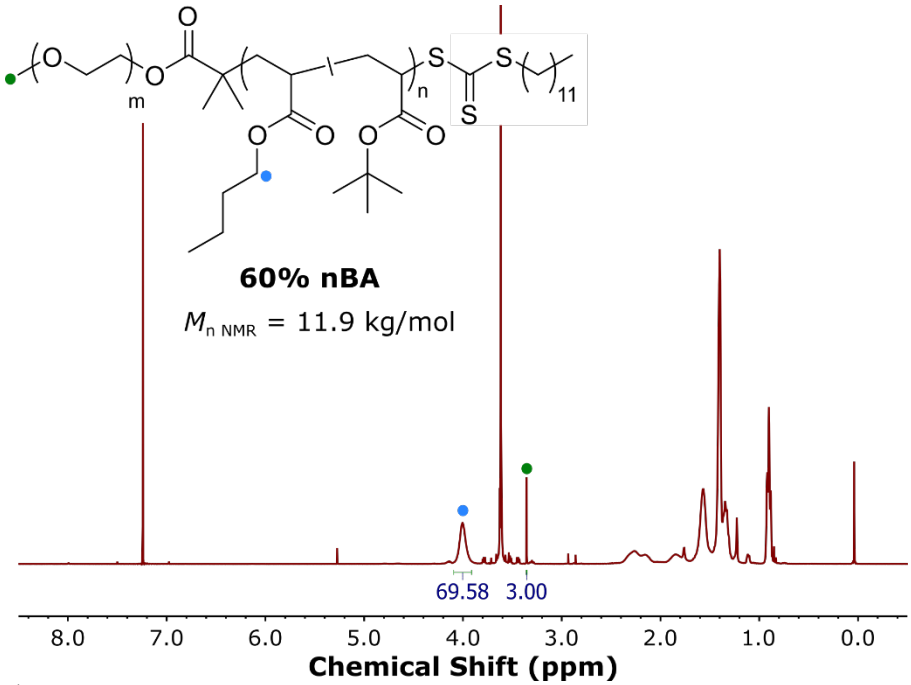

Figure 5S16. ^{1}H NMR spectrum of polymer **1c** (PEG-*b*-P(*n*BA-*ran*-*t*BA)).

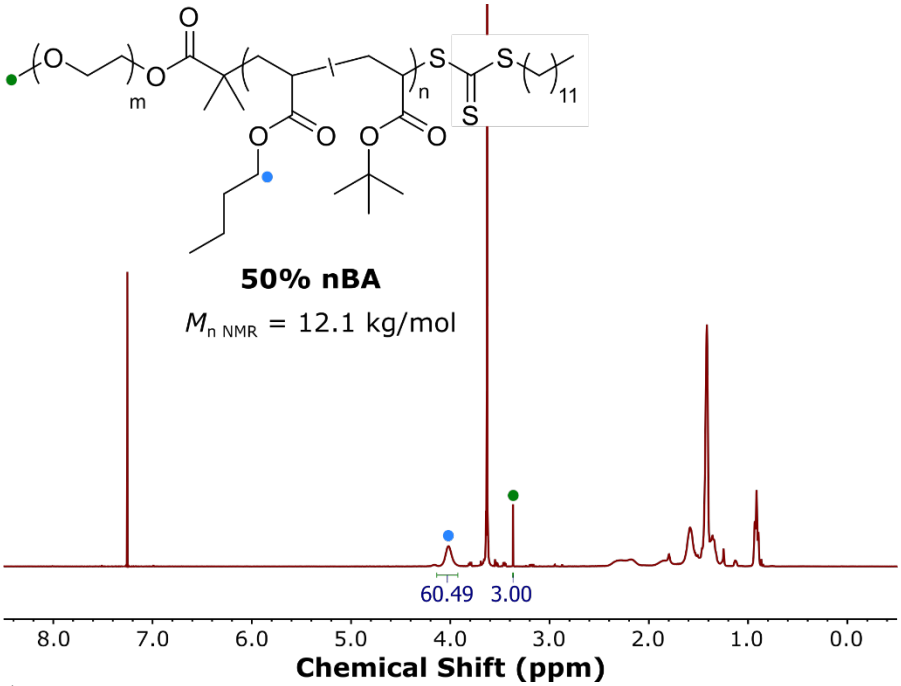

Figure 5S17. ^{1}H NMR spectrum of polymer **1d** (PEG-*b*-P(*n*BA-*ran*-*t*BA)).

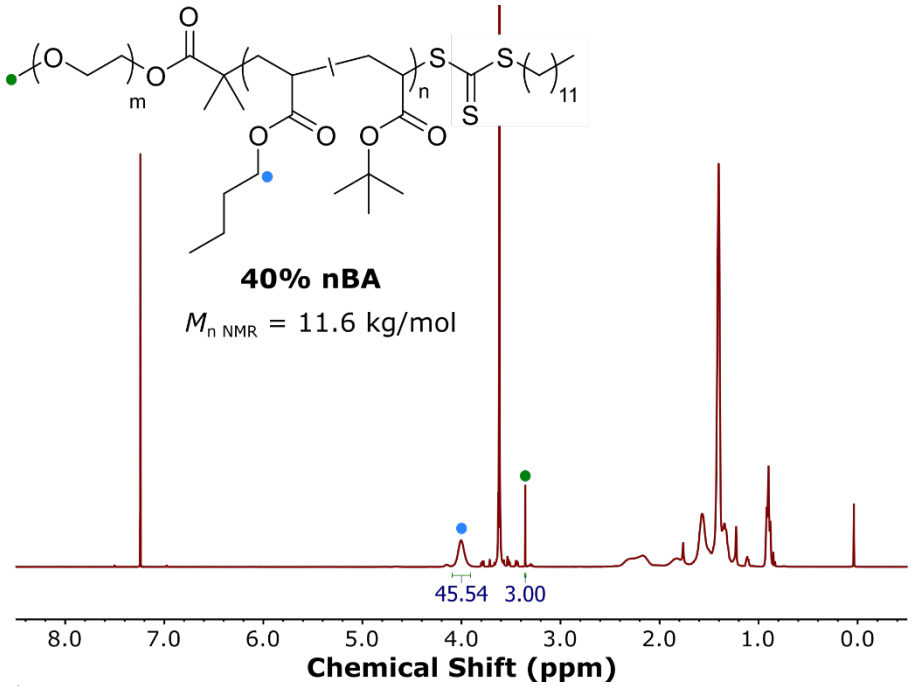

Figure 5S18. ^{1}H NMR spectrum of polymer **1e** (PEG-*b*-P(*n*BA-*ran*-*t*BA)).

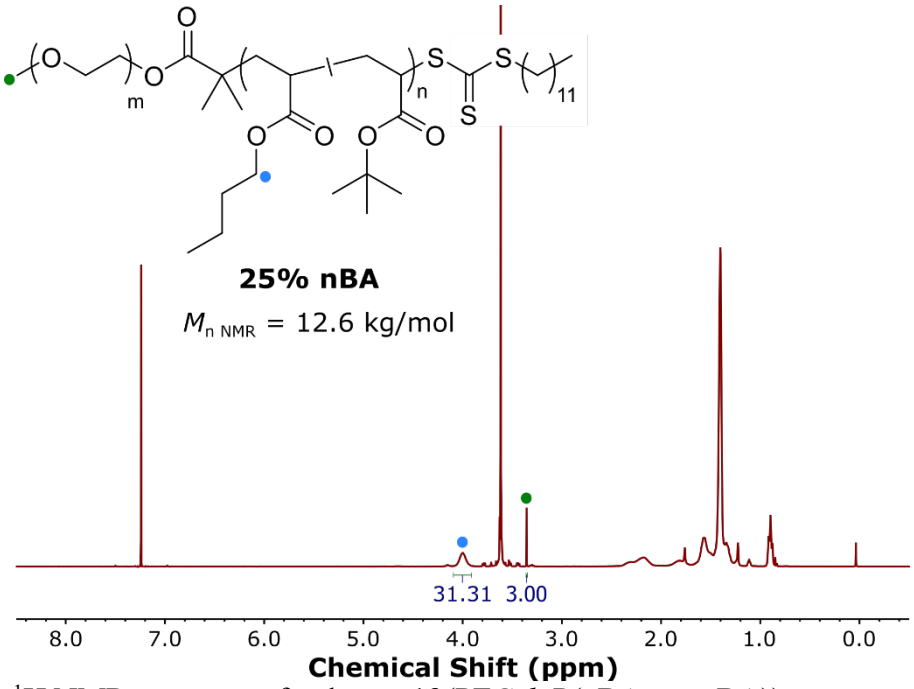

Figure 5S19. ^{1}H NMR spectrum of polymer **1f** (PEG-*b*-P(*n*BA-*ran*-*t*BA)).

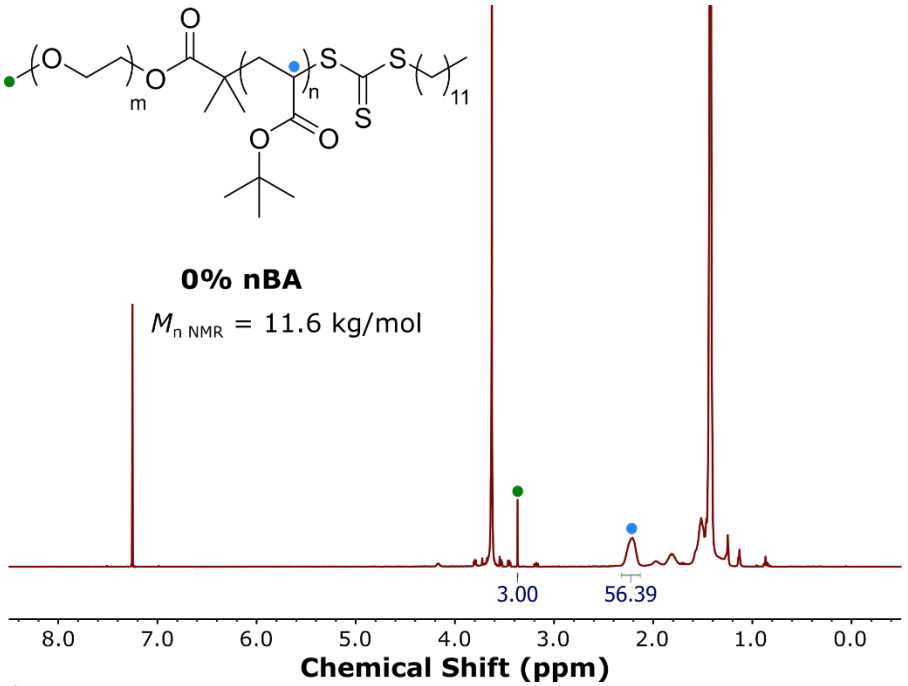

Figure 5S20. ^{1}H NMR spectrum of polymer **1g** (PEG-*b*-P(*t*BA)).

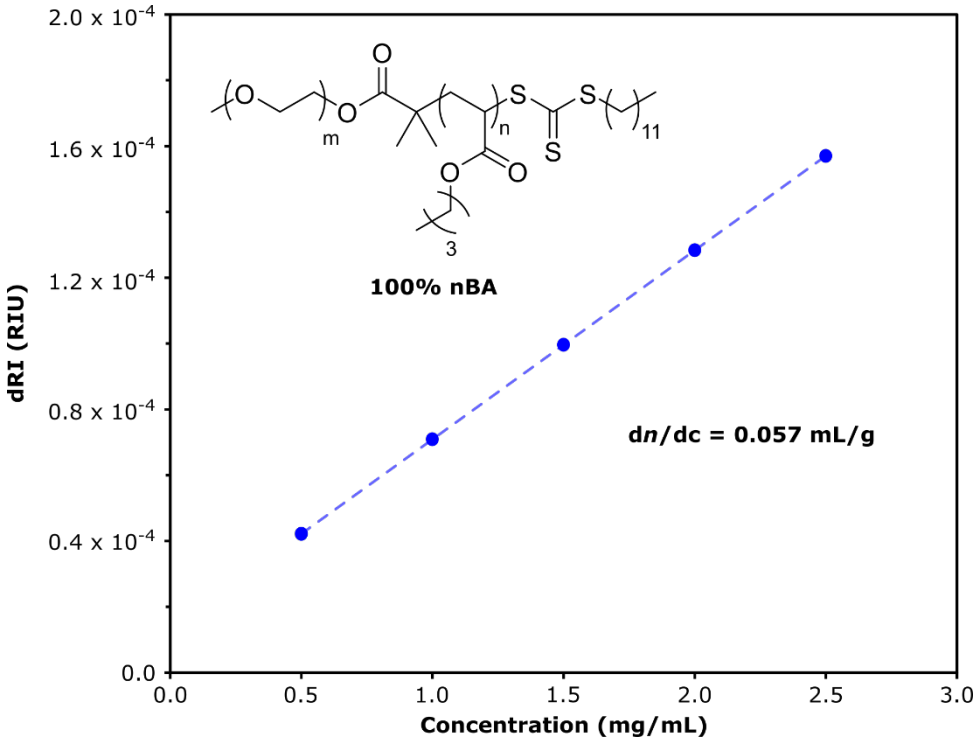

Figure 5S21. Concentration versus differential refractive index plot for polymer **1a** (PEG-*b*-P(*n*BA)). Measurements performed in THF at 25 °C.

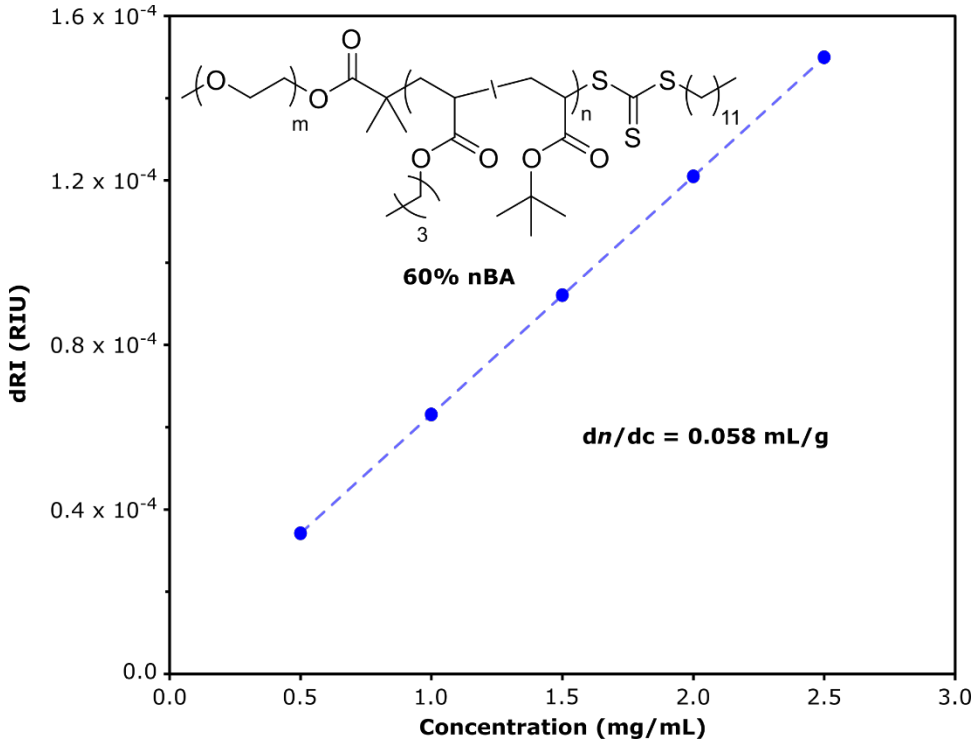

Figure 5S22. Concentration versus differential refractive index plot for polymer **1c** (PEG-*b*-P(*n*BA-*ran*-*t*BA)). Measurements performed in THF at 25 °C.

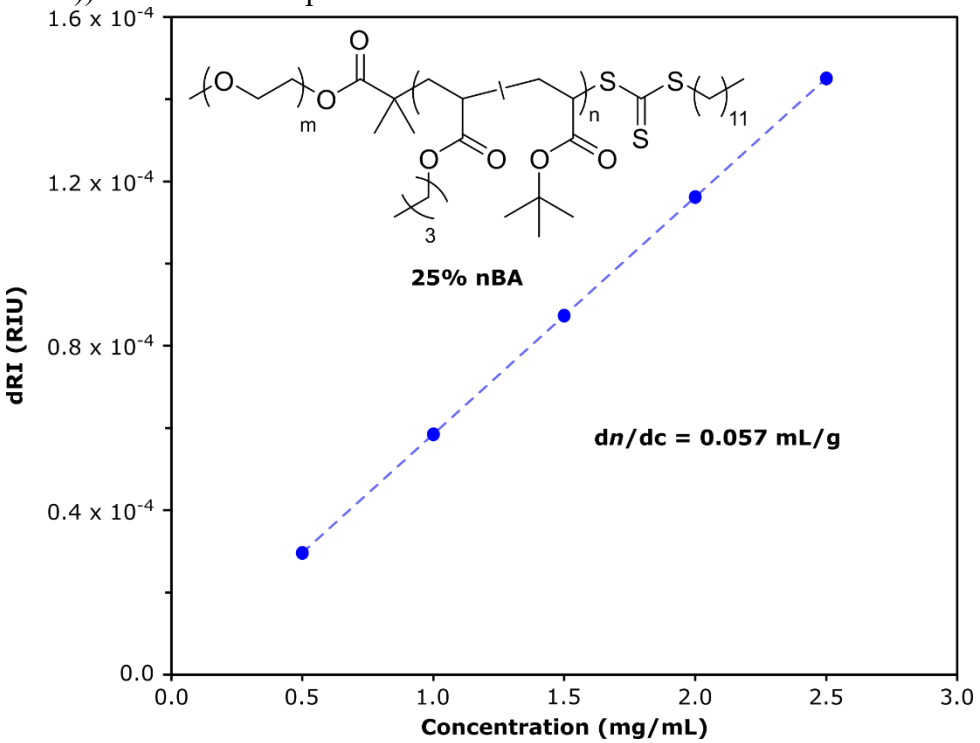

Figure 5S23. Concentration versus differential refractive index plot for polymer **1f** (PEG-*b*-P(*n*BA-*ran*-*t*BA)). Measurements performed in THF at 25 °C.

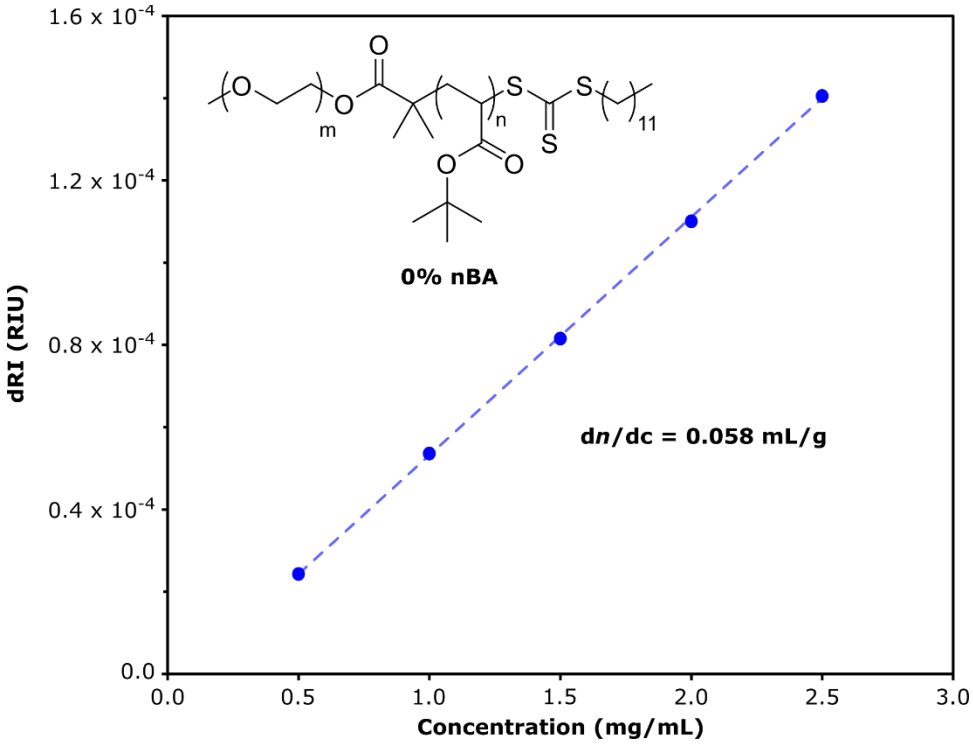

Figure 5S24. Concentration versus differential refractive index plot for polymer **1g** (PEG-*b*-P(*t*BA)). Measurements performed in THF at 25 °C.

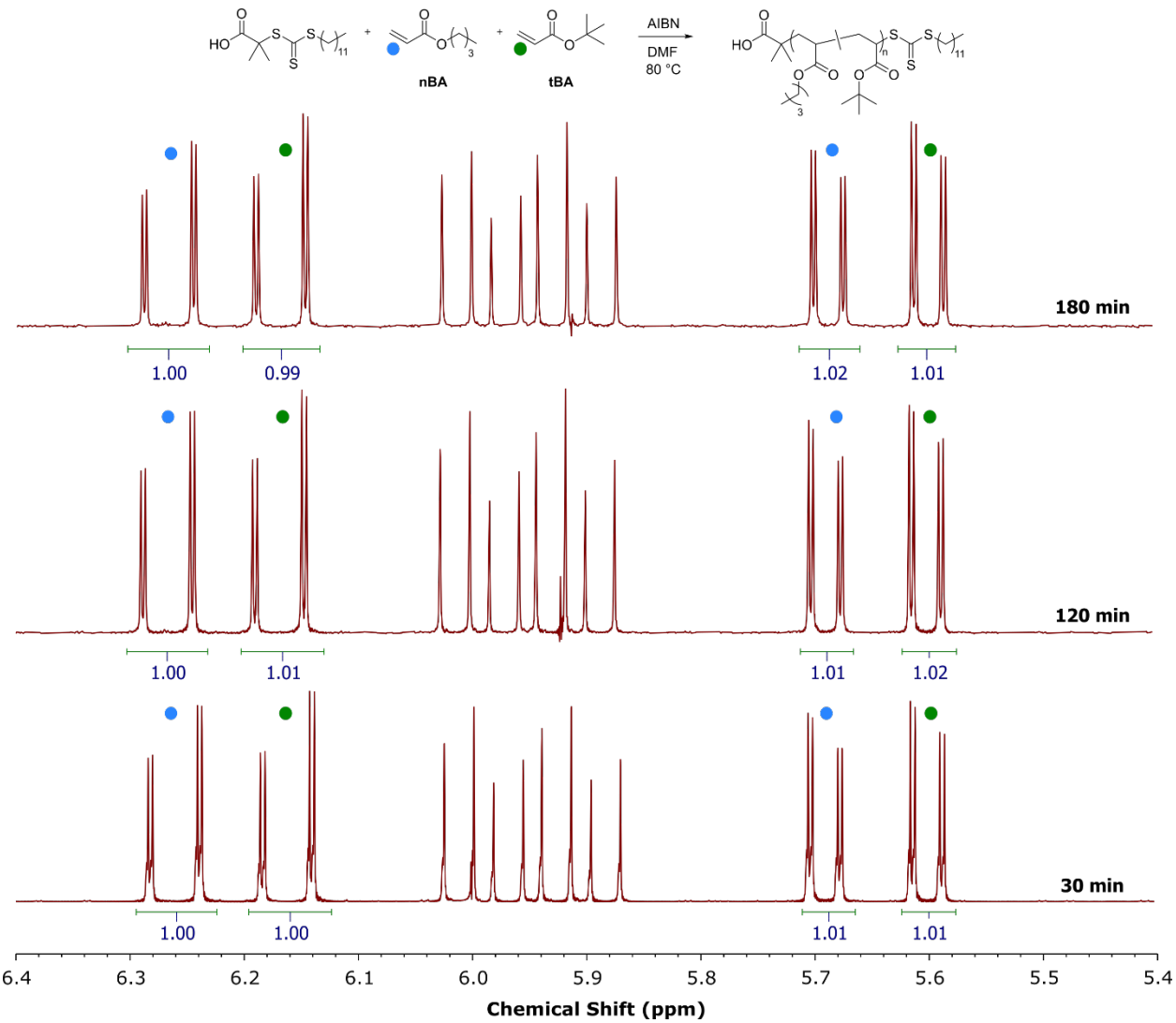

Figure 5S25. ^{1}H NMR spectra of aliquots of an *n*BA/*t*BA polymerization at several timepoints. The colored dots denote the vinyl proton signals of *n*BA or *t*BA monomer. The ratio of signals does not change over the course of the polymerization, signifying the monomers are incorporating into the polymer equally.

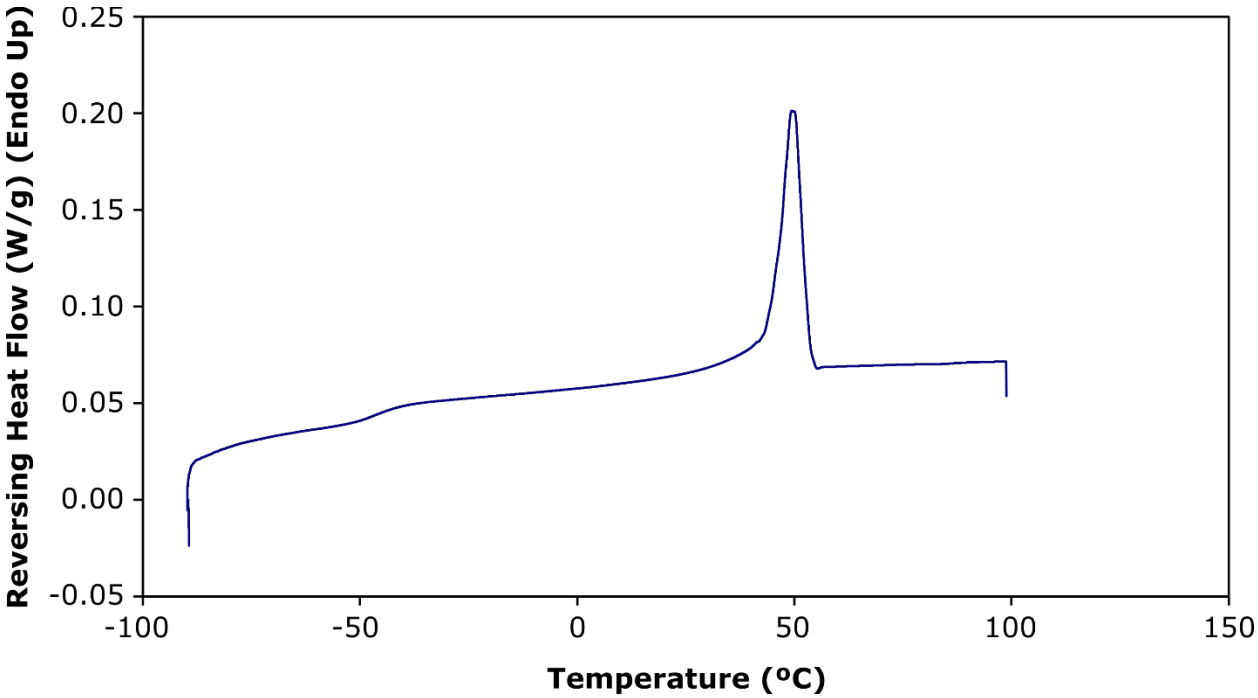

Figure 5S26. DSC trace of polymer **1a** (PEG-*b*-P(*n*BA)). Second heating cycle shown.

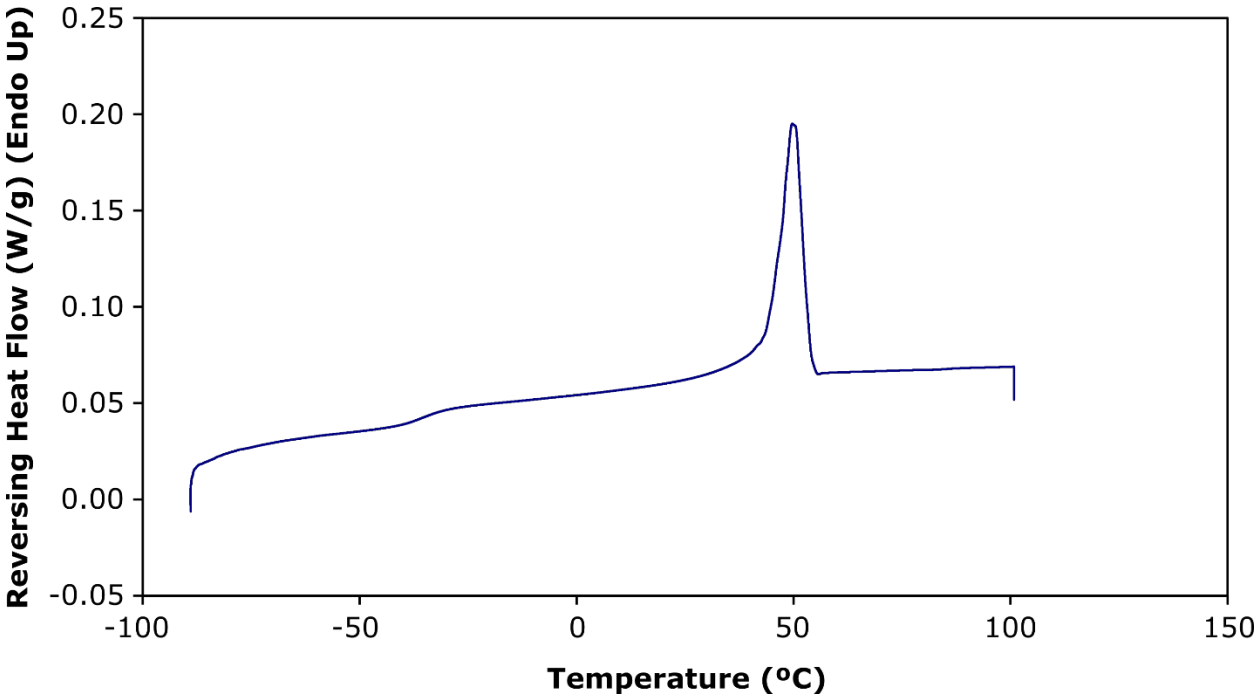

Figure 5S27. DSC trace of polymer **1b** (PEG-*b*-P(*n*BA-*ran*-*t*BA)). Second heating cycle shown.

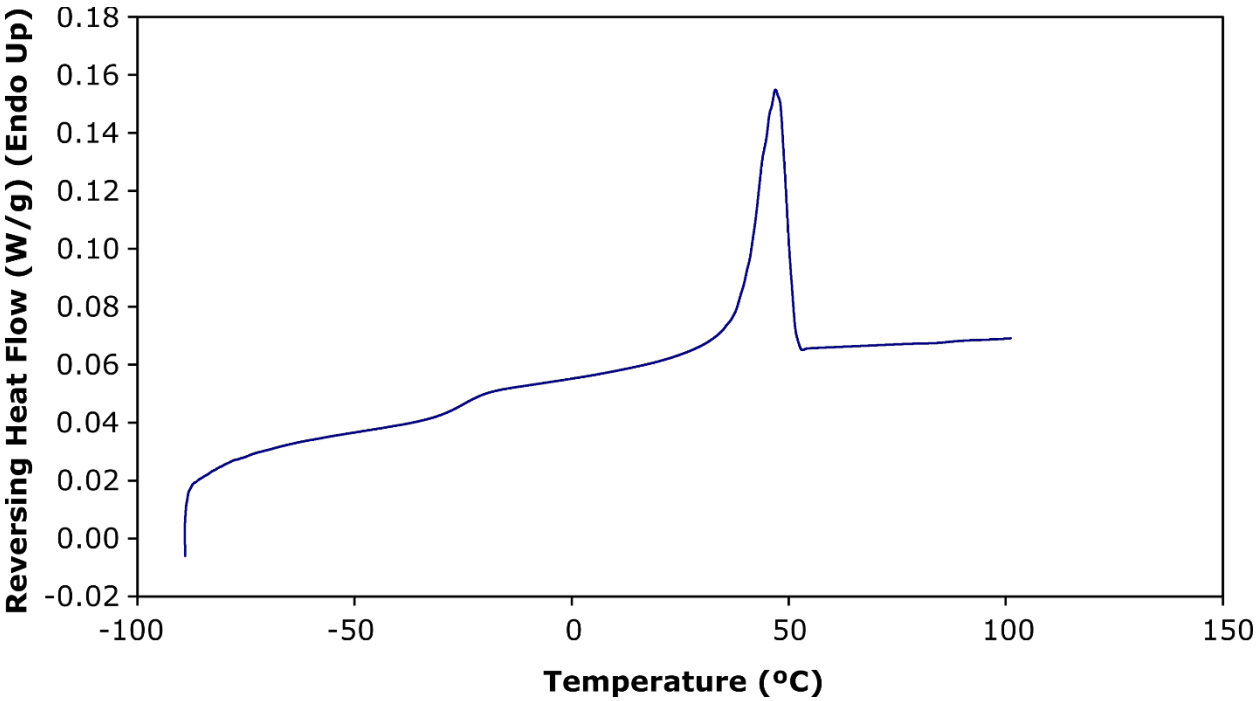

Figure 5S28. DSC trace of polymer **1c** (PEG-*b*-P(*n*BA-*ran*-*t*BA)). Second heating cycle shown.

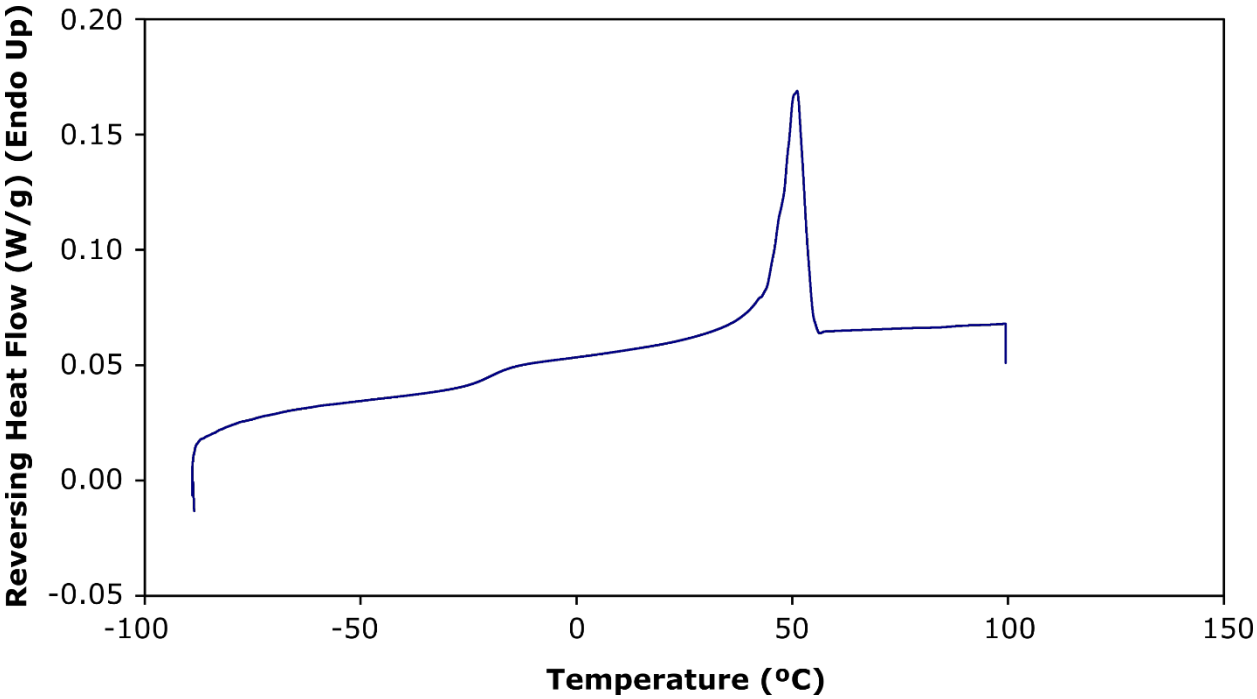

Figure 5S29. DSC trace of polymer **1d** (PEG-*b*-P(*n*BA-*ran*-*t*BA)). Second heating cycle shown.

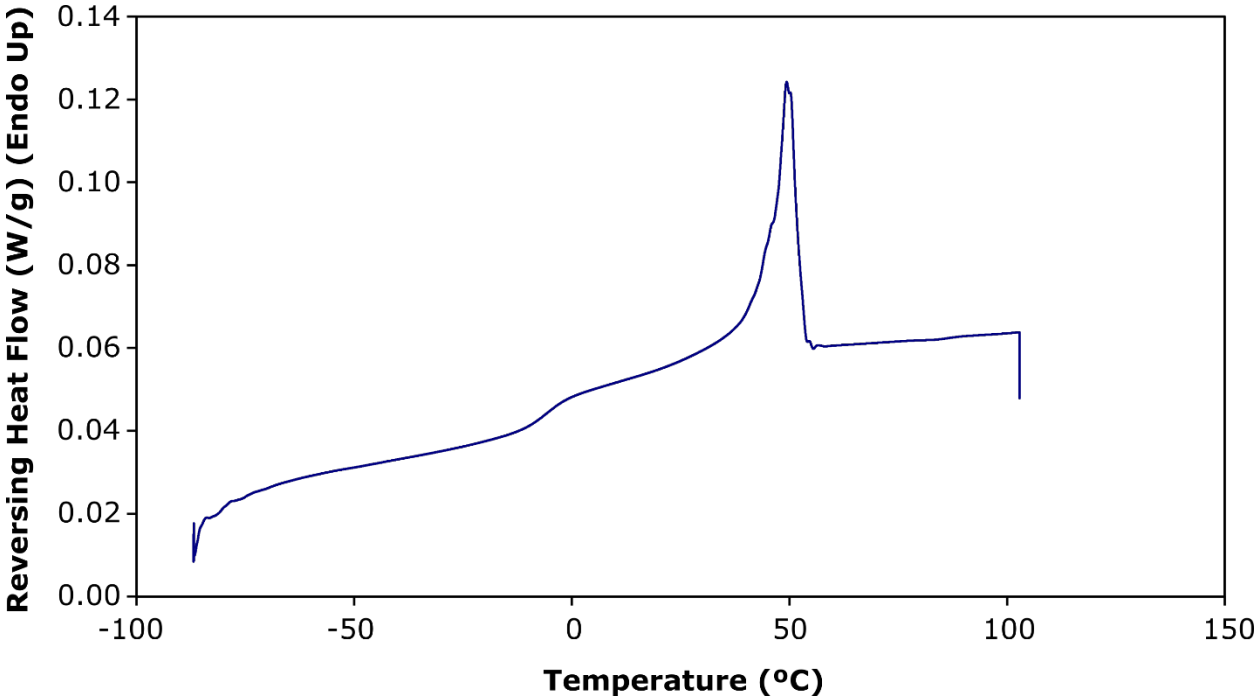

Figure 5S30. DSC trace of polymer **1e** (PEG-*b*-P(*n*BA-*ran*-*t*BA)). Second heating cycle shown.

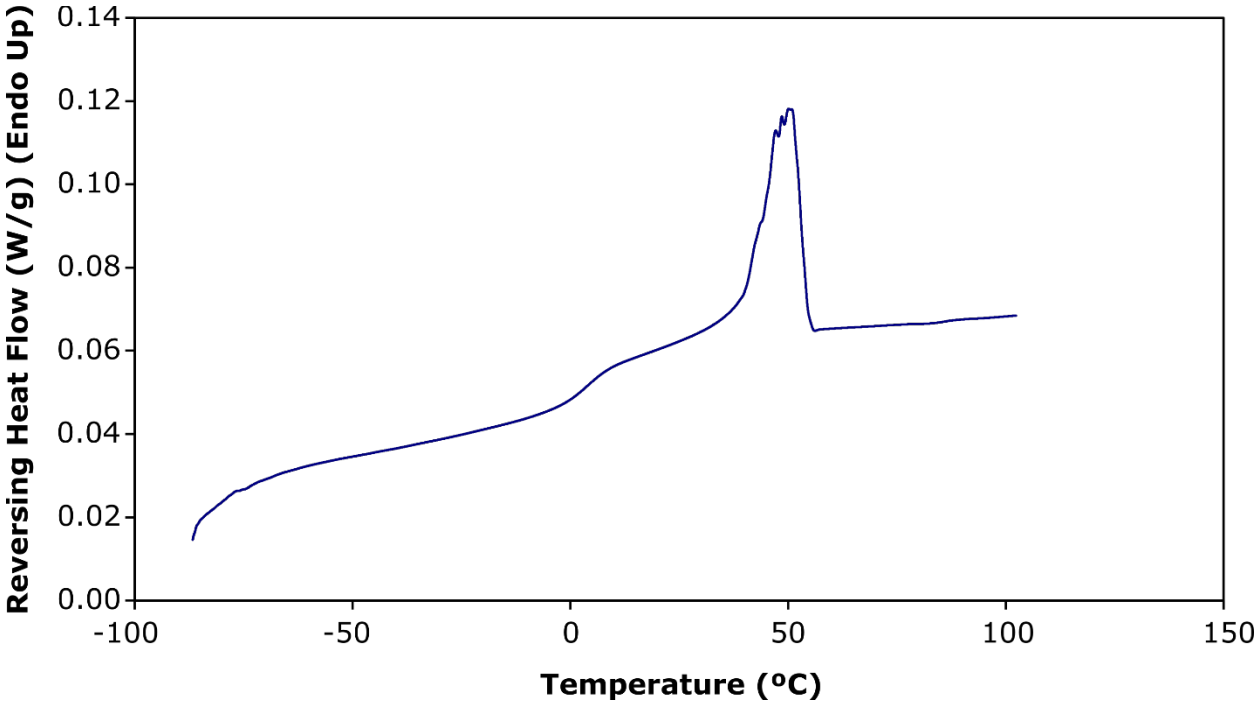

Figure 5S31. DSC trace of polymer **1e** (PEG-*b*-P(*n*BA-*ran*-*t*BA)). Second heating cycle shown.

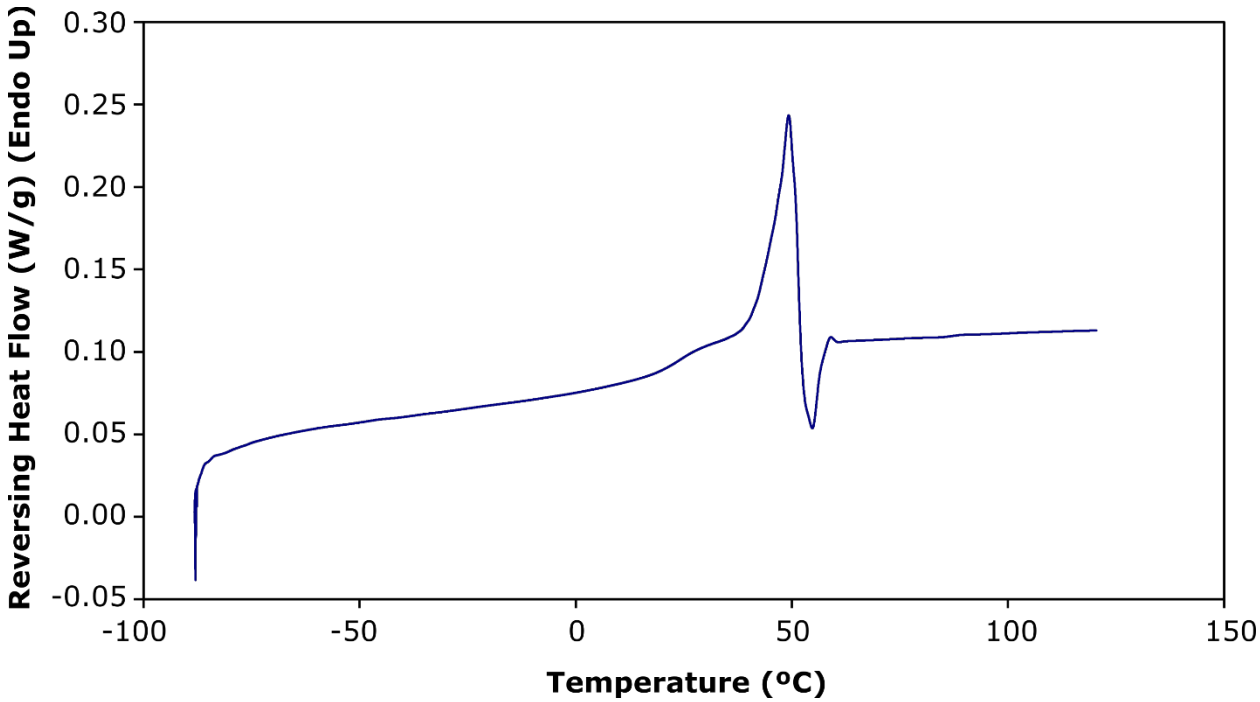

Figure 5S32. DSC trace of polymer **1g** (PEG-*b*-P(*t*BA)). Second heating cycle shown.

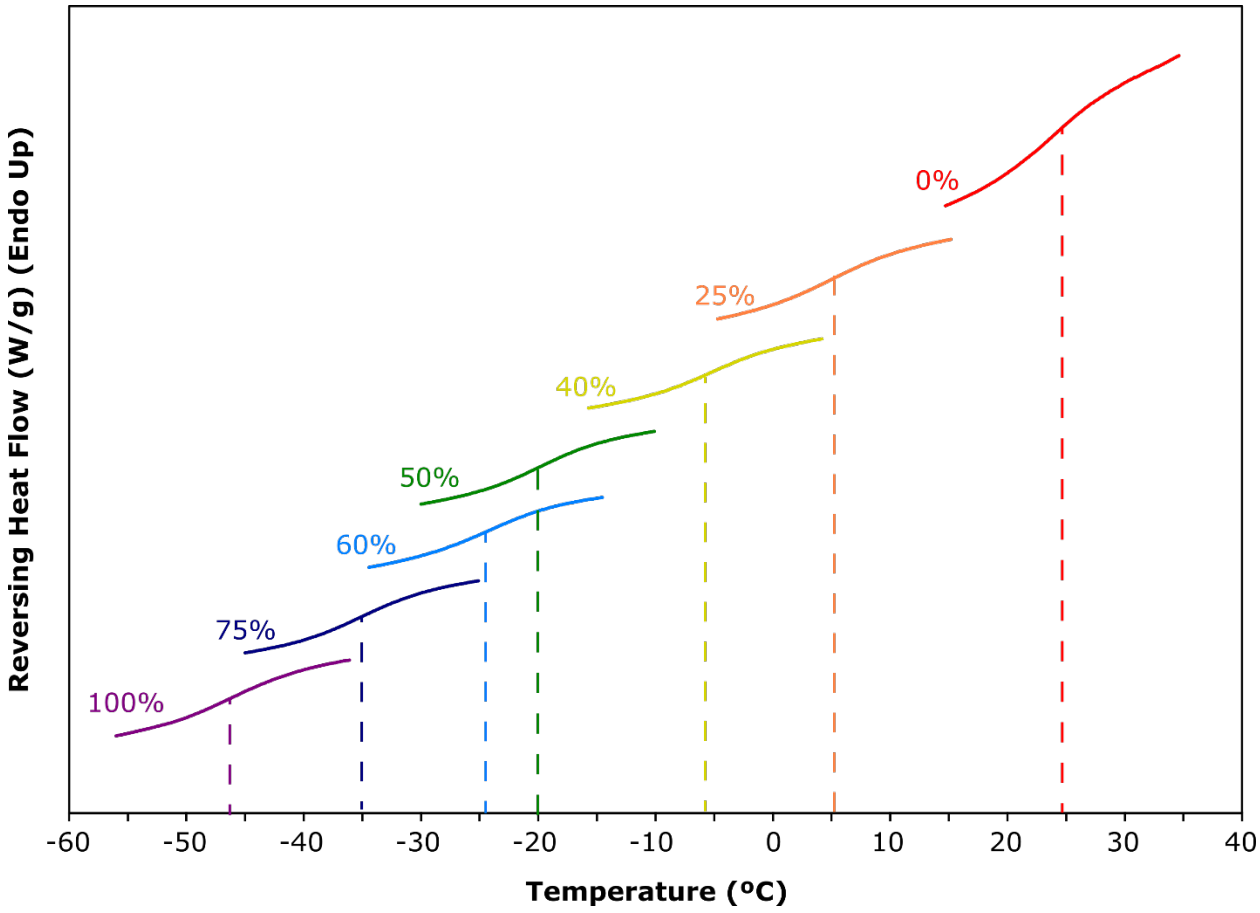

Figure 5S33. Excerpts from DSC traces of polymers **1a-g** highlighting glass transition temperatures for hydrophobic blocks. Second heating cycle shown.

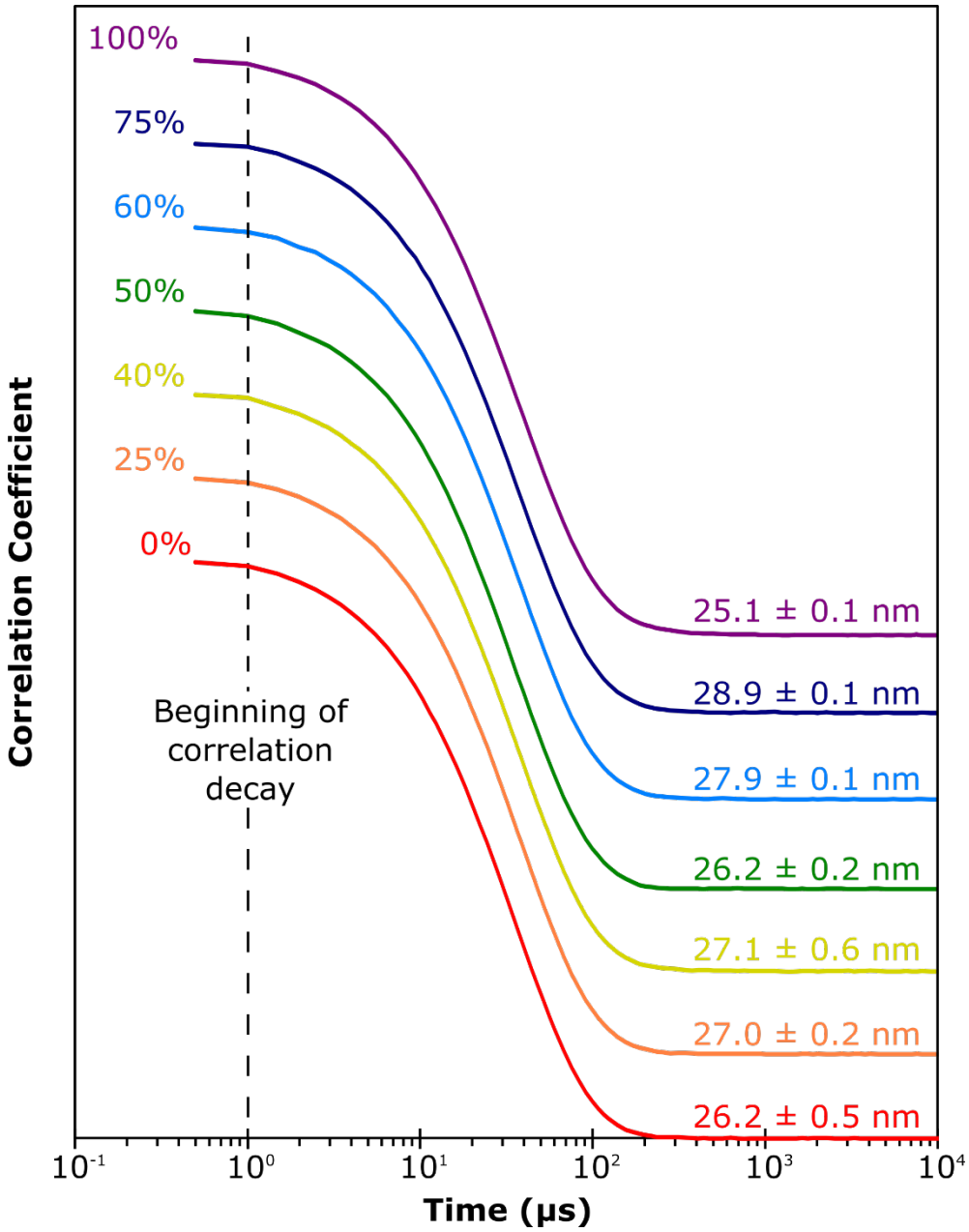

Figure 5S34. Correlation decay functions for micelle solutions (5 mg/mL in DI H_2O) of polymers **1a-g**. Intensity average hydrodynamic diameters calculated using CONTIN particle size distribution analysis.

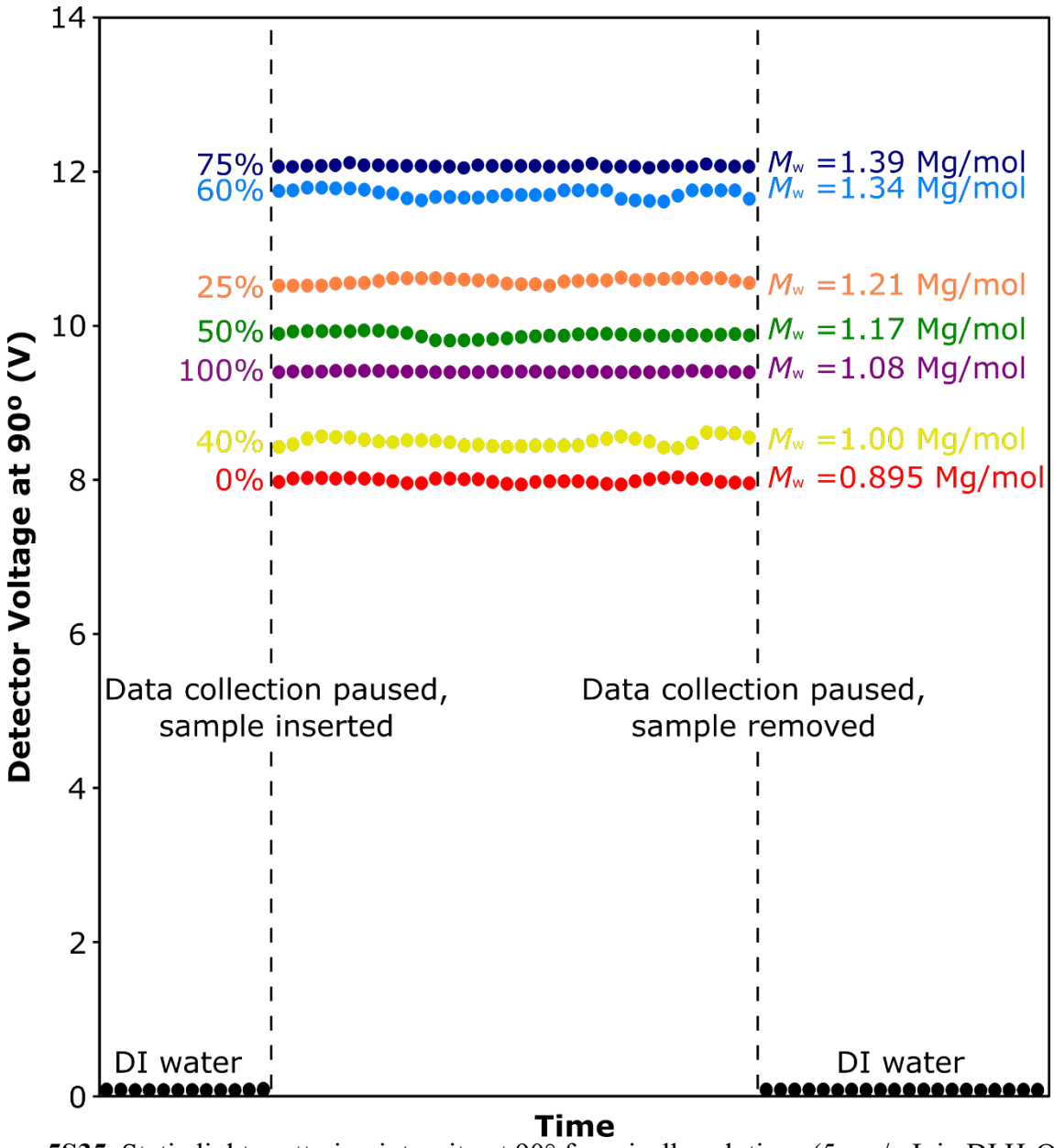

Figure 5S35. Static light scattering intensity at 90° for micelle solutions (5 mg/mL in DI H_2O) of polymers **1 a-g**. M_w calculated through multi-angle light scattering analysis using ASTRA VII software.

Equation S5.1.

$$N_{agg} = \frac{(M_w \; of \; polymer \; micelle)}{(M_w \; of \; block \; copolymer)}$$

Table 5S1. DLS Characterization of micelles from polymers **1a-g**.

Polymer	Mol% nBA[a]	Number average D_h (nm)[b]	Volume average D_h (nm)[b]	Intensity average D_h (nm)[b]	Micelle PDI[c]
1a	100	19.5 ± 0.1	21.9 ± 0.1	25.1 ± 0.1	0.014
1b	75	18.6 ± 0.1	19.5 ± 0.1	28.9 ± 0.1	0.110
1c	60	20.2 ± 0.1	23.4 ± 0.1	27.9 ± 0.1	0.060
1d	50	19.7 ± 0.2	22.3 ± 0.1	26.2 ± 0.2	0.046
1e	40	20.0 ± 0.1	22.9 ± 0.2	27.1 ± 0.6	0.051
1f	25	20.2 ± 0.2	23.1 ± 0.2	27.0 ± 0.2	0.043
1g	0	19.0 ± 0.2	21.9 ± 0.1	26.2 ± 0.5	0.059

[a] *n*BA/*t*BA molar ratio measured by ^{1}H NMR spectroscopy. [b] Hydrodynamic diameter measured by DLS at 5 mg/mL in DI H_2O. Result reported as average of 3 measurements with error reflecting standard deviation. [c] Micelle polydispersity index measured by DLS at 5 mg/mL in DI H_2O.

NMR diffusometry acquisition details and signal-decay plots

Self-diffusion coefficients of polymers in solution were determined using a 400 MHz (9.4 T) Bruker Avance III WB NMR spectrometer, equipped with a MIC probe coupled to a Diff60 single-axis (z) gradient. The pulsed-gradient stimulated echo (PGSTE) sequence[3] was used for ^{1}H diffusometry with a 90° RF pulse length of 4.5 μs, a half sinusoid gradient pulse length of δ = 3.14 ms (effective rectangular pulse length = 2 ms), diffusion time Δ = 25 ms, and post-gradient delay = 1 ms for all measurements. Maximum gradient strengths were adjusted in the range 200-500 G·cm^{-1} to achieve 80 – 99% signal attenuation in 32 steps. Sufficient signal-to-noise ratio (SNR) for each data point was achieved with 32 – 256 scans. Acquisition times and relaxation delay times were each 1 s, and 3 Hz line broadening was applied during data processing. Relaxation delay times of 1 s were used to allow complete relaxation for polymer signals. At elevated temperature, the sample was equilibrated for more than 10 min before running experiments at the set temperature to thermally equilibrate.

1D ^{1}H NMR spectra on micelle solutions were acquired with 32 scans, acquisition time of 1.5 s, relaxation delay time of 3 s, and processing with 3 Hz line broadening.

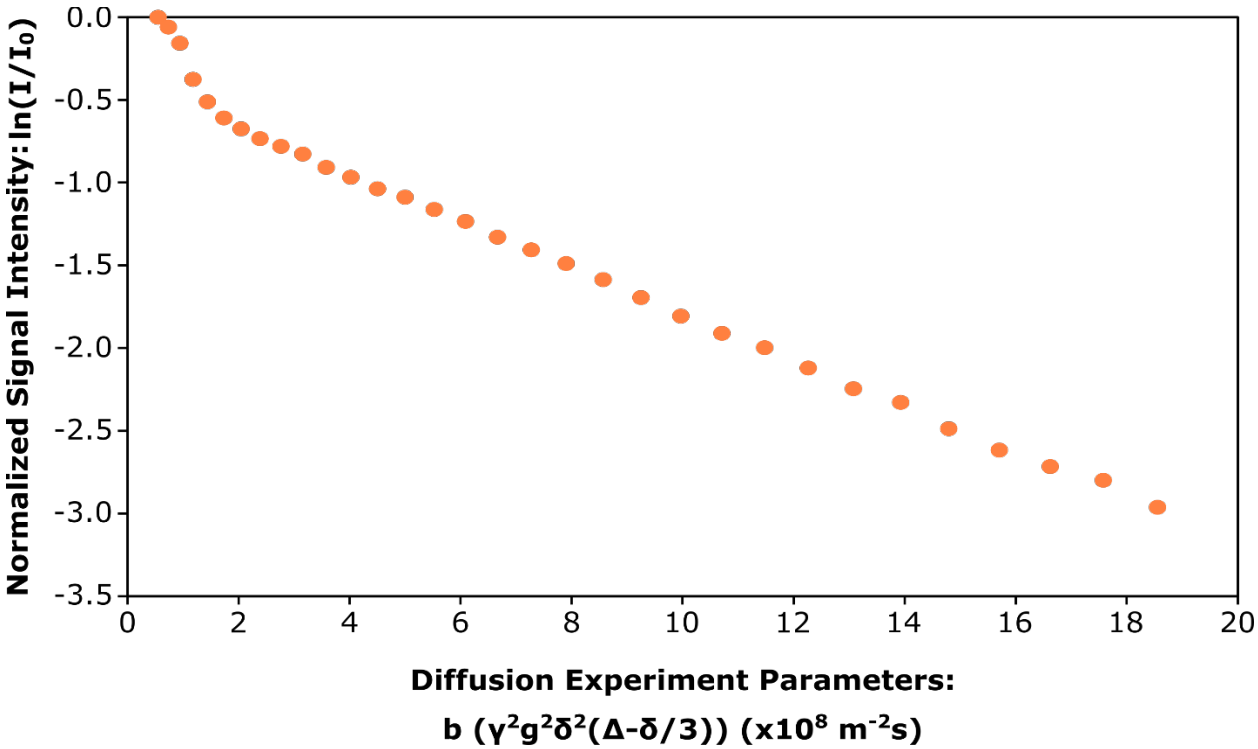

Figure 5S36. NMR diffusometry signal decay curve of micelle sample from polymer **1b** (25% *n*BA) at 25 °C.

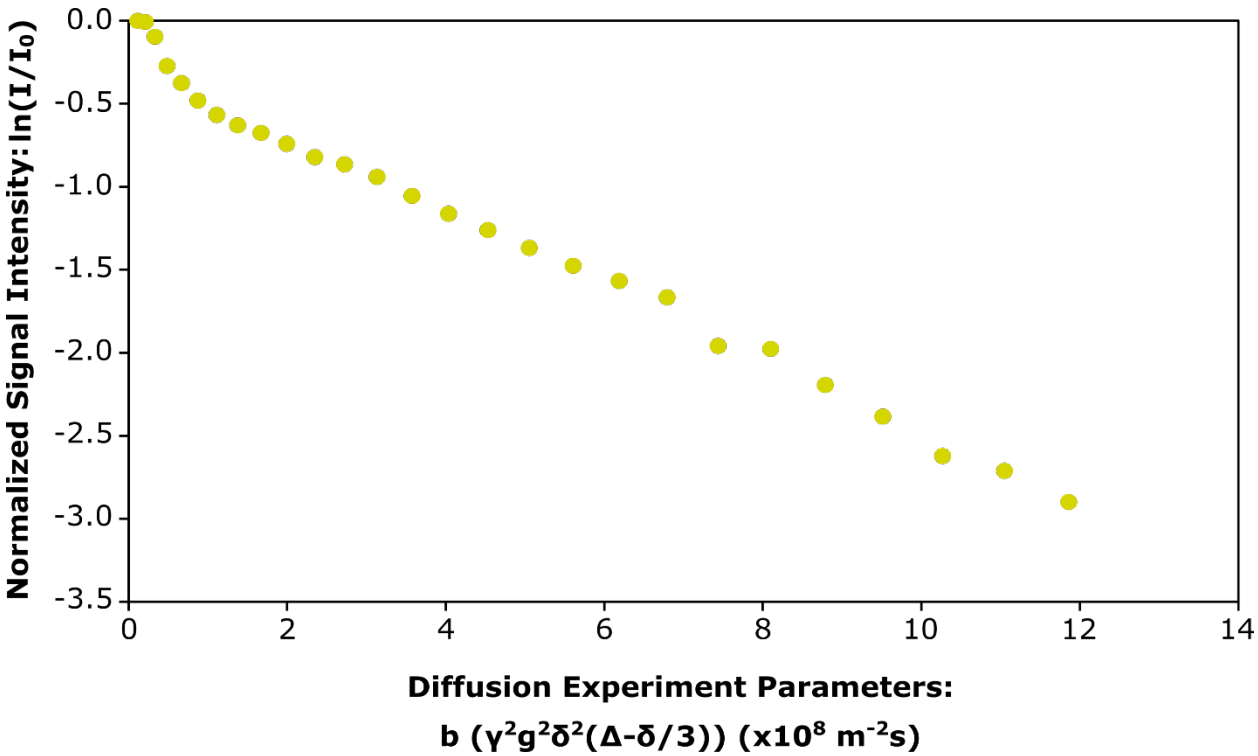

Figure 5S37. NMR diffusometry signal decay curve of micelle sample from polymer **1c** (40% *n*BA) at 25 °C.

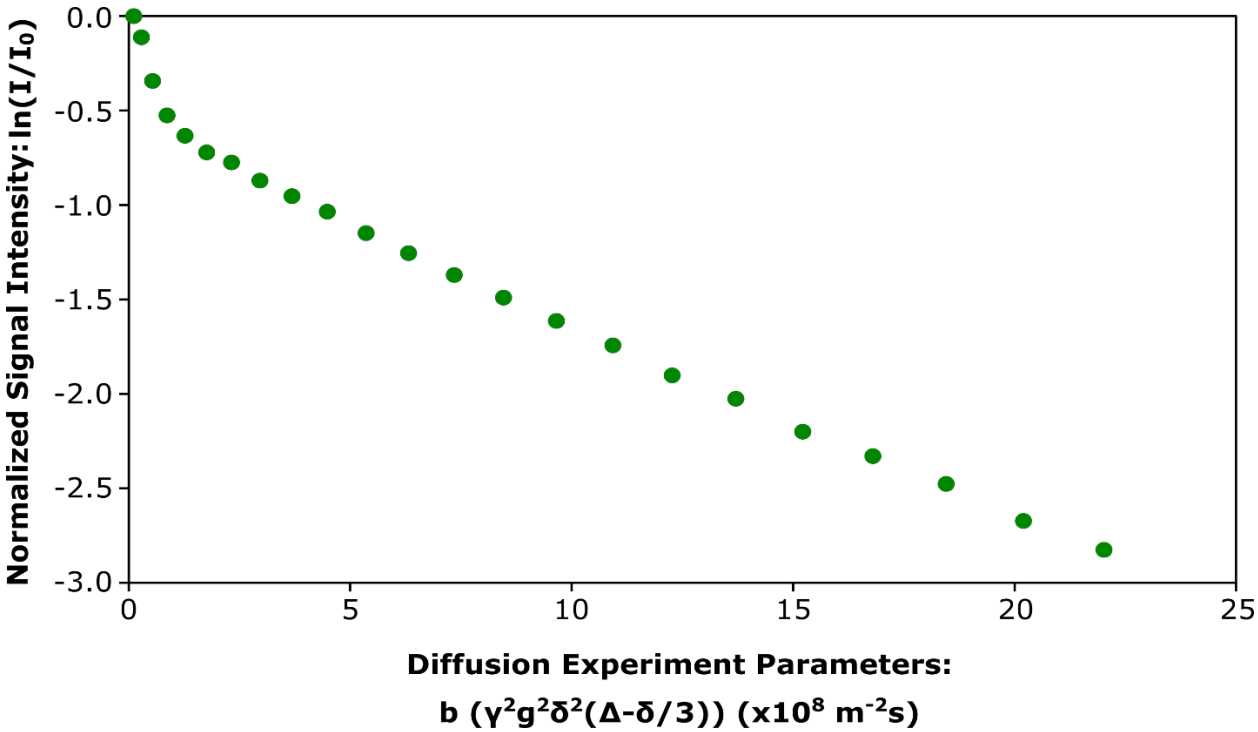

Figure 5S38. NMR diffusometry signal decay curve of micelle sample from polymer **1d** (50% *n*BA) at 25 °C.

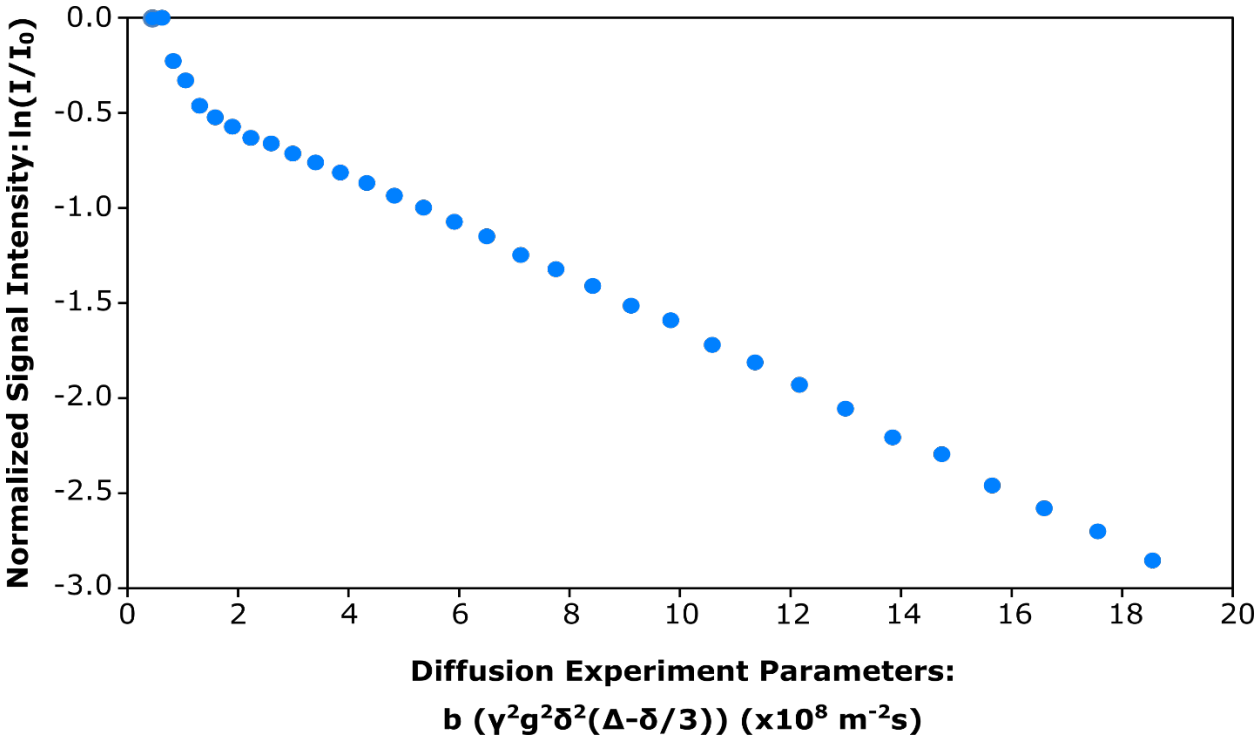

Figure 5S39. NMR diffusometry signal decay curve of micelle sample from polymer **1e** (60% *n*BA) at 25 °C.

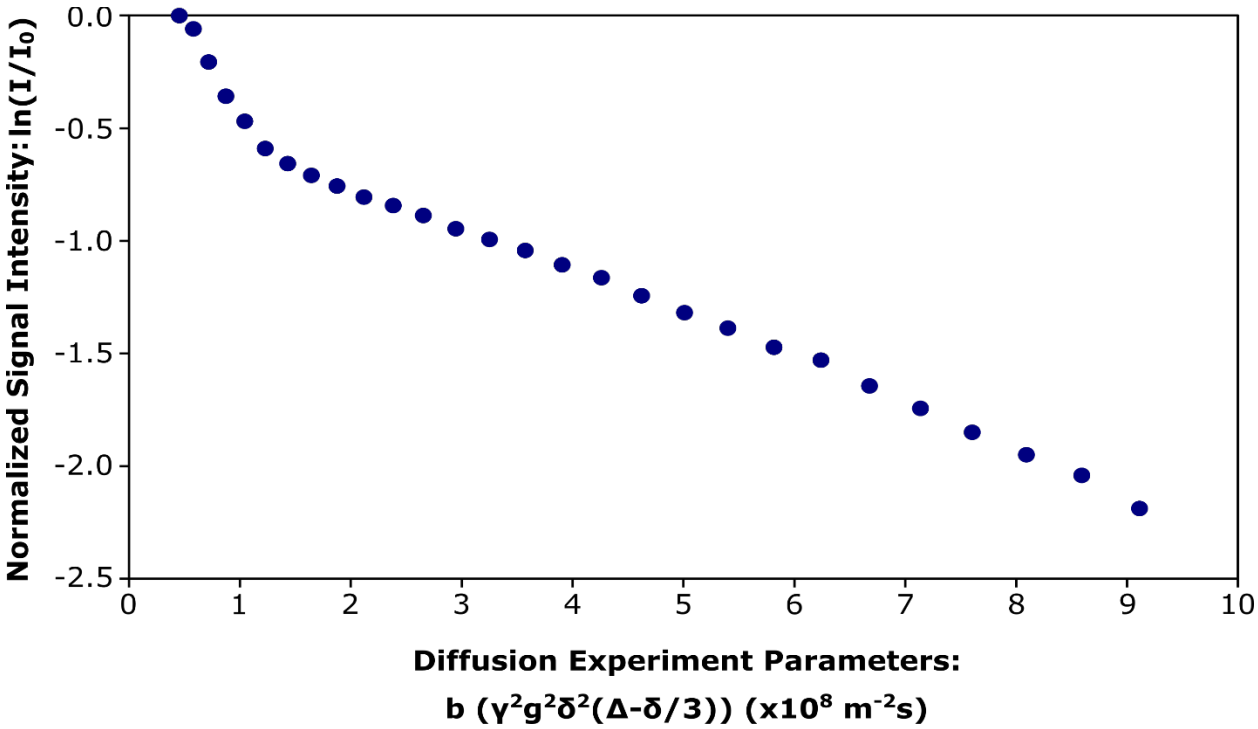

Figure 5S40. NMR diffusometry signal decay curve of micelle sample from polymer **1f** (75% *n*BA) at 25 °C.

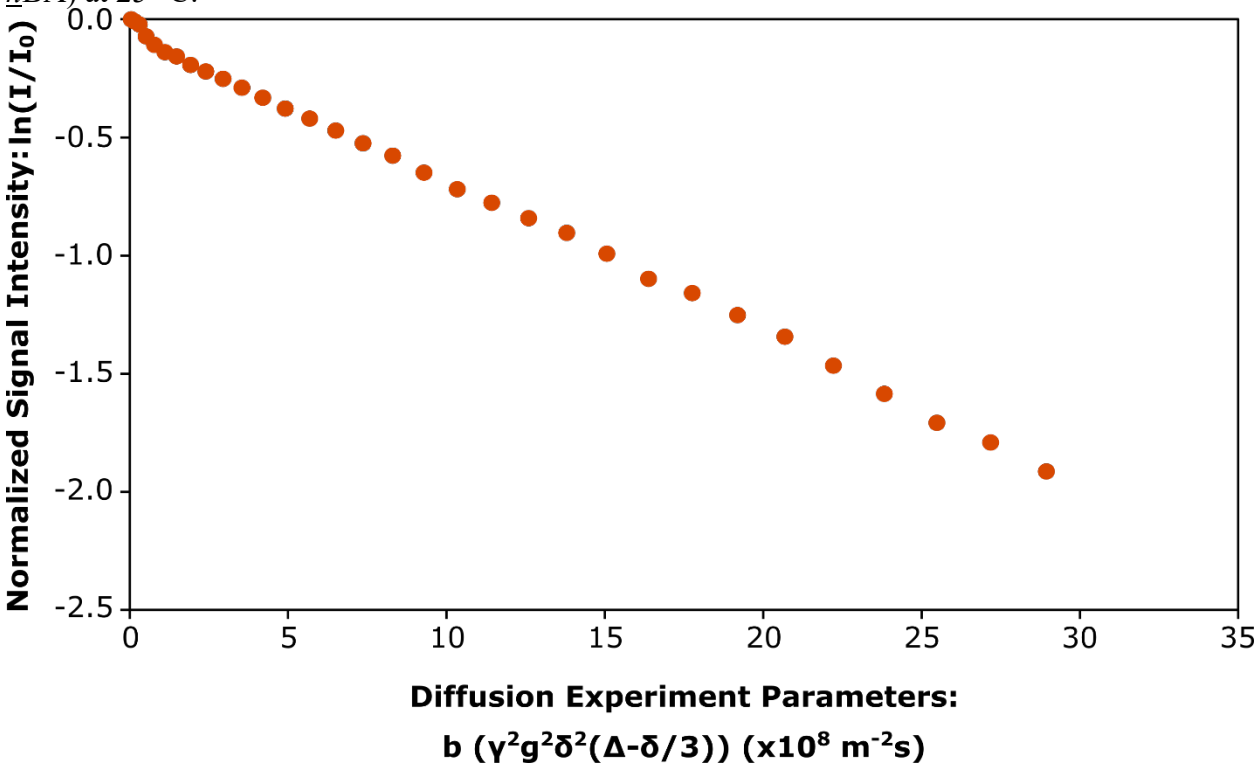

Figure 55S41. NMR diffusometry signal decay curve of micelle sample from polymer **1b** (25% *n*BA) at 15 °C.

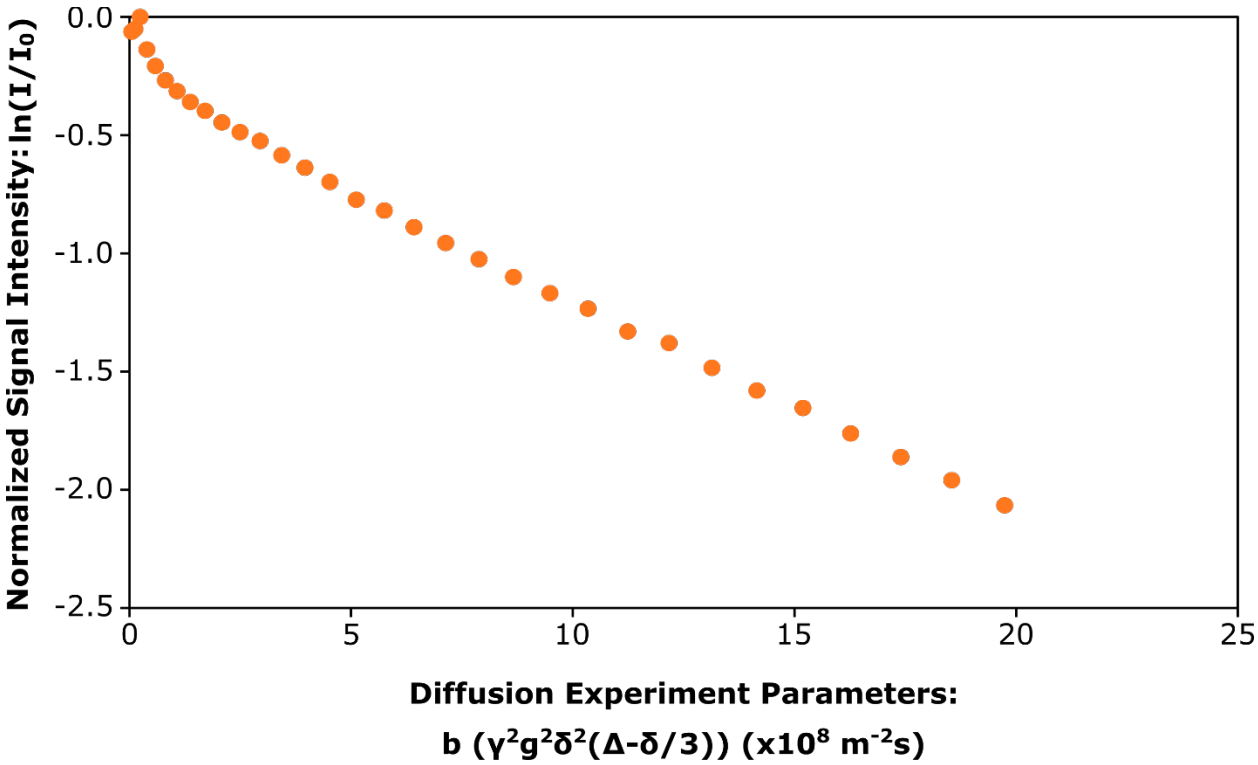

Figure 5S42. NMR diffusometry signal decay curve of micelle sample from polymer **1b** (25% *n*BA) at 35 °C.

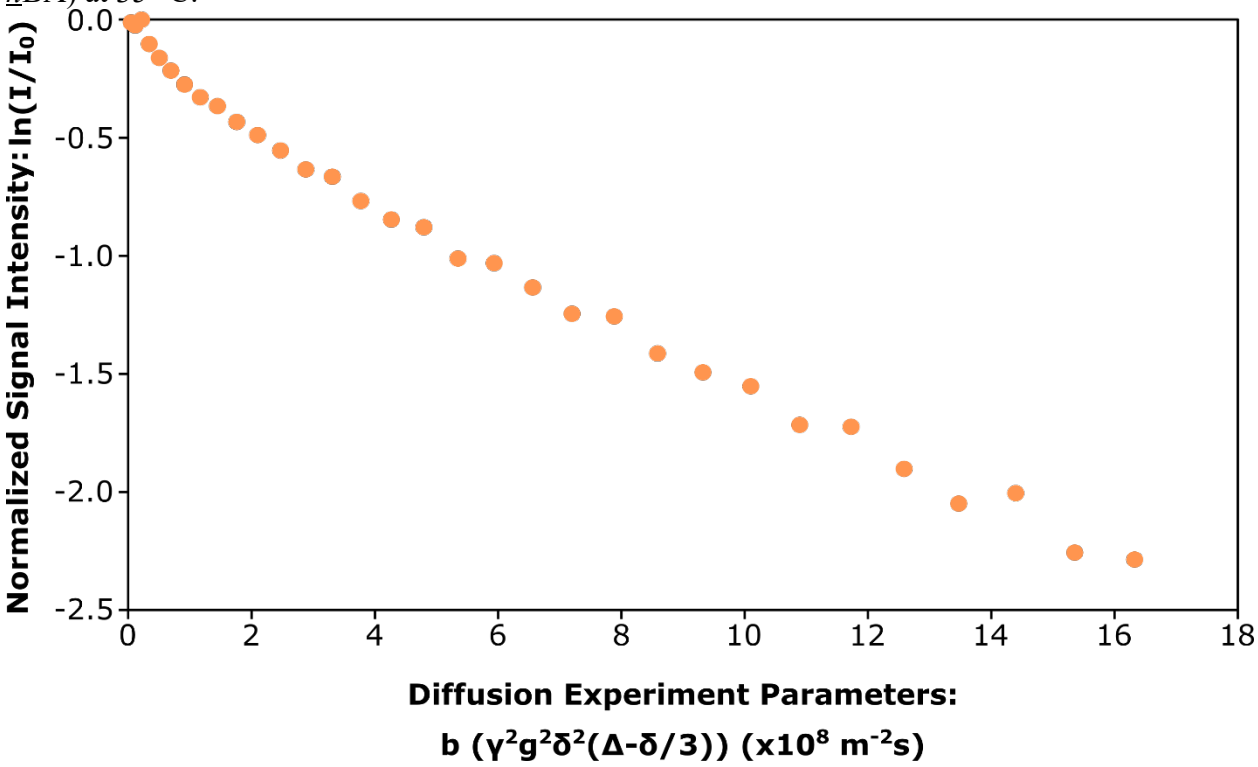

Figure 5S43. NMR diffusometry signal decay curve of micelle sample from polymer **1b** (25% *n*BA) at 45 °C.

Determination of Kmicellization from unimer concentration

Based on nonionic micelle theory[4-5], we can determine the equilibrium constant of unimer association (Table S2, also known as the micellization constant $K_{micellization}$) from these measurements. Note that we cannot state unambiguously that these systems are at equilibrium, but they are at least in quasi-equilibrium since they are stable for two days or more. Note that we are operating in the high aggregation number regime ($N_{agg} \approx 100$). We use the measured free unimer concentration as the concentration at which the free unimers are in (quasi) equilibrium with the micelles.

Table 5S2. Determination of $K_{micellization}$ based on polymer composition.

Mol% *n*BA	M_n (avg of NMR+GPC) (g/mol)	[Polymer] (M)	Unimer mole fraction	[Unimer] (M)	$K_{micellization}$ (M^{-1})
100	12100	0.00041	0.55	0.00023	4400
75	12000	0.00042	0.36	0.00015	6700
60	11900	0.00042	0.29	0.00012	8200
50	12700	0.00039	0.37	0.00015	6900
40	11700	0.00043	0.33	0.00014	7100
25	12800	0.00039	0.25	0.00010	10000
0	11700	0.00043	0	0	*

All samples measured at 5 mg/mL concentration. *unimer concentration below measurable limit, so $K_{micellization}$ very large.

Discussion of intermediate region in signal decay curves

There is always an intermediate region of intensity that does not lie on either line in a two-component Stejskal-Tanner plot, regardless of temperature and other experimental parameters. This intermediate region depends on several factors, including (1) the difference between the two D values (the closer they are, the broader the intermediate region), (2) the relative magnitudes of the two components, and (3) if there is polydispersity in one or other of the components. This intermediate region is most prominent in the signal decay curve of the 25% *n*BA micelles at 55

°C. It is possible in this case, that there may be some spread in micelle size and there may be aggregates that are not uniform size at this temperature. We have previously seen evidence with diffusometry of micelle size dispersity and/or strong size dependencies near transition temperatures/compositions. [6-7] Note, however, that there is always curvature in the intermediate regime where straight lines do not overlap the signal data points. Straight lines were inserted into Fig. 3E to guide the eye as to the identities of the two separate diffusion coefficients, and these do not represent the actual fit line. Figure S44 below shows an actual fit line that cleanly yields two diffusion coefficients and overlaps the intermediate curved region.

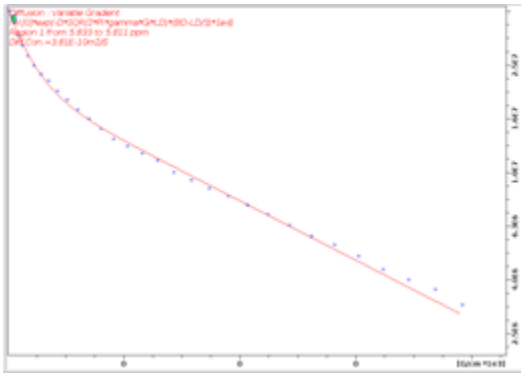

Figure 5S44. NMR diffusometry signal decay curve and fit line from polymer **1b** at 55 °C. Note that the dashed lines in Figure 3E of the main paper are not fit lines, but are simply to guide the eye to distinguish between single-component vs. two-component NMR signal decay curves.

References:

1. Skey, J.; O'Reilly, R. K., Facile one pot synthesis of a range of reversible addition–fragmentation chain transfer (RAFT) agents. *Chem. Commun.* **2008**, (35), 4183-4185.

2. Chong, D.; Tan, J.; Zhang, J.; Zhou, Y.; Wan, X.; Zhang, J., Dual electrical switching permeability of vesicles via redox-responsive self-assembly of amphiphilic block copolymers and polyoxometalates. *Chem. Commun.* **2018**, *54* (56), 7838-7841.

3. Callaghan, P. T.; Lelievre, J., The size and shape of amylopectin: A study using pulsed-field gradient nuclear magnetic resonance. *Biopolymers* **1985**, *24* (3), 441-460.

4. H-J Butt, K. G., M. Kappl, *Physics and Chemistry of Interfaces*. Wiley: Weinheim, Germany, 2003; p 373.

5. Phillips, J. N., The energetics of micelle formation. *Transactions of the Faraday Society* **1955**, *51* (0), 561-569.

6. Kidd, B. E.; Li, X.; Piemonte, R. C.; Cooksey, T. J.; Singh, A.; Robertson, M. L.; Madsen, L. A., Tuning Biocompatible Block Copolymer Micelles by Varying Solvent Composition: Dynamics and Populations of Micelles and Unimers. *Macromolecules* **2017**, *50* (11), 4335-4343.

7. Li, X.; Cooksey, T. J.; Kidd, B. E.; Robertson, M. L.; Madsen, L. A., Mapping Coexistence Phase Diagrams of Block Copolymer Micelles and Free Unimer Chains. *Macromolecules* **2018**, *51* (20), 8127-8135.

Appendix II. Supporting Information for: Quantification of Dynamics and Kinetics of Oleic Acid Ligands to Understand PbS Quantum Dot Capping using NMR Spectroscopy

Veera Venkata Shravan Uppala[1], Jennica E. Kelm[2], Christian Y. D. Lassalle[2], Jillian L. Dempsey[2], and Louis A. Madsen[2]

[1]Department of Chemistry and Macromolecules Innovation Institute, Virginia Polytechnic Institute and State University, Blacksburg, Virginia 24061, United States

[2]Department of Chemistry, University of North Carolina, Chapel Hill, North Carolina 27599-3290, United States

1. NMR timescale for a 1D NMR and NMR Diffusometry Measurements

Along with the chemical specificity, NMR instrument can also study dynamics on multiple time and length scales. Typically, the time scale of an NMR measurement is dependent on the type of experiment and the states of the nuclei probed. For a simple 1D NMR measurement, the time scale is dependent on the chemical shift difference ($\delta\nu$) of the two states of the molecule that is being observed. In our case, we are observing the dynamics of ligand on QD surface (ν_{bound}) and the free ligand (ν_{free}) in solvent. Hence the NMR timescale (τ) for a 1D NMR measurement is given by Equation 6S1.

$$\frac{1}{timescale\ (\tau)} = \frac{\pi \cdot \delta\nu}{\sqrt{2}} \qquad \text{6S1}$$

where $\delta\nu = \nu_{bound} - \nu_{free}$ is the chemical shift difference of oleic acid ligand in bound and free states as shown in the **Figure 6S1** below. For OA and QD system, measured on a 600 MHz instrument, $\tau = 3.9\ ms$ for a 1D spectrum. However, in an NMR diffusometry experiment τ is dependent on the experimental parameter 'diffusion time' (Δ) (details of Δ in the Experiment section of the manuscript). For our NMR diffusometry measurements, we set Δ = 25 ms for diffusion coefficient measurements. However, for some control experiments, we increased Δ = 200 ms to observe any changes in the NMR spectrum of the alkenyl proton signal. We did not observe any changes in the NMR spectrum as well as the dynamics of the OA ligand with varying Δ. This study provides a qualitative understanding on the exchange time for ligand binding/unbinding, which is $> 200\ ms$.

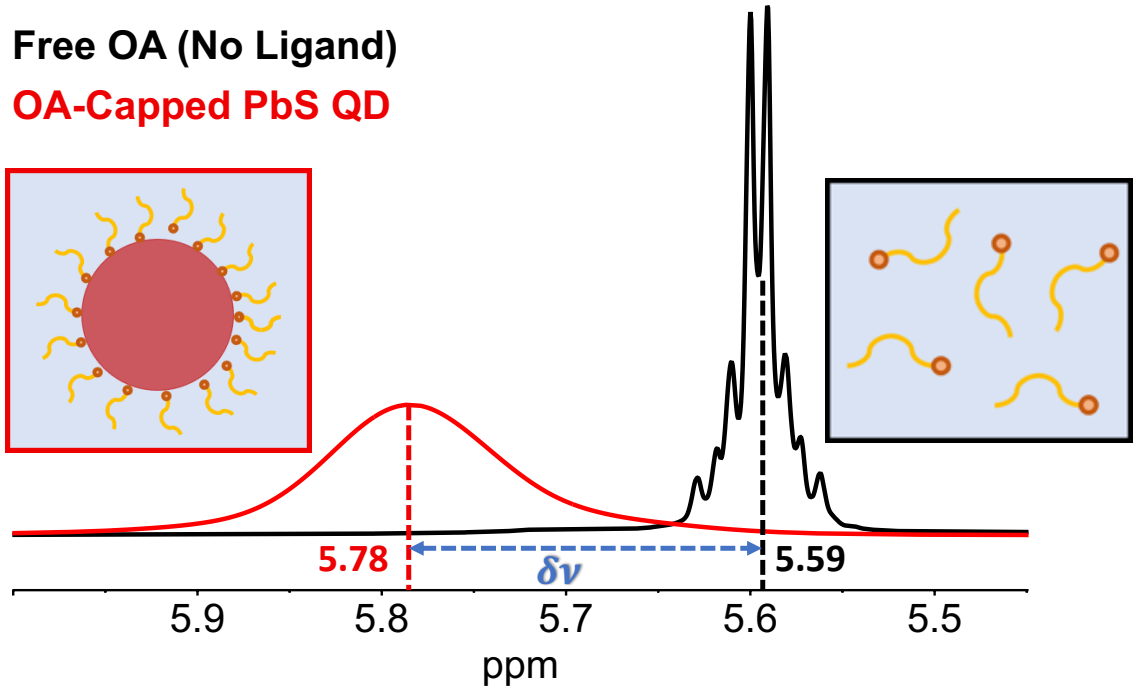

Figure 6S18: ^{1}H NMR spectrum of free and bound oleic acid ligand measured on a 600 MHz instrument. The chemical shift difference ($\delta\nu$) between the two states tells us about the timescale of the measurement.

2. ^{1}H NMR Spectrum of 1-Octadecene and Diffusion Studies with and without PbS QDs

Free 1-Octadecene (ODE) and ODE in OA capped PbS QD solution have diffusion coefficients equal to 12×10^{-10} $m^2\cdot s^{-1}$ which is ten times greater than the diffusion coefficient of bound oleic acid (OA, 1.3×10^{-10} $m^2\cdot s^{-1}$) as shown in **Figure 6S2**. The faster diffusion coefficient of ODE indicates that the ODE with only alkenyl group at the end of the chain does not interact with the surface of PbS QD particles. This control experiment further justifies that the oleic acid binding/association with PbS QD surface occurs because of the acetate group on the chain. Also, oleic acid ligand binding/association with alkenyl bond requires greater entropic penalty and hence it is thermodynamically not favorable to have such associations.

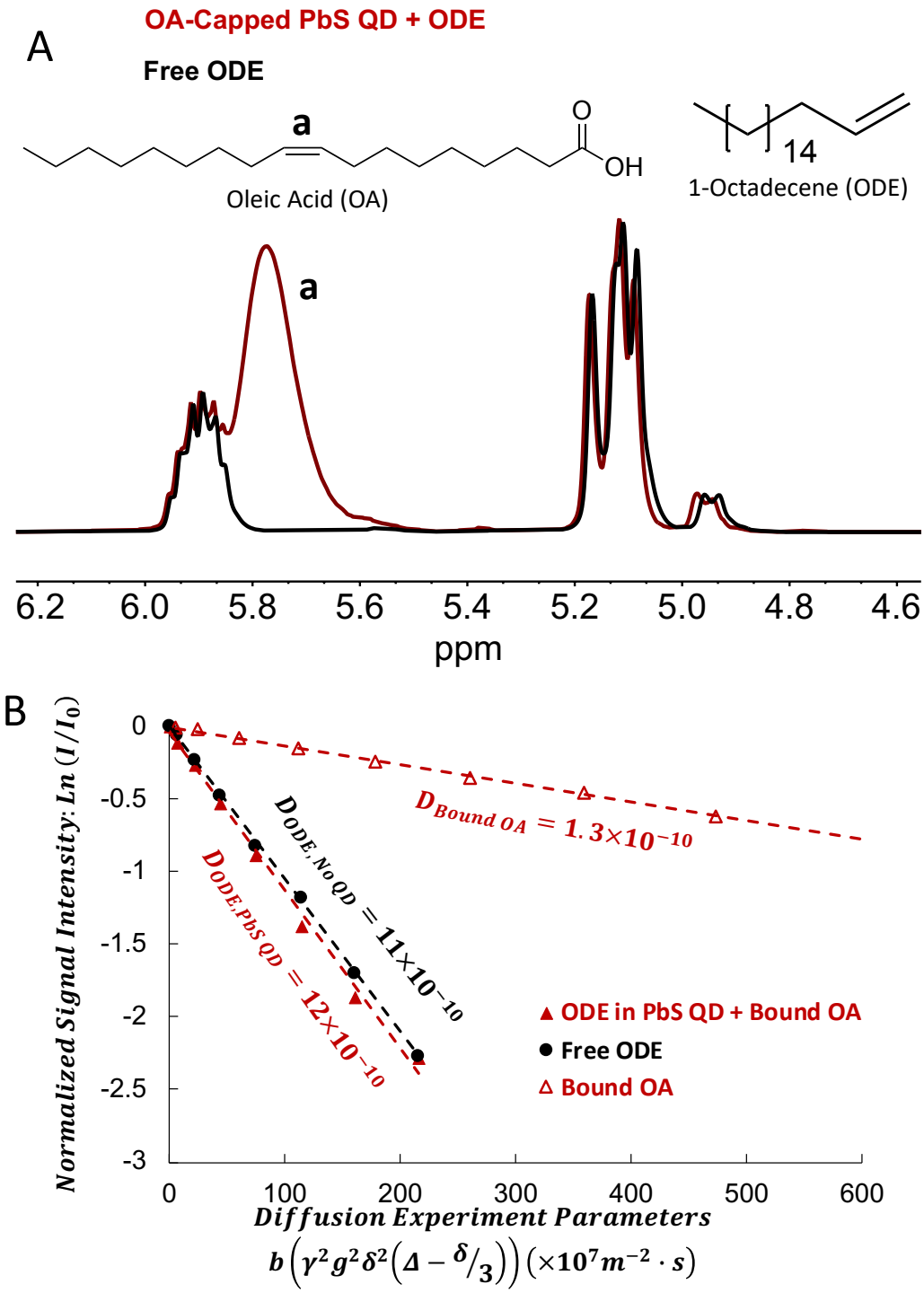

Figure 6S19: A. ^{1}H NMR spectrum of free 1-octadecene (ODE) ligand in toluene-d_8 (black) and 1-octadecene ligand in OA-capped PbS QD toluene-d_8 solution (red). **B**. Diffusion coefficient ($m^2 \cdot s^{-1}$) of free ODE ligand (black, circle) in toluene-d_8 and ODE in OA capped PbS QD solution (red, triangle) using NMR diffusometry. Diffusion coefficient of the OA that is capped to PbS QD is also measured (red, hollow triangle).

3. ^{1}H NMR Spectrum of Oleic Acid Ligand Titrated in Ligand capped PbS QD Solution.

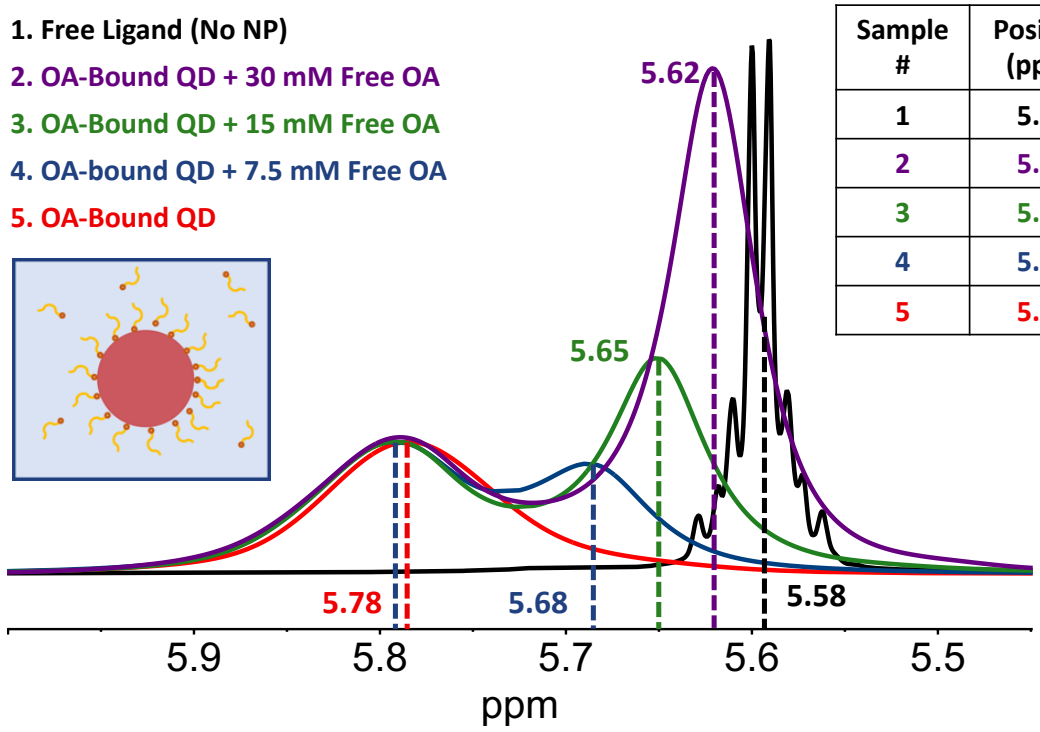

Sample #	Position (ppm)	FWHM (Hz)
1	5.59	~ 7
2	5.62	32.6
3	5.65	36.9
4	5.68	43.1
5	5.78	60

Figure 6S20: ^{1}H NMR measurements using 600 MHz instrument. Upfield shift of the exchanging oleic acid (OA) signal (sample #2, #3, #4) and increase in full width at half maximum (values in the table) with increase in free OA titrated in the PbS QD solution. The spectrum also includes only free OA ligand in toluene-d8 sample (# 1, black) and bound ligands capped to PbS QD particles in solution (#5, red) along with their peak widths (Hz) and chemical shifts listed in the table.

The above ^{1}H NMR measurements were made on 600 Mhz Bruker NMR instrument. The bound ligand signals from all samples are scaled equally except for the free ligand sample (#1, black trace). We can see that the exchanging signal has an upfield shift from 5.68 ppm to 5.62 ppm as the concentration of free oleic acid increases in the solution. This attributes that the exchanging signal chemical shift is dependent on the population fractions of QD-*associated* OA ligand and free OA ligand (**Equation 6.3** from manuscript). As the concentration of the free ligand in exchange is increased, the exchanging signal's chemical shift moves towards non-exchanging free ligand's chemical shift (5.58 ppm) as shown in the **Figure 6S3.**

4. PbS QD Particle and Ligand Shell Size Determination using NMR Diffusometry and TEM

We measure the size (hydrodynamic diameter, $d_{H,QD}$) of the PbS QD particle at room temperature (23 °C) from NMR diffusometry measurements using Stokes-Einstein Equation

$$D_{QD} = \frac{2kT}{c\pi\eta d_{H,QD}} \quad \text{6S2}$$

where k is the Boltzmann constant, T is the temperature, D_{QD} is the diffusion coefficient of OA-capped PbS QD particle in solution, η is the bulk solution viscosity, and $c\pi$ is a prefactor, which in this case is 6π for spherical particles that are very large and diffusing in a surrounding medium of small molecules.[1]

The diffusion coefficient of pure toluene measured at 23 °C is 2.21×10^{-9} $m^2 \cdot s^{-1}$ and the measured viscosity of pure toluene is 0.575 mPa·s.[2] We assume the hydrodynamic radius of toluene remains same in QD solutions, because the concentration QD particle is low and hence insignificant to affect the toluene structure. However, the viscosity of the bulk solution changes when the OA-capped QD particles are introduced in the solution. This change in viscosity can be measured from diffusion coefficient measurement of toluene in the solution using the relationship $\eta D = constant$. The measured diffusion coefficient of toluene in the solution at 23 °C and their viscosities for solutions containing varying titration concentration of OA is shown in **Table 6S1** below. The measured diffusion coefficients are within the error limits of the diffusometry experiment. Since diffusion coefficient of toluene in all solutions is close, the viscosity of the solution is same for all samples.

Table 6S3: Diffusion coefficient of toluene molecule in PbS QD solution titrated with excess of oleic acid ligands in the solution. The viscosity of the QD solutions does not change appreciably with increase in excess oleic acid ligand in the solution.

Sample	Toluene Diffusion Coefficient ($m^2 \cdot s^{-1}$)	Viscosity ($mPa \cdot s^{-1}$)
0 mM OA (Pure)	22.1×10^{-10}	0.575
QD + Bound + 7.5mM OA	21.6×10^{-10}	0.588
QD + Bound + 15 mM OA	21.8×10^{-10}	0.583
QD + Bound + 30 mM OA	20.5×10^{-10}	0.619

Based on NMR Diffusometry measurements (**Table 6S2**), the diffusion coefficients of the PbS QD particles remained constant despite increasing the titration concentration of OA. This consistency suggests that only a monolayer of ligands binds/associates on the surface of PbS QD particle (**Figure 6S4**). By applying **Equation 6S2**, we determined the size of the free oleic acid ligand ($d_{H,lig}$), allowing for an estimation of QD particle core (d_{QD}) diameter to be approximately 3.6 nm. Notably, Tunneling Electron Microscopy (TEM) measured the diameter QD particle 3 nm. The differences in particle sizes from TEM and NMR measurements fall within the error limits of the measurements.

The particle size discrepancy from both measurements may result from multiple factors. Firstly, the pre-factor $c\pi$ for a free ligand molecule is expected to be lower than 6π as the molecule is slightly larger than surrounding toluene-d8 solvent medium. This disparity will contribute to the observed error difference in size between NMR and TEM measurements. Secondly, our assumption that the ligand's conformation remains unchanged in both solvent and near the QD surface may not be entirely accurate. If the ligand undergoes a transition from random coil to extended conformation as it approaches the QD surface, this could result in a smaller core particle

size determined from NMR measurements. However, the precise nature of these conformational changes remains incompletely understood and requires further investigation.

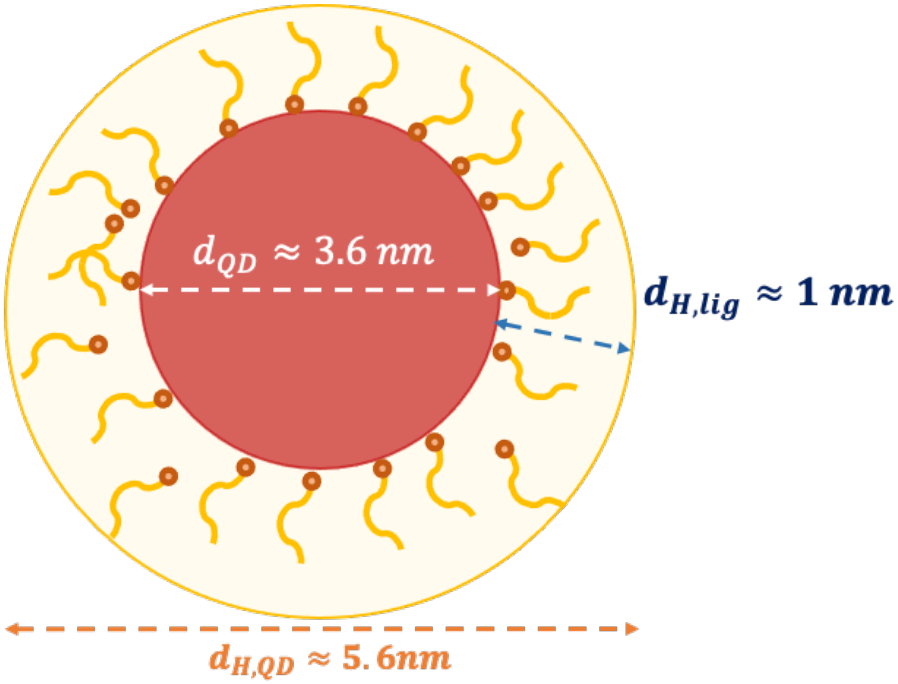

Figure 6S21: Hydrodyanmic diameter of PbS QD particle capped with OA ligand and the diameter of the free OA are determined using Stokes-Einstein equation (**Equation S2**).

Table 6S4: Diffusion Coefficients of OA-capped PbS QD (D_{QD}) particle and free OA (D_{lig}) ligand in toluene-d_8 solution and their hydrodynamic diameters ($d_{H,QD}$, $d_{H,lig}$) measured using **Equation 6S2** .

	Diffusion Coefficients ($10^{-10}m^2/s$)		Hydrodynamic Diameter (nm)	
Sample	D_{QD}	D_{ligand}	$d_{H,QD}$	$d_{H,ligand}$
QD + Bound OA	1.3 ± 0.1	7.1 ± 0.1	5.6 ± 0.4	1.0 ± 0.1
OA-capped QD + 7.5 mM OAH	1.2 ± 0.1	7.1 ± 0.1	6.2 ± 0.4	1.0 ± 0.1
OA-capped QD +15 mM OAH	1.3 ± 0.1	7.1 ± 0.1	5.6 ± 0.4	1.0 ± 0.1
OA-capped QD + 30 mM OAH	1.3 ± 0.1	7.1 ± 0.1	5.6 ± 0.4	1.0 ± 0.1

Diffusion coefficients and hydrodynamic diameter of the PbS QD particle remained same in all samples indicating a monolayer of OA shell on QD particle surface.

5. Total Number of Pb Atoms on the Surface of PbS QD particle

Bulk PbS has a rock salt (face-centered-cubic, FCC) structure with each unit-cell face containing one Pb^{2+} and S^{2-} atom (**Figure 6S5**). To determine the number of Pb surface atoms, we assume that the QD particle has FCC packing structure. The atomic radii of Pb^{2+} and S^{2-} ($r_{Pb^{2+}}$ and $r_{S^{2-}}$) are 0.12 and 0.18 nm respectively[3], giving us the diagonal of the unit cell $d_{unit} = 0.6$ nm. The number of atoms on the QD surface can be determined from the **Equations 6S3-6S5**

$$Area\ of\ PbS\ \ unit\ cell\ face = \left(\frac{{d_{unit}}^2}{2}\right) = 0.18\ nm^2 \qquad 6S3$$

$$Surface\ area\ of\ QD\ particle = \ \pi {d_{QD}}^2 = 40.71\ nm^2 \qquad 6S4$$

$$Total\ Number\ of\ Surface\ Atoms\ on\ a\ QD\ particle = \frac{4\pi {d_{QD}}^2}{{d_{unit}}^2} \approx 450 \qquad 6S5$$

QD particle of size 3.6 nm has a total of 450 atoms on the surface. However, PbS QDs exhibit a non-stoichiometric behavior at the surface which was studied by Rutherford backscattering spectroscopy (RBS)[3] and the ratio of Pb:S atoms depend on the size of the QD particle. For a QD particle with a size of 3.6 nm the Pb:S ratio measured was 1.37:1. With this factor in consideration, the number of Pb atoms on the surface is approximately 260 atoms.

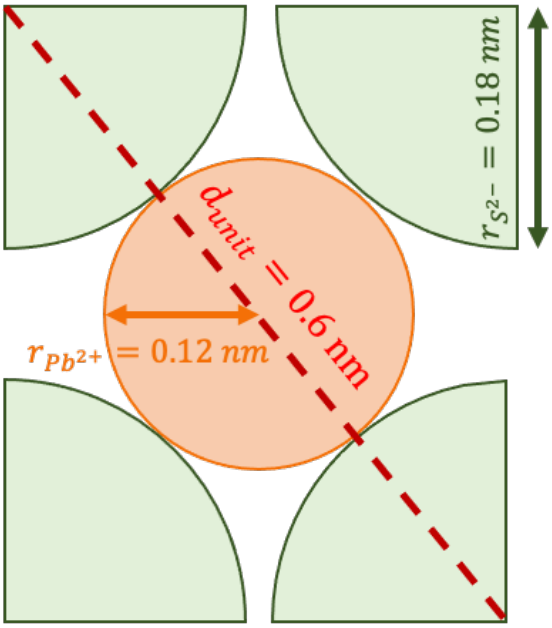

Figure 6S22: Face of a rock salt PbS unit cell having face-centered-cubic structure. The atomic radii of Pb^{2+} and S^{2-} are 0.12 and 0.18 nm respectively.

6. Determination of Average Number of Ligands in Different States per PbS QD

The number of Oleic Acid Ligands per quantum dot is determined by adding an internal standard, Ferrocene, in NMR solution. Approximately, 1mM of ferrocene is added to the toluene solution containing 0.15mM of QDs with unknown concentration of bound oleic acid ligand encapsulating and stabilizing the QDs (see experimental section in manuscript for more details). Three new batch of control samples were prepared from the above stock solution by adding 7.5, 15 and 30 mM of oleic acid ligands (50, 100, 200 times equivalence to QD concentration). Approximately 600 μL of each of those solutions (including stock solution) were taken in an NMR tube and were quantified using 1D ^{1}H NMR. All the samples were prepared in inert N_2 conditions, and the tube was glass-flame sealed to stabilize the QDs synthesized for longer periods.

In NMR, for accurate quantification of molecular concentration, it is utmost important to have a pulse sequence with a very long relaxation delay time (t_{rd}) to ensure complete spin magnetic moment to relax back from transverse xy plane direction to z direction. For accurate

quantification, its generally recommended that the repetition time (T_R) for each scan should be greater than 5 times the largest spin-lattice relaxation time ($T_{1,largest}$) as shown in the equation below.

$$T_R = t_{aq} + t_{rd} > 5 \times T_{1,largest} \quad \text{6S6}$$

The acquisition time (t_{aq}), for the experiment, is fixed to 2 s for better signal-to-noise ratio. Hence only relaxation delay time (t_{rd}) is changed according to $T_{1,largest}$ of the solution. The spin-lattice relaxation process is usually longer when the samples are prepared in inert conditions that lacks O_2 in the environment. The presence of O_2 provides an additional relaxation pathway through dipolar interactions between O_2 and the proton nuclei probed. The measured spin-lattice relaxation time constant T_1 for ferrocene proton peak was 30 s and for oleic acid it was 1s. Therefore, for accurate quantitative measurements, we used a 15° pulse angle time and implemented a t_{rd} of 100 s between each scan to ensure more than 99.9% of the signal is relaxed along z-direction. Then the signal acquired were phase corrected and integrated to quantify the moles of oleic acid ligands ($Moles_{OA}$) from ferrocene standard as shown in the equation S1.

$$Moles_{OA} = 5 \times Moles_{ferrocene} \times \left(\frac{IA_{OA}}{IA_{ferrocene}}\right) \quad \text{6S7}$$

Where IA_{OA} and $IA_{ferrocene}$ are the integral area under the oleic acid (6.0-5.4 ppm) and ferrocene peak (4.1 ppm) respectively as shown in **Figure 6S6**. Since ferrocene signal (4.1 ppm) is contributed by 10 aromatic protons and the oleic acid near 5.8 ppm is contributed by 2 alkenyl protons, we multiply a factor '5' to quantify the concentration of oleic acid from ferrocene.

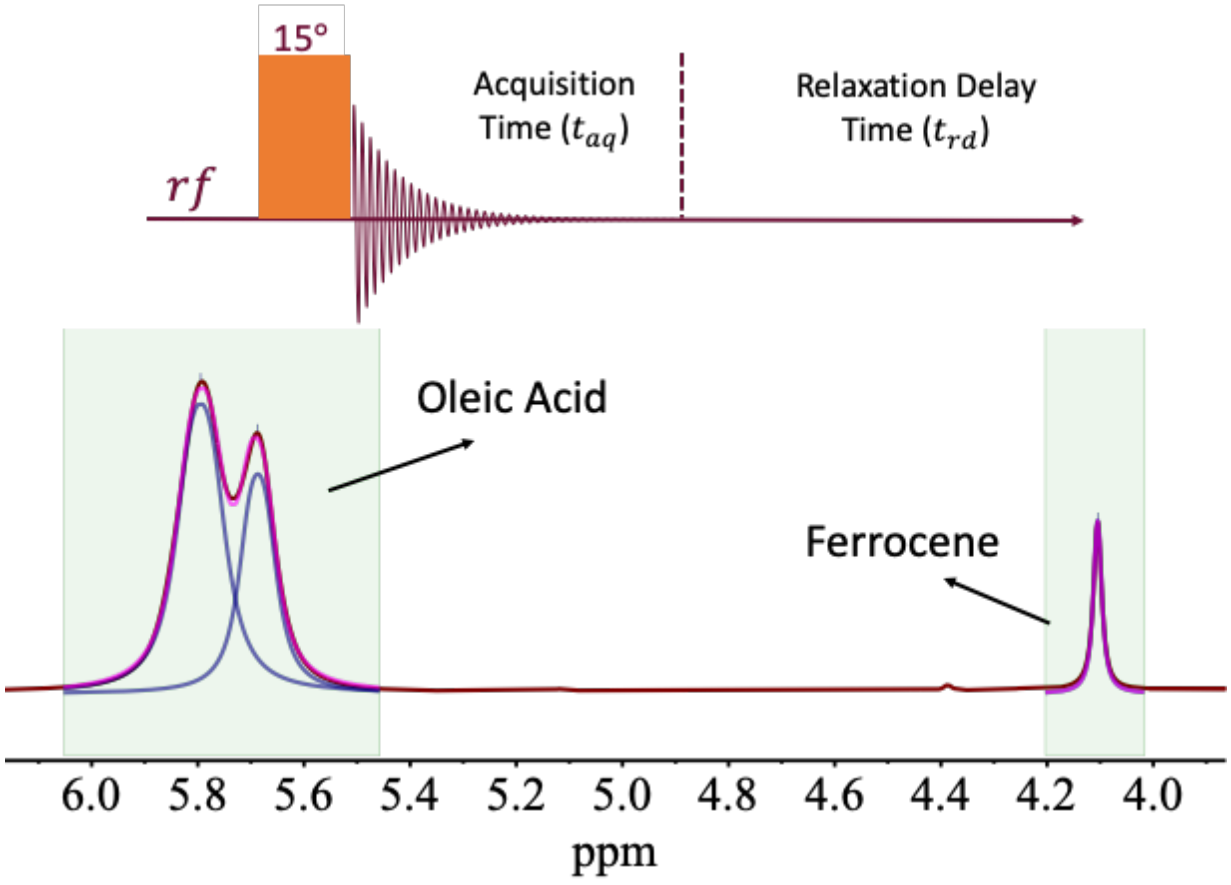

Figure 6S23: Quantifying oleic acid ligand concentration using ferrocene internal standard and quantitative-NMR technique.

The **Table 6S3** below lists number of oleic acid per quantum dot particle quantified for 4 samples containing only bound ligand before and after titrating excess of free oleic acid ligands in solution. The concentration of ferrocene and quantum dots were known when the samples were prepared (more details in the manuscript), and the concentration of oleic acid is determined using **Equation 6S7**.

Table 6S5: Quantification of oleic acid ligands per quantum dot particle using quantitative-NMR. Ferrocene integral combined with oleic acid integral and using **Equation 6S7** gives us ligand number per quantum dot.

Sample	Oleic Acid Integral	Ferrocene Integral	Ferrocene (μMoles)	QD (μMoles)	OA (μMoles)	OA per QD
QD + Bound OA	1	0.2106	0.60	0.09	14.2	158
QD + (Bound + 7.5mM OA)	1	0.1446	0.58	0.09	20.0	222
QD + (Bound + 15 mM OA)	1	0.1142	0.57	0.09	25.1	279
QD + (Bound + 30 mM OA)	1	0.0829	0.57	0.09	34.6	385

It is expected as the titration concentration of oleic acid is increased from 7.5 mM to 15mM, the number of ligands per quantum dot is expected to increase by 50 and similarly when increased to 30mM the ligand number per QD increased by 150. However, the difference in the ligand count per quantum dot measured from quantitative NMR has an error of 10%.

The population fractions of each ligand in different state (bound, QD associated, and free) were determined by combining 1D and diffusion NMR experiments (more details in the manuscript). In a 1D experiment, we observe two peaks from alkenyl protons of oleic acid near 6-5.5 ppm range. The broader peak near 5.8 ppm corresponds to the ligands bound to the quantum dot. The broadness of the peak also tells us that the ligand molecules are tumbling slower in the solutions compared to the free peak and hence we observe a broader peak compared to peak from free ligands in solution.

We also studied the changes in population fraction of the ligand in each state with increased titrated concentration of free oleic acid ligands with respect to temperature and were able to determine the absolute number of ligands in each state per quantum dot as shown in the **Table 6S4** below.

Table 6S6: Quantified number of ligands in each state per PbS quantum dot particle for samples containing varied concentration of oleic acid titrated in the solution. Quantified at temperatures from 23 °C to -10 °C

	Number of Ligands per PbS Quantum Dot Particle									
	OA + Bound	OA-Bound QD + 7.5mM OA (Total # = 222)			OA-Bound QD + 15mM OA (Total # = 279)			OA-Bound QD + 30mM OA (Total # = 385)		
Temperature (C)	Bound	Bound	QD Assoc	Free	Bound	QD Assoc	Free	Bound	QD Assoc	Free
23	158	141	58	23	127	62	90	119	75	191
10	158	159	44	19	138	66	75	132	45	208
0	158	175	31	17	160	75	44	140	42	203
-10	158	173	41	8	166	74	39	155	68	162

Bound =$[Ligand - Bound\ Site]$, QD Assoc =$[Ligand - Associated\ Site]$, Free =$[Free\ Ligand]$

7. Chemical Shift of PbS QD-Associated Oleic Acid Ligand

Table 6S7: Chemical Shift Position of the QD-Associated ligand determined using **Equation 6.3**. The chemical shift of associated ligand indicates that the associated and bound ligands have similar chemical environment. Hence it is accurate to assume that the associated and bound ligands have same diffusion coefficients.

	Ligand Population Fraction Contributed in Fast Exchange		Chemical Shifts of Ligands			
Sample	Free (%)	Associated (%)	Bound	Exchaning	Free	Associated
QD + Bound	N/A	N/A	**5.78**	N/A	5.58	N/A
QD + Bound + 7.5mM OA	28.5	71.5	**5.79**	5.69	5.58	**5.74**
QD + Bound + 15mM OA	59.0	41.0	**5.79**	5.65	5.58	**5.76**
QD + Bound + 30 mM OA	73.2	26.7	**5.79**	5.62	5.58	**5.76**

8. Understanding Exchange Kinetics from Dynamic NMR Spectroscopy

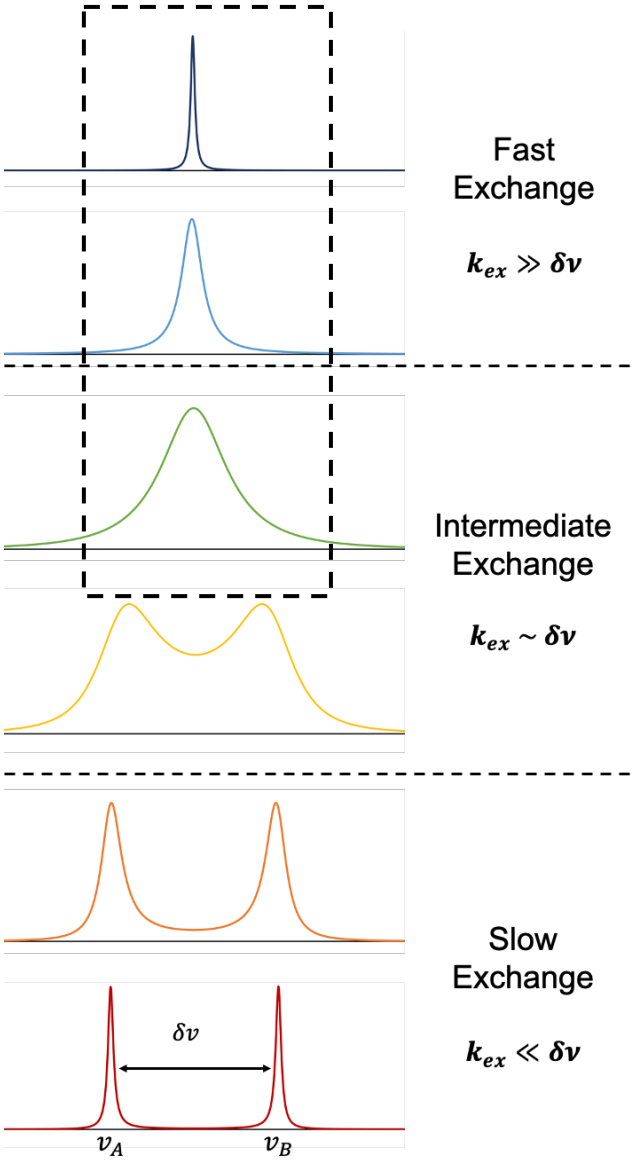

Figure 6S24: Understanding two state exchange kinetics of a molecule using Dynamic NMR. The exchanging process can be classified in three regimes which is dependent on the exchange rate (k_{ex}) and chemical shift difference ($\delta\nu$) between the two states that is in very slow exchange. For our sample, the observed exchange regime is highligeted in the box.

In a slow exchange regime, we observe two distinct narrow NMR signal peaks of both molecular states (ν_A, ν_B), and the width of the peak broadens when the exchange rate increases as shown in **Figure 6S7.** In an intermediated exchange regime, the signal peaks begin to coalesce

into a single peak. In a fast exchange regime, the coalesced single exchanging peak further sharpens indicating the nuclei of the probed moleucle is in very fast exchange between states. The exchange regimes depends on the chemical shift difference δv $(= \nu_A - \nu_B)$ of the moleucle in two states that are not exchanging and the exchange rate k_{ex} of the molecule between two states. For our samples the exchange regime is changed from intermediate state to fast exchange state as the temperature increases from -10 to 23°C as highlighted by the box. **Figure 6S8** below further indicates the change in integral and width of exchanging signal with respect to temperature for sample containing PbS QD particles with 15mM of excess of oleic acid titrated in the solution. These changes further indicates the change in dynamics and kinetics of ligand encapsulaiton of PbS QD particles.

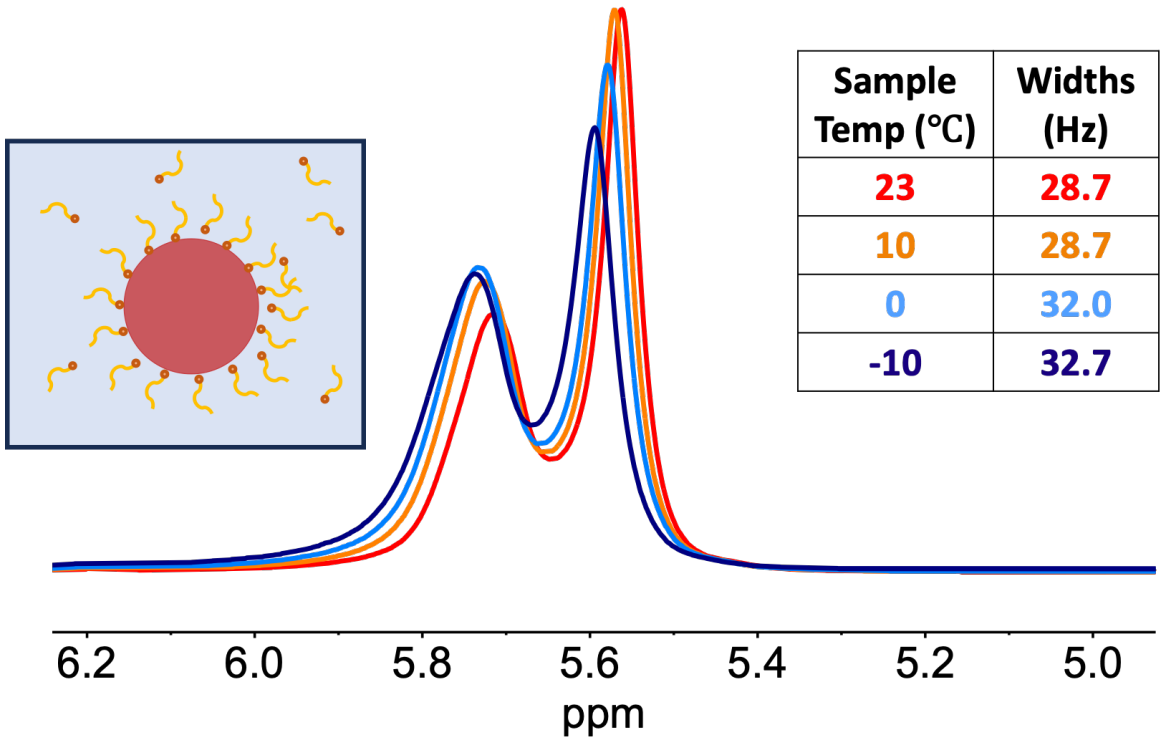

Figure 6S25: Change in FWHM, integral and chemical shift of exchanging signal (ν_{ex}) of alkenyl proton (H_a) of OA as temperature of the solution is lowered from 23°C to -10°C for OA-bound PbS QD with 15 mM of OA titrated into the solution.

9. Spin-Spin Relaxation Time Constant T_2 Measurements of Free Oleic Acid and Bound Oleic Acid Ligand in Toluene-d8 Solution.

The spin-spin relaxation time T_2 for only free oleic acid and bound oleic acid were measured using a modified CPMG (Carl-Purcell-Meiboom-Gill) pulse sequence to compensate for J modulation that significantly affect T_2 values measured using a standard CPMG experiment. The pulse sequence for the experiment is given in the Figure S9 below and the pulse program is listed below. This program was initially developed by Dr. Gareth A. Morris' group[4], and we adopted it by adding a $90°_y$ pulse and same phase cycling to existing CPMG pulse sequence to reduce the effect of J-modulation. The table S6 below lists the spin-lattice relaxation time of bound ligand and free ligand with respect to temperature.

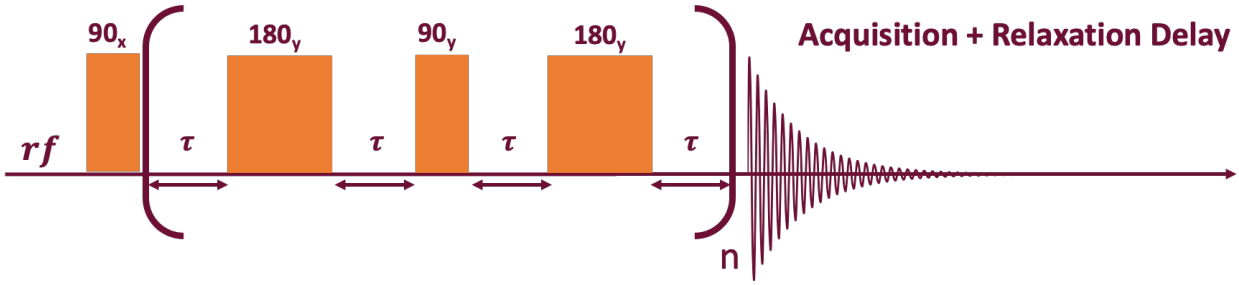

Figure 6S26: Modified CPMG pulse sequence to reduce the effect of J-modulation. Achieved by inserting a $90°_y$ pulse between spin echoes.

Modified CPMG Pulse Sequence to compensate for J-modulation

```
;avance-version (12/01/11)
;T2 measurement using Carr-Purcell-Meiboom-Gill sequence compensated for coupling
;$CLASS=HighRes
;$DIM=2D

#include <Avance.incl>

"p2=p1*2"
"d11=30m"

1 ze
2 d1
```

```
  p1 ph1
3 d20
 p2 ph2
 d20
  p1 ph3
d20
  p2 ph2
d20
 lo to 3 times c
 go=2 ph31
  d11 wr #0 if #0 ivc
  lo to 1 times td1
exit

ph1=0 2 ;90d excitation x -x
ph2=1 ;180 refocus y
ph3=1 1 3 3 ;90d refocus y -y
ph31=0 2 0 2

;pl1 : f1 channel - power level for pulse (default)
;p1 : f1 channel -  90 degree high power pulse
;p2 : f1 channel - 180 degree high power pulse
;d1 : relaxation delay; 1-5 * T1
;d11: delay for disk I/O                    [30 msec]
;d20: fixed echo time to allow elimination of diffusion
;     and J-mod. effects
;vc : variable loop counter, taken from vc-list
;ns: 4 * n
;ds: 16
;td1: number of experiments = number of values in vc-list
;define VCLIST
;d20: d20 should be << 1/J ,but > (50 * P2)
```

Table 6S8 : Temperature dependent spin-spin relaxation time of free ($T_{2,free}$) and associated ($T_{2,asso}$) ligands using modified CPMG experiment

Temperature (°C)	$T_{2,free}$ (s)	$T_{2,assoc}$ (s)
-10	0.51	0.030
0	0.62	0.036
10	0.70	0.044
23	0.78	0.053

10. Activation Energy of Slow Ligand Exchange Process

As previously discussed, NMR can investigate dynamics across multiple time and length scales. To qualitatively estimate the exchange time for ligand binding and unbinding to the quantum dot (QD) surface, we employed NMR diffusometry measurements. In this measurement, the time scale is governed by the diffusion time (D). At room temperature (25°C), the alkenyl protons of exhibited two distinct signal peaks (near 5.6 and 5.8 ppm) on the spectrum when measured at $D = 25\,ms$. Notably, no observable changes in the spectrum as well as the ligand dynamics when Δ increased to $200\,ms$. This observation indicates that the exchange time for binding/unbinding is very slow and >$200\,ms$. Given that this exchange rate is temperature-dependent, we can quantify this dependency using an Arrhenius equation

$$k_{ex,slow} = k_{ex,\infty} e^{-\frac{E_{a,slow}}{RT}} \qquad 6S8$$

Where $k_{ex,\infty}$ is the exchange rate at infinite temperature and $E_{a,slow}$ is the activation energy for binding/unbinding process.

Ligands, that undergo both slow and fast exchange processes, transitions between the free solvent environment to the restrictive QD surface environment. Despite different ligand interactions on the QD surface, these processes share similarities in ligand environments between the states. Given the analogous nature of these processes, we can reasonably assume that the $k_{ex,\infty}$ for both exchange processes to be equal. To understand the energetics of the slow exchange process, we further assumed an exchange time for binding/unbinding to be equal to 200 ms. From these parameteric value assumptions, we determined the activation energy for slow exchange process to be $E_{a,slow} \approx 100\ KJ/mol$. This value is significantly higher than the activation energy for fast exchange process ($E_{a,slow} \approx 5 \times E_{a,fast}$).

Figure 6S10 gives a comprehensive understanding on the energetics of the oleic acid ligand exchange from free solvent state to QD surface state (association/binding) providing information on binding mechanism and stability of ligands on QD surface. This can indeed open up new avenues for molecular dynamic (MD) simulations, which can further elucidate the entire exchange process. By leveraging the energetics data through simulations, researchers can gain more detailed and dynamic understanding of the ligand exchange process leading to improved control over QD surface chemistry, better prediction of QD properties and ultimately, the development of more efficient and stable QD-based devices and applications.

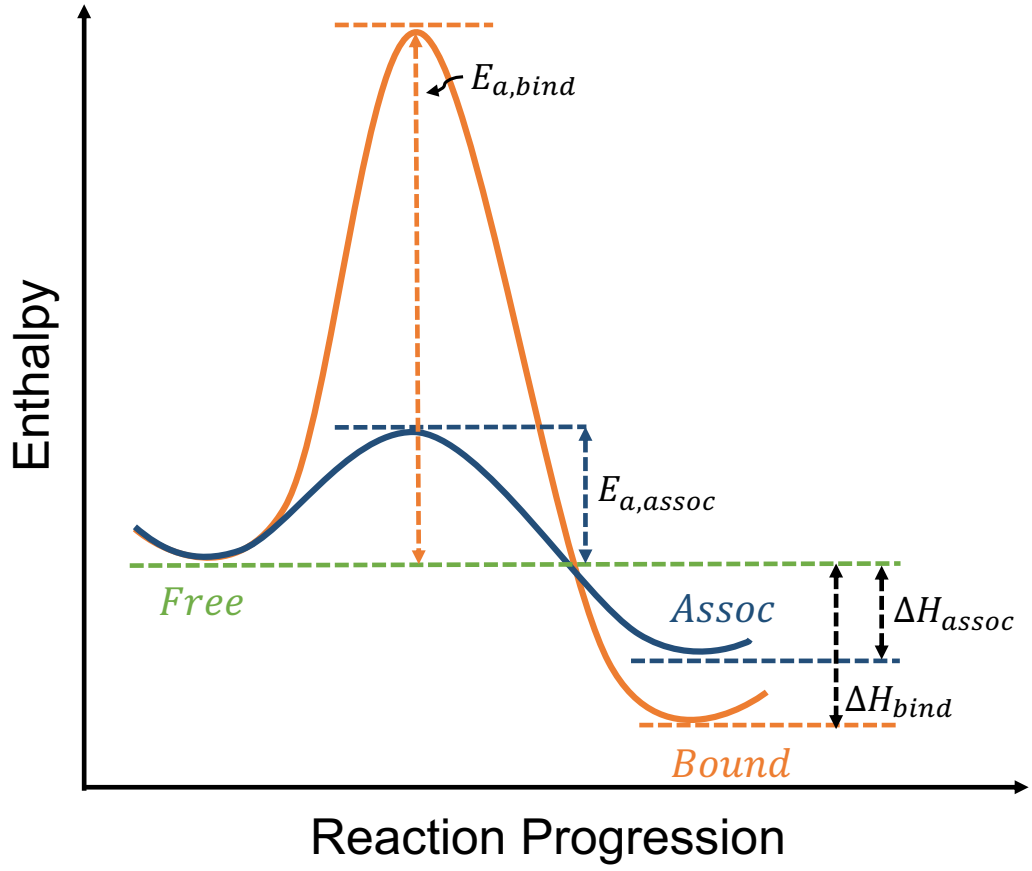

Figure 6S10: Enthalpy diagrams for ligand binding and association on the QD surface. The ΔH for both these processes is differed by a factor 2 (from section 3 of Results and discussion) but their activation energies (E_a) are differed by a factor 5. These diagrams clearly indicate the stronger interactions by bound ligands on the QD surface.

References

(1) Costigliola, L.; Heyes, D. M.; Schrøder, T. B.; Dyre, J. C. Revisiting the Stokes-Einstein Relation without a Hydrodynamic Diameter. *Journal of Chemical Physics* **2019**, *150* (2). https://doi.org/10.1063/1.5080662.

(2) Santos, F. J. V.; Nieto De Castro, C. A.; Dymond, J. H.; Dalaouti, N. K.; Assael, M. J.; Nagashima, A. Standard Reference Data for the Viscosity of Toluene. *J Phys Chem Ref Data* **2006**, *35* (1), 1–8. https://doi.org/10.1063/1.1928233.

(3) Moreels, I.; Lambert, K.; Smeets, D.; De Muynck, D.; Nollet, T.; Martins, J. C.; Vanhaecke, F.; Vantomme, A.; Delerue, C.; Allan, G.; Hens, Z. Size-Dependent Optical Properties of Colloidal PbS Quantum Dots. *ACS Nano* **2009**, *3* (10), 3023–3030. https://doi.org/10.1021/nn900863a.

(4) Aguilar, J. A.; Nilsson, M.; Bodenhausen, G.; Morris, G. A. Spin Echo NMR Spectra without J Modulation. *Chemical Communications* **2012**, *48* (6), 811–813. https://doi.org/10.1039/c1cc16699a.

Appendix III. Python code for fitting NMR data to the lineshape function (Chapter 6)

```
# Importing all Necessary libraries for running the code
import pandas as pd
import numpy as np
from scipy.optimize import least_squares
import matplotlib.pyplot as plt
from scipy.optimize import fmin_slsqp
from scipy.optimize import Bounds
from scipy.optimize import minimize

# Reading the deconvoluted csv file for 23C generated by MNova
OA_QD_6_23 = pd.read_csv('/Users/shravanuppala/Documents/Documents/chemistry/VT/2023 Fall/UNC-QD/Sample6_VT/Sample6_23C.csv')
#Does not contain frequency column only ppm column

#Adding frequency column to the table; ppm multiplied by 600 since sample measured on 600 MHz
OA_QD_6_23['Freq'] = 600*OA_QD_6_23['ppm']

# Renaming the column heads to Exch and Non_Exch
OA_QD_6_23 = OA_QD_6_23.rename(columns={'Peak 1': 'Non_Exch_Int', 'Peak 2': 'Exch_Int'})

# Creating new dataframes containing datapoints only from Exchange peak and Non-Exchange peak
Exch_fit = OA_QD_6_23[['Freq', 'Exch_Int']]
Non_Exch = OA_QD_6_23[['Freq', 'Non_Exch_Int']]

# Identifying the frequency at which maximum intensity occurs for exchanging peak
max_int_freq = Exch_fit.loc[Exch_fit['Exch_Int'].idxmax()] # this will let us know the exchange peak position
max_int_freq_va= max_int_freq['Freq']#

# checking the frequency at which maximum intensity occurs for non-exchaning peak
max_int_NE_freq = Non_Exch.loc[Non_Exch['Non_Exch_Int'].idxmax()]


max_int_NE_freq_va = max_int_NE_freq['Freq']

# Filtering intensities which are <5% in Exch_int column as they can affect the fitting of the curve
```

```
Filter_constraint = 0.05*Exch_fit['Exch_Int'].max()
Exch_fit_filter = Exch_fit[(Exch_fit['Exch_Int']>=Filter_constraint)]


# Filtering intensities which are <5% in Non_Exch_int column as they can affect the fitting of the curve

Filter_constraint_NE = 0.05*Non_Exch['Non_Exch_Int'].max()
Non_Exch_filter = Non_Exch[(Non_Exch['Non_Exch_Int']>=Filter_constraint_NE)]


## Creating a list of parametric constants used in complete lineshape and lorentzian function ##

Population_Free = 0.59
# Fraction determined from diffusion coefficients; partition fractions

Population_Bound = 1-Population_Free
# Fraction determined from diffusion coefficients; partition fractions

FWHM_Free_Hz = 0.41
# Value Determined using modified CPMG experiment for only Free Oleic Acids in Toluene

T2_Free_s = 1/(np.pi*FWHM_Free_Hz)

FWHM_Bound_Hz = 6.01
# Value Determined using modified CPMG experiment for only bound OA to QD with no free ligands

T2_Bound_s = 1/(np.pi*FWHM_Bound_Hz)

Free_ppm = 5.580
# determined from the free Oleic Acid peak in toluene with no QD in solution

Free_Hz = 600*Free_ppm
# Converting the free ligand peak position from ppm to hz; Measurement made on 600 MHz instrument

Average_HZ = max_int_freq_va
# chemical shift of exchange peak in Hz

Bound_HZ = (Average_HZ-(Population_Free*Free_Hz))/Population_Bound
# QD associated ligand position can be determined from known Exchange and free signal chemical shifts

delta_freq = Bound_HZ-Free_Hz
```

```
# small delta frequency is a constant which is the frequency distance between ligand peaks in different state

S_const = ((Population_Free/T2_Bound_s)+(Population_Bound/T2_Free_s))
# creating this constant to simplify the lineshape function when it is defined

NEP_position = max_int_NE_freq_va
# Non Exchaning Peak's chemical shift in Hz

Peak_width_NE = 55.3
# this is the FWHM of non exchanging peak determined by deconvoluting using MNova


## FITTING EXCHANGE PEAKS ##
# creating a new Delta_Freq column in Exch_fit_filter dataframe using a simple formula shown below
# Creating it for both original and filtered data Sets. Both data sets will be used later
Exch_fit['Delta_Freq_Ex'] = 0.5*(Free_Hz+Bound_HZ)-Exch_fit['Freq']
Exch_fit_filter['Delta_Freq_Ex'] = 0.5*(Free_Hz+Bound_HZ)-Exch_fit_filter['Freq']
Exch_fit_filter.head()

# Defining Complete lineshape Function to generate "Stimulated Data"

def fit_func_exch(df, params):

    # Variable Parameters used for fitting our experimental data
    Tau, C0 = params
    # Formula for variable "P"
    P = (Tau)*((1/(T2_Bound_s*T2_Free_s))\
              -(4*np.pi*np.pi*df['Delta_Freq_Ex']*df['Delta_Freq_Ex'])\
              +(np.pi*np.pi*delta_freq*delta_freq))\
              +(Population_Free/T2_Free_s)\
              +(Population_Bound/T2_Bound_s)

    # Formula for variable  "Q"
    Q = (Tau)*((2*np.pi*df['Delta_Freq_Ex'])\
              -(np.pi*delta_freq)\
              *(Population_Bound - Population_Free))

    # Formula for variable "R"
    R = ((2*np.pi*df['Delta_Freq_Ex'])\
        *(1+((Tau)*((1/T2_Free_s)+(1/T2_Bound_s))))\
        +((np.pi*delta_freq*(Tau))*((1/T2_Free_s)-(1/T2_Bound_s)))\
        +((np.pi*delta_freq)*(Population_Bound-Population_Free)))

    # Complete Lineshape Function for generating Exchanging signal S(v)
```

```
    S = C0*((P*(1 + ((Tau)*S_const)))+ Q*R)/((P*P)+(R*R))

    return S

## TWO TYPES OF OPTIMIZATION FUNCTION IS USED ##
# Both Functions will be iteratively applied to get

# to get the initial guess values of Tau, C0 parameters
def objective_func_LS(params):
    y_fit = fit_func_exch(Exch_fit_filter, params)  # Calculate the fitted data using the fitting
function
    residuals = Exch_fit_filter['Exch_Int'] - y_fit  # Calculate the residuals
    return residuals

# to get more accurate values of Tau, C0 parameters
def objective_func_min(params):
    y_fit = fit_func_exch(Exch_fit_filter, params)  # Calculate the fitted data using the fitting
function
    residuals = (Exch_fit_filter['Exch_Int'] - y_fit)*(Exch_fit_filter['Exch_Int'] - y_fit) # Calculate
the residuals
    residuals_sum = residuals.sum()
    cost_fn = (residuals_sum**0.5)/(2*len(residuals))
    return cost_fn

# Preparing the data and initial Guesses
x_data = Exch_fit_filter['Freq']
y_data = Exch_fit_filter['Exch_Int']

initial_guess = [0.0009, 8865980.212]

# Giving constraints conditions

param_bounds_Tau = (0,2)
param_bounds_C = (0, np.inf)

param_bounds = Bounds([0, 2], [0, np.inf], [0, np.inf])

# Minimize function enables boundary conditions on the parameters used
result1_0 = minimize(objective_func_min, initial_guess, bounds = [(0, 2),(0, np.inf)])
result1_0.x
# Narrowing Down the initial guesses for the curve-fit and use it for Least Squares as it gives
better fit

Second_guess = result1_0.x
result_0 = least_squares(objective_func_LS, Second_guess, method='trf', verbose=1)
result_0.x
```

```
# Using minimization function and second guess to see if we get improved results
Third_guess = result_0.x
result2_0 = minimize(objective_func_min, Third_guess, bounds = [(0, 2),(0, np.inf)])
result2_0

# Utilizing Lease square function and guesses from result2_0 to see if we find improved fits
Fourth_guess = result2_0.x
result3_0 = least_squares(objective_func_LS, Fourth_guess, method='trf', verbose=1)
result3_0.x
# Continue the above cycle till you observe no changes in value of the results from each iteration


def Fitted_Intensities(Exch_fit_filter, params):

    # Variable Parameters used for fitting our experimental data
    Tau, C0 = params
    # Formula for variable "P"

    P = (Tau)*((1/(T2_Bound_s*T2_Free_s))\
            -(4*np.pi*np.pi*Exch_fit_filter['Delta_Freq_Ex']*Exch_fit_filter['Delta_Freq_Ex'])\
            +(np.pi*np.pi*delta_freq*delta_freq))\
            +(Population_Free/T2_Free_s)\
            +(Population_Bound/T2_Bound_s)

    # Formula for Q
    Q = (Tau)*((2*np.pi*Exch_fit_filter['Delta_Freq_Ex'])\
            -(np.pi*delta_freq)\
            *(Population_Bound - Population_Free))

    # Formula for variable "R"
    R = ((2*np.pi*Exch_fit_filter['Delta_Freq_Ex'])\
        *(1+((Tau)*((1/T2_Free_s)+(1/T2_Bound_s))))\
        +((np.pi*delta_freq*(Tau))*((1/T2_Free_s)-(1/T2_Bound_s)))\
        +((np.pi*delta_freq)*(Population_Bound-Population_Free)))

    # Formula for Signa Intensity Exchanging S(v)
    S = C0*((P*(1 + ((Tau)*S_const)))+ Q*R)/((P*P)+(R*R))

    return S

# Generating the Stimulated Data based on the results generated by Least_Square and
Minimization function
# Stimulated Data is used for plotting the data and for visual comparison of the fit
y_Stim_LS = Fitted_Intensities(Exch_fit_filter,result3_0.x)
y_Stim_min = Fitted_Intensities(Exch_fit_filter,result2_0.x)
```

```
# Plotting Experimental Data and Stimulated Intensity Data taht is generated using LS and Min function with Experimental Data
# The below plots are purely for comparison purpose
x = Exch_fit_filter['Freq']
y1 = Exch_fit_filter['Exch_Int']
y2 = y_Stim_LS
y3 = y_Stim_min
plt.plot(x, y1, label = 'Experiment')
plt.plot(x, y2, label = 'Stimulated_Least_Squares')
plt.plot(x, y3, label = 'Stimulated_Minimization')

plt.xlabel('Frequency(hz)')
plt.ylabel('Signal Intensity')

plt.legend()
plt.title('Comparing LS and Min function Stimulated Data and Experimental Data')

plt.show()


y_Stim_LS_unfiltered = Fitted_Intensities(Exch_fit,result3_0.x)
y_Stim_min_unfilterd = Fitted_Intensities(Exch_fit,result2_0.x)

## Plotting the generated Intensity values using LS and Min function with Experimental Data
x = Exch_fit['Freq']
y1 = Exch_fit['Exch_Int']
y2 = y_Stim_LS_unfiltered
y3 = y_Stim_min_unfilterd
plt.plot(x, y1, label = 'Experiment')
plt.plot(x, y2, label = 'Stimulated_Least_Squares')
#plt.plot(x, y3, label = 'Stimulated_Minimization')

plt.xlabel('Frequency(hz)')
plt.ylabel('Signal Intensity')

plt.legend()
plt.title('Comparing LS and Min function Stimulated Data and Experimental Data')

plt.show()


# The next step is to fit the Non-Exchanging deconvoluted peak with Lorentzian Equation

# Definining Delta Frequency for Non-Exchange system
```

```
Non_Exch_filter['Delta_Freq_NonEx'] = Non_Exch_filter['Freq']-NEP_position

Non_Exch['Delta_Freq_NonEx'] = Non_Exch['Freq']-NEP_position
Non_Exch_filter.head()


# Defining the Fit_function for Non-Exchanging System. Lorentzian curve is used and only one
Variable parameter 'C1'

def fit_func_NE(df, param):

    # Formula for Signal Intensity Non-exchanging S(V)
    C1 = param
    S_ne = (C1 / 2*np.pi) * ((Peak_width_NE / 2) / \
          ((df['Delta_Freq_NonEx'] * df['Delta_Freq_NonEx']) + ((Peak_width_NE / 2) *
(Peak_width_NE/ 2))))

    return S_ne

def objective_func_LS_NE(param):
    y_fit = fit_func_NE(Non_Exch_filter, param)  # Calculate the fitted data using the fitting
function
    residuals_NE = Non_Exch_filter['Non_Exch_Int'] - y_fit  # Calculate the residuals
    return residuals_NE

# to get more accurate values of C1 parameter
def objective_func_min_NE(param):
    y_fit = fit_func_NE(Non_Exch_filter, param)  # Calculate the fitted data using the fitting
function
    residuals_NE = (Non_Exch_filter['Non_Exch_Int'] - y_fit)*(Non_Exch_filter['Non_Exch_Int']
- y_fit) # Calculate the residuals
    residuals_sum_NE = residuals_NE.sum()
    cost_fn_NE = (residuals_sum_NE**0.5)/(2*len(residuals_NE))
    return cost_fn_NE

initial_guess_C1 = [150000] # initial guess for C1 parameter in Lorentzian Function

result_0_NE = minimize(objective_func_min_NE, initial_guess_C1, bounds = [(0, np.inf)])
# result_0_NE.x # execute this step to check if the values remain same in next iterations

result1_0_NE = least_squares(objective_func_LS_NE, initial_guess_C1, method='trf',
verbose=1)
# result1_0_NE.x # execute this step to check if the values remain same in next iterations

def Fitted_Intensities_NE(df, param):
```

```
    # Formula for Signal Intensity Non-exchanging S(V)
    C1 = param
    S_ne = (C1 / 2*np.pi) * ((Peak_width_NE / 2) / \
          ((df['Delta_Freq_NonEx'] * df['Delta_Freq_NonEx']) + ((Peak_width_NE / 2) *
(Peak_width_NE/ 2))))

    return S_ne

# Fitting for filtered Non-Exchanging signal data
y_Stim_min_NE = Fitted_Intensities_NE(Non_Exch_filter,result1_0_NE.x)
y_Stim_LS_NE = Fitted_Intensities_NE(Non_Exch_filter,result_0_NE.x)

# Fitting for unfiltered Exchanging signal data
y_Stim_min_NE_unfilter = Fitted_Intensities_NE(Non_Exch,result1_0_NE.x)
y_Stim_LS_NE_unfilter = Fitted_Intensities_NE(Non_Exch,result_0_NE.x)

# Plotting Non-Exchanging Peak from experiment and comparing with Stimulated data
generated from LS and Min

x_data_NE = Non_Exch_filter['Freq']
y_data_NE = Non_Exch_filter['Non_Exch_Int']

plt.plot(x_data_NE, y_data_NE, label = 'Experiment_NE')
plt.plot(x_data_NE, y_Stim_LS_NE, label = 'Simulated_Least_Squares')
plt.plot(x_data_NE, y_Stim_min_NE, label = 'Simulated Minimization')

plt.xlabel('Frequency(hz)')
plt.ylabel('Signal Intensity')

plt.legend()
plt.title('Comparing filtered Simulated Data and Experimental Data of Non-Exchanging Peak')

plt.show()

# Comparing Stimulated data using Minimization and LS with Experimental Non-Exchanging
Data

x_data_NE_unfilter = Non_Exch['Freq']
y_data_NE_unfilter = Non_Exch['Non_Exch_Int']

plt.plot(x_data_NE_unfilter, y_data_NE_unfilter, label = 'Experiment_NE')
plt.plot(x_data_NE_unfilter, y_Stim_LS_NE_unfilter, label = 'Simulated_Least_Squares')
plt.plot(x_data_NE_unfilter, y_Stim_min_NE_unfilter, label = 'Simulated Minimization')

plt.xlabel('Frequency(hz)')
plt.ylabel('Signal Intensity')
```

```
plt.legend()
plt.title('Comparing unfiltered Simulated Data and Experimental Data of Non-Exchanging Peak')

plt.show()


# Comparing Experimental Data with Stimulated Data generated by iterating Complete lineshape
and Lorentzian fn
Total_Intensity = y_Stim_LS_unfiltered + y_Stim_min_NE_unfilter
Experiment_Data = OA_QD_6_23['Intensity']

# Plotting Experimental Data and Stimulated Data

x_t = OA_QD_6_23['Freq']
y_TI = Total_Intensity
y_exp = Experiment_Data

plt.plot(x_t, y_TI, label = 'Simulated Total Intensity')
plt.plot(x_t, y_exp, label = 'Experimental Intensity')

plt.xlabel('Frequency(hz)')
plt.ylabel('Signal Intensity')

plt.legend()
plt.title('Comparing Simulated Data and Experimental Data of Exchaning and Non-Exchanging
peak')

plt.show()

plt.gca().invert_xaxis()# inverting x-axis values

x_ppm = x_t = OA_QD_6_23['ppm']

plt.plot(x_ppm, y_exp, label = '1D NMR Spectrum', color='#79BAEC', linewidth=3)
plt.plot(x_ppm, y_TI, label = 'Lineshape Fit', color='#0041C2', linewidth =2.5,
linestyle='dashed')

plt.xlabel('ppm', fontsize = 18)

plt.legend(fontsize = 12, frameon=False, labelcolor='black')
plt.xticks(fontsize=16)

ax = plt.gca()

# Remove top, right and left graph borders/spines
```

```
ax.spines['top'].set_visible(False)
ax.spines['right'].set_visible(False)
ax.spines['left'].set_visible(False)
ax.spines['bottom'].set_linewidth(1.5)
ax.yaxis.set_ticks([])
```